**UNIVERSITY OF STRASBOURG**

**UNIVERSIDADE FEDERAL DO RIO GRANDE DO SUL**

**ÉCOLE DOCTORALE DES SCIENCES CHIMIQUES / PROGRAMA DE PÓS-GRADUAÇÃO EM QUÍMICA**

**Institut de Chimie de Strasbourg – UMR 7177 / Instituto de Química UFRGS**

# THESIS

Presented by

## Yuri Clemente ANDRADE SOKOLOVICZ

on: September 27, 2019

to obtain the degree of

**Doctor from the University of Strasbourg and Universidade Federal do Rio Grande do Sul**

Discipline / Specialty: Chemistry / Organometallic Chemistry

## Sustainable Transformations of CO$_2$ in Methanol and New Polymeric Graphene Nanocomposites

| THESIS directed by: | Mr. DAGORNE Samuel | Dr., Unistra and |
| | Mr. SCHREKKER Henri Stephan | Dr., UFRGS |

| MEMBERS OF THE JURY: | Mr. LOUIS Benoît | Dr., Unistra |
| | Mr. CURTI MUNIZ Edvani | Dr., UEM |
| | Mr. ROGÉRIO ZENI Gilson | Dr., UFSM |
| | Mr. ZIMNOCH DOS SANTOS João Henrique | Dr., UFRGS |
| | Mr. RIBEIRO GREGÓRIO José | Dr., UFRGS |

**UNIVERSITY OF STRASBOURG**

**UNIVERSIDADE FEDERAL DO RIO GRANDE DO SUL**


**ÉCOLE DOCTORALE DES SCIENCES CHIMIQUES / PROGRAMA DE PÓS-GRADUAÇÃO EM QUÍMICA**

**Institut de Chimie de Strasbourg – UMR 7177 / Instituto de Química UFRGS**


Yuri Clemente Andrade Sokolovicz


# Sustainable Transformations of $CO_2$ in Methanol and New Polymeric Graphene Nanocomposites


Tese apresentada como requisito parcial para a obtenção do grau de Doutor em Química


Prof. Dr. Henri Stephan Schrekker
Orientador

Prof. Dr. Samuel Dagorne
Orientador


Porto Alegre, setembro/2019

A presente tese foi realizada inteiramente pelo autor, exceto as colaborações as quais serão devidamente citadas nos agradecimentos, no período entre outubro/2015 e setembro/2019, no Instituto de Química da Universidade Federal do Rio Grande do Sul sob Orientação do Professor Doutor Henri Stephan Schrekker e no Instituto de Química da Universidade de Estrasburgo sob Orientação do Professor Doutor Samuel Dagorne. A tese foi julgada adequada para a obtenção do título de Doutor em Química pela seguinte banca examinadora:

**Comissão Examinadora:**

Prof. Dr. Benoît Louis

Prof. Dr. Edvani Curti Muniz

Prof. Dr. Gilson Rogério Zeni

Prof. Dr. João Henrique Zimnoch
dos Santos

Prof. Dr. José Ribeiro Gregório

Orientador
Prof. Dr. Henri Stephan Schrekker

Orientador
Prof. Dr. Samuel Dagorne

Aluno
Yuri Clemente Andrade Sokolovicz

# ACKNOWLEDGMENTS

Achieving a double Ph.D. degree from one of the best universities in Brazil and one of the best and most reputable universities in Europe requires a lot of dedication and support.

This thesis is mainly dedicated to my family in the persons of my parents, mother Maria Sokolovicz and father Sérgio Sokolovicz, for supporting and motivating me throughout this challenging period.

To my two supervisors: Samuel Dagorne and Henri Stephan Schrekker for the opportunity to share the immense knowledge they have.

To Michèle Oberson de Souza for her immense support in making the cotutelle process possible.

A special acknowledgment is dedicated to all the members of the laboratory on the French side: Frédéric for being my supervisor in the first 6 months at Unistra, David, Jean Charlie, Anaelle, Andrieli and Rosita. Pierre and Beatrice, permanent researchers at UMR 7177.

To my colleagues of the TECNOCAT laboratory in Brazil: Debora, Júlia, Leonildo, Vinícius, Kauana, Juliana and Joana.

To the technicians and administrative employees of both Unistra and UFRGS.

To Clarissa Martins Leal Schrekker for the microbiological experiments with the reduced graphene oxide/PLLA biomaterials.

Finally, to all the other people/friends who helped me in one-way or another during the process.

# ABBREVIATIONS AND REPRESENTATIONS

| | |
|---|---|
| Ac | Acetate |
| Ar | Aryl |
| Bu | Butyl |
| BMS | Borane dimethylsulfide |
| HBcat | 1,3,2-Benzodioxaborole |
| Calc | Calculated |
| Conv | Conversion |
| DCM | Dichloromethane |
| DMA | Dynamic mechanical analysis |
| Eq | Equivalent |
| GPC | Gel permeation chromatography |
| HBpin | Pinacolborane |
| HBcat | Catecholborane |
| $^{i}$Pr | Isopropyl |
| LA | Lactide |
| L-LA | (S,S)-lactide = (3S)-cis-3,6-dimethyl-1,4-dioxan-2,5-dione |
| $M_n$ | Number-average molecular weight |
| $M_w$ | Weight-average molecular weight |
| NMR | Nuclear magnetic resonance |

| | |
|---|---|
| PDI | Polydispersity index |
| PLA | Poly(lactic acid) |
| PLDA | Poly(*D*-lactic acid) |
| PLLA | Poly(*L*-lactic acid) |
| Ref | Reference |
| ROP | Ring-opening polymerization |
| SEM | Scanning electron microscopy |
| $^t$Bu | *tert*-Butyl |
| TBA | Tetrabutylammonium |
| TBAAc | Tetrabutylammonium Acetate |
| Tg | Glass-transition temperature |
| Theo | Theoretical |
| THF | Tetrahydrofuran |
| TON | Turnover number |
| TOF | Turnover frequency |
| $CH_3OBpin$ | Methoxyborane |
| HOCOBpin | Formoxyborane |
| 9-BBN | 9-borabicyclo[3.3.1]nonane |

**Contents**

# 1   INTRODUCTION

## 1.1   Environmental impact of $CO_2$

The search for energy sources to enable the first industrial revolution machines production discovered in coal an excellent material capable of generating high temperatures, considered then the "ideal" and cheap candidate at that time. Nevertheless, excessive burning of fossil fuels has emitted increasing levels of carbon dioxide ($CO_2$) as a combustion product, which affected the important $CO_2$ balance that exists in the Earth's ecosystem. This resulted in increasing $CO_2$ levels in the atmosphere throughout the last century.

The annual $CO_2$ emissions from cement, liquid fuel (e.g. oil), solid fuel (e.g. coal), gas (e.g. natural gas), and gas flaring reached 140 billion ton in 2013 compared to a neglectable amount before the start of the first industrial revolution in 1860 (**Figure 1**).[1] **Figure 2** represents the emission of $CO_2$ by sector,[2] identifying the sector of generation of electricity by heating as the main responsible, followed by manufacturing and construction, and transportation on roads.
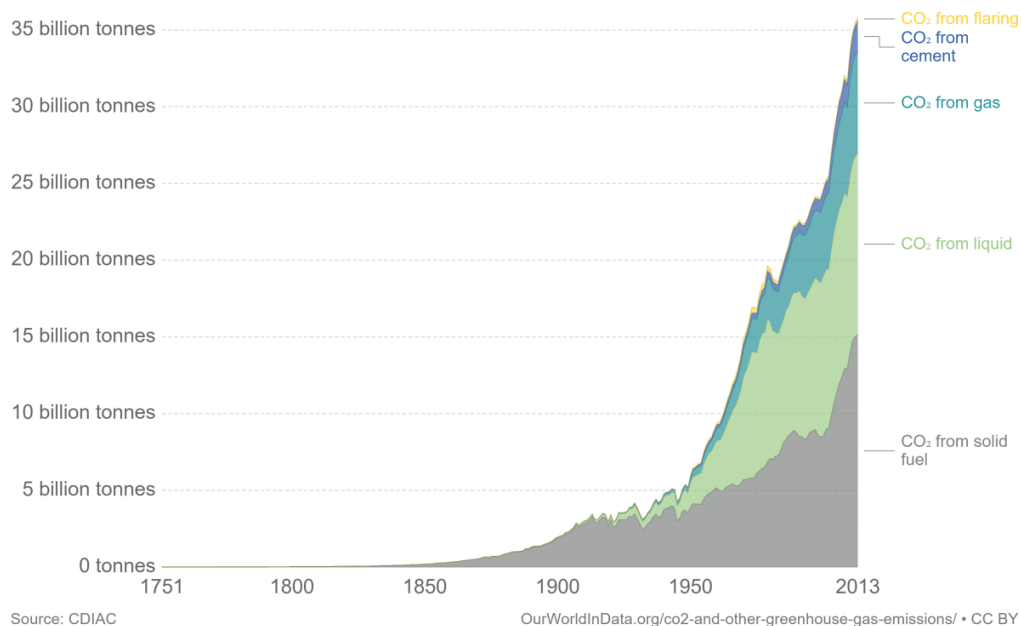
**Figure 1**. Worldwide $CO_2$ emissions by source.[1]
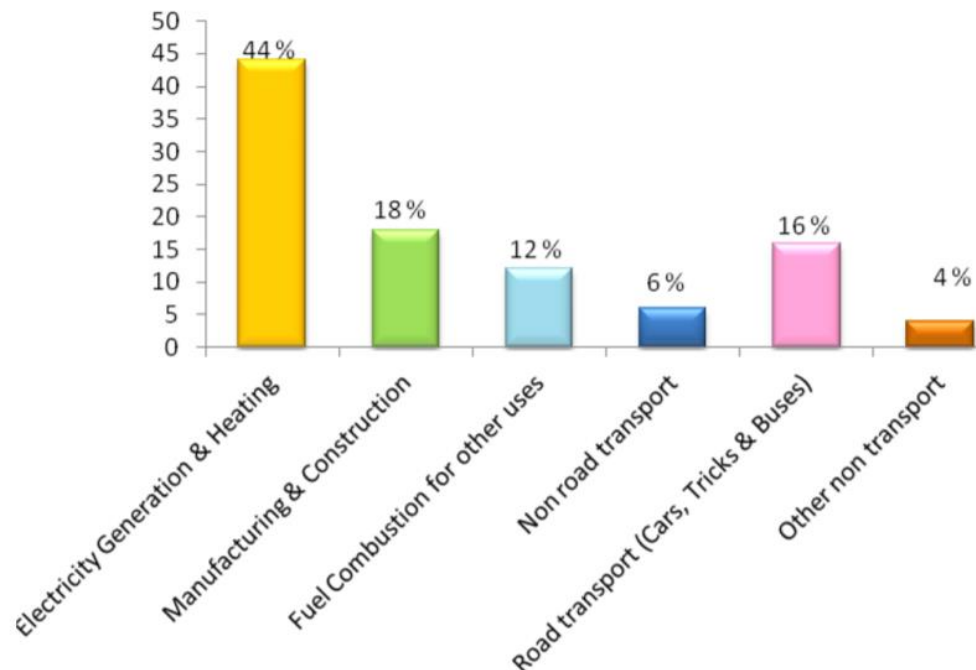
**Figure 2**. Emission of $CO_2$ in each sector.[2]

The excess of $CO_2$ in the atmosphere increases the absorption of the infrared waves emitted by the sun and also those reflected by the surface of the Earth. This process is called the greenhouse effect[3],[4] and increases the temperature of the Earth's atmosphere, being the main cause of global warming and, as a consequence, climate changes[5]: snow melt[6], rising sea levels[7], increasing global wave power[8], ocean acidification[9], increasing occurrence of hurricanes, among others. The most dangerous event would be a substantial water vaporization to the space, which in a normal scenario would happen only at an ocean surface temperature of 110 °C. At elevated atmospheric $CO_2$ concentrations this could occur at lower temperature, showing the critical importance to start normalizing the $CO_2$ emissions.[3]

Recently, its widely devastating potential was noted with the emergence of three tropical hurricanes of high category on the southwest coast of the United States (**Figure 3**), which impacted on the economy and in people's lives. This event has occurred due

to heating above normal of the Pacific waters, being the consequence of global warming, which is related to the emission of $CO_2$.
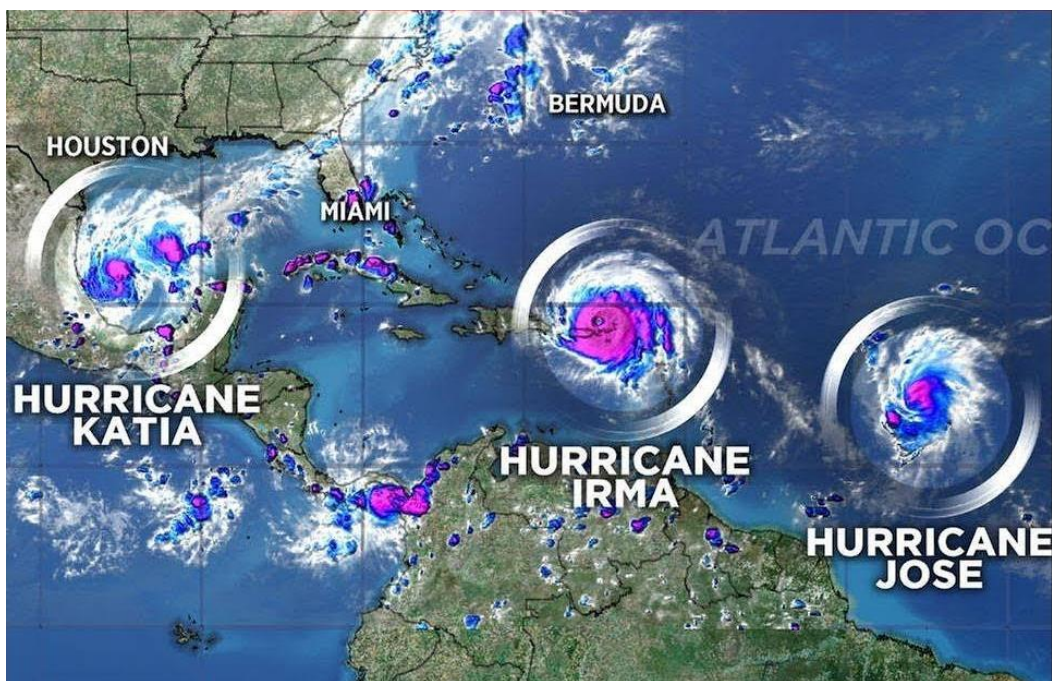


**Figure 3**. Three hurricanes in the Atlantic at the same time.
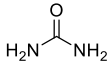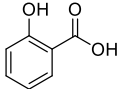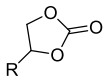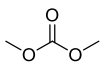
In this scenario, the development of novel $CO_2$-based technologies for the renewable production of fuels, chemicals and materials is highly desired.

### 1.1.1  Context of catalytic $CO_2$ transformations in chemicals, materials and fuels

Currently, our "quality" of life is greatly affected by petroleum-derived products, including, i.e. fuels, plastics and chemicals.[10] The amount of $CO_2$ emitted annually was 30 billion tons in 2006. Although $CO_2$ is thermodynamically very stable, synthetic transformation of $CO_2$ into chemicals, materials and fuels are possible.[11] As is shown in **Table 1**, the amount of $CO_2$ consumed to produce chemicals, fuels and materials was 114 million tons, representing only 0.4% of the total amount emitted.[1],[11] Interestingly, $CO_2$ already accounts for 74% of the raw material for the annual production of urea, an important chemical widely used in our society. Overall, 70-80% of the petroleum is used

as fuel source,[12] and the combustion of these fuels releases huge amounts of $CO_2$, which could serve as renewable source for fuel production by transforming it, for example, into methanol. Currently, only 2% of $CO_2$ is applied as feedstock for methanol production and new technologies have to be developed to increase its use (**Table 1**). It is important to note that not only methanol but also formic acid can be generated during the reduction of $CO_2$, justifying the importance of the advancement of chemistry in this area for the development of biorefineries. Formic acid is widely used today, representing an annual production of 700 thousand tons and there is still no industrial process that uses $CO_2$ as a raw material for its production. In addition, $CO_2$ can also be used for the production of materials like polycarbonates.[11]

**Table 1**. Chemicals, fuels and materials produced from $CO_2$.[11]

| Chemical | Molecular formula | Annual production | Annually utilized $CO_2$ as feedstock |
| --- | --- | --- | --- |
| Urea | | 150 million tons | 112 million tons |
| Methanol | $CH_3OH$ | 100 million tons | 2 million tons |
| Salicylic acid | | 70 thousand tons | 30 thousand tons |
| Formic acid | | 700 thousand tons | |
| Cyclic carbonates | | 80 thousand tons | 40 thousand tons |
| Di-methyl carbonate | | 10 million tons | |

The development of these transformations with the synthetic incorporation of the $CO_2$ one-carbon building block is still in its infancy. New methods should be discovered in the near future in both academia and industry having a positive environmental impact through the establishment of $CO_2$-based biorefineries.

## 1.2 Catalytic reduction of $CO_2$ by hydroboranes

Recent advances in the last 10 years in homogeneous catalysis have led to the emergence and development of new techniques for $CO_2$ reduction with various reducing agents, being hydrogenation,[13] hydrosilylation[14] and hydroboration[15] the most often used. The hydrogenation process would be the ideal process for large-scale $CO_2$ uptake. Although the reduction of $CO_2$ in formic acid has noticeably advanced, it is still not sufficient for industrial scale production.[16] The $CO_2$ hydrogenation into methanol also needs further improvement.[17] Similarly, the reduction of $CO_2$ into methanol with hydrosilanes and hydroboranes is still in its infancy.[15] As such, this thesis explored the catalyzed reduction of $CO_2$ with hydroboranes as an alternative.

During the $CO_2$ reducing process in presence of an hydroborane, the formation of formoxyborane, bis(boryl)acetal and methoxyborane, together with its co-product bis(boryl)ether, may be observed (**Scheme 1**). In this process, the reaction begins with a hydride transfer in the presence of a catalyst. There are mainly three types of catalytic transformations that can take place: metal hydride, Lewis base and Lewis pair catalysis. In addition, hydroborates can also reduce $CO_2$.[15]
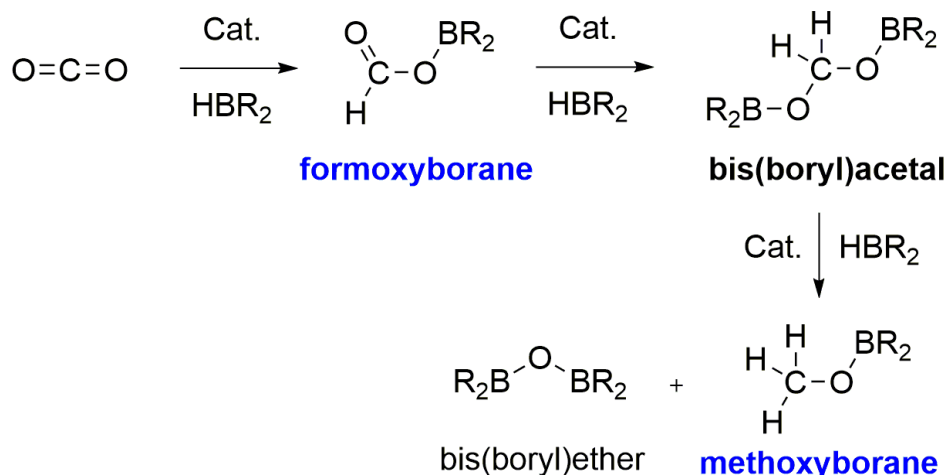
**Scheme 1**. Catalytic reduction of $CO_2$ in the presence of hydroboranes.

### 1.2.1  Metal hydride catalysts

The first example of a catalytic $CO_2$ reduction with a borane was reported by Guan *et al.*[18] Methoxycatecholborane ($CH_3OBcat$) and bis(boryl)ether (CatBOBcat) were generated selectively by using the nickel hydride species **1** and catecholborane (HBcat) after 1 h at room temperature with a turnover number (TON) of 495 and a turnover frequency (TOF) of 495 h$^{-1}$ (**Scheme 2**).
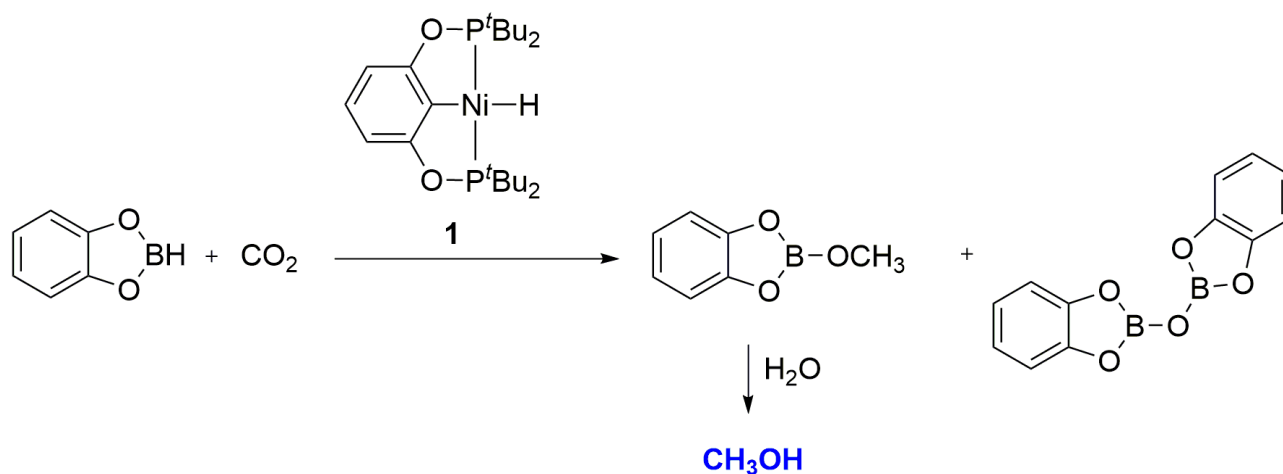


**Scheme 2**. Reduction of $CO_2$ catalyzed by Ni-H.

They proposed the metal hydride-based catalytic cycle for the $CO_2$ hydroboration (**Scheme 3**). This mechanism starts with the reversible insertion of $CO_2$ into the Ni-H forming NiOCOH, which in the presence of HBcat leads to the formation of HCOOBcat. Posteriorly, one more equivalent of HBcat reduces HCOOBcat to formaldehyde. Finally, additional equivalents of the HBcat produce $CH_3OBcat$ and regenerate the initial catalyst.
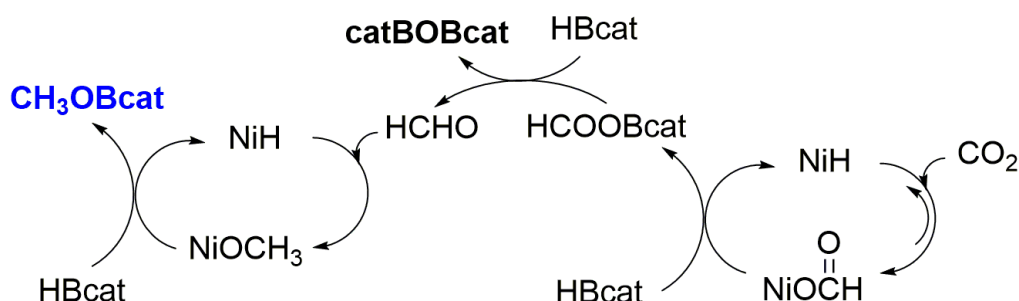


**Scheme 3**. Mechanism proposed by Guan for the Ni-H-catalyzed $CO_2$ reduction.

Sabo-Etienne *et al.*[19] reported the use of pinacolborane (HBpin) in the $CO_2$ reduction. The ruthenium complex **2** (**Figure 4**) was employed as catalyst. A mixture of five products was obtained using 10 mol% of **2** (**Scheme 4**). Among them, the reductive coupling of two $CO_2$ molecules (marked structure in **Scheme 4**) was reported for the first time.
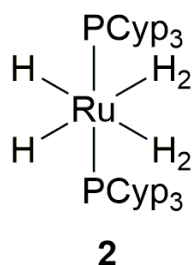


**Figure 4**. Ruthenium catalyst **2**.
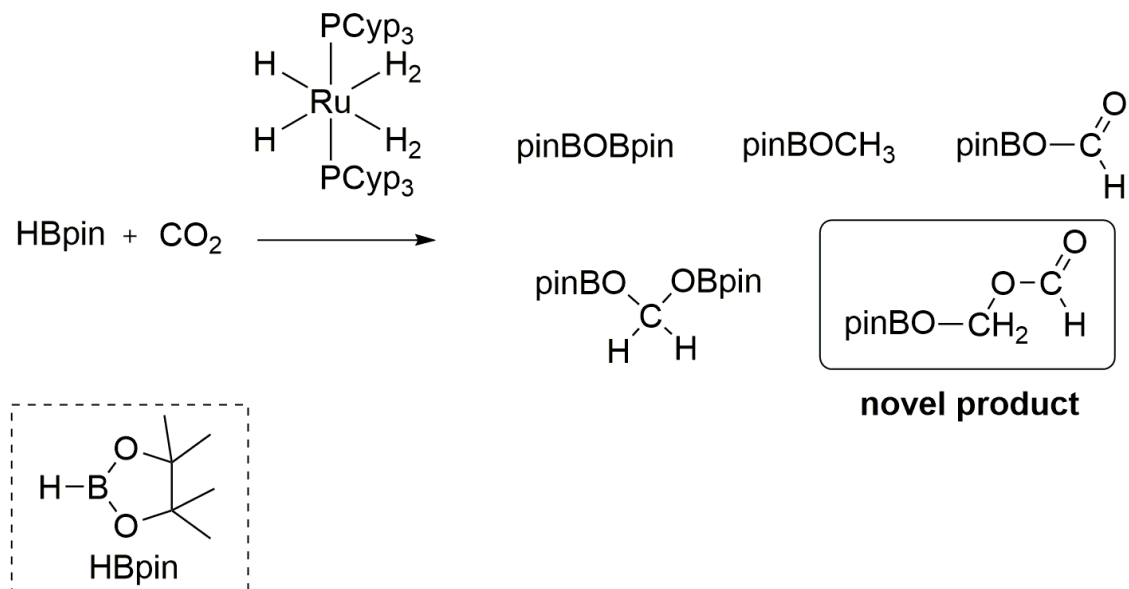
**Scheme 4**. $CO_2$ reduction with HBpin and ruthenium complex **2**.

Hill *et al.* reported the hydroborane-mediated $CO_2$ reduction with alkaline earth metal hydride catalysts.[20] The hydroborane used was HBpin and the magnesium (**3**) and calcium (**4**) catalysts (**Figure 5**) were selective for the formation of methoxyborane ($CH_3OBpin$) under mild conditions (T = 60 ºC), using THF as solvent. A drawback of this catalytic system is its low activity (TON: 10, TOF: 0.14 h$^{-1}$).



Ar = 2,6-di-*iso*propylphenyl
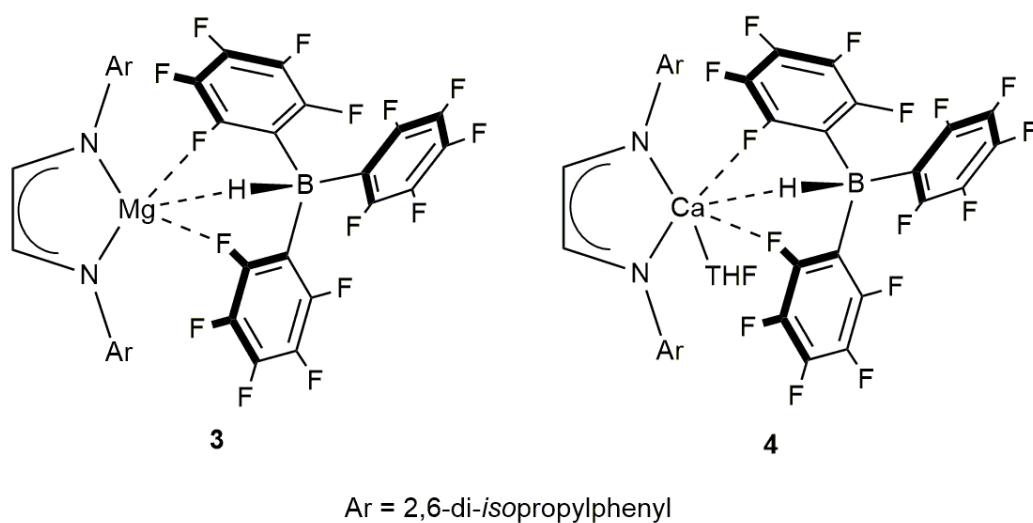
**Figure 5**. Magnesium and calcium complexes **3** and **4**.

The gallium hydride complex **5** (**Figure 6**) catalyzed the reduction of $CO_2$ with HBpin,[21] which further opened the range of metals that can be used as catalysts for this type of reaction. This catalytic system was also selective for methoxyborane formation and the activity was similar to the previous earth metal-hydride complex reported by Hill.[20] The mechanism starts with the insertion of $CO_2$ into the Ga-H bond, leading to the Ga-OCOH formation. The latter, in presence of HBpin, forms MeOBpin and pinBOBpin (**Scheme 5**).



**5**
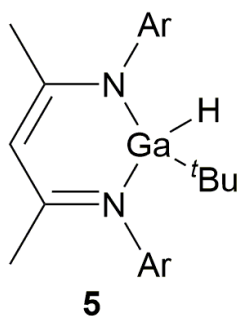
Ar = 2,6-di-*iso*propylphenyl

**Figure 6**. Gallium hydride complex **5**.



Ar = 2,6-di-*iso*propylphenyl
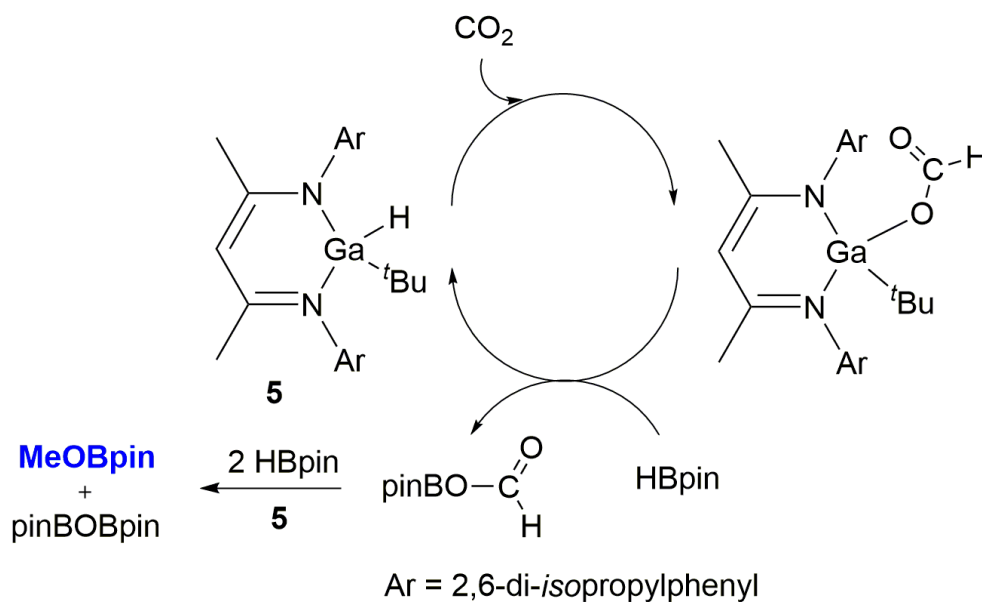
**Scheme 5**. $CO_2$ reduction to methoxyborane with HBpin catalyzed by Ga-H complex **5**.

The development of a selective catalytic $CO_2$ hydroboration process for the formation of the formic acid equivalent took more time. Shintani and Nozaki[22] reported in 2013 the first reduction of $CO_2$ with HBpin and a Cu-O$^t$Bu complex,[23] which forms the Cu-H complex **6** (**Figure 7**) after reacting with HBpin (**Scheme 6**).
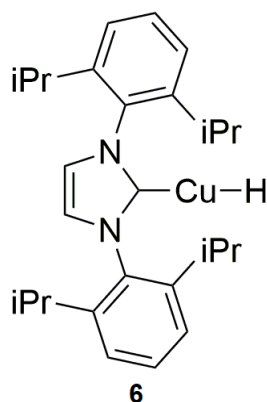


**Figure 7**. Copper hydride complex **6**.

Although the activity of this system was low, this was achieved under very mild conditions (T = 35 ºC). Investigations of the catalytic cycle demonstrated a similar mechanism to that proposed in previous studies. $CO_2$ inserted into the Cu-H bond forming Cu-OCOH, which then reacted with HBpin to afford the more stable formoxyborane, pinBOCOH. Finally, reacting this product with an acidic agent produced formic acid.
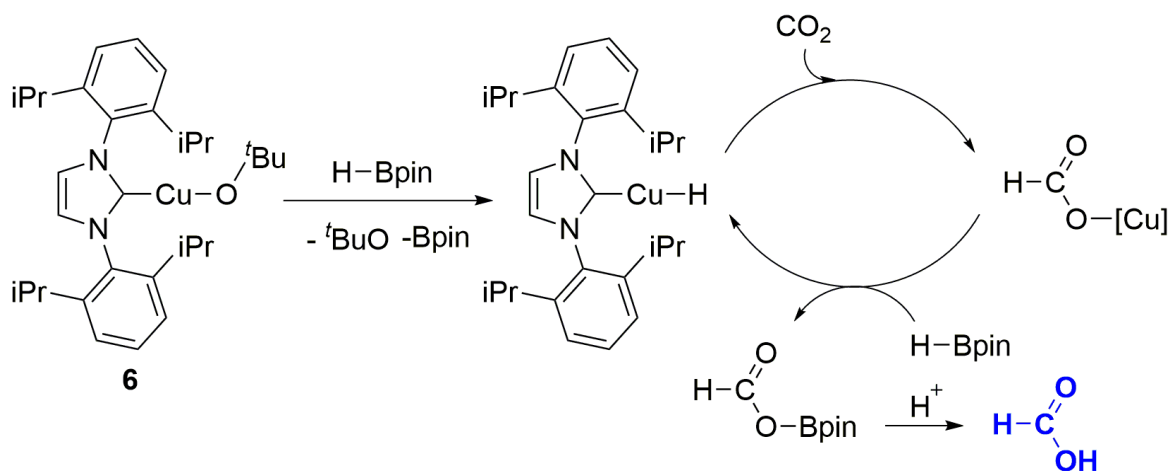


**Scheme 6**. Proposed mechanism for the Cu-H-catalyzed $CO_2$ reduction with HBpin.

Hazari *et al.* reported on the selective formation of borane formate in the catalytic reduction of $CO_2$ with hydroboranes, employing a Pd-H catalyst, complex **7** (**Figure 8**) that was formed *in situ* through reaction with HBpin. A high activity (TOF: 1550 $h^{-1}$) was achieved at room temperature.[24]
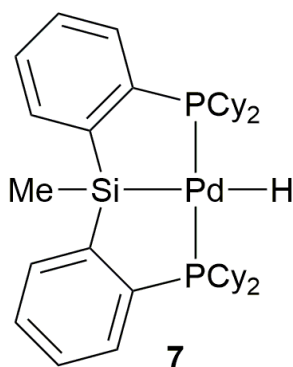


**Figure 8**. Pd-H complex **7** formed *in situ* in the $CO_2$ reduction with HBpin.

Basically, all metal hydride catalysts described so far follow the mechanism in which the metal-hydride leads to the formate group (M-OCOH) after insertion of $CO_2$. Followed by the abstraction of the -OCOH group by the borane forming formoxyborane, which can be stable or react with another borane. Therefore, the compounds bis(boryl)acetal or methoxyborane may be formed. It is important to point out that methoxyborane can be easily transformed into methanol by reacting with water. The reported mechanism for the Pd-H catalyst is represented in **Scheme 7**.[18]
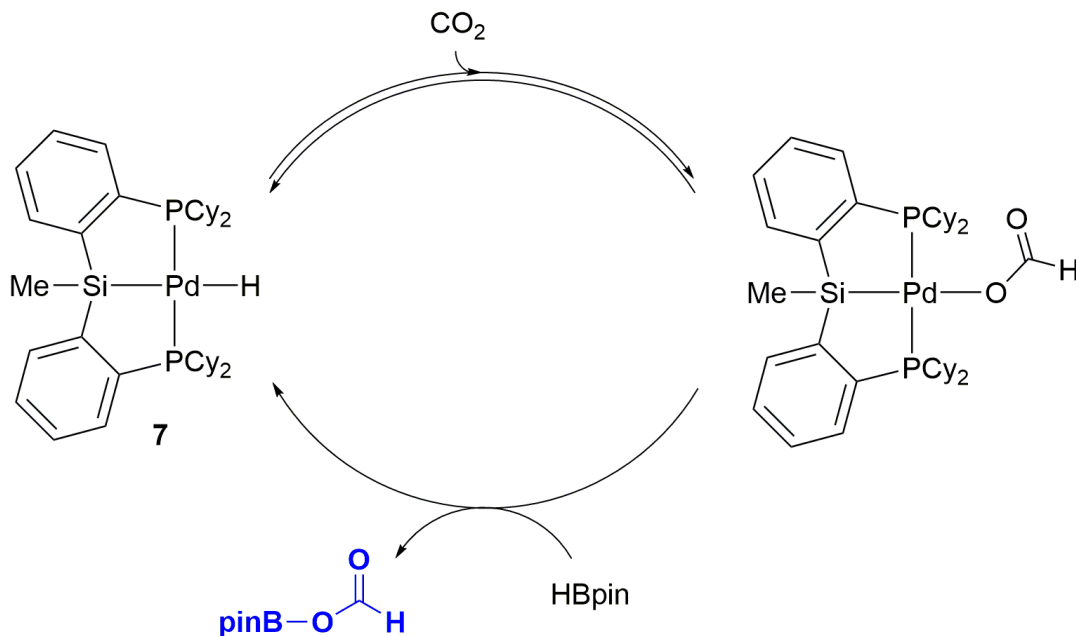
**Scheme 7**. Proposed mechanism for the Pd-H-catalyzed $CO_2$ reduction with HBpin.

### 1.2.2  Lewis base catalysts

The $CO_2$ reduction with hydroboranes by using metal-free catalysts could be environmentally favorable. Recently, Cantat *et al.* reported that organic Lewis bases are also suitable catalysts for such reaction.[25] Nitrogen bases such as TBD, Me-TBD and DBU and other guanidine and amidine derivatives (**8**, **9** and **10**; **Figure 9**) reduced $CO_2$ in the presence of the boranes 9-borabicyclo[3.3.1]nonane (9-BBN) and HBcat. The best activity for Me-TBD reached a TON of 648 and a TOF of 33 $h^{-1}$.
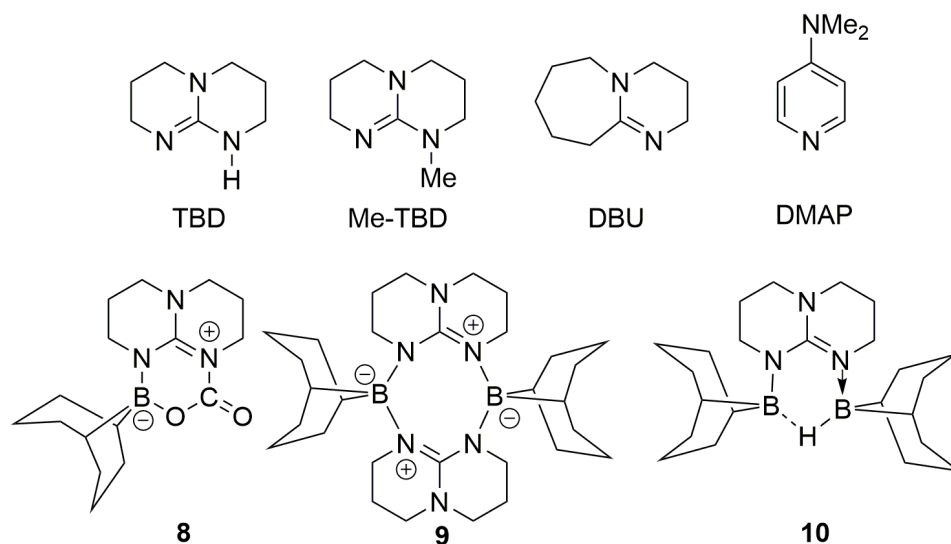
**Figure 9**. Lewis base catalysts in the $CO_2$ reduction with boranes.

Theoretical calculations were performed to better understand the type of activation (**Scheme 8**). It is interesting to note that the catalytic reaction can be initiated in two different ways, depending on the base used as catalyst. The hydroborane activation (a) was observed when MeTBD was employed, which changed into $CO_2$ activation (b) with TBD as catalyst.
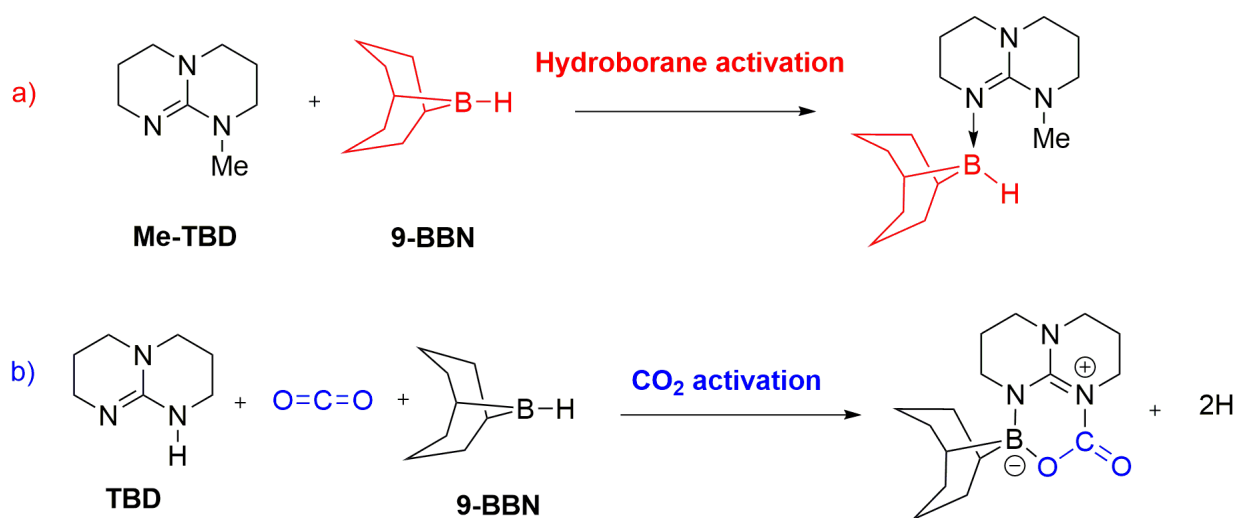


**Scheme 8**. Types of activation with MeTBD or TBD as catalyst.

Stephan *et al.* reported the ability of phosphines (**Figure 10**) to reduce $CO_2$ in the presence of hydroboranes.[26] The highest activity was achieved with the phosphine $^tBu_3P$, reaching a TON of 5,500 and a TOF of 170 $h^{-1}$ for methoxyborane formation. Mechanistically, both the phosphine and the hydroborane activate $CO_2$ simultaneously, thus generating a dual activation process (**Scheme 9**).
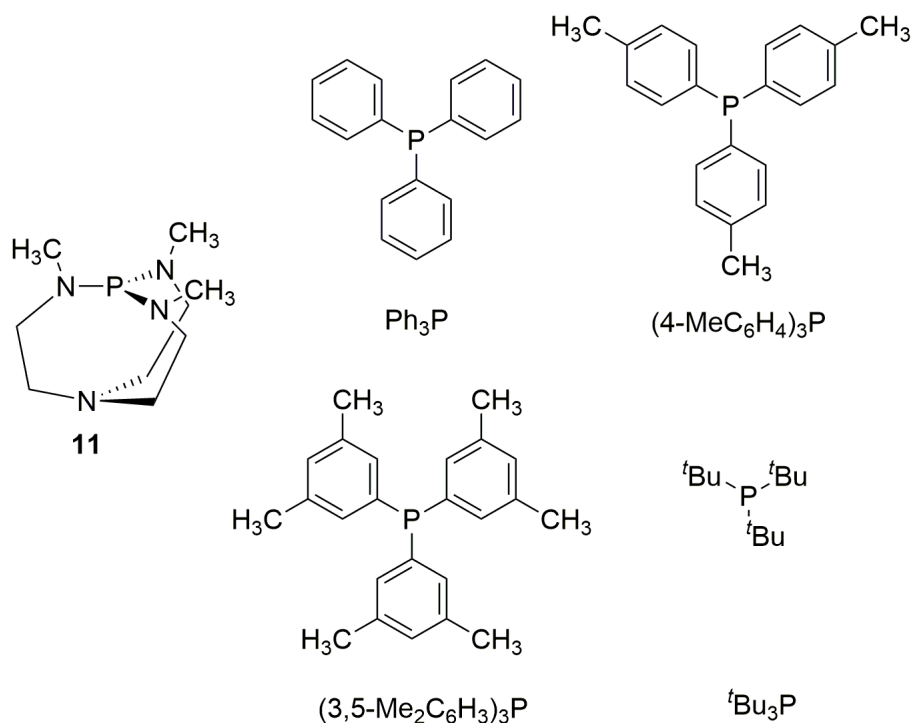


**Figure 10**. Phosphines Lewis base catalysts.
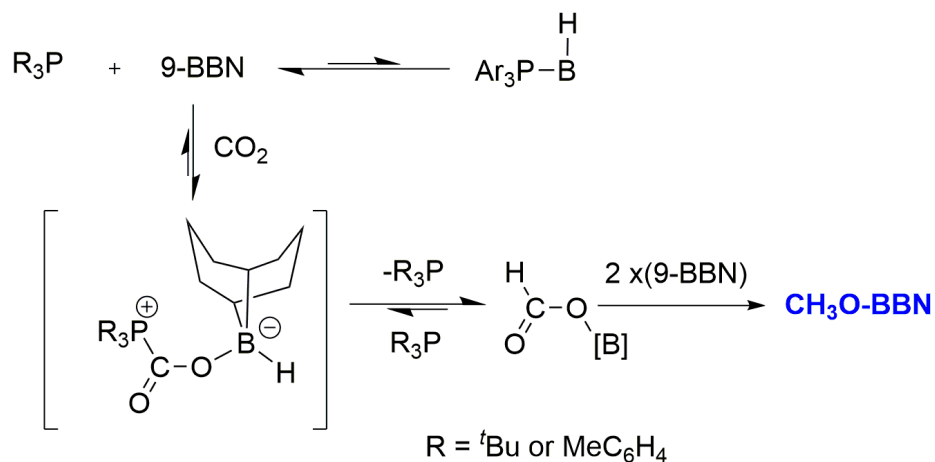


**Scheme 9**. $CO_2$ reduction with $R_3P$ and 9-BBN.

### 1.2.3  Lewis pair catalysts

Maron *et al.*[27] reported the first use of $H_3B.SMe_2$ as borane in a non-metallic system for the reduction of $CO_2$ (**Scheme 10**), which can be considered as a landmark study inasmuch as it is cheaper compared to the other boranes. The activity found was the highest reported so far for boroxyne (TON = 2950, TOF = 973 $h^{-1}$).
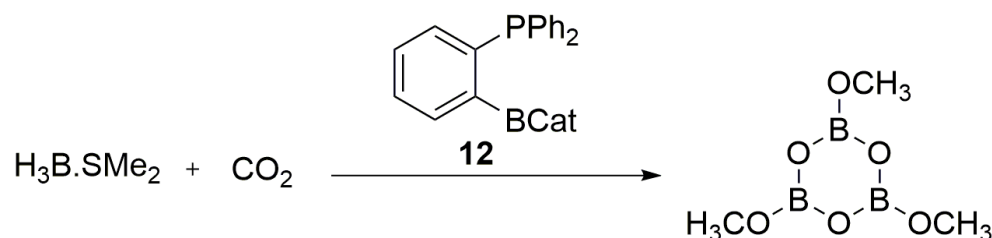


**Scheme 10**. Borane-mediated $CO_2$ reduction to boroxyne with **12** as catalyst.

In addition, they successfully demonstrated the use of an ambiphilic phosphine-borane catalyst. Catalyst **12** acts as both an electrophile and a nucleophile in the reaction with $CO_2$. Bouhadir *et al.*[28] reported the isolation and characterization of the product depicted in **Figure 11**.
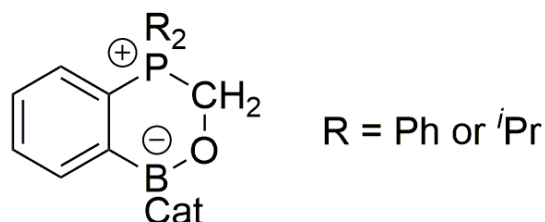


**Figure 11**. Product of the reaction between catalyst **12** and 1 equiv. of $CO_2$.

The first example of an aluminum-mediated $CO_2$ reduction with complex **13** and $NH_3BH_3$ was reported by Stephan[29] (**Scheme 11**). The interaction of **13** with $CO_2$ occurred in an ambiphilic manner and the treatment of the resulting product with water afforded methanol. A drawback of this system is that it is non catalytic. So far, only one Al-catalyzed system has been reported.[30]
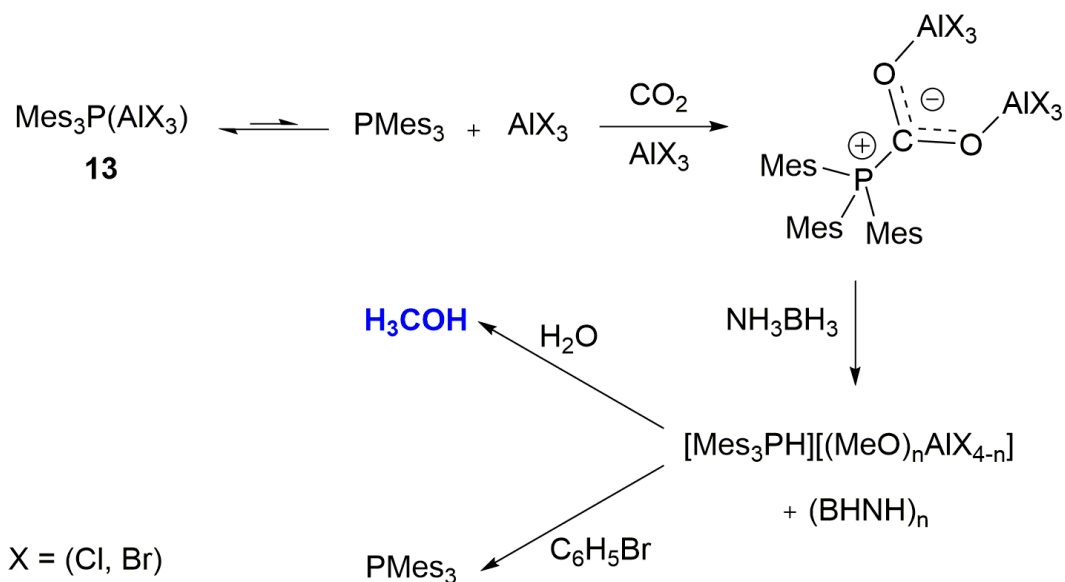
**Scheme 11**. Non-catalytic reduction of $CO_2$ into methanol using Al complex **13**.

Stephan *et al.* reported on the ability of the catalysts **15** and **16** (**Figure 12**) to reduce $CO_2$ with HBpin, HBcat and $H_3B.SMe_2$ as boranes.[31]
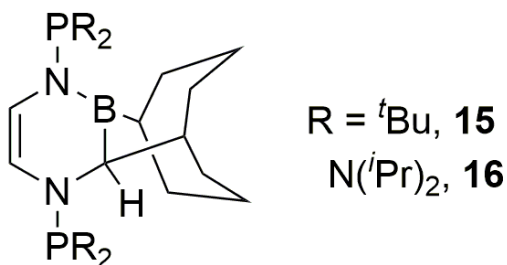


**Figure 12**. Catalysts **15** and **16**.

The mechanism starts (**Scheme 12**) with an ambiphilic activation of $CO_2$ with the frustrated Lewis pair catalysts (FLP). Interestingly, HBpin drove the reaction selectively to the formation of formoxyborane. When using HBcat, a higher activity was achieved for the selective methoxyborane generation.
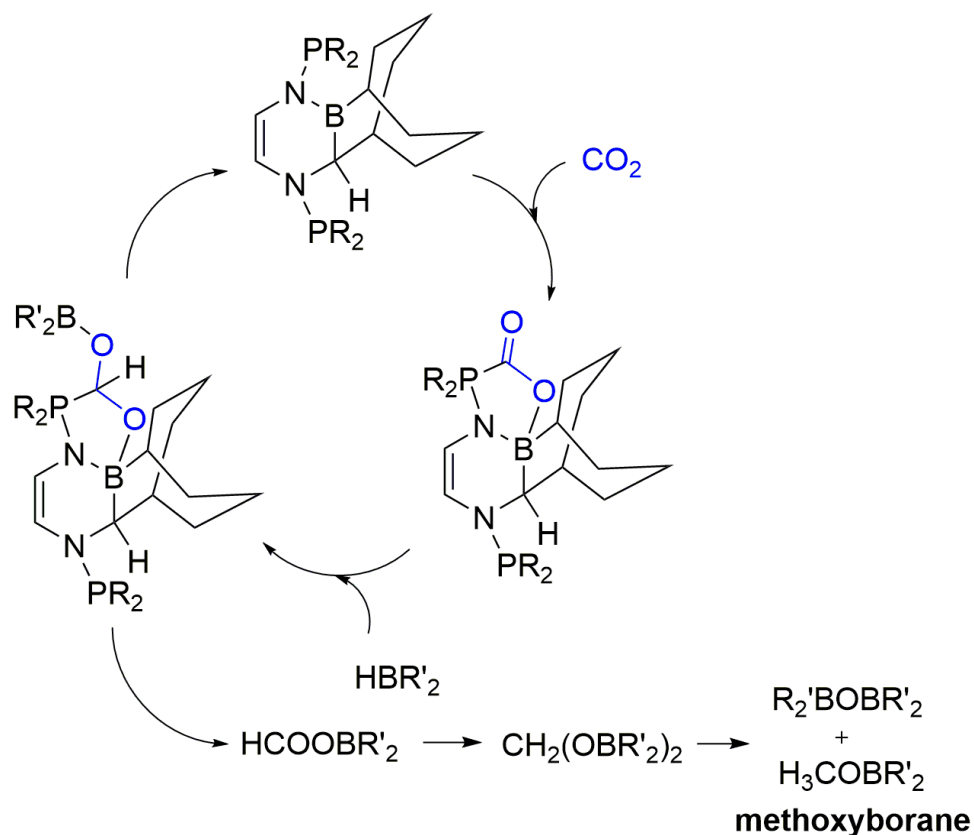
**Scheme 12**. Catalysts **15** and **16** and their ambiphilic activation mechanism for the $CO_2$ reduction into methoxyborane.[31]

### 1.2.4 Hydroborate catalysts

Fontaine *et al.* reported on the use of several bases capable of reducing $CO_2$ into boroxine using $BH_3.SMe_2$.[32] It is interesting to note that this work was also the first to perform this type of reaction using hydroborate catalyst **17** (**Figure 13**).
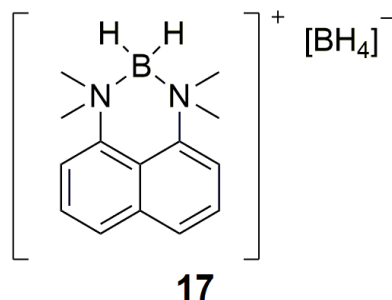
**Figure 13**. Hydroborate catalyst **17**.

Another interesting aspect of this work was that the mechanism of the catalytic cycle (**Scheme 13**), in the presence of $BH_3.SMe_2$, was elucidated by the successful isolation of its intermediates. The proposed catalytic cycle initially starts by the borane-dimethylsulfide activation by the bidentate ligand forming a boronium-borohydride ion pair. In the next step, the highly active $[BH_4]^-$ reacts with $CO_2$ forming $[HCOO]^-$ and releasing $BH_3$. Both react and $HCOOBH_2$ is generated, which after reacting with $BH_3.SMe_2$ is able to generate boroxine.



**Scheme 13**. $CO_2$ reduction mechanism with hydroborate **17** as catalyst and $BH_3.SMe_2$.
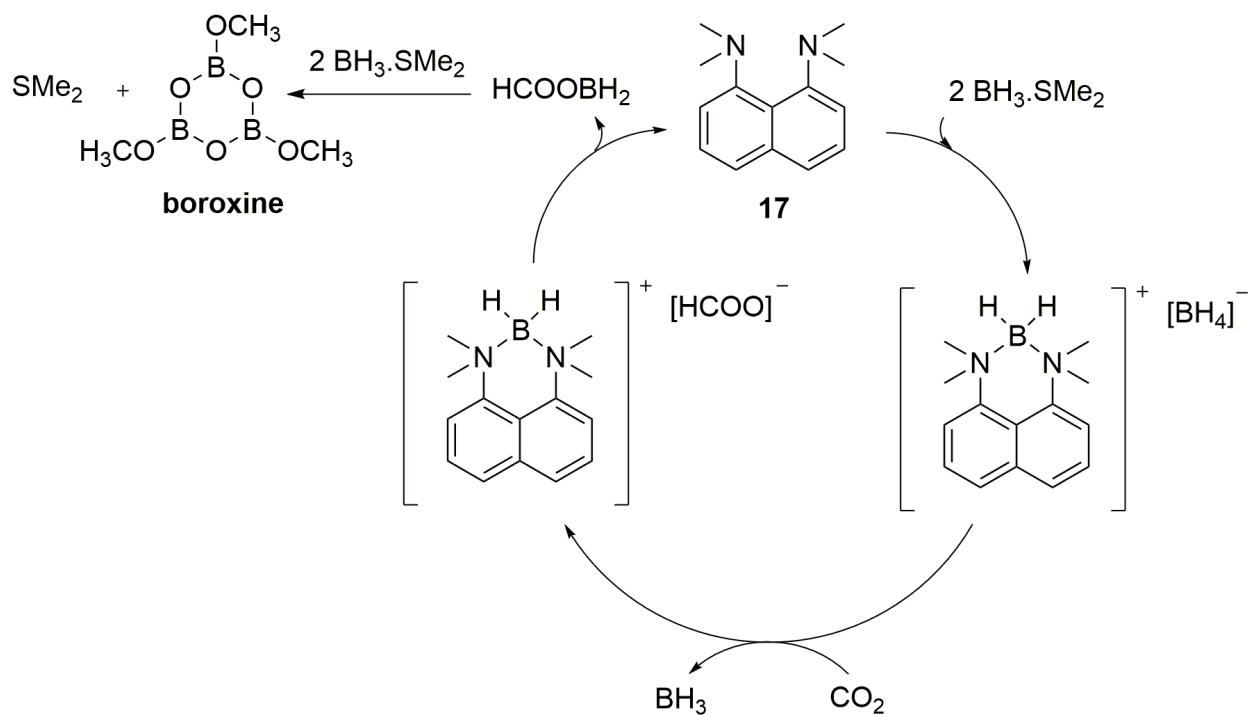
Early in 1977, Brown *et al.* were the first to report the formation of a methanol precursor, trimethoxyboroxine, by reacting MeCOOH with $CO_2$ in the presence of $BH_3$ and THF (**Scheme 14**).[33]
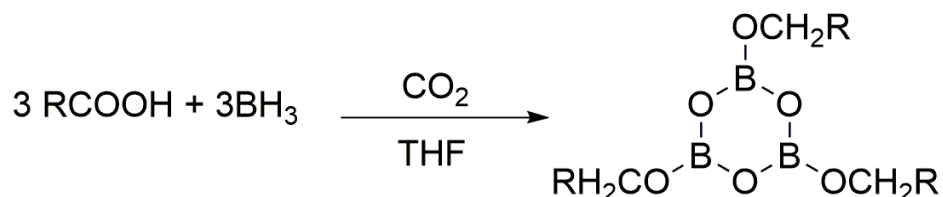
**Scheme 14**. First reduction of $CO_2$ into a boroxine using boranes.

In the same way, Mézailles *et al.*[34] reported on the successful use of catalysts **18** and **19** (**Scheme 15**), which were effective in the reduction of $CO_2$ into trimethoxyboroxine. In the same way as found by Fontaine, catalyst **18**, in the presence of $H_3B.SMe_2$, forms **19**, which is more active than **18**.
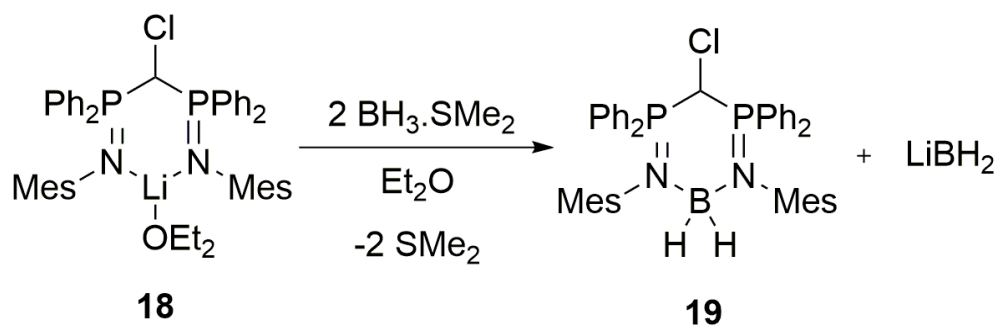
**Scheme 15**. Catalyst **18** and catalyst **19**.

Mizuta *et al.*[35] reported on the reduction of $CO_2$ into trimethoxyborane, using $NaBH_4$ and sodium formate (HCOONa) as catalysts (**Scheme 16**). The great advantage of this system is the simplicity of the catalyst, yielding 78% of boroxine with both catalysts. It is important to note that no mechanism was proposed in this work.

BH$_3$.THF

or

$\xrightarrow{\text{CO}_2}$

BH$_3$.THF
+0.5 mol% NaBH$_4$
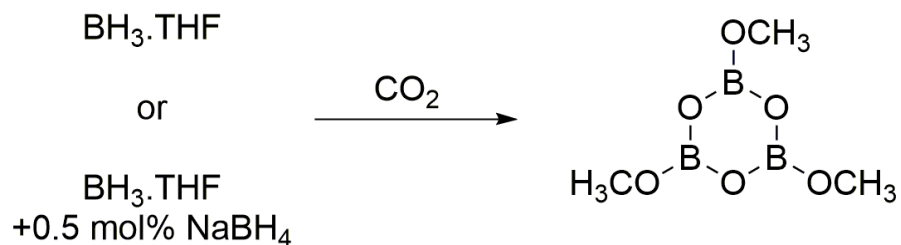
**Scheme 16**. CO$_2$ reduction into a boroxine using NaBH$_4$ as catalyst.

## 1.3  World polymers production

The discovery and large-scale synthesis of the first organic polymers in the early 1940s opened the door to the synthesis of other polymeric materials, being generically called "plastics". These materials have significant global importance from that moment on. They have revolutionized our society, and are widespread in industry, hospitals, vehicles, homes, and leisure materials. Polymers began to be manufactured on a large scale around 10 years after their discovery and in 2015 represented an amount of 322 million tons (**Figure 14**).[36]
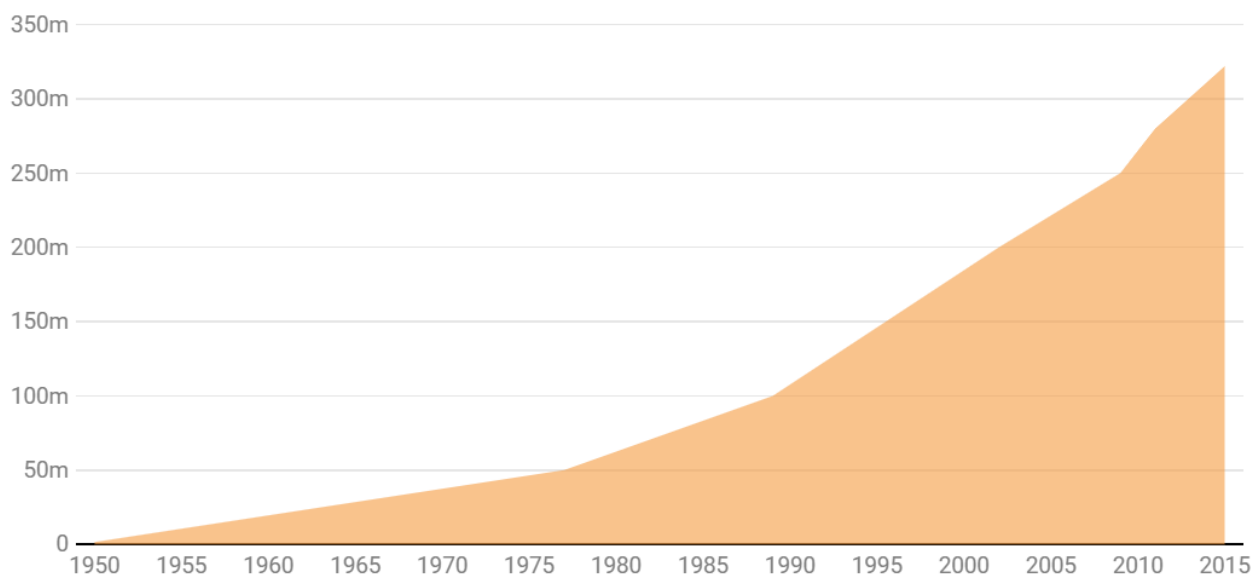
**Figure 14**. World production of plastics.[36]

Among the various synthetic polymeric types, polyolefins dominate the global market (**Figure 15**). Polyolefin-based plastics are the most widely used polymers in our society and are widespread materials in all aspects of our daily life since its production.[37],[38] Common types of olefins-based polymers are: low density polyethylene (LDPE) and high density polyethylene (HDPE). Other widely used plastics are polypropylene (PP), polystyrene (PS), polyvinyl chloride (PVC), polyurethane (PU), polyphthalamide (PPA) and polyethylene terephthalate (PET).
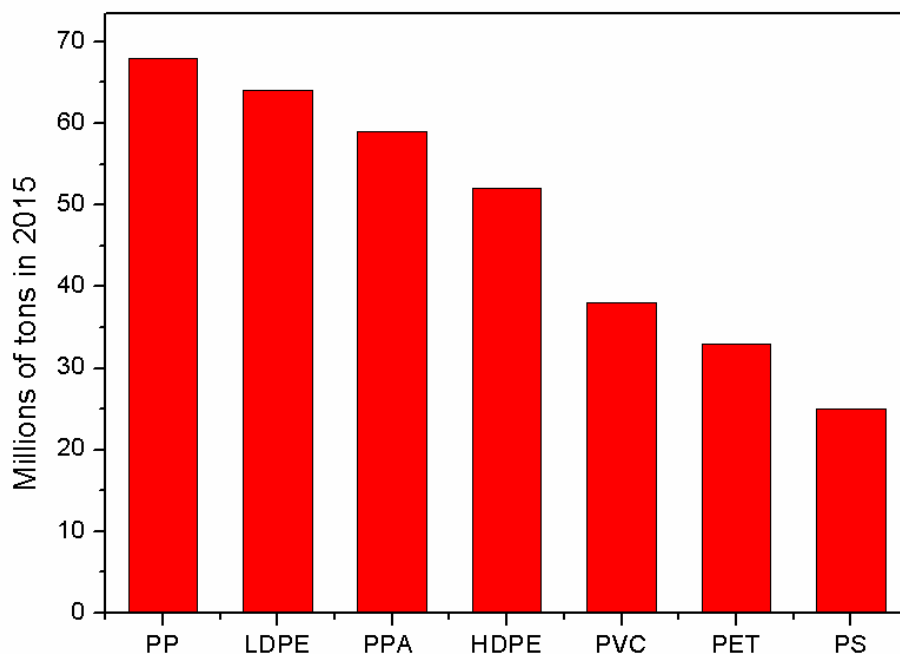


**Figure 15**. World production of plastics by type.[39]

Unfortunately, these polymers are made from olefins that are produced by thermal breakdown of heavy hydrocarbons in the steam catalytic cracking of petroleum. This process requires high temperatures between 750 and 850 °C for the massive burning of fossil fuels, which results in large emissions of carbon dioxide into the atmosphere.[40],[41] Thus, the enhancement of mechanical and thermal properties of the biopolymers could match the properties with the petroleum-based polymers in order to replace them.

### 1.3.1  PLA: a bio-sourced and biodegradable polymer

Among the biodegradable polymers, poly-(Lactic acid) (PLA) is a renewable polymer once its precursor lactic acid is produced by the fermentation of corn and sugar beet polysaccharides originated from the photosynthesis process (**Figure 17**), which involves $CO_2$ utilization as carbon source.



Sunlight strikes chlorophyll molecules in leaves and is captured.

Chlorophyll

Water

Glucose

Carbon Dioxide

Oxygen

Water and carbon dioxide are taken from the environment.  Glucose is formed and oxygen is released.
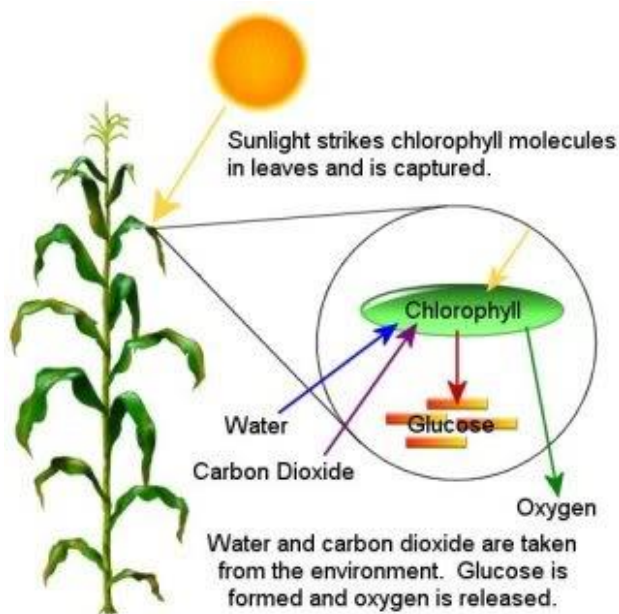
**Figure 17**. Photosynthesis process in corn plants.

This biodegradable thermoplastic, PLA, has found several applications in the biomedical area and as packaging commodities. Due to fossils resources depletion, such a material is also considered as an alternative to petrochemically-sourced polyolefins, which would also reduce the $CO_2$ level in the atmosphere.[42] Meanwhile, polyolefins are low cost, have attractive mechanical and thermal properties and remain by far the most widely used synthetic polymers nowadays.[43]

### 1.3.2  PLA synthesis, types and mechanisms

The industrial production process currently employed for the large-scale synthesis of PLA utilizes the tin(II) bis (2-ethylhexanoate) complex as catalyst, known as tin(II) octanoate, $(Sn(Oct)_2)$ (**Figure 18**).[44] This complex is commercially available, stable and therefore easy to handle. Very importantly, it is soluble in the fused lactide monomer, thus not requiring the use of solvent, which greatly reduces the costs of the process. Moreover, it has high activity at higher temperatures such as 140-180 °C, which is within the range applied in the synthesis of PLA, and results in the synthesis of high molecular weight PLA (up to 106 Da). Nevertheless, tin is a toxic metal that must be removed for applications in areas such as medicine.
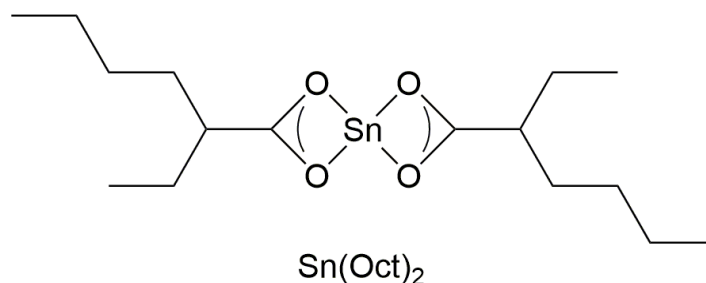


Sn(Oct)$_2$

**Figure 18**. Structure of tin(II) octanoate [Sn(Oct)$_2$].[44]

Commercial PLA is synthesized via ring-opening polymerization (ROP) of *L*-Lactide, as represented in the **Figure 19**.
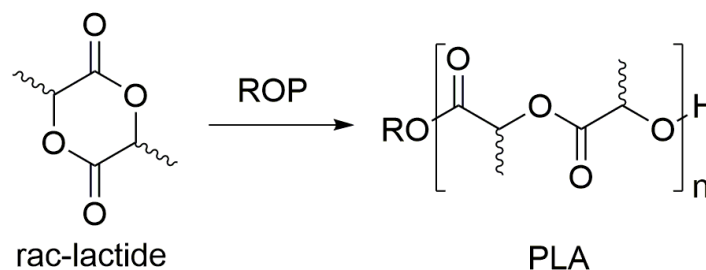


rac-lactide                    PLA

**Figure 19**. Synthesis of PLA through ROP of *rac*-lactide.

The ROP has gained considerable attention in the last 20 years for the synthesis of different types of PLA such as isotactic poly-(L-lactic acid) (PLLA) and poly-(d-lactic acid) (PDLA), heterotactic PLA, and syndiotactic PLA (**Figure 20**). Some of these polymers feature enhanced thermal and mechanical properties. As the ROP process uses an alcohol initiator that forms a covalent bond with the first monomer of the growing PLA chain (**Schemes 17** and **18**), this opens access to the addition of different functional end-groups into the polymeric chain.[42]
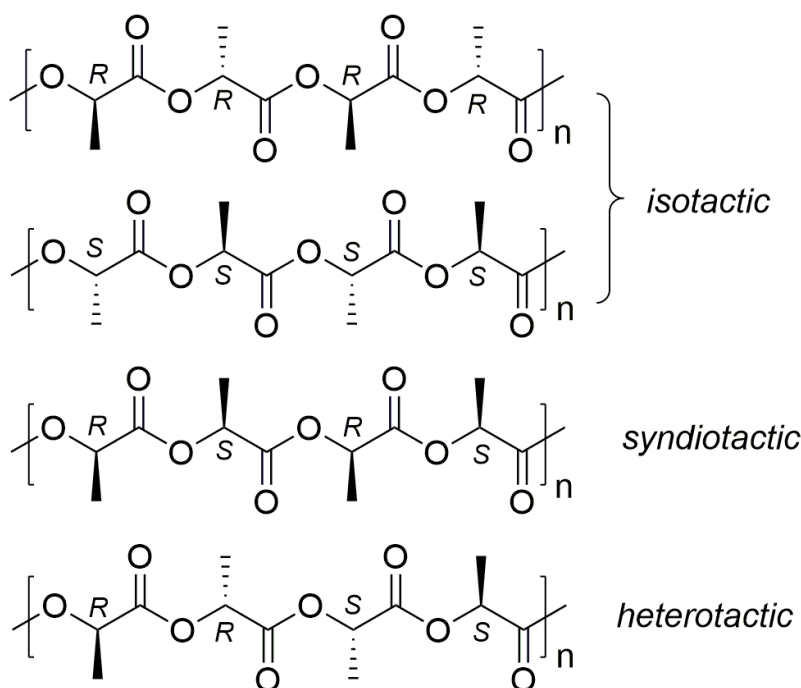


**Figure 20**. Different types of polylactides.[45]

Regarding the mechanism of lactide ROP, this can occur in many ways. Without the application of catalysts, the mechanisms can be: (a) electrophilic activation of the monomer or (b) chain-end activation. In the presence of a catalyst, the mechanism can be of two types: (c) activated monomer or (d) coordination/insertion.

The initiation step of the activated monomer mechanism (**Scheme 17**) is the activation of the ester carbonyl group through the coordination of a Lewis acid species, typically a metal. Next, a nucleophilic attack by the alcohol initiator at the carbonyl group

cleaves the O-acyl bond. This is followed by the propagation step, being the incorporation of subsequent monomers to grow the polymer chain. Finally, this polymerization is terminated by hydrolysis of the stable ML-OH species, removing the organometallic complex from the polymeric structure. Interestingly, the structure of the nucleophile remains as end-group in the polymer chain.
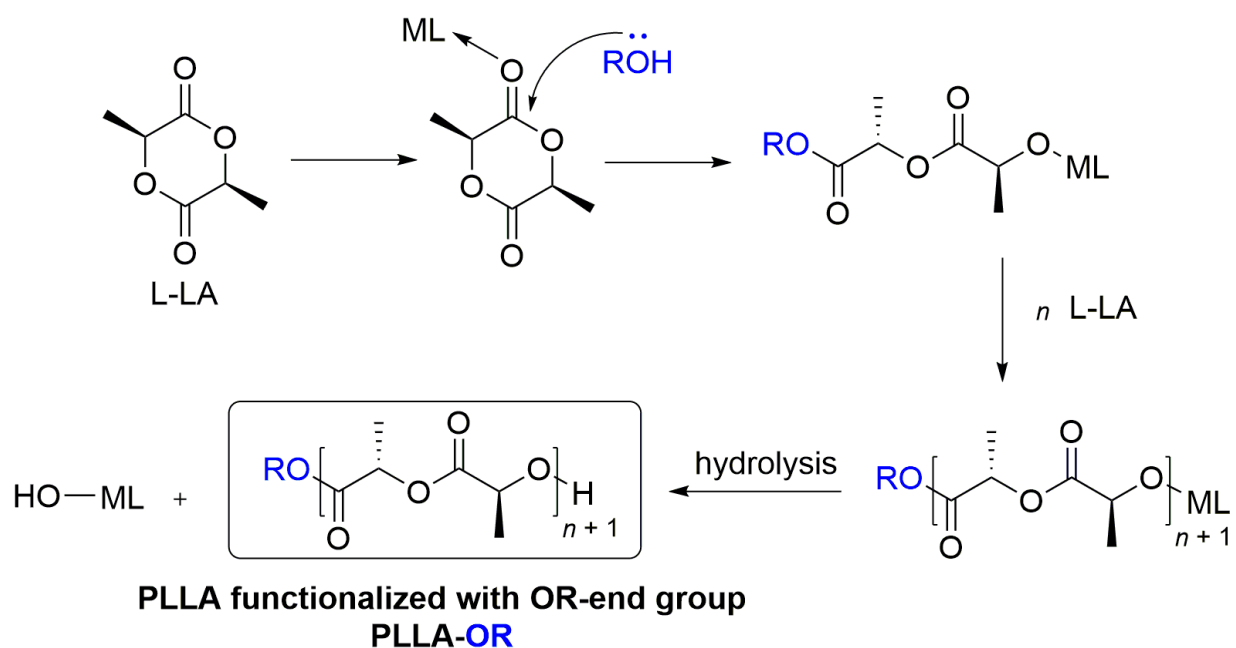


**Scheme 17**. ROP of L-LA in a monomer activated mechanism.[46]

The coordination/insertion mechanism (**Scheme 18**) was reported by Dittrich and Schulz[47] in the early 70s and was proven experimentally almost 20 years later by Kricheldorf[48] and Teyssié.[49] First, monomer coordination occurs at the electron-deficient metal center. Posteriorly, monomer insertion occurs into the metal-alkoxide bond. From that moment on the release of the monomer ring tension favors the ring opening with the acyl-oxygen cleavage. Subsequently, a propagation species is formed in which the repetitive monomer addition occurs, resulting in a continuously growing PLA chain. This reaction is also terminated with the hydrolysis of the propagation species.

**PLLA functionalized with X-end group**
**PLLA-X**
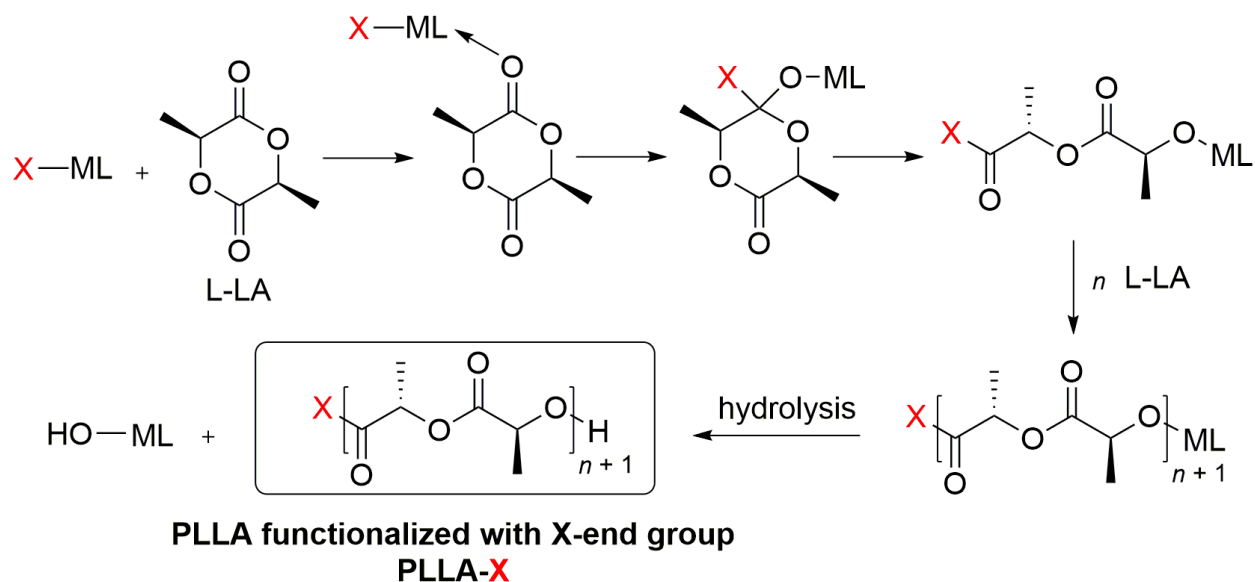
**Scheme 18**. ROP of L-LA through a coordination/insertion mechanism.[47]

Thus, the fixation of $CO_2$ by plants, as occurs in corn, results in the formation of sugars that can be fermented and subsequently dehydrated, leading to the formation of lactic acid. This monomer can be subjected to the ROP to form the biopolymer PLA, being indirectly derived from $CO_2$. The direct and indirect use of $CO_2$ for the synthesis of chemicals, fuels and materials is the central theme of this thesis and unites the next chapters.

## 1.4    References

[1]    Source: Our World in Data – **2019**.

[2]    M. Aresta, A. Dibenedetto, A. Angelini, *Chem. Rev.* **2014**, *114*, 1709–1742.

[3]    M. Popp, H. Schmidt, J. Marotzke, *Nat. Commun.* **2016**, *7*, 1–10.

[4]    A. D. Ellington, J. W. Szostak, *Lett. To Nat.* **1990**, *346*, 818–822.

[5]    V. Eyring, P. M. Cox, G. M. Flato, P. J. Gleckler, G. Abramowitz, P. Caldwell, W. D. Collins, B. K. Gier, A. D. Hall, F. M. Hoffman, G. C. Hurtt, A. Jahn, C. D. Jones, S. A. Klein, J. P. Krasting, L. Kwiatkowski, R. Lorenz, E. Maloney, G. A. Meehl, A. G. Pendergrass, R. Pincus, A. C. Ruane, J. L. Russell, B. M. Sanderson, B. D. Santer, S. C. Sherwood, I. R. Simpson, R. J. Stouffer, M. S. Williamson *Nat. Clim. Chang.* **2019**, *9*, 102–110.

[6]    T. P. Barnett, J. C. Adam, D. P. Lettenmaier, *Nature* **2005**, *438*, 303–309.

[7]    I. D. Haigh, T. Wahl, E. J. Rohling, R. M. Price, C. B. Pattiaratchi, F. M. Calafat, S. Dangendorf, *Nat. Commun.* **2014**, *5*, 1–11.

[8]    I. J. Losada, *Nat. Commun.* **1948**, 1–14.

[9]    C. L. Hurd, A. Lenton, B. Tilbrook, P. W. Boyd, *Nat. Clim. Chang.* **2018**, *8*, 686–694.

[10]    O. C. Eneh *J. Appl. Sci.* **2011**, *12*, 2084–2091.

[11]    E. Alper, O. Y. Orhan, *Petroleum* **2017**, *3*, 109–126.

[12]    I. International Energy Agency, **2016**, 2015–2017.

[13]    S. Saeidi, N. A. S. Amin, M. R. Rahimpour, *J. $CO_2$ Util.* **2014**, *5*, 66–81.

[14]    F. J. Fernández-Alvarez, A. M. Aitani, L. A. Oro, *Catal. Sci. Technol.* **2014**, *4*, 611–624.

[15]    S. Bontemps, *Coord. Chem. Rev* **2016**, *308*, 117–130.

[16]    For $CO_2$ hydrogenation into formic acid, check the following articles: (a) F. Gassner, W. Leitner, *J. Chem. Soc., Chem. Commun.* **1993**, 1465–1466. (b) S. S. Bosquain, A. Dorcier, J. P. A. Dyson, M. Erlandsson, L. Gonsalvi, G. Laurenczy, M. Peruzzini, *Appl. Organomet. Chem.* **2007**, *21*, 947–951. (c) P. G. Jessop, T. Ikariya, R. Noyori, *Nature* **1994**, *368*, 231–233. (d) Y. Himeda, N. Onozawa-Komatsuzaki, H. Sugihara, K. Kasuga, *Organomet.* **2007**, *26*, 702–712. (e) R. Tanaka, M. Yamashita, K. Nozaki, *J. Am. Chem. Soc.* **2009**,*131*, 14168–14169.

[17]    (a) M. Everett, D. F. Wass, *Chem. Commun.* **2017**, *53*, 9502–9504. (b) S. Kar, J. Kothandaraman, A. Goeppert, G. K. S. Prakash, *J. $CO_2$ Utilizat.* **2018**, *23*, 212–218.

[18]    S. Chakraborty, J. Zhang, J. A. Krause, H. Guan, *J. Am. Chem. Soc.* **2010**, *132*, 8872–8873.

[19]    S. Bontemps, L. Vendier, S. Sabo-Etienne, *Angew. Chem. Int. Ed.* **2012**, *51*, 1671–1674.

[20]    M. D. Anker, M. Arrowsmith, P. Bellham, M. S. Hill, G. Kociok-Kohn, D. J. Liptrot, M. F. Mahon, C. Weetman *Chem. Sci.* **2014**, *5,* 2826–2830.

[21]    J. A. B. Abdalla, I. M. Riddlestone, R. Tirfoin, S. Aldridge, *Angew. Chem. Int. Ed.* **2015**, *54*, 5098–5102.

[22]    R. Shintani, K. Nozaki, *Organometallics* **2013**, *32*, 2459–2462.

[23]    N. P. Mankad, D. S. Laitar, J. P. Sadighi, *Organometallics* **2004**, *23*, 3369–3371.

[24]    H. Suh, L. M. Guard, N. Hazari, *Chem. Sci.* **2014**, *5*, 3859–3872.

[25]    C. N. Gomes, E. Blondiaux, P. Thuéry, T. Cantat, *Chem. Eur. J.* **2014**, *20*, 7098–7106.

[26]    T. Wang, D. W. Stephan, *Chem. Commun.* **2014**, *50,* 7007–7010.

[27]    M. Courtemanche, M. Légaré, L. Maron, F. Fontaine, *J. Am. Chem. Soc.* **2013**, *135*, 9326−9329.

[28]    R. Declercq, G. Bouhadir, D. Bourissou, M. Légaré, M. Courtemanche, K. S. Nahi, N. Bouchard, F. Fontaine, L. Maron, *ACS Catal.* **2015**, *5*, 2513−2520.

[29]    G. Ménard, D. W. Stephan, *J. Am. Chem. Soc.* **2010**, *132*, 1796–1797.

[30]    (a) M. Courtemanche, J. Larouche, M. Légaré, W. Bi, L. Maron, F. Fontaine, *Organomet.* **2013**, *32*, 6804−6811. (b) F. Fontaine, E. Rochette, *Acc. Chem. Res.* **2018**, *51*, 454−464.

[31]    T. Wang, D. W. Stephan, *Chem. Eur. J.* **2014**, *20*, 3036–3039.

[32]    M. Légaré, M Courtemanche, F. Fontaine, *Chem. Commun.* **2014**, *50*, 11362–11365.

[33]    H. C. Brown, T. P. Stocky, *J. Am. Chem. Soc.* **1977**, 8218–8226.

[34]    S. Y. Ho, C. So, N. Saffon-Merceron, N. Mézailles, *Chem. Commun.* **2015**, *51*, 2107–2110.

[35]    K. Fujiwara, S. Yasuda, T. Mizuta, *Organometallics* **2014**, *33*, 6692–6695.

[36]    Source: Plastics Europe.

[37]    S. L. Aggarwal, O. J. Sweeting, *Chem. Rev.* **1957**, *57*, 665–742.

[38]    H. A. Maddah, *Am. J. Polym. Sci.* **2016**, *6*, 1–11.

[39]    R. Geyer**,** J. R. Jambeck, K. L. Law, *Sci. Adv.* **2017**, *3*, 1-5.

[40]    I. M. Artyukhov, E. S. Bezmozgin, A. B. Gushchevskii, V. N. Petrov, N. D. Shevkunov, **Fuel and Oil Chemistry and Technology**, 1st ed., *Vol. 14*, **1978**.

[41]    F. M. Alotaibi, S. González-Cortés, M. F. Alotibi, T. Xiao, H. Al-Megren, G. Yang, P. P. Edwards, *Catal. Today* **2018**, *317*, 86–98.

[42]    O. Dechy-Cabaret, B. Martin-Vaca, D. Bourissou *Chem. Rev.* **2004**, *104*, 6147–6176.

[43]    N. K. Boaen, M. A. Hillmyer, *Chem. Soc. Rev.* **2005**, *34*, 267–275.

[44]    S. Jacobsen, P. Degée, H. G. Fritz, P. Dubois, R. Jérôme *Polym. Eng. Sci.* **1999**, *39, (7)*, 1311–1319.

[45]    G. W. Coates, J. *Chem. Soc., Dalton Trans.* **2002**, 467–475.

[46]    F. Hild, L. Brelot, S. Dagorne, *Organometallics* **2011**, *30*, 5457–5462.

[47]    W. Dittrich, R. C. Schulz, *Angew. Makromol. Chem.* **1971**, *15*, 109–126.

[48]    H. R. Kricheldorf, M. Berl, N. Scharnagl, *Macromolecules* **1988**, *21*, 286–293.

[49]    P. Dubois, C. Jacobs, R. Jérôme, P. Teyssié, *Macromolecules* **1991**, *24*, 2266–2270.

# 2   CHAPTER I - ALUMINUM TRIPOD (O-O-O) HYDRIDE COMPLEXES CATALYZE THE BORANE-MEDIATED REDUCTION OF CARBON DIOXIDE INTO METHOXYBORANE AND FORMOXYBORANE

Chapter I - Aluminum Tripod (O-O-O) Hydride Complexes Catalyze the Borane-Mediated Reduction of
Carbon dioxide into Methoxyborane and Formoxyborane

37
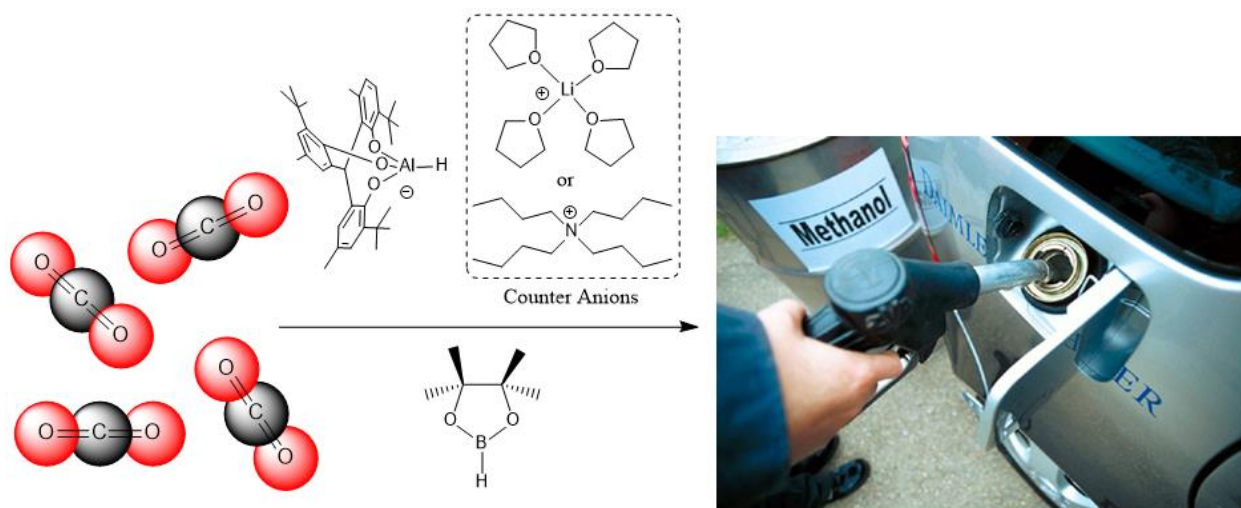


Graphical Abstract

## Abstract

*Herein, we report about the application of two new aluminum hydride complexes and two new (L)AlOCOH complexes in the borane reduction of $CO_2$ to produce formoxyborane and methoxyborane. The complexes used were: $\eta^3$-O,O,O-{$(C_{11}H_{14}O)_3$CH}AlH Li(THF)$_4$ (**1**), $\eta^3$-O,O,O-{$(C_{11}H_{14}O)_3$CH}AlOCOH Li(THF)$_4$ (**2**), $\eta^3$-O,O,O-{$(C_{11}H_{14}O)_3$CH}AlH TBA (**3**) and $\eta^3$-O,O,O-{$(C_{11}H_{14}O)_3$CH}AlOCOH TBA (**4**). When applying 10 mol% of the complexes **1** and **2**, a selectivity >98% for the methoxyborane was obtained. In contrast, the use of the same amount of **3** and **4** resulted in the selective formation of formoxyborane (>97%). The highest catalytic activity found was for complex **3** (TON: 1,920 and TOF: 48 h$^{-1}$). Solvent-free reactions were performed successfully using complex **3**. In addition, a mechanism different from the previously reported for hydroboration employing M-H has been proposed. Although the development of an industrial process for the borane-mediated reduction of $CO_2$ as source for methanol or formic acid is in its infancy, this study contributes to this objective.*

Chapter I - Aluminum Tripod (O-O-O) Hydride Complexes Catalyze the Borane-Mediated Reduction of
Carbon dioxide into Methoxyborane and Formoxyborane

39

## 2.1   Introduction

There is only one report in the literature using aluminum catalyst for $CO_2$ reduction with boranes. Interestingly, such aluminum complexes were not metal hydride species.[1] This was one of the motivating forces to start this project. The annual production of methanol is 100 million tons and the amount produced with $CO_2$ as feedstock represents only 2 million tons, 2% of the total. In addition, formic acid has an annual production of 700 thousand tons and none of the industrial processes uses $CO_2$ as raw material. These factors show the huge potential that $CO_2$-based processes could have in the production of both methanol and formic acid.[2]

Since the discovery of Guan *et al.* of M-H-based catalysts for the borane-mediated $CO_2$ reduction, the scope covers the following species: Ni-H,[3] Ru-H,[4] Mg-H and Ca-H,[5] Pd-H,[6] Pt-H,[7], and Cu-H.[8] Although an Al-based Lewis pair complex, acting as an ambiphilic activator of $CO_2$, was reported to reduce $CO_2$, no catalytic system based on Al-H catalyst exists.[1],[9],[10] As aluminum is an abundant, cheap and non-toxic metal, such a catalytic system holds great promise.

Understand the mechanism is an important step for the development of new catalyst systems. And you are invited to join us in this thesis to understand how the mechanism played a key role in the **chapter I**, opening the access for us to development of metal-free systems described in the **chapter II**. Herein, we aim the investigation of the HBpin-mediated $CO_2$ reduction using two aluminum hydride complexes (**1** and **3**) and two aluminum formate complexes (**2** and **4**) (**Figure 1**). The complexes used were: $\eta^3$-O,O,O-{$(C_{11}H_{14}O)_3$CH}AlH Li(THF)$_4$ (**1**), $\eta^3$-O,O,O-{$(C_{11}H_{14}O)_3$CH}AlOCOH Li(THF)$_4$ (**2**), $\eta^3$-O,O,O-{$(C_{11}H_{14}O)_3$CH}AlH TBA (**3**) and $\eta^3$-O,O,O-{$(C_{11}H_{14}O)_3$CH}AlOCOH TBA (**4**). These complexes were tested under solvent-free conditions and the catalytic performance was optimized. Mechanistic investigations were performed to support the optimization of this catalytic system.
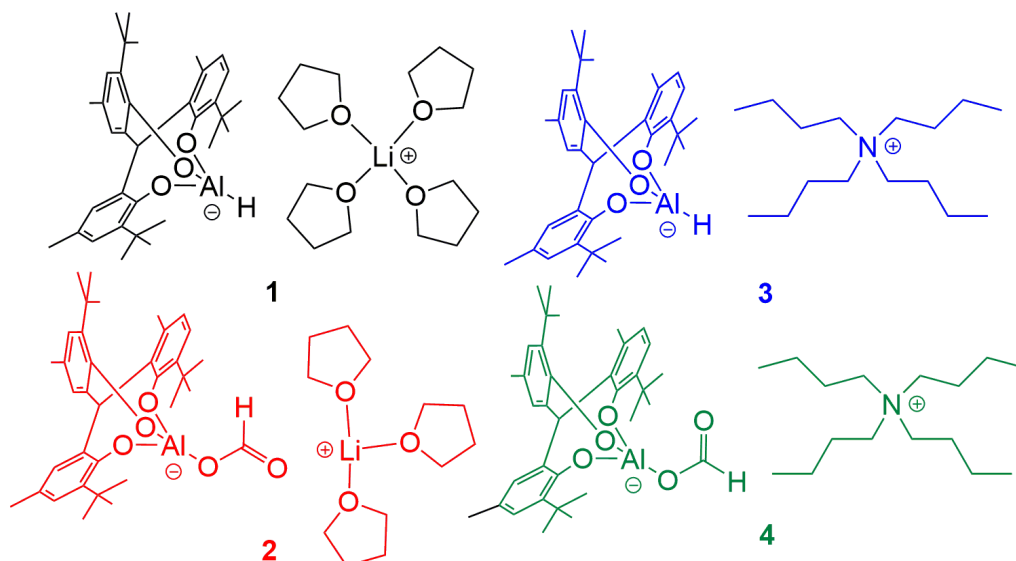
**Figure 1**. Aluminum complexes used in the HBpin-mediated reduction of $CO_2$.

Based on the mechanisms reported for M-H catalysts, the expected mechanism for an Al-H-catalyzed $CO_2$ reduction with a hydroborane is presented in **Scheme 1**. As such, after the $CO_2$ insertion, metathesis between the AlOCOH species and HBpin would occur.
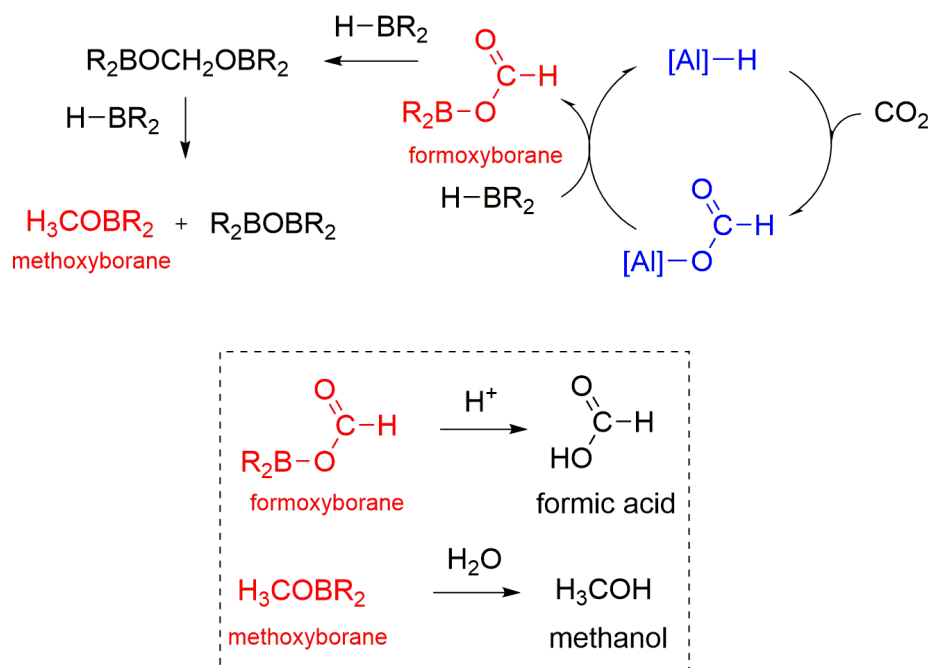


**Scheme 1**. Expected mechanism for reduction of $CO_2$ with boranes using Al-H catalysts.

## 2.2 Results and discussions

Initially, the performance of the aluminum-based anionic catalysts (**Figure 1**) was studied *in situ* by NMR under the following conditions (**Table 1**): 10 mol% Al-H, HBpin, $C_6D_6$, 90 ºC. For the Al-H complex **1** with the Li(THF)$_4$ cation, a 96% conversion was achieved at 44 h with a methoxyborane selectivity of 98% (**Entry 1**). When applying the formate-complex **2** (**Entry 2**), which originated from the insertion of $CO_2$ into the metal hydride of complex **1**, the selectivity was the same but the catalytic activity significantly reduced (99% conversion after 74 h), reducing the TOF from 0.21 to 0.14 h$^{-1}$.

**Table 1**. Aluminium tripod complexes as catalysts for the reduction of $CO_2$ with boranes.



| Entry | Catalyst | Catalyst mol% | Solvent | time (h) | Conv. (%)[b] | TON[c] | TOF (h$^{-1}$) [d] | HOCOBpin (%)[e] | pinBOCH$_2$OBpin (%)[e] | H$_3$COBpin (%)[e] |
|---|---|---|---|---|---|---|---|---|---|---|
| 1 | **1** | 10* | $C_6D_6$ | 44 | 96" | 9.6 | 0.22 | - | 2 | 98 |
| 2 | **2** | 10* | $C_6D_6$ | 74 | 99" | 9.9 | 0.13 | - | 2 | 98 |
| 3 | **3** | 10* | $C_6D_6$ | 6 | 95" | 9.5 | 1.6 | 97 | 3 | - |
| 4 | **3** | 1** | $C_6D_6$ | 1 | 11" | 11 | 11 | 99 | 1 | - |
| 5 | **3** | 1** | $C_6D_6$ | 2 | 14" | 14 | 7 | 98 | 2 | - |
| 6 | **3** | 1** | $C_6D_6$ | 3 | 15" | 15 | 5 | 77 | 4 | 18 |
| 7 | **3** | 1** | $C_6D_6$ | 4 | 18" | 18 | 5 | 52 | 5 | 43 |
| 8 | **3** | 1** | $C_6D_6$ | 5 | 21" | 21 | 4 | 32 | 4 | 63 |
| 9 | **3** | 1** | $C_6D_6$ | 19 | 61" | 61 | 3 | 5 | 1 | 94 |
| 10 | **3** | 1** | $C_6D_6$ | 25 | 71" | 71 | 3 | 4 | 1 | 95 |
| 11 | **3** | 1** | $C_6D_6$ | 49 | 95" | 95 | 2 | 4 | 0 | 96 |
| 12 | **3** | 0.1*** | $C_6D_6$ | 45 | 95" | 950 | 21 | 1 | - | 99 |
| 13 | **3** | 0.1*** | - | 22 | 97' | 970 | 44 | 1 | - | 99 |
| 14 | **3** | 0.05*** | - | 40 | 96' | 1920 | 48 | - | - | >99 |
| 15 | **4** | 10* | $C_6D_6$ | 6 | 87' | 8.7 | 1.5 | 99 | 1 | - |

[b] Conv. = conversion - calculated by (') $^1$H NMR through the integration of characteristic signals of the internal standard and the products or (") by $^{11}$B NMR through integration of the products signals. [c] TON = turnover number. [d] TOF = turnover frequency. [e] Selectivity - determined by $^1$H NMR through the integration of the three products signals.

The drop in activity may be explained by the fact that complex **2** is much more stable due to the coordination of its lithium cation to the formate carbonyl oxygen. Interestingly, complex **3** with the TBA cation (**Entry 3**) catalyzed the reaction with a conversion of 95% in 6 h and a TOF of 1.6 $h^{-1}$, being 7 times more productive compared to complex **1** (**Entry 1**), and the formate species HOCOB(pin) was formed in 97% selectivity.

After identifying complex **3** as the most promising catalyst, its potential was explored in further detail. The catalyst loading was lowered to 1 mol% and analyzing the reaction at different times performed a kinetic study (**Entries 4**-**11**). This reduction of $CO_2$ with HBpin can lead to the formation of three products, which was studied *in situ*. **Figure 2** shows the variation of product selectivity with time. Up to 3 hours, the first reduction product HOCOBpin was formed selectively (**Entries 4**-**6**). Once the amount of the second reduction product $pinBOCH_2OBpin$ increased, it remained low throughout the entire process, which indicated that it was transformed quickly to the final reduction product methoxyborane. After 4 h (**Entry 7**), formoxyborane and methoxyborane were formed in similar amounts. With the passing of the reaction time (**Entries 8**-**11**), the turned more selectivity towards the methoxyborane formation. After reaching a conversion of 95% after 49 h (**Entry 11**), the TON and TOF were 95 and 2 $h^{-1}$, respectively, with 96% selectivity for methoxyborane.

Chapter I - Aluminum Tripod (O-O-O) Hydride Complexes Catalyze the Borane-Mediated Reduction of Carbon dioxide into Methoxyborane and Formoxyborane

43
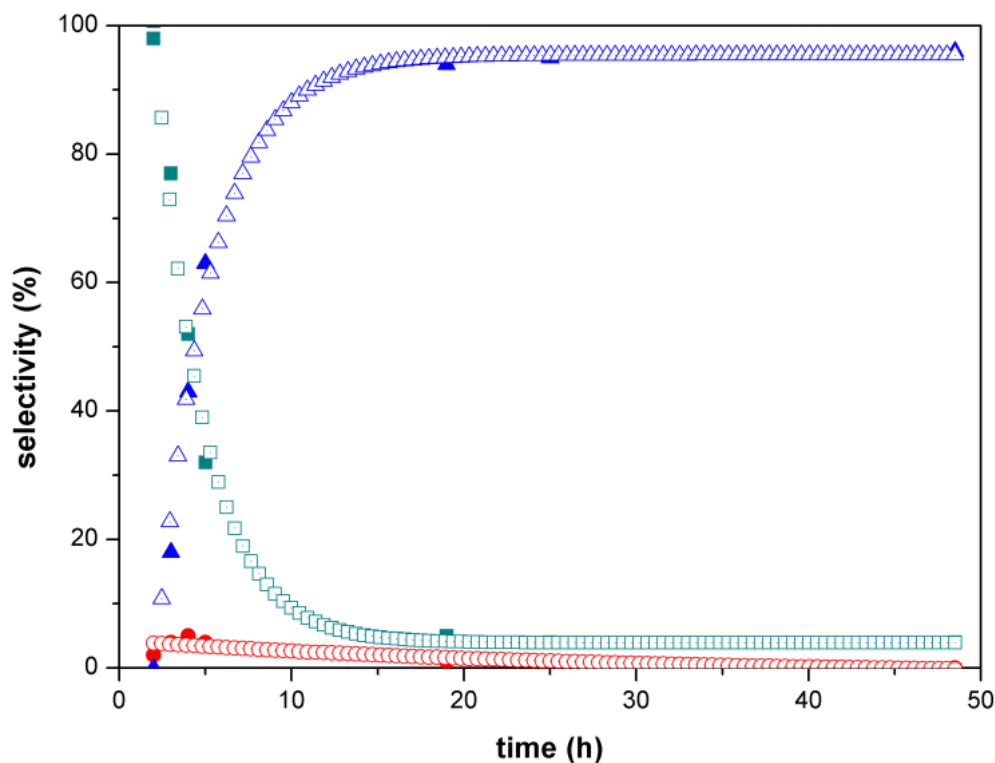


**Figure 2**. Temporal monitoring of the reduction of $CO_2$ in the presence of HBpin and complex **3** (1 mol%). Conditions: $C_6D_6$; 90 °C. Products formation in time: HOCOBpin (green ■ ), pinBOCH$_2$Bpin (red ● ) e H$_3$COBpin (blue ▲ ).

The selective formation of methoxyborane remained also with further reduced catalyst loadings (**Entries 12-14**). When applying 0.1 mol% of catalyst **3** (**Entry 12**), a TON of 950 and a TOF of 21 h$^{-1}$ were obtained after 45 h. Interestingly, the same reaction was successfully performed without solvent (**Entry 13**), resulting in a higher catalytic activity (TON = 970) and productivity (TOF = 44 h$^{-1}$) after 22 h. Under this solventless condition, 0.05 mol% of catalyst **3** generated the highest TON of 1920 and TOF of 48 h$^{-1}$ after 40 h (**Entry 14**). In the case of 10 mol% of complex **4** (**Entry 3**; TOF of 1.5 h$^{-1}$), a similar catalytic productivity was obtained compared to complex **3** (**Entry 3**; TOF of 1.6 h$^{-1}$), being both selective for the formoxyborane formation. This finding can be explained by the catalytic cycle, intra-converting complex **3** into complex **4,** and catalyst 1 to 2, in the presence of $CO_2$.

The high selectivity for the formation of methoxyborane was deduced from the ^{1}H NMR spectra (**Figures 3** and **5**), showing a signal at 3.51 ppm that grew during the course of the reaction. This signal is reported in literature as the characteristic peak of $H_3CO$-Bpin in $C_6D_6$.[11] Among the other reduction products, only peaks with low intensities were observed for pinB-$OCH_2O$-Bpin (5.49 ppm) and formoxyborane (8.21 ppm).[11]



**Figure 3.** ^{1}H NMR spectra (400 MHz, $C_6D_6$) of the reduction of $CO_2$ in the presence of HBpin and complex **3** (1 mol%). Conditions: $C_6D_6$; temperature = 90 °C.

In the ^{11}B NMR spectra (**Figures 4** and **6**), formoxyborane (22.3 ppm) was observed in the first hours as the major product after $CO_2$ injection. As the reaction proceeded, complete conversion to methoxyborane (22.8 ppm) and pinB-O-Bpin (21.9 ppm) was observed, which is in agreement with previously reported spectral data.[11] In the ^{13}C NMR spectrum (**Figure 7**), the formation of the characteristic methoxyborane peak was observed at 52.22 ppm.[11] The signal at 125.17 ppm refers to free $CO_2$, while

those at 82 ppm and 24 ppm are for the quarternary carbons and -CH$_3$ groups, respectively, for both H$_3$CO-Bpin and pinB-O-Bpin.
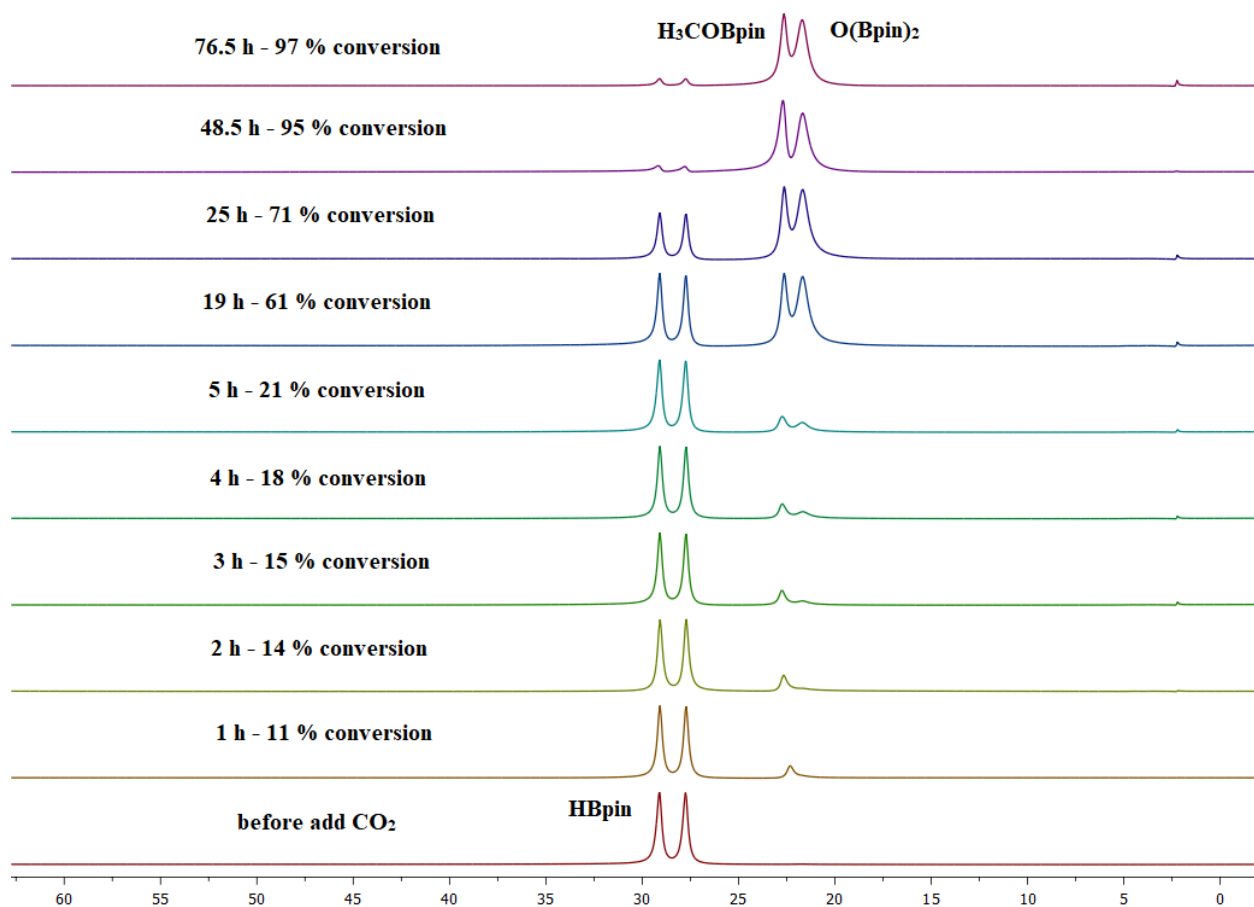


**Figure 4**. $^{11}$B NMR spectra (128 MHz, C$_6$D$_6$) of the reduction of CO$_2$ in the presence of HBpin and complex **3** (1 mol%). Conditions: C$_6$D$_6$; temperature = 90 °C.

## 2.2.1  Al-catalyzed CO$_2$ reduction with boranes: products identification.

The methoxyborane and bis(boryl)ether compounds were characterized *in situ* by $^1$H and $^{11}$B NMR (**Figures 5** and **6**). Methoxyborane has characteristic peaks at 3.44 ppm and 22.49 ppm in the $^1$H and $^{11}$B NMR spectra, respectively. Methoxyborane was also observed in the $^{13}$C NMR spectrum through its peak at 52.22 ppm (**Figure 7**). For formoxyborane, its characteristic peaks appeared at 8.20 ppm (**Figure 8**) and 21.62 ppm (**Figure 9**) in the $^1$H and $^{11}$B NMR spectra, respectively.[11]

**Figure 5**. $^1$H NMR spectrum (400 MHz, $C_6D_6$) after the reduction of $CO_2$ in the presence of HBpin and complex **3** (0.1 mol%). Conditions: solvent free; temperature = 90 ºC; time = 22 h; internal standard = hexamethylbenzene. Conversion = 97%.

**Figure 6.** $^{11}B$ NMR spectrum (128 MHz, $C_6D_6$) after the reduction of $CO_2$ in the presence of HBpin and complex **3** (0.1 mol%). Conditions: solvent free; temperature = 90 °C; time = 22 h. Conversion = 97%.
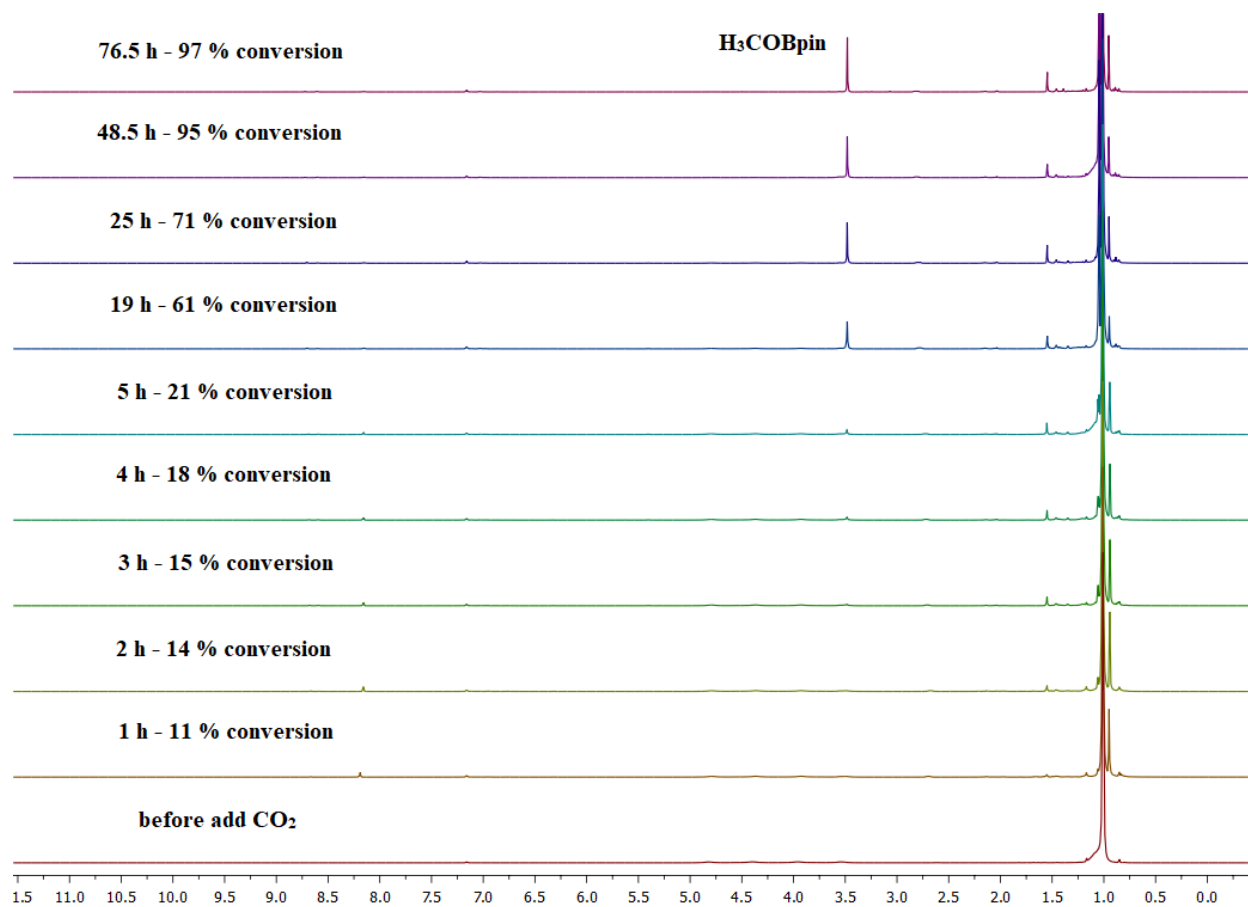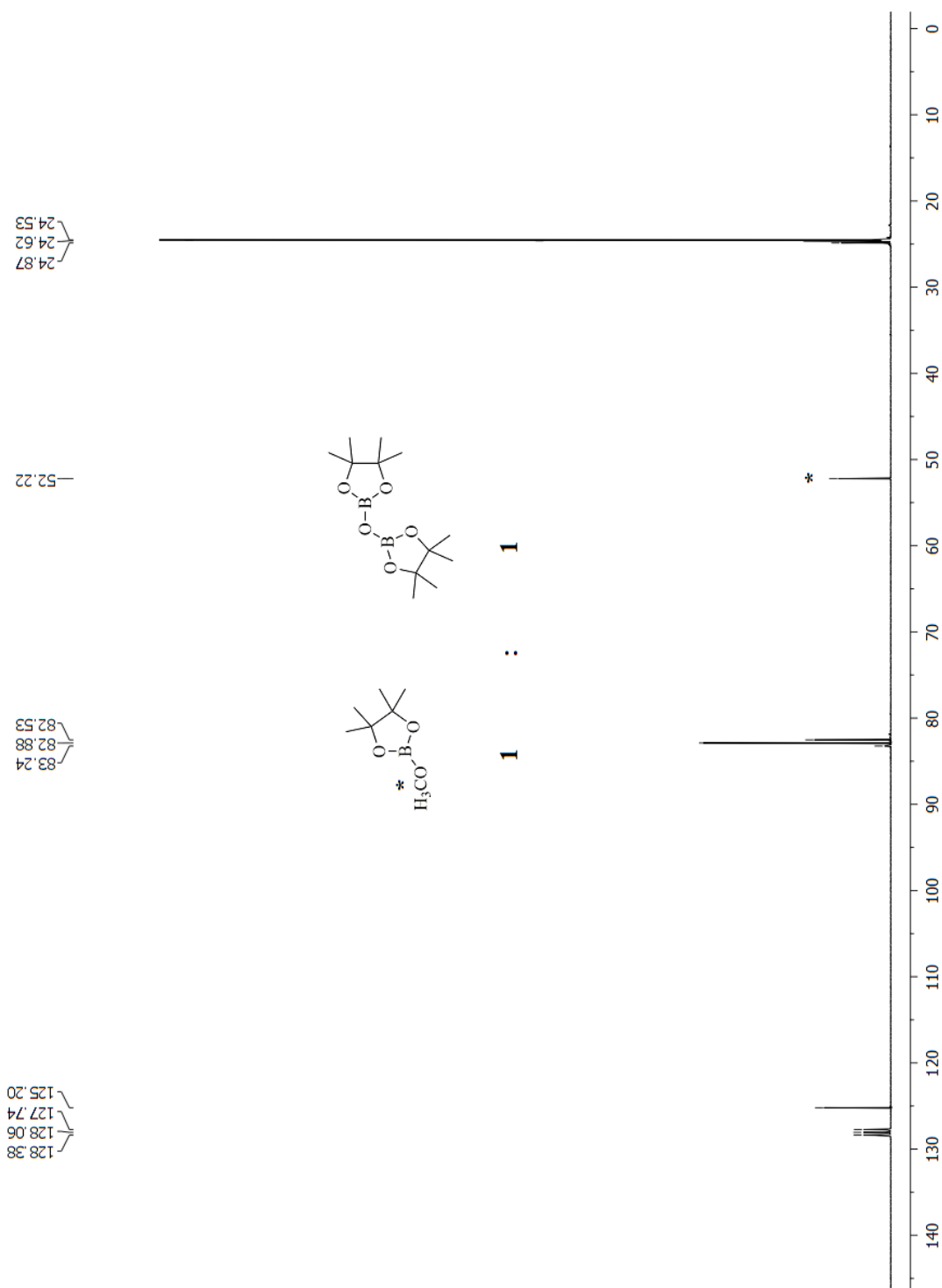
**Figure 7**. $^{13}$C NMR spectrum (75 MHz, C$_6$D$_6$) after the reduction of CO$_2$ in the presence of HBpin and complex **3** (0.1 mol%). Conditions: C$_6$D$_6$; temperature = 90 ºC; time = 50.5 h. Conversion = 90%; Selectivity for methoxyborane = 99 %. Free CO$_2$: 125.20 ppm; unreacted HBpin: 83.24 and 24.87 ppm.
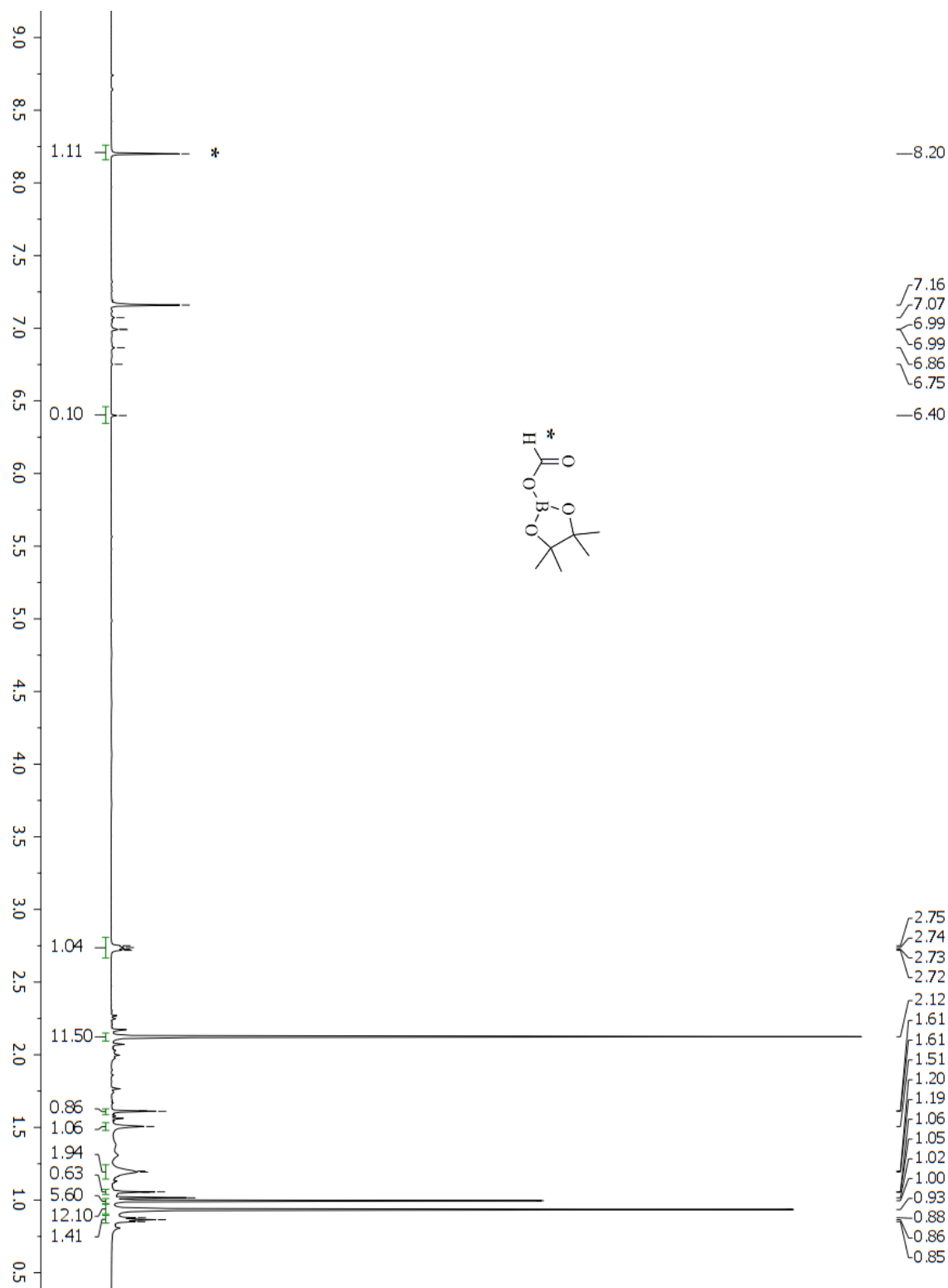
**Figure 8**. $^1$H NMR spectrum (500 MHz, C$_6$D$_6$) after the reduction of CO$_2$ in the presence of HBpin and complex **4** (10 mol%). Conditions: C$_6$D$_6$; temperature = 90 °C; time = 6 h; internal standard = hexamethylbenzene. Conversion = 68%.
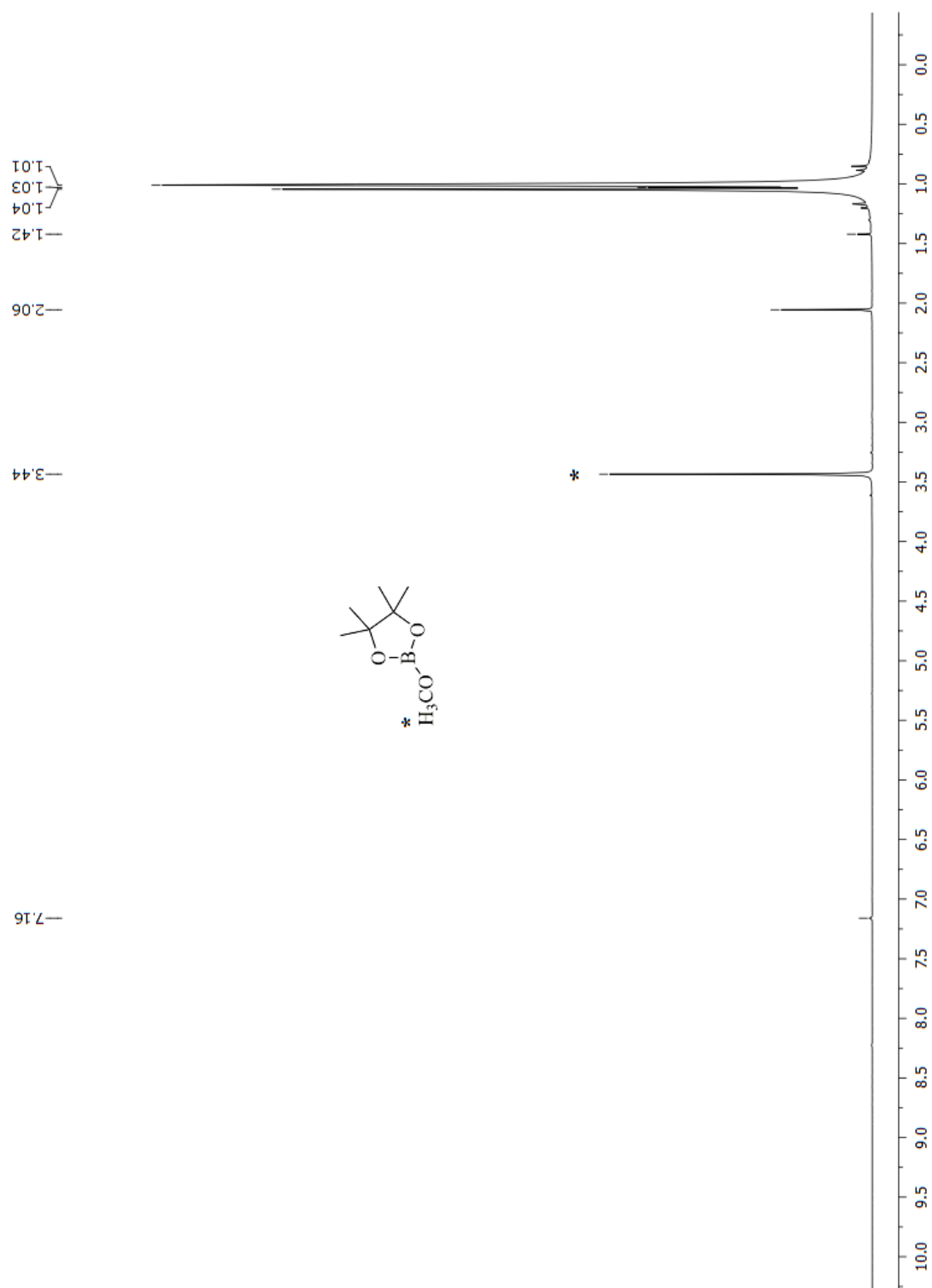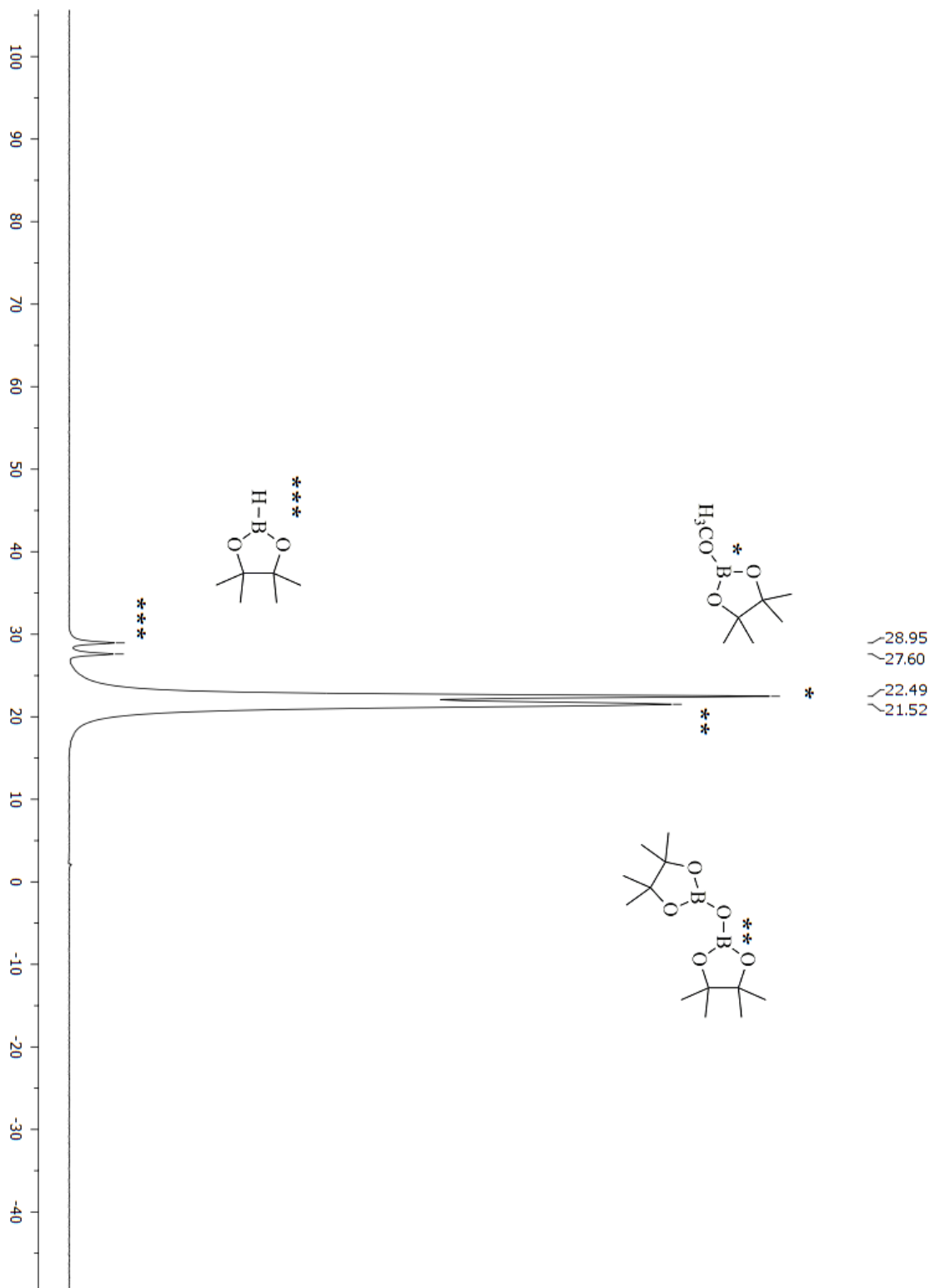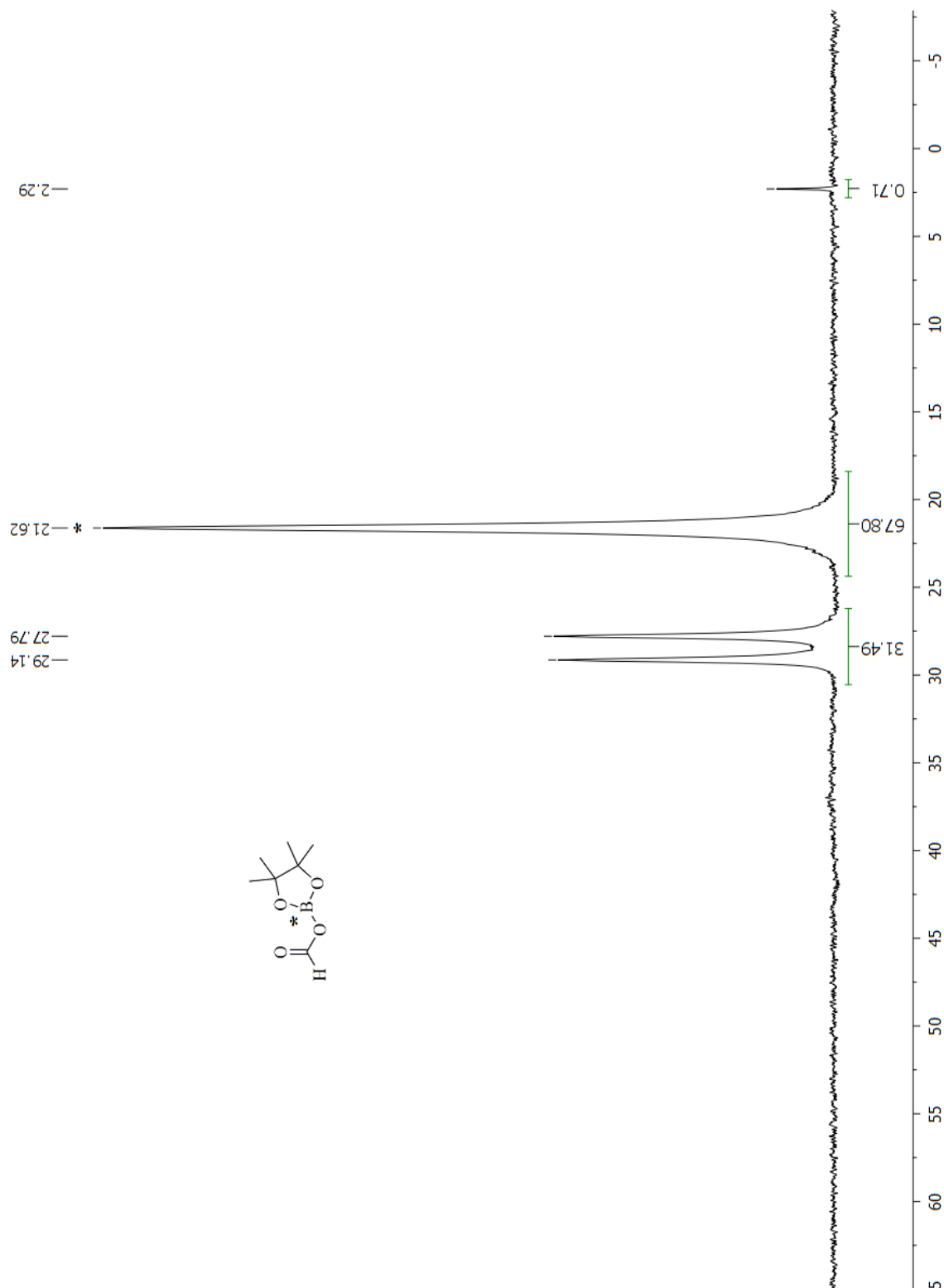
**Figure 9**. $^{11}B$ NMR spectrum (128 MHz, $C_6D_6$) after the reduction of $CO_2$ in the presence of HBpin and complex **4** (10 mol%). Conditions: $C_6D_6$; temperature = 90 ºC; time = 6 h; internal standard = hexamethylbenzene. Conversion = 68%.

Scheme 1 shows the mechanism that has been reported for metal hydride species, which was also expected for this catalytic system. Interestingly, it was observed a different mechanistic behavior, following a different activation of the borane species. The proposed mechanism for complex 3 (Scheme 2) starts with the coordination of $CO_2$ on the aluminum centre. Subsequently, a migratory insertion of $CO_2$ into the Al-H bond forms the aluminum formate complex (L)Al-OCOH. In the traditional metal-hydride mechanism (Scheme 1), the borane activation process occurs through metathesis between the M-OCOH complex and HBpin species forming formoxyborane and regenerating the M-H catalyst. With the aluminum catalysts, we hypothesize that this takes place through another mechanism. Now, the formate-group of the Al-OCOH complex activates the borane species HBpin. Next, the reaction with $CO_2$ releases the first reduction product, formoxyborane, and regeneras the catalytic species Al-OCOH. Formoxyborane is the most stable product and was selectively formed under certain conditions as given in Table 1.
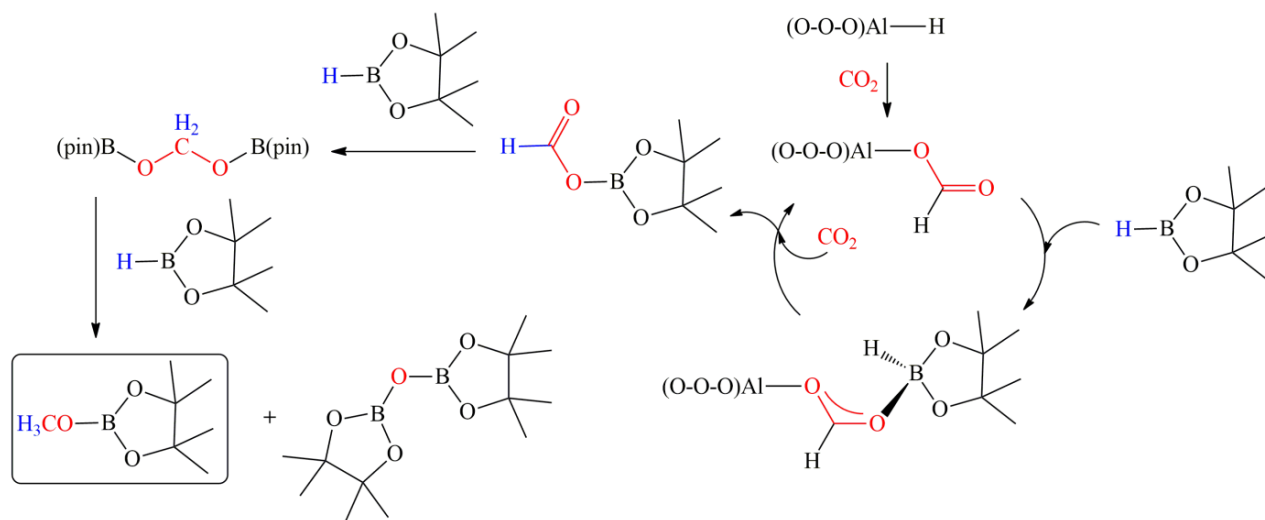


Scheme 2. Proposed mechanism for the reduction of $CO_2$ with hydroboranes and tripod (O-O-O) aluminum hydride complexes as catalysts.

The first reduction product pinBOCOH may react further with one more equivalent of HBpin forming the second reduction product bis(boryl)acetal, pinB-

$OCH_2O$-Bpin. This product reacts directly with another equivalent of HBpin that leads to the formation of methoxyborane and bis(boryl)ether (pinB-O-Bpin) as co-product. This final product is of greater interest in the context of renewable liquid fuels and methanol-based transformations as it can be easily hydrolyzed to form methanol.

The kinetics for the HBpin-mediated reduction of $CO_2$ was investigated with 1 mol% of complex **3**. The results in the graph ln [(HBpin /(HBpin)$_0$] x time form a straight line, which indicates a first order reaction rate in HBpin (**Figure 10**). Thus the velocity equation is defined as v = k$_{obs}$ [HBpin] and, for a given set of conditions (i.e. catalyst 1 mol%, $CO_2$ pressure of 1.5 bar and T = 90 ºC) the reaction rate depends only on the concentration of HBpin present in the reaction mixture. The kinetics for complex **1** was also investigated at 10 mol% (**Figure 11**) and the same first-order behavior was observed.
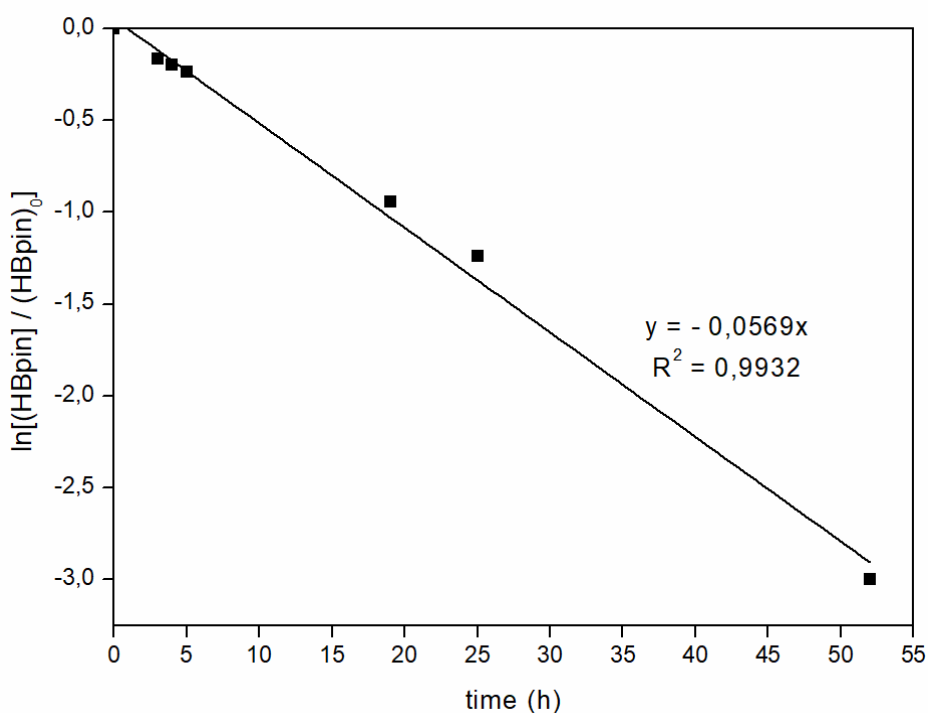


**Figure 10**. Graph of ln[(HBpin)/(HBpin)$_0$] x time for the reduction of $CO_2$ in the presence of HBpin and complex **3** (1 mol%). Conditions: $C_6D_6$; T = 90 ºC.

The graph shows $\ln[(HBpin)/(HBpin)_0]$ on the y-axis (ranging from 0,0 to -2,5) versus time (h) on the x-axis (ranging from 0 to 50). The linear fit is given by:

$y = -0{,}05706x$
$R^2 = 0{,}9952$
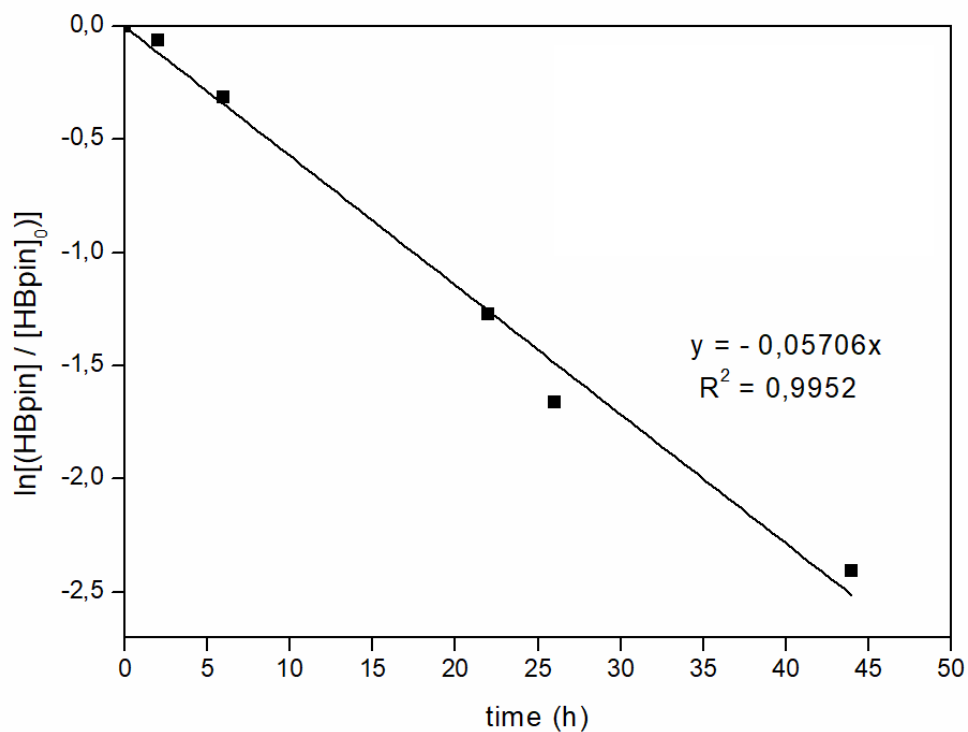
**Figure 11**. Graph of $\ln[(HBpin)/(HBpin)_0]$ x time for the reduction of $CO_2$ in the presence of HBpin and complex **1** (10 mol%). Conditions: $C_6D_6$; T = 90 °C.

## 2.3   Conclusion

$CO_2$ was successfully reduced into the methanol precursor in a solvent-free borane-mediated system that has the potential for a sustainable industrial process based on large-scale $CO_2$ utilization. Homogeneous catalysis involving hydroboration reactions of $CO_2$ with pinalcolborane constitutes one of the first examples of aluminum-based catalysts for such catalytic reactions. Four aluminum hydride (**1** and **3**) and formate (**2** and **4**) were synthesized, isolated and applied. All of them were active catalysts in the borane-mediated reduction of $CO_2$. According to the amount of employed catalyst, important precursors for the chemistry and energy sector were formed, formoxyborane and methoxyborane, which can be easily transformed into formic acid and methanol, respectively. As the Al-H catalysts did not follow the metal-hydride mechanism, a new mechanism was proposed. This mechanism suggests that a simple acetate salt could also perform the $CO_2$ reduction in the presence of hydroboranes by an acetate-catalyzed borane activation, which is the central topic of the next chapter.

Chapter I - Aluminum Tripod (O-O-O) Hydride Complexes Catalyze the Borane-Mediated Reduction of
Carbon dioxide into Methoxyborane and Formoxyborane

55

## 2.4   References

[1]    M. Courtemanche, J. Larouche, M. Légaré, W. Bi, L. Maron, F. Fontaine *Organomet.* **2013**, *32*, 6804−6811.

[2]    E. Alper, O. Y. Orhan, *Petroleum* **2017**, *3*, 109–126.

[3]    S. Chakraborty, J. Zhang, J. A. Krause, H. Guan, *J. Am. Chem. Soc.* **2010**, *132*, 8872–8873.

[4]    S. Bontemps, L. Vendier, S. Sabo-Etienne, *Angew. Chem. Int. Ed.* **2012**, *51*, 1671–1674.

[5]    M. D. Anker, M. Arrowsmith, P. Bellham, M. S. Hill, G. Kociok-, D. J. Liptrot, M. F. Mahon, C. Weetman, **2014**, 2826–2830.

[6]    H. Suh, L. M. Guard, N. Hazari, *Chem. Sci.* **2014**, *5*, 3859–3872.

[7]    L. J. Murphy, H. Hollenhorst, R. McDonald, M. Ferguson, M. D. Lumsden, L. Turculet, *Organomet.* **2017**, *36*, 3709−3720.

[8]    R. Shintani, K. Nozaki, *Organomet.* **2013**, *32*, 2459–2462.

[9]    N. P. Mankad, D. S. Laitar, J. P. Sadighi, *Organomet.* **2004**, *23*, 3369–3371.

[10]   G. Ménard, D. W. Stephan, *J. Am. Chem. Soc.* **2010**, *132*, 1796–1797.

[11]   S. Bontemps, L. Vendier, S. Sabo-Etienne, *Angew. Chem. Int. Ed.* **2012**, *51*, 1671–1674.

# 3 CHAPTER II - ACCESS TO METHANOL: CONVERSION OF CARBON DIOXIDE THROUGH HYDROBORATION CATALYSIS USING THE SIMPLE ACETATE ANION AS CATALYST
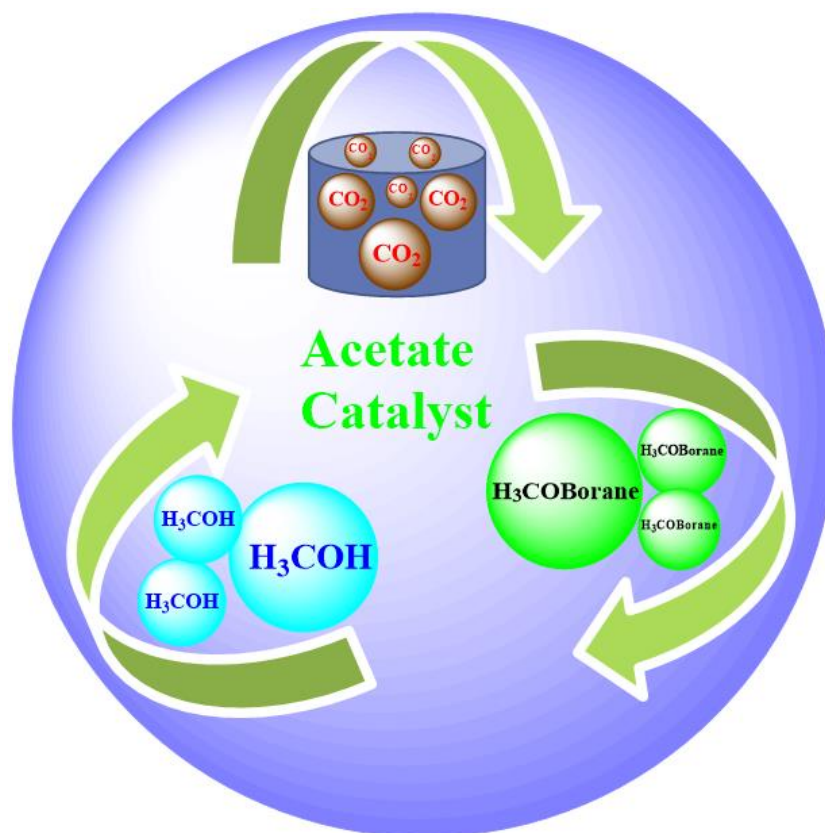
Graphical Abstract

**Abstract**

*Herein, we report about the use of very simple, cheap and stable acetate salts - sodium, potassium and tetrabutylammonium acetate (TBAAc) - for the reduction of $CO_2$ with the hydroboranes HBpin and BMS for the first time. The acetate salts showed high selectivity for methoxyborane (>94%). The solubility of TBAAc played a key role leading the reaction to work in solvent-free conditions with HBpin and increasing more than twice the TON: 970 and TOF reaching 51 $h^{-1}$ using 0.1 mol% of the catalyst. Although it was not possible to carry out the reaction with BMS under solvent-free conditions, it showed a higher activity (TON: 2,490 and TOF: 124 $h^{-1}$) compared to HBpin. The intermediates 1 and 2 where characterized in situ leading us to propose the mechanism for the HBpin-mediated reaction, which starts with the hydroborane activation by the acetate anion as we predicted in **Chapter I**.*

## 3.1    Introduction

Due to environmental and economic problems, as well as the probable shortage of petroleum-based chemicals, materials and fuels, it is desirable to develop a $CO_2$-based biorefinery to supply these products.[1] As stated in the literature review of this thesis, $CO_2$ can be converted into methanol. Nevertheless, the industry produces methanol mainly from non-renewable fossil sources. Homogeneous catalysis could promote the substitution of these depleting and polluting sources by the $CO_2$ reduction in the presence of hydroboranes, producing either formic acid or methanol precursors. Although several studies were reported about the successful preparation of methanol, until now, the industrial implementation of these processes has been thwarted by the use of either inefficient catalysts[2] or expensive and unstable catalysts.[3][4] The proposed mechanism for the reduction of $CO_2$ in the presence of HBpin and Al-H catalysts (**Chapter I**) suggested the potential use of simple acetate salts in this reaction, which is the topic of this chapter.

In the literature, Lewis base catalysts for hydroboration of $CO_2$ were already reported. Important to note that the reaction can start in two ways: (a) with the activation of $CO_2$ or (b) the activation of hydroborane.[5],[6]

In addition, Lewis pair catalysts can also perform $CO_2$ hydroboration. In this case the reaction begins by an ambiphilic activation of the $CO_2$ with the frustrated Lewis Pairs catalysts (FLP).[7],[8],[9],[10],[11]

## 3.2    Results and Discussion

This project aimed at developing an acetate-catalyzed hydroboration for the selective $CO_2$ reduction into a methanol precursor (methoxyborane) to match the industrial demand. Acetate salts are available on a large scale, inexpensive, stable and non-toxic, making them catalysts of choice for sustainable processes. As a consequence, this strategy has the potential to contribute effectively to the development

of a biorefinery-based industry. Sodium, potassium and tetrabutylammonium acetate were tested as catalysts in the hydroboration of $CO_2$, varying the borane species, catalyst loading, solvent, and reaction temperature (**Table 1**).

**Table 1**. Acetate salt-catalyzed reduction of $CO_2$ by hydroboration into methoxyborane and boroxine.
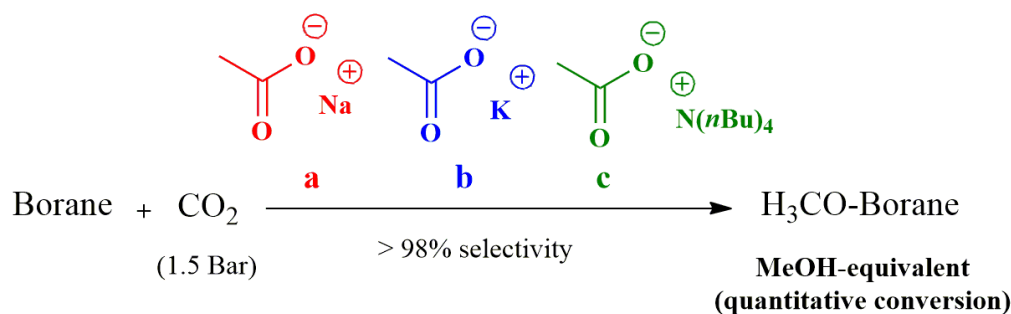


| Entry | Borane | Catalyst | Catalyst (mol%) | Solvent | Temperature (ºC) | Time (h) | Conv.[a] (%) | TON[b] | TOF (h⁻¹)[c] |
|---|---|---|---|---|---|---|---|---|---|
| 1 | HBpin | a | 0.6 | $C_6D_5Br$ | 120 | 65 | 96 | 580 | 9 |
| 2 | HBpin | b | 0.1 | $C_6D_5Br$ | 120 | 65 | 94 | 940 | 14 |
| 3 | HBpin | c | 0.1 | $C_6D_6$ | 90 | 46 | 94 | 940 | 20 |
| 4 | HBpin | c | 1 | $C_6D_6$ | 90 | 20 | 96 | 96 | 5 |
| 5 | HBpin | c | 0.1 | - | 90 | 19 | 97 | 970 | 51 |
| 6 | $H_3B-S(Me)_2$ | c | 0.1 | $C_6D_6$ | 40 | 40 | 63 | 1890 | 47 |
| 7 | $H_3B-S(Me)_2$ | c | 0.1 | $C_6D_6$ | 60 | 20 | 83 | 2490 | 124 |
| 8 | $H_3B-S(Me)_2$ | c | 0.1 | - | 40 | 20 | - | - | - |

[a] Conv. = conversion. [b] TON = turnover number; calculated by the integration of the ¹H NMR specific signals of the products HOCOBpin (8.21 ppm), pinBOCH₂OBpin (5.49 ppm) and methoxyborane (3.51 ppm),[12] using hexamethylbenzene as internal standard; and by comparison of the ¹¹B NMR spectra of the reagent and products. [c] TOF = Turnover frequency = TON/reaction time.

Initially, this reaction was explored with the more reactive HBpin borane and the sodium and potassium acetate salts as catalysts (**Entries 1**-**2**). Bromobenzene ($C_6D_5Br$) as solvent and the reaction temperature of 120 ºC were necessary to solubilize the catalysts. Both acetates revealed to be active and selective catalysts for $CO_2$ reduction. The ¹H NMR spectrum of the reaction products showed a new peak at 3.46 ppm, which confirmed the production of $CH_3OBpin$.[12] This was accompanied by the formation of

the pinBOBpin co-product. TON of 580 and 940 were achieved with the sodium and potassium catalysts, respectively. Considering the facile and fast conversion of methoxyborane into methanol by a simple hydrolysis at RT,[12] this process represents a promising strategy for the sustainable production of methanol.

Tetrabutylammonium acetate (TBAAc) as catalyst enabled using the less polar benzene ($C_6D_6$) as solvent, reaching a TON of 940 and TOF of 20 h$^{-1}$ with the same catalyst loading of 0.1 mol% at 90 °C (**Entry 3**). Higher TBAAc contents resulted in lower TON, being consistent with its role as catalyst (**Entries 3-4**). Taking advantage of the physical properties of TBAAc and the solubility of HBpin in liquid $CO_2$, a solventless approach was tested, which exhibited a slightly better catalytic performance (TOF = 51 h$^{-1}$) (**Entry 3** *vs* **5**). Although less reactive, borane dimethyl sulfide (BMS) is an economically more attractive alternative than HBpin as borane source. The catalytic reaction with BMS as a borane source ($C_6D_6$) also resulted in the catalytic reduction of $CO_2$ at 40 °C, showing a new peak at 3.40 ppm (**Figure S11**) in the $^1$H NMR spectra, which corresponds to the methanol precursor boroxine $(CH_3OBO)_3$ (**Entry 6**).[13]

A further increase of the reaction temperature to 60 °C afforded the highest TON and TOF of 2490 and 124 h$^{-1}$, respectively (**Entry 7**). When applying this catalytic system under solventless conditions at 40 °C (**Entry 8**), no product was formed. This means that further optimization of this acetate-based catalyst system is necessary to proceed under solventless conditions. The inability of the HBpin to react with $CO_2$ without catalyst is known in the literature.[14]

The reduction by hydroboration was followed by both $^1$H and $^{11}$B NMR. Spectra of the TBAAc-catalyzed (0.1 mol%) hydroboration of $CO_2$ (1.5 bar) with HBpin in $C_6D_6$ at 90 °C are shown in **Figure 1** ($^1$H) and **Figure 2** ($^{11}$B). During the course of this reaction, **Figure 1** shows an increasing intensity of the methoxyborane signal at 3.46 ppm. **Figure 2** shows a steady decrease of the intensity of the HBpin doublet at 29.03 and 27.67 ppm, which corresponds to its consumption. Two novel signals appeared at 22.57 and 21.59 ppm, corresponding to H$_3$COBpin and pinBOBpin, respectively. These signals increased with time, being in agreement with the selective formation of the methanol precursor.[12]

**Figure 1**. $^1$H NMR spectra (400 MHz, $C_6D_6$) of the reduction of $CO_2$ in the presence of HBpin and TBAAc (0.1 mol%). Conditions: $C_6D_6$; T = 90 ℃; internal standard = hexamethylbenzene.
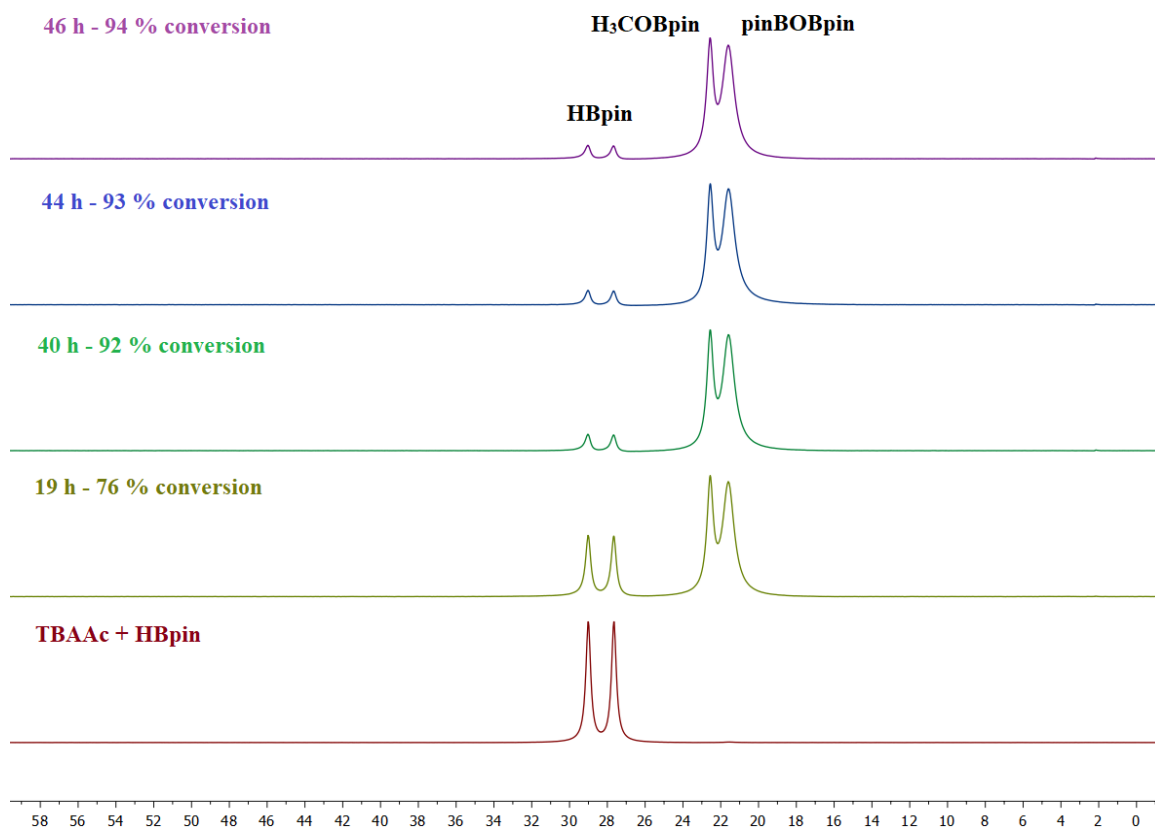
**Figure 2**. $^{11}$B NMR spectra (128 MHz, $C_6D_6$) of the TBAAc-catalyzed (0.1 mol%) hydroboration of $CO_2$ (1.5 bar) with HBpin at 90 °C. Internal standard = hexamethylbenzene.

The three reduction products were evidenced *in situ* by NMR during the reaction with 0.1 mol% TBAAc at 90 ° C (**Figure 3**). The first pinacolborane $CO_2$ reduction product, HOCOBpin, appeared at 8.19 ppm. The second reduction product, pinBOCH$_2$OBpin, appeared at 5.35 ppm. And the third reduction product, H$_3$COBpin, appeared at 3.46 ppm (**Figure S3**).
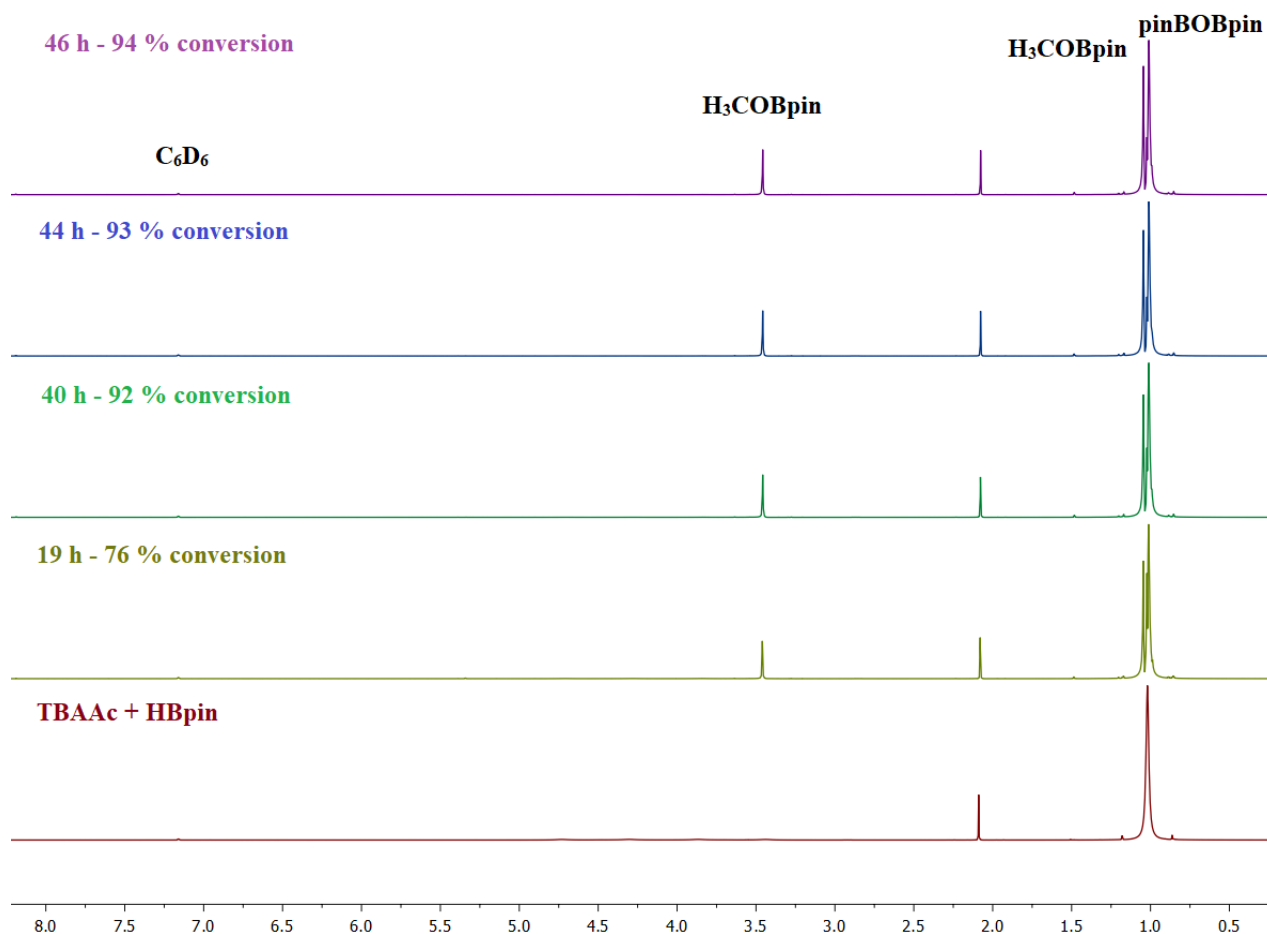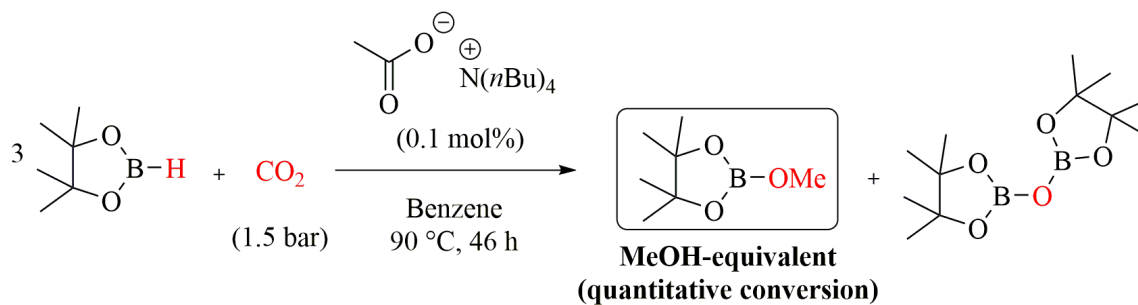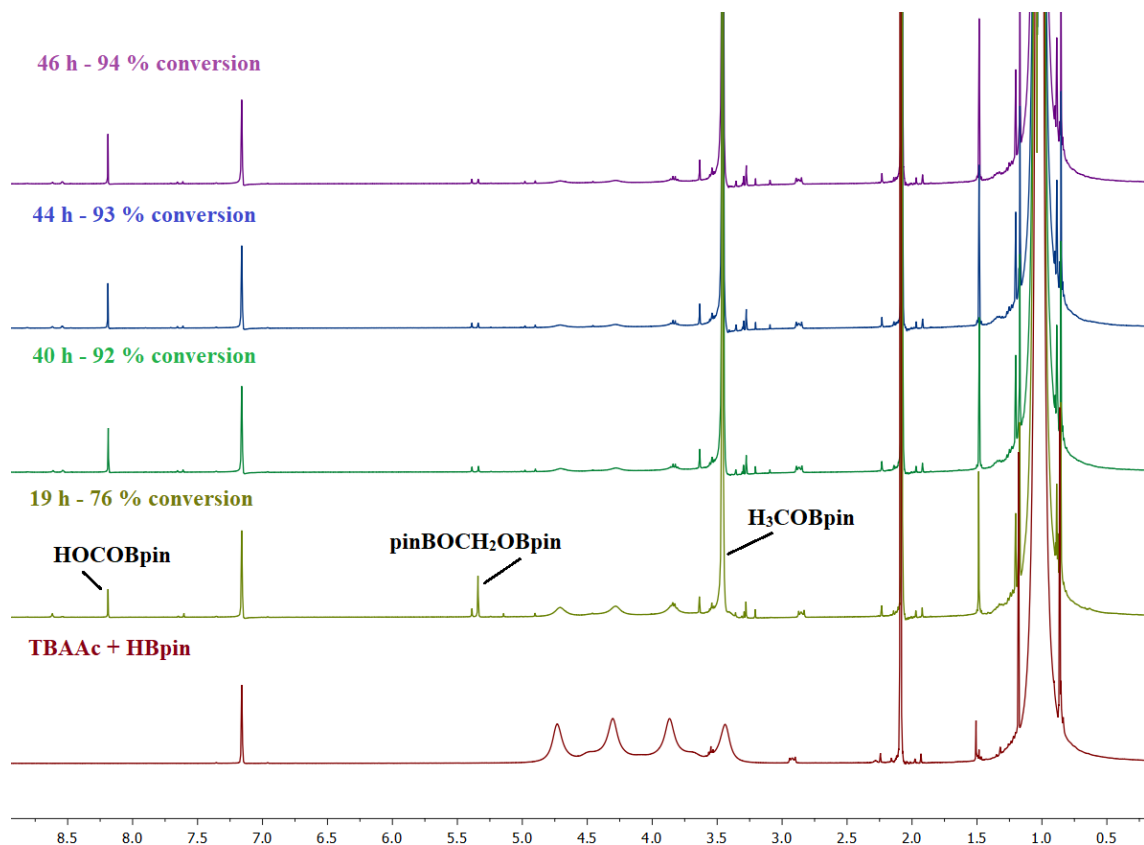
**Figure 3**. $^1$H NMR zoomed spectra (400 MHz, $C_6D_6$) of the reduction of $CO_2$ in the presence of HBpin and TBAAc (0.1 mol%). Conditions: $C_6D_6$; T = 90 ºC; internal standard = hexamethylbenzene.  HOCOBpin (8.19 ppm), pinBOCH$_2$OBpin (5.34 ppm) and H$_3$COBpin (3.46 ppm).[12]

The role of the acetate catalyst in the reduction of $CO_2$ with HBpin was studied under stoichiometric conditions, performing a series of NMR studies (**Figure 4**). After 1 h at room temperature, the $^1$H (**Figure 4**), $^{11}$B (**Figure 5**) and $^{13}$C (**Figure 6**) NMR spectra indicated the formation of intermediate **1**, a borate species resulting from the addition of the acetate ion to HBpin.
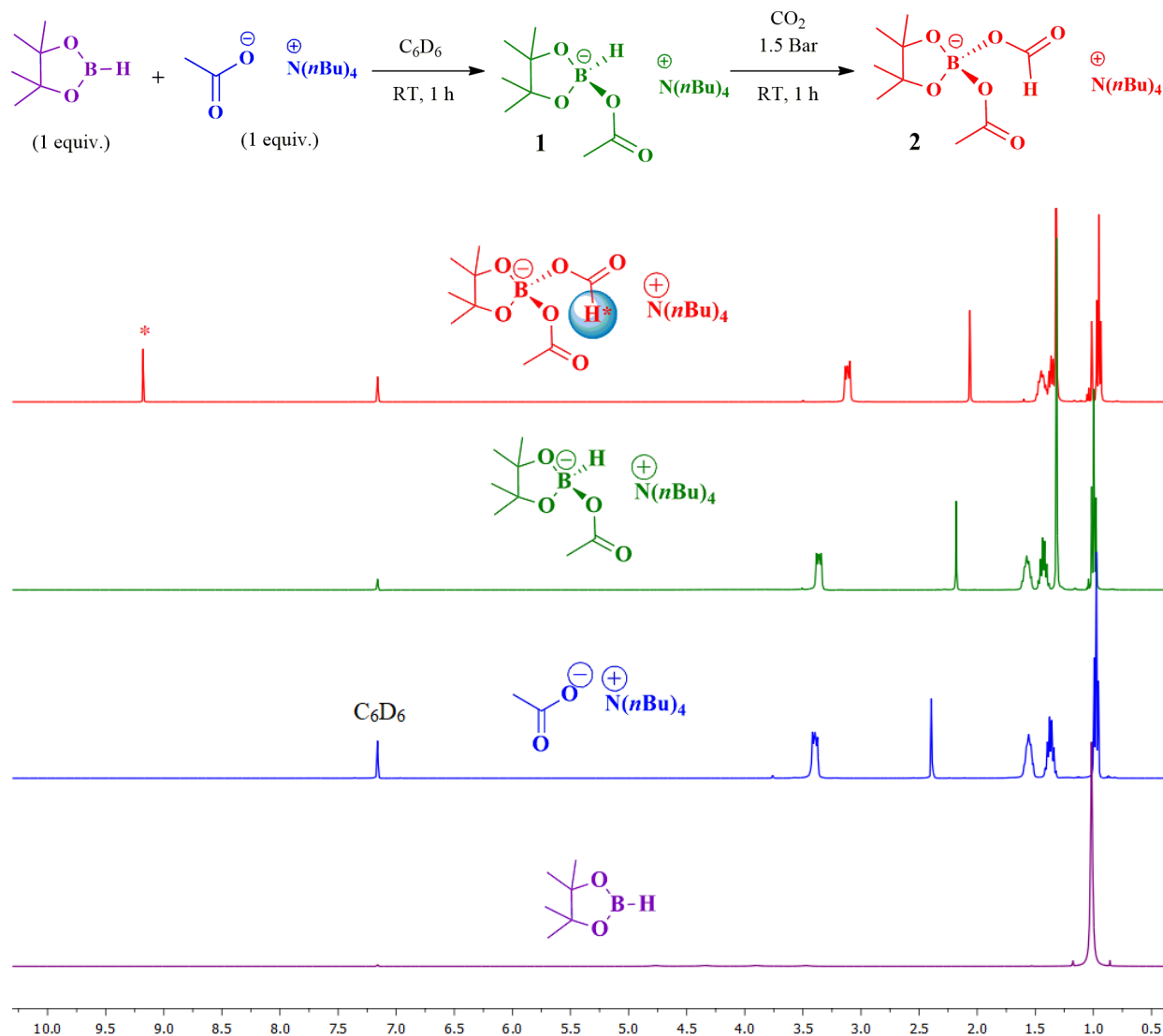
**Figure 4.** $^1$H NMR spectra (400 MHz, $C_6D_6$) of HBpin; TBAAc; a 1:1 mixture of TBAAc and HBpin after 1 h at room temperature; and after subsequent addition of $CO_2$ and 1 h at room temperature.

Attempts to isolate this compound were unsuccessful as decomposition occurred. Subsequently, excess of $CO_2$ was added to intermediate **1** to quantitatively afford the corresponding formate insertion product **2** (**Figure 4**), a likely intermediate in the acetate-catalyzed $CO_2$ hydroboration with HBpin. A new signal appeared at 9.18 ppm in the $^1$H NMR spectrum after 1 h at room temperature (**Figure 7**), in line with the formation of a formate species. Species **2** was fully characterized by $^{11}$B (**Figure 8**), $^{13}$C (**Figure 9**), HSQC (**Figure 10**) and HMBC (**Figure 11**) NMR, confirming its identity.
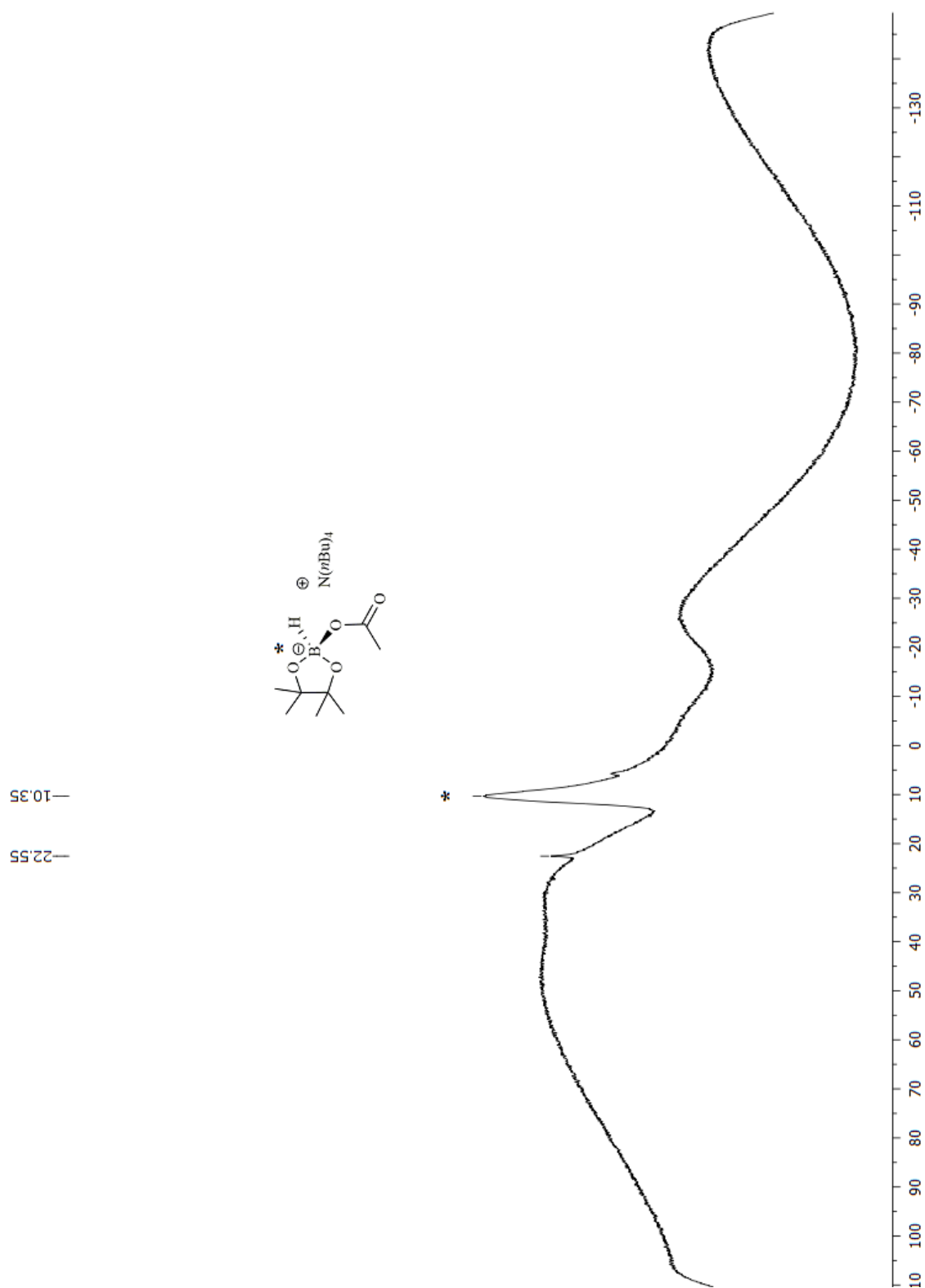
**Figure 5**. $^{11}$B NMR spectrum (128 MHz, $C_6D_6$) of the stoichiometric reaction between TBAAc and HBpin in $C_6D_6$, after 1 h at room temperature.
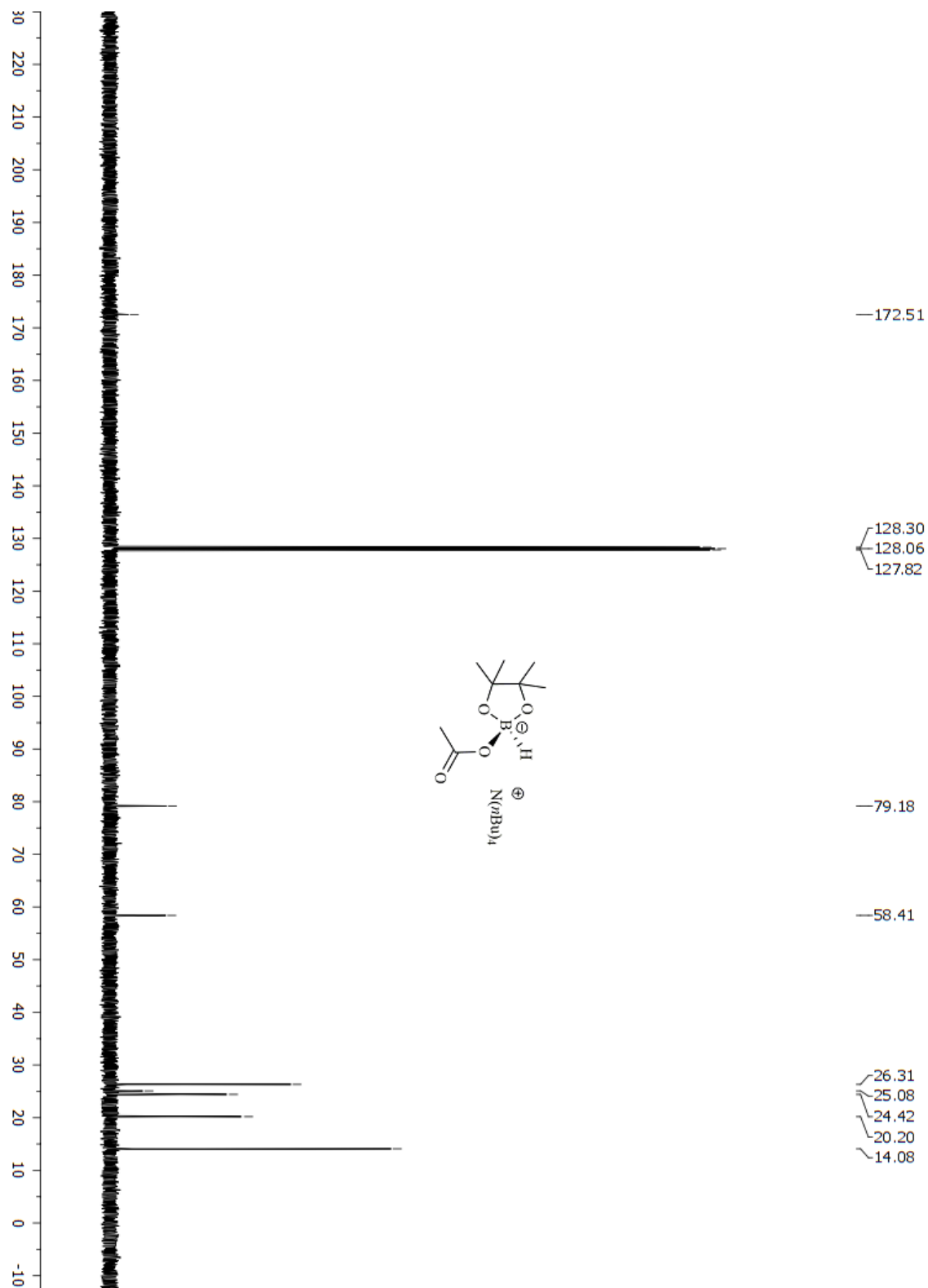
**Figure 6.** $^{13}C$ NMR spectrum (101 MHz, $C_6D_6$) of the stoichiometric reaction between TBAAc and HBpin in $C_6D_6$, after 1 h at room temperature.
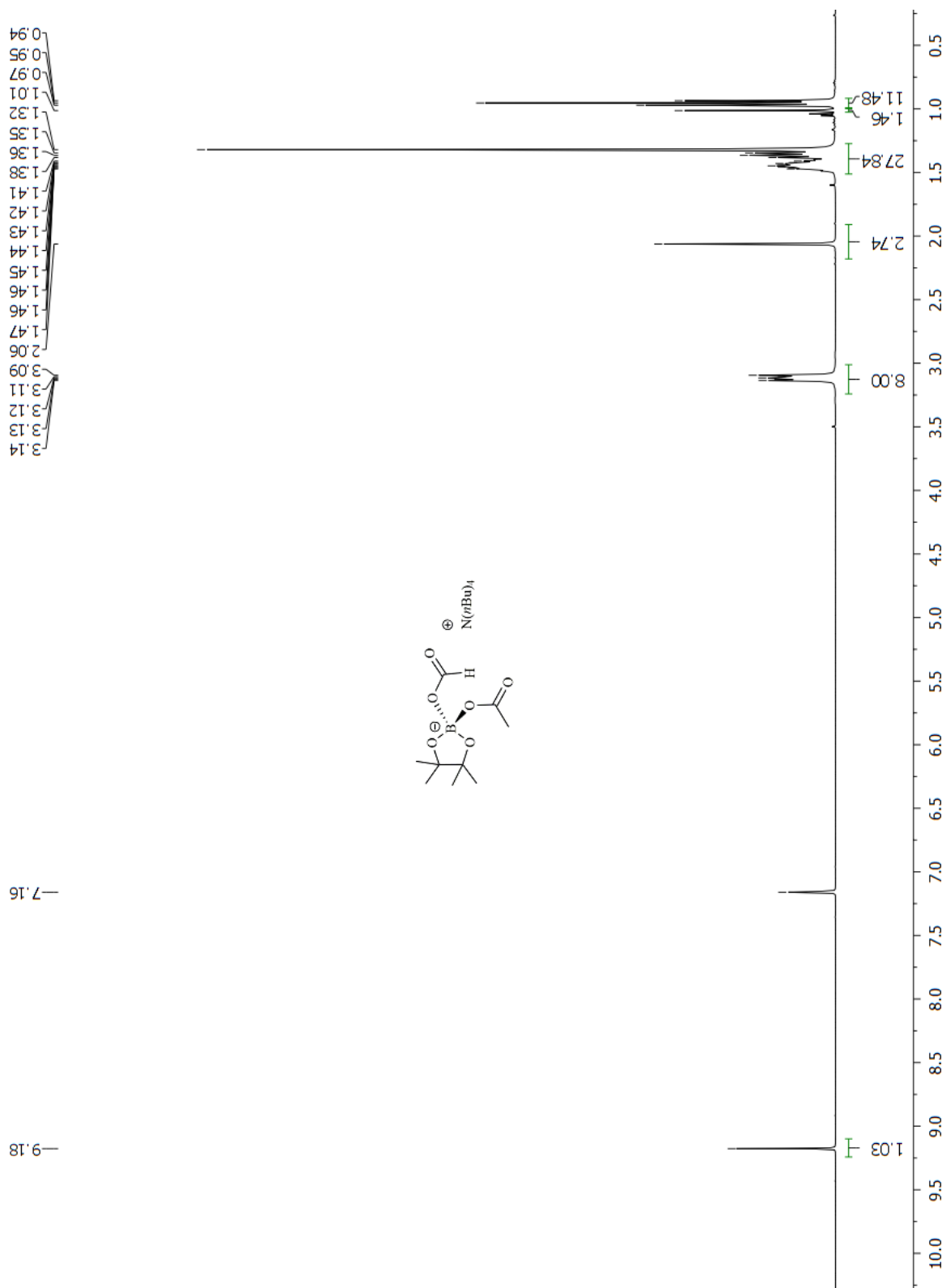
**Figure 7**. $^1$H NMR spectrum (400 MHz, C$_6$D$_6$) of compound **1** in the presence of CO$_2$ after 1 h at room temperature.
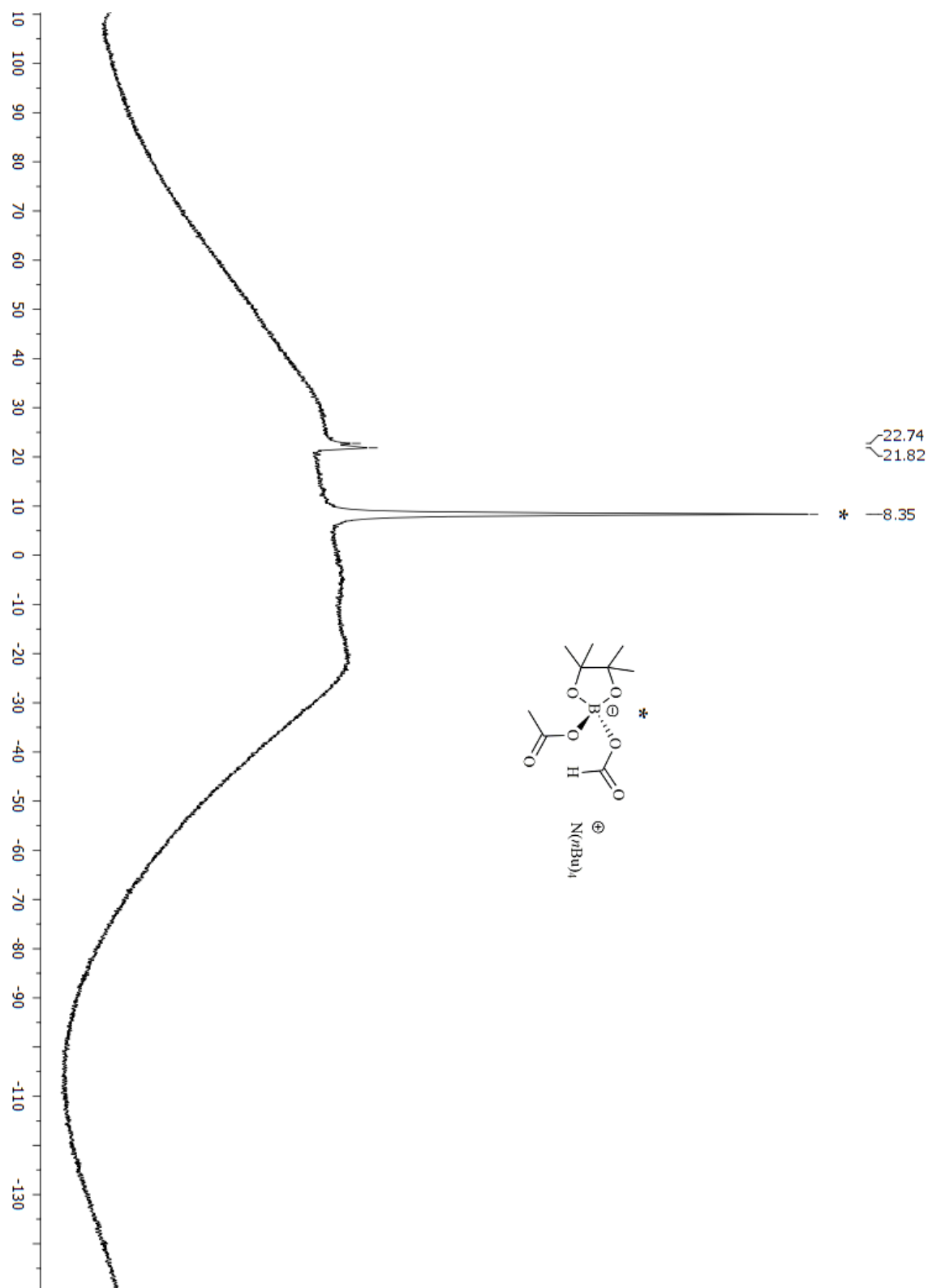
**Figure 8.** $^{11}$B NMR spectrum (128 MHz, $C_6D_6$) of compound **1** in the presence of $CO_2$ after 1 h at room temperature.
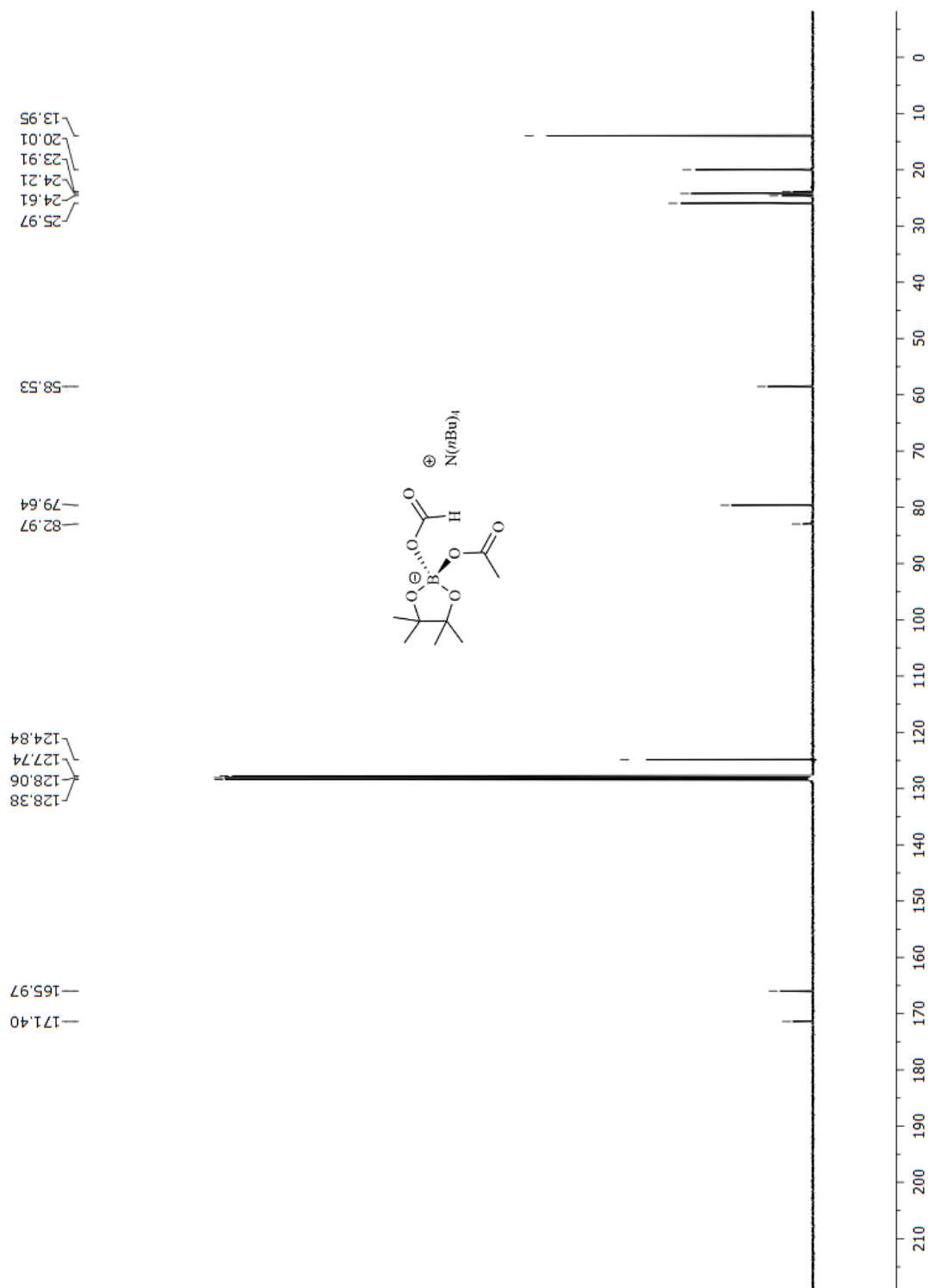
**Figure 9.** $^{13}C$ NMR spectrum (101 MHz, $C_6D_6$) of compound **1** in the presence of $CO_2$ after 1 h at room temperature. The peaks at 82.97 and 23.91 ppm indicate unreacted HBpin. The peak at 124.84 ppm belongs to free $CO_2$.
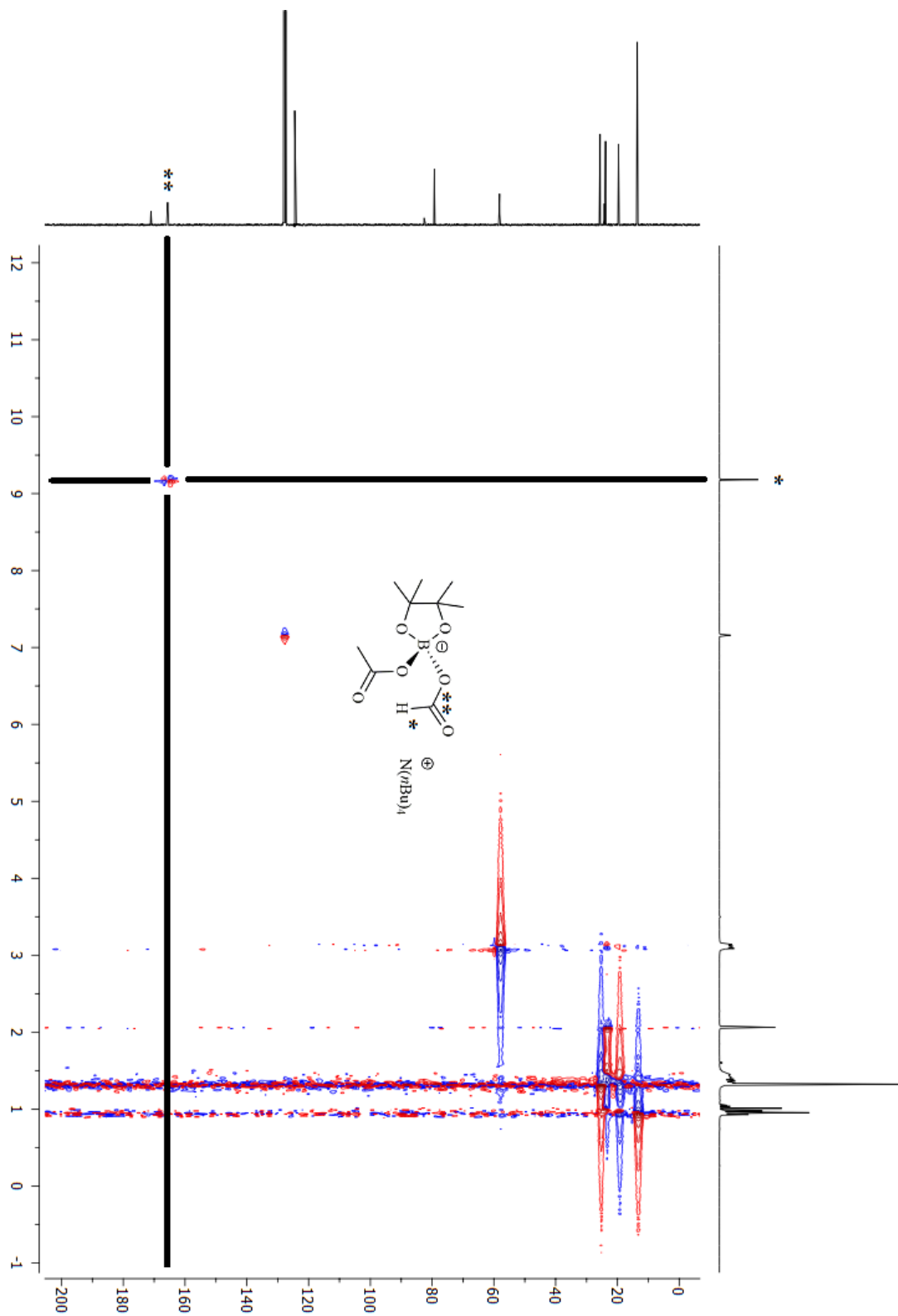
**Figure 10**. HSQC NMR spectrum ($C_6D_6$) of compound **1** in the presence of $CO_2$.
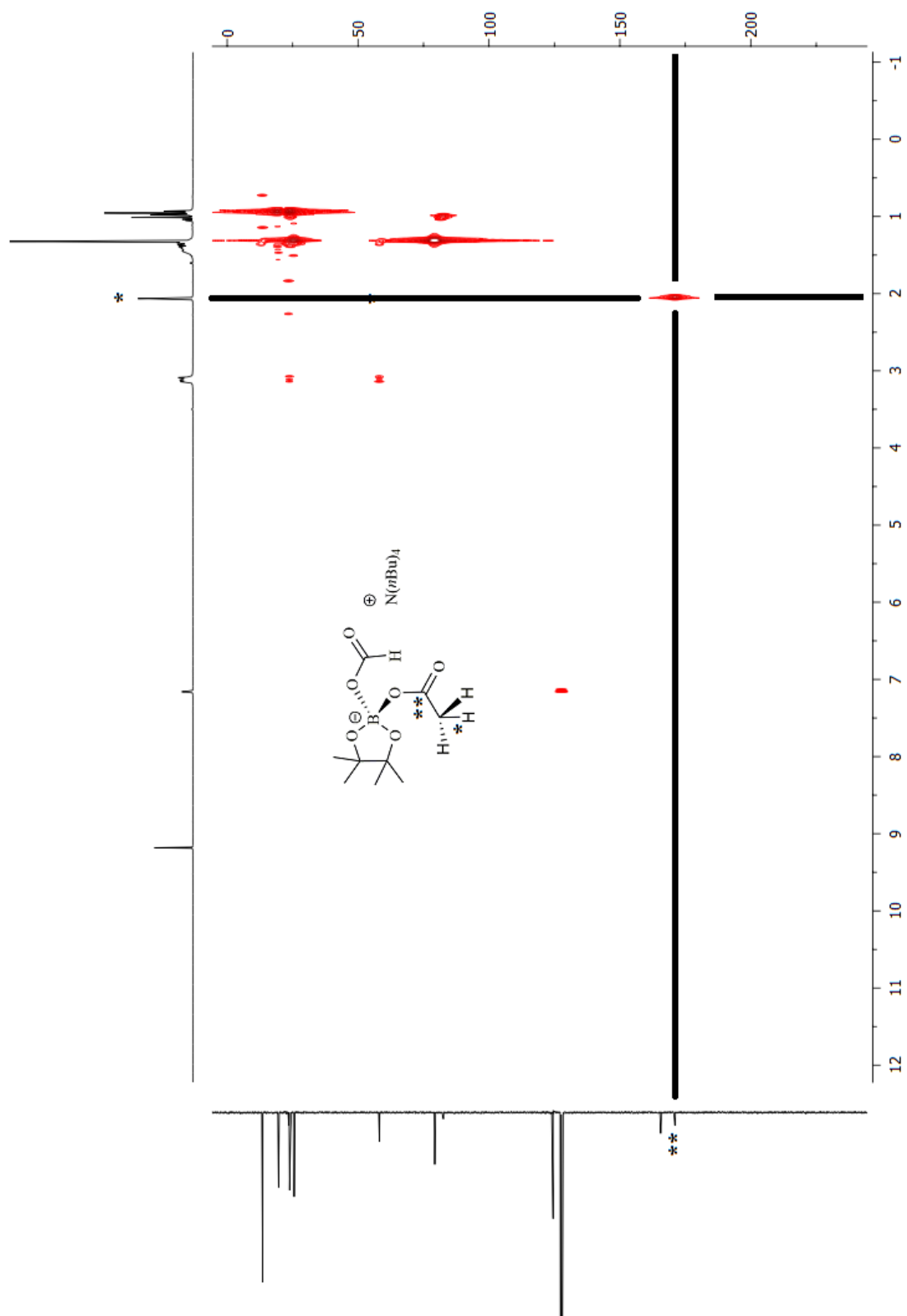
**Figure 11**. HMBC NMR spectrum ($C_6D_6$) of compound **1** in the presence of $CO_2$.

Based on the results obtained in the stoichiometric reaction between TBAAc and HBpin, we propose the catalytic cycle presented in **Scheme 1**. Initially, the acetate-catalyst activates the hydroborane, forming the more nucleophilic hydroborate species **1**. This enables the reaction of $CO_2$ into the B-H bond to form **2**. The reaction between **2** and HBpin; and the addition of another equivalent of $CO_2$ generates HOCOBpin and regenerates **2**. HOCOBpin reacts with another HBpin to form $pinBOCH_2OBpin$, which in the presence of one more equivalent of HBpin finally generates $CH_3OBpin$ and pinBOBpin.
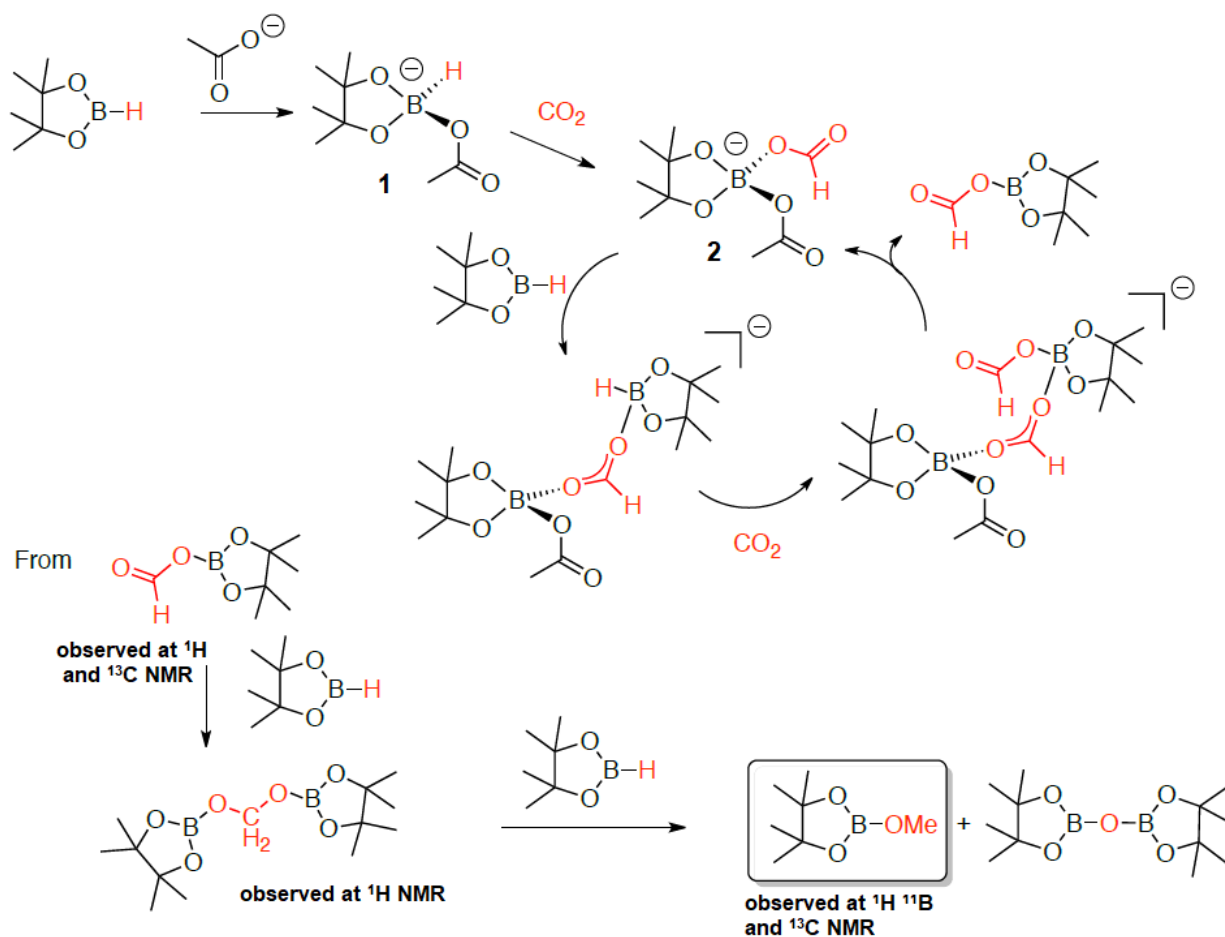


**Scheme 1**. Proposed mechanism for the acetate-catalyzed reduction of $CO_2$ with HBpin.

### 3.3   Conclusion

In conclusion, acetate salts are promising catalysts for the selective hydroborane promoted reduction of $CO_2$ into methoxyborane methanol precursors. Interestingly, this catalytic system allows performing this reaction under solvent-free conditions, which is an attractive feature for industrial applications. Therefore, these results could represent an important advance for the further implementation of a $CO_2$-based biorefinery for fuels and chemicals considering the abundance, simplicity, cheapness and stability of those catalysts.

## 3.4  References

[1]  (a) E. de Jong, A. Higson, P. Walsh, M. Wellisch, *A Rep. Prep. IEA Bioenergy-Task* **2011**, 1–36. (b) M. Aresta, A. Dibenedetto, A. Angelini *Chem. Rev.* **2014**, *114(3)*, 1709–1742.

[2]  S. Saeidi, N. A. S. Amin, M. R. Rahimpour, *J. CO$_2$ Util.* **2014**, *5*, 66–81.

[3]  F. J. Fernández-Alvarez, A. M. Aitani, L. A. Oro, *Catal. Sci. Technol.* **2014**, *4*, 611–624.

[4]  S. Bontemps, *Coord. Chem. Rev* **2016**, *308*, 117–130.

[5]  C. N. Gomes, E. Blondiaux, P. Thuéry, T. Cantat, *Chem. Eur. J.* **2014**, *20*, 7098–7106.

[6]  T. Wang, D. W. Stephan, *Chem. Commun.* **2014**, *50*, 7007–7010.

[7]  M. Courtemanche, M. Légaré, L. Maron, F. Fontaine, *J. Am. Chem. Soc.* **2013**, *135*, 9326−9329.

[8]   R. Declercq, G. Bouhadir, D. Bourissou, M. Légaré, M. Courtemanche, K. S. Nahi, N. Bouchard, F. Fontaine, L. Maron, *ACS Catal.* **2015**, *5*, 2513−2520.

[9]  G. Ménard, D. W. Stephan, *J. Am. Chem. Soc.* **2010**, *132*, 1796–1797.

[10] M. Courtemanche, J. Larouche, M. Légaré, W. Bi, L. Maron, F. Fontaine, *Organomet.* **2013**, *32*, 6804−6811.

[11] T. Wang, D. W. Stephan, *Chem. Eur. J.* **2014**, *20*, 3036–3039.

[12] S. Bontemps, L. Vendier, S. Sabo-Etienne, *Angew. Chem. Int. Ed.* **2012**, *51*, 1671–1674.

[13]  M. A. Courtemanche, M. A. Légaré, L. Maron, F. G. Fontaine, *J. Am. Chem. Soc.* **2013**, *135*, 9326–9329.

[14] S. Bontemps, L. Vendier, S. Sabo-Etienne, *Angew. Chem. Int. Ed.* **2012**, *51*, 1671–1674.

# 4 CHAPTER III - ORGANOMETALLIC-CATALYZED SYNTHESIS OF HIGH MOLECULAR WEIGHT POLY-(L-LACTIC ACID) WITH A COVALENTLY ATTACHED IMIDAZOLIUM SALT: PERFORMANCE-ENHANCED REDUCED GRAPHENE OXIDE-PLLA BIOMATERIALS

Chapter III - Organometallic-Catalyzed Synthesis of High Molecular Weight Poly-(L-Lactic Acid) with a
Covalently Attached Imidazolium Salt: Performance-Enhanced Reduced Graphene Oxide-PLLA
Biomaterials

81
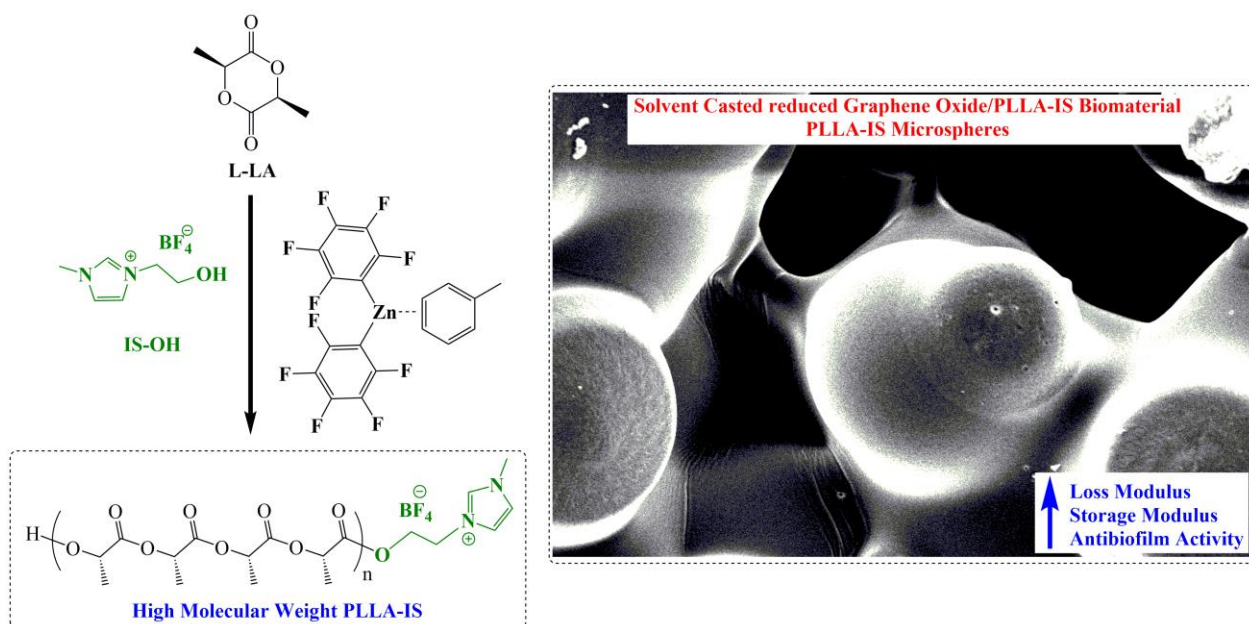
Graphical Abstract

## Abstract

*Herein, we report the synthesis of imidazolium salt end-functionalized PLLA (PLLA-IS) and its application in the preparation of reduced graphene oxide-PLLA composites. When applying the imidazolium salt 1-(2-hydroxyethyl)-3-methylimidazolium tetrafluoroborate as initiator, the organometallic $Zn(C_6F_5)_2$toluene complex polymerized L-lactide into high molecular weight PLLA-IS (Mn up to 56k). The presence of this imidazolium functionality enhanced the PLLA-reduced graphene oxide interaction, which promoted a homogenous dispersion of this filler when applying a solvent casting procedure. Significant improvements in the mechanical properties were obtained, reaching 148% and 105% for the loss and storage moduli, respectively. Besides, the composite **PLLA-IS/rGO-1%** inhibited the growth of fungal biofilms, including C. tropicalis (43%) and C. albicans (34%). Altogether, these materials have the properties for novel applications, including those of biomaterials.*

## 4.1   Introduction

Advances in global warming urged academia and industry to look for new alternatives that enable the replacement of polyolefin-derived materials. PLA is a biopolymer derived from sugar, which is biosynthesized by corn, using light, $H_2O$ and $CO_2$, contributing to the use of chemicals derived from $CO_2$.

PLLA polymer properties can be improved by adding nanofillers, e.g. carbon nanotubes[1],[2], graphene[3]-[6] and $SiO_2$[7],[8]. Graphene (**Figure 1**) is composed of one-atom-thick planar sheets of $sp^2$-bonded carbon atoms and features outstanding mechanical, thermal[9] and electrical[10] properties. In particular, it is considered as one of the strongest materials ever tested with a breaking strength about two hundred times of steel.[9] Thus, while still in its infancy, the use of graphene as a nanocomponent in polymer composites holds the greatest promises regarding the potential access to novel and improved materials.
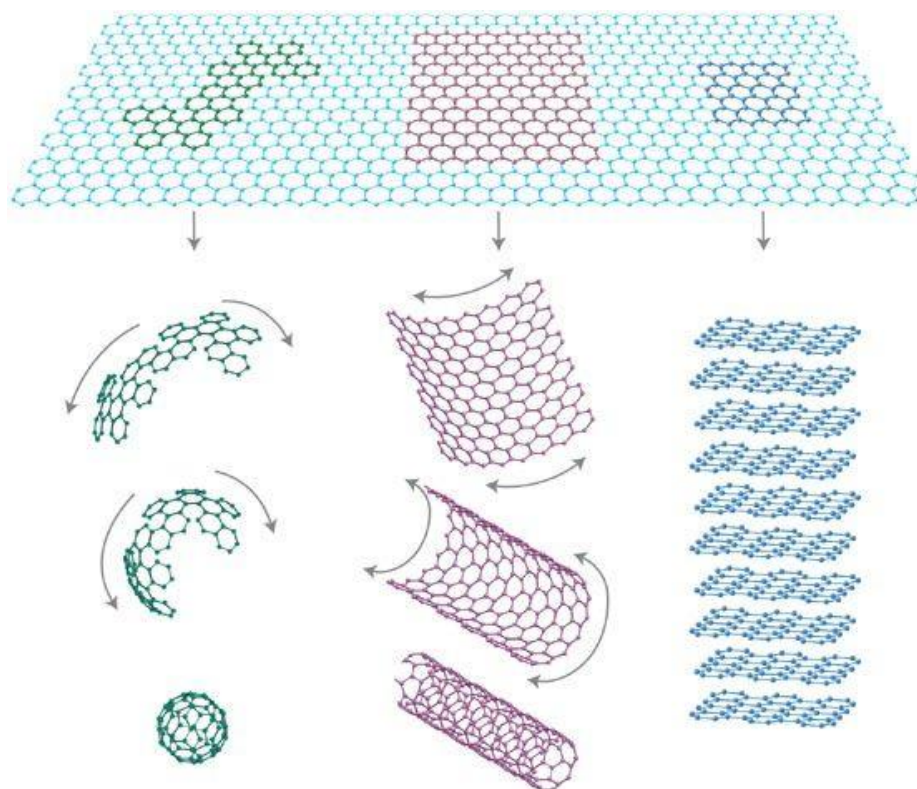


**Figure 1**. Graphene as precursor of buckyballs, nanotubes and graphite.[6]

Imidazolium salts (IS) are recognized as being suitable compatibilizing electrolyte agents due to the presence of surfactant-like cation and anion in its composition.[11] These tunable salts have unique properties depending on the nature of the cation and anion, leading to a large array of applications with such entities[12][13], most notably in the nanocomposite[14,15] and bioengineering[16] fields. In a recent work, IS dispersed in a PLLA matrix increased the storage and loss moduli, thermal resistance, as well as the microbial antibiofilm inhibition of the final material.[17] IS also exhibit potentially strong binding affinities with $sp^2$-carbon-based nanostructures, and PLLA with covalently attached IS (PLLA-IS) enhanced the dispersion of carbon nanotubes (CNT) in a polymeric matrix.[18]

Herein, the ROP of renewable L-lactide (**L-LA**) with an organometallic Zn complex using an imidazolium salt containing an alcohol group as initiator to functionalize the PLLA chain with an IS-end group (PLLA-IS). The $Zn(C_6F_5)_2$toluene complex catalyzed the ROP affording higher molecular weight PLLA-IS, which improved the interfacial interaction with reduced graphene oxide (rGO). Novel solvent-casted PLLA-IS/rGO bionanocomposites (**Figure 2**) with performance-enhanced mechanical and thermal properties, and fungal antibiofilm activity's were obtained, suggesting their potential application as biomaterials.



**Figure 2**. Proposed interaction between PLLA-IS and reduced graphene oxide.

## 4.2   Results and discussion

The present study aimed at combining graphene dispersion capability and IS-functionalized PLLA antibiofilm properties to form a new reinforced biomaterial. IS-end-functionalized PLLA (PLLA-IS) were shown to be accessible through ROP 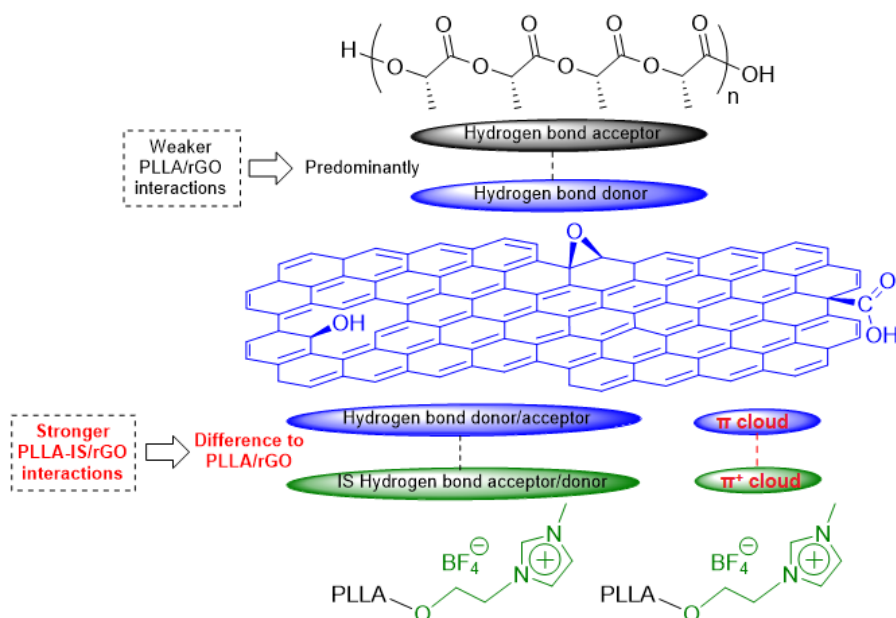of lactide by organocatalytic routes, but only low molecular weight PLLA-IS – maximum of 10,000 g/mol.[18] Access to higher molecular weight PLLA in a controlled manner is best-achieved using organometallic ROP catalysts. Nevertheless, access to PLLA-IS could not be achieved using catalyst $Sn(Oct)_2$,[19] the industrially implemented lactide ROP catalyst for PLLA synthesis.[19],[20] To date, access to PLLA-IS material through organometallic routes is not documented and would preferably involve cheap and earth-abundant metal sources.

Accordingly, due to the lower toxicity of Zn  (vs. Sn), Zn-based lactide ROPis of current interest and, in that regard, it was earlier reported that the Lewis acidic $Zn(C_6F_5)_2$ effectively polymerizes lactide in the presence of an alcohol initiator (such as BnOH) to produce BnO-end-functionalized PLLA.[21] Such approach was further exploited to successfully prepare PLLA-IS, thus involving the ROP of L-lactide and in the presence of an imidazolium alcohol moiety (**IS-OH**).

$Zn(C_6F_5)_2$(toluene) and 1-(2-hydroxyethyl)-3-methylimidazolium tetrafluoroborate (**IS-OH**) were used as catalyst and initiator, respectively, for the ROP of L-Lactide (L-LA). After an initial optimization process, the reaction temperature was set at 80 °C and toluene was chosen as solvent, which led to the effective preparation of PLLA-IS, as deduced from characterization data (NMR, MALDI-TOF, GPC). All ROP runs are compiled in **Table 1** and were conducted with different catalyst/initiator/monomer ratios. The GPC traces are all monomodal and the relatively narrow polydispersity's (PDI < 1.5) are in line with a controlled ROP process.

**Table 1**. **L-LA** ROP catalyzed by $Zn(C_6F_5)_2$toluene/**IS-OH**.[a]
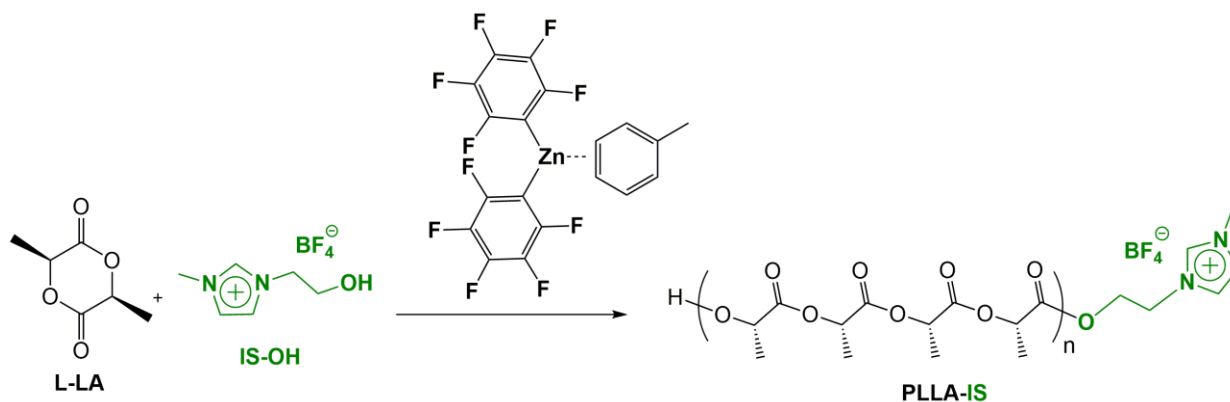


| Entry | Zn/IS-OH/L-LA | [L-LA]/[IS-OH] | t (min) | Conv (%)[c] | $M_{n\ theor}$[d] | $M_n$[e] | PDI[f] |
|---|---|---|---|---|---|---|---|
| 1 | 1/3/150 | 50 | 45 | 90 | 6,678 | 13,294 | 1.24 |
| 2 | 1/3/150 | 50 | 80 | 95 | 7,049 | 15,200 | 1.12 |
| 3 | 1/3/200 | 66 | 60 | 95 | 9,331 | 12,077 | 1.20 |
| 4 | 1/3/200 | 66 | 32 | 77 | 7,563 | 8,608 | 1.20 |
| 5 | 1/3/300 | 100 | 30 | 33 | 4,827 | 6,596 | 1.49 |
| 6 | 1/3/300 | 100 | 45 | 66 | 9,654 | 13,208 | 1.37 |
| 7 | 1/3/300 | 100 | 50 | 91 | 13,310 | 10,450 | 1.51 |
| 8 | 1/3/300 | 100 | 80 | 97 | 14,188 | 19,372 | 1.44 |
| 9 | 1/3/300 | 100 | 100 | 97 | 14,188 | 21,140 | 1.51 |
| 10 | 1/5/300 | 40 | 32 | 74 | 6,558 | 5,773 | 1.17 |
| 11 | 1/3/600 | 200 | 45 | 30 | 8,712 | 19,802 | 1.21 |
| 12 | 1/3/600 | 200 | 100 | 72 | 20,909 | 55,748 | 1.33 |
| 13 | 1/5/1000 | 200 | 6 h | 97 | 28,169 | 48,181 | 1.50 |
| 14 | 1/10/1000 | 100 | 6 h | 98 | 14,334 | 16,701 | 1.52 |
| 15 | 1/20/1000 | 50 | 6 h | 98 | 7,272 | 9,044 | 1.35 |

[a] Conditions: Toluene, $[L-LA]_0$ = 1 M, 80 ºC. [b] Reaction time in minutes. [c] L-LA conversion (calculated by 1H NMR integrating the monomer and polymer peaks). [d] Theoretical Mn = [[(ML-LA)0 x MwL-LA/(IS-OH)] + MwIL-OH] x conversion. [e] Measured by GPC in THF (30 ºC), using a polystyrene standard and a correction factor of 0.58. [f] Polydispersity obtained by GPC in THF (30 °C).

At lower initiator/catalyst ratio's (**Table 1**, **entries 1-9**, **11-12**), the experimental $M_n$ values were higher than the theoretical ones, which indicated a slower initiation *vs.* propagation in the present ROP process. The latter may be related to the steric hindrance of the **IS-OH** initiator.

Satisfyingly, higher initiator/catalyst ratios of ≥10 (**Table 1**, **entries 14 and 15**) resulted in a good agreement of theoretical and experimental Mn values, suggesting that **IS-OH** acted as an effective polymer chain transfer agent as the ROP proceeded and that lactide ROP catalysis mediated by $Zn(C_6F_5)_2$/**IS-OH** may occur in an immortal manner.

Indeed, the formation of chain-length-controlled PLLA-IS with Mn values matching the initial initiator/catalyst ratio is characteristic of an immortal ROP process. It is important that the use of $Zn(C_6F_5)_2$ as catalyst provided for the first time access to high molecular weight PLLA-IS, Mn up to 48,000 Da (**Table 1**, **entry 13**), which is of interest from an industrial point of view.

We propose the activated monomer mechanism (**Scheme 1**) for the functionalization of PLLA with IS (PLLA-IS). The mechanism initiates by the activation of the ester carbonyl group through the coordination of the Lewis acid species, $Zn(C_6F_5)_2$, and the subsequent nucleophile attack of the IS to the carbonyl group. Soon after, the polymerization process begins with cleavage of the O-acyl bond. In the next step, the propagation is initiated as more monomer molecules participate in the reaction. Finally, the IS containing alcohol group of the nucleophile remains in the polymer chain forming then PLLA-IS.
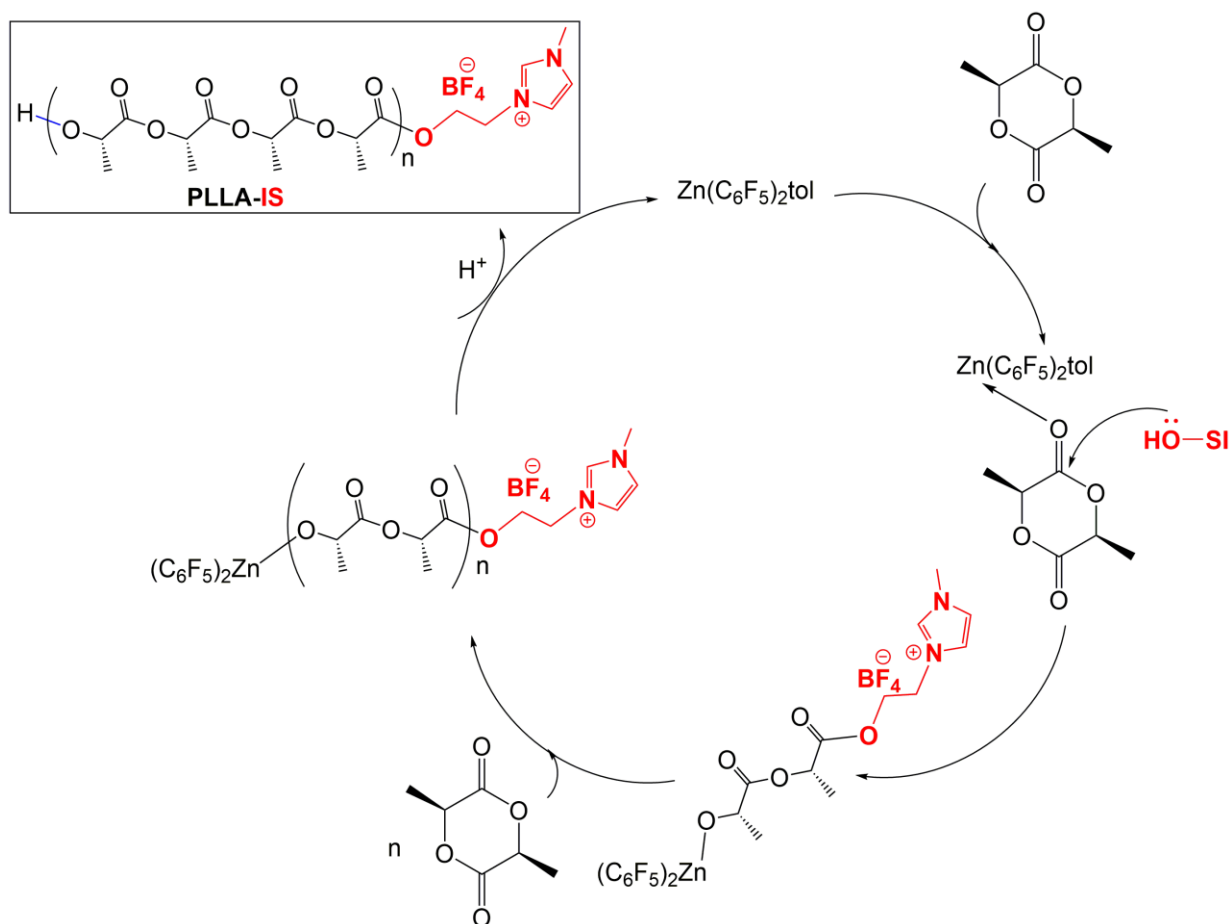
**Scheme 1**. Proposed monomer-activated mechanism for the formation of PLLA-IS with the organometallic catalyst $Zn(C_6F_5)_2$tol.

The controlled character of the ROP process was further evidenced through kinetic studies: i) a reaction rate with an observed first order in monomer was observed with a 2-3 min induction period for ROP initiation (**Figure 3**); and ii) a linear correlation between the PLLA-IS's Mn and monomer conversion (**Figure 4**). These data confirmed a controlled immortal polymerization for the preparation of PLLA-IS.
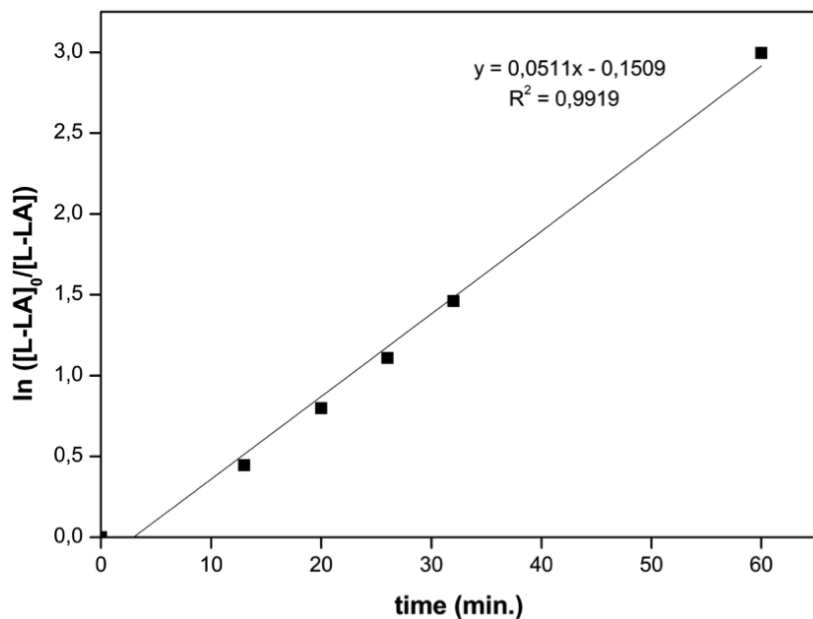
**Figure 3**. Graph of ln ([L-LA]$_0$/[L-LA]) *versus* time (min.) for the PLLA-IS prepared. Conditions: Zn/**IS-OH**/[L-LA]$_0$ = 1/3/200 (Table 1, entry 3).
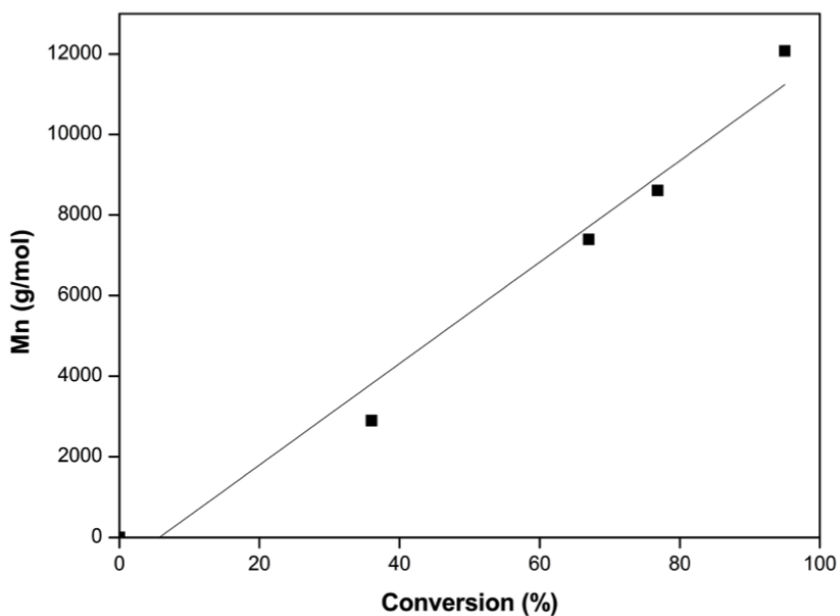


**Figure 4**. Graph of Mn (g/mol) *versus* conversion (%) for the PLLA-IS prepared. Conditions: Zn/**IS-OH**/[L-LA]$_0$ = 1/3/200 (Table 1, entry 3).

The formation of imidazolium-end-functionalized PLLA was deduced from NMR data (**Figures 5-6, and S5-S7**).
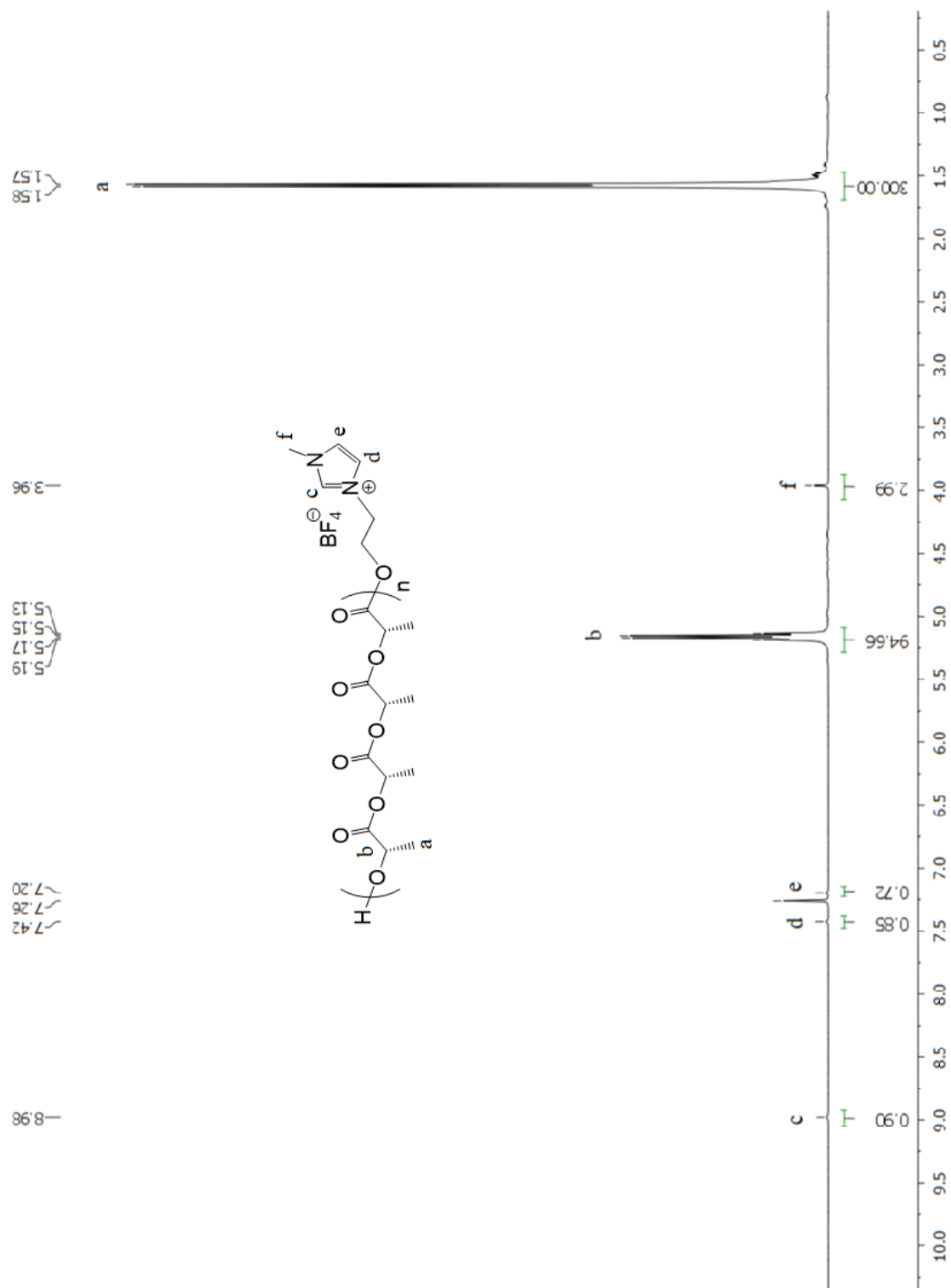
**Figure 5**. $^1$H NMR spectrum (500 MHz, $C_6D_6$) of PLLA-IS in $CDCl_3$. Conditions: **L-LA** (1000 equiv.), $[L\text{-}LA]_0 = 1$ M, **IS-OH** (20 equiv.), $Zn(C_6F_5)_2$toluene (1 equiv.), 80 °C, toluene.
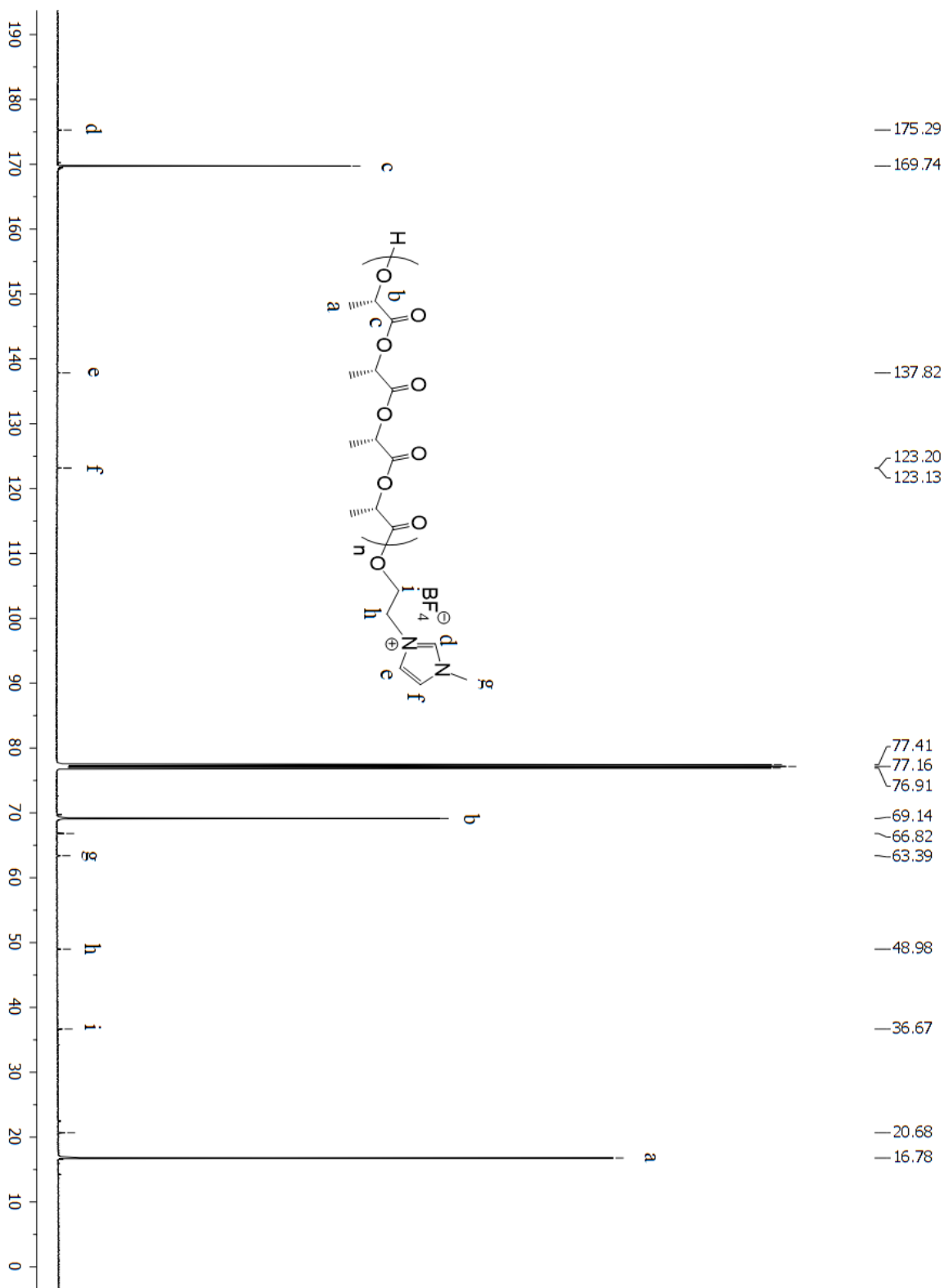
**Figure 6**. $^{13}$C NMR spectrum (126 MHz, CDCl$_3$) of PLLA-IS in CDCl$_3$. Conditions: **L-LA** (1000 equiv.), [L-LA]$_0$ = 1 M, **IS-OH** (20 equiv.), Zn(C$_6$F$_5$)$_2$toluene (1 equiv.), 80 ºC, toluene.

The formation of imidazolium-end-functionalized PLLA was also confirmed from MALDI-TOF spectrometric analyses (**Figures 7-8**). All these characterization data agree with the formation of PLLA chains covalently end-functionalized with the IS-O group (PLLA-IS). In particular, the MALDI-TOF mass spectrum presented in **Figure 7** is consistent with a Gaussian PLLA-IS product mass distribution, and the experimental mass values are in agreement with the calculated values (**Figure 8**).
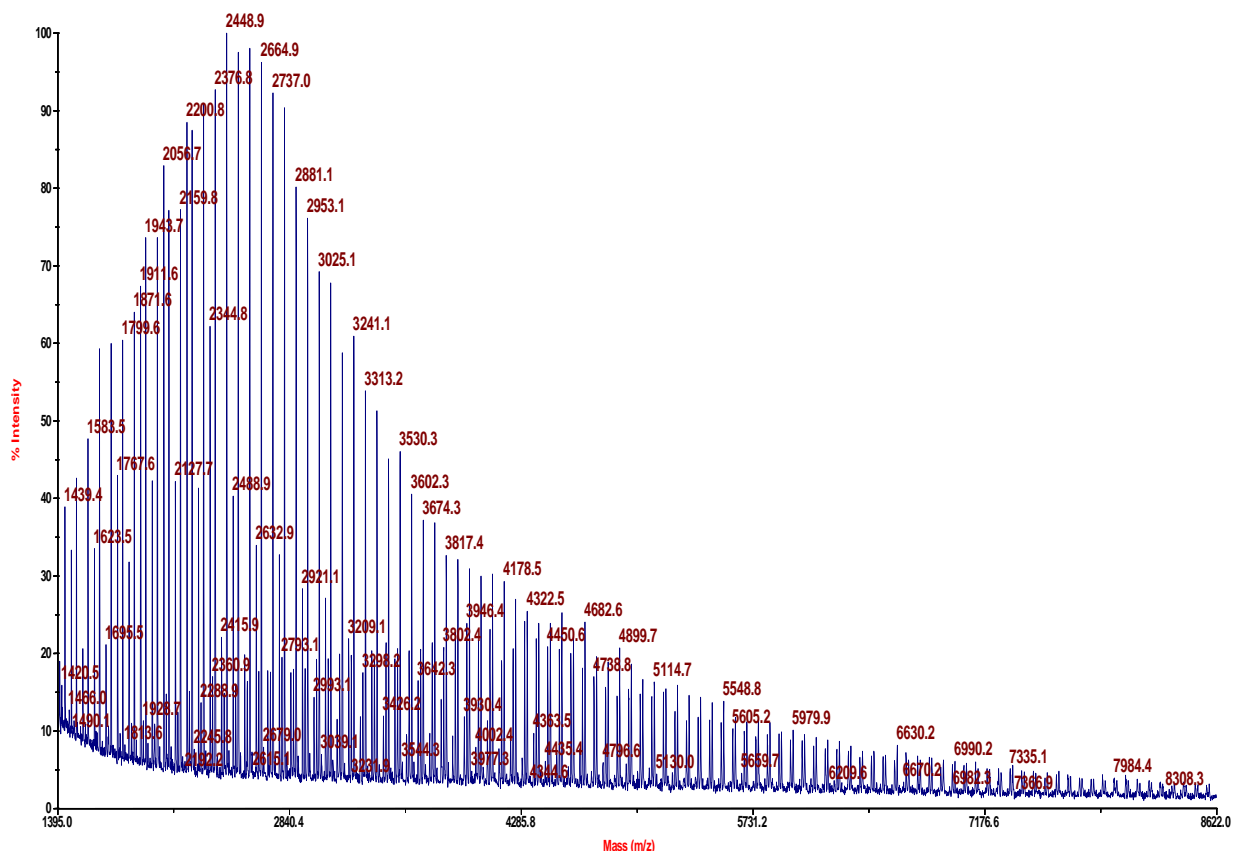


**Figure 7**. Positive ion MALDI-TOF mass spectrum for PLLA-IS (DCTB magic matrix + KTFA). Conditions: **L-LA** (200 equiv.), $[\text{L-LA}]_0 = 1$ M, **IS-OH** (3 equiv.), $Zn(C_6F_5)_2$toluene (1 equiv.), 80 ºC, toluene.

A second distinct distribution is visible indicative of transesterification side reactions as the ROP proceeds. Such side reactions likely also rationalize the slightly broad PDI values of the produced PLLA-IS (**Table 1**).

Chapter III - Organometallic-Catalyzed Synthesis of High Molecular Weight Poly-(L-Lactic Acid) with a
Covalently Attached Imidazolium Salt: Performance-Enhanced Reduced Graphene Oxide-PLLA
Biomaterials

93
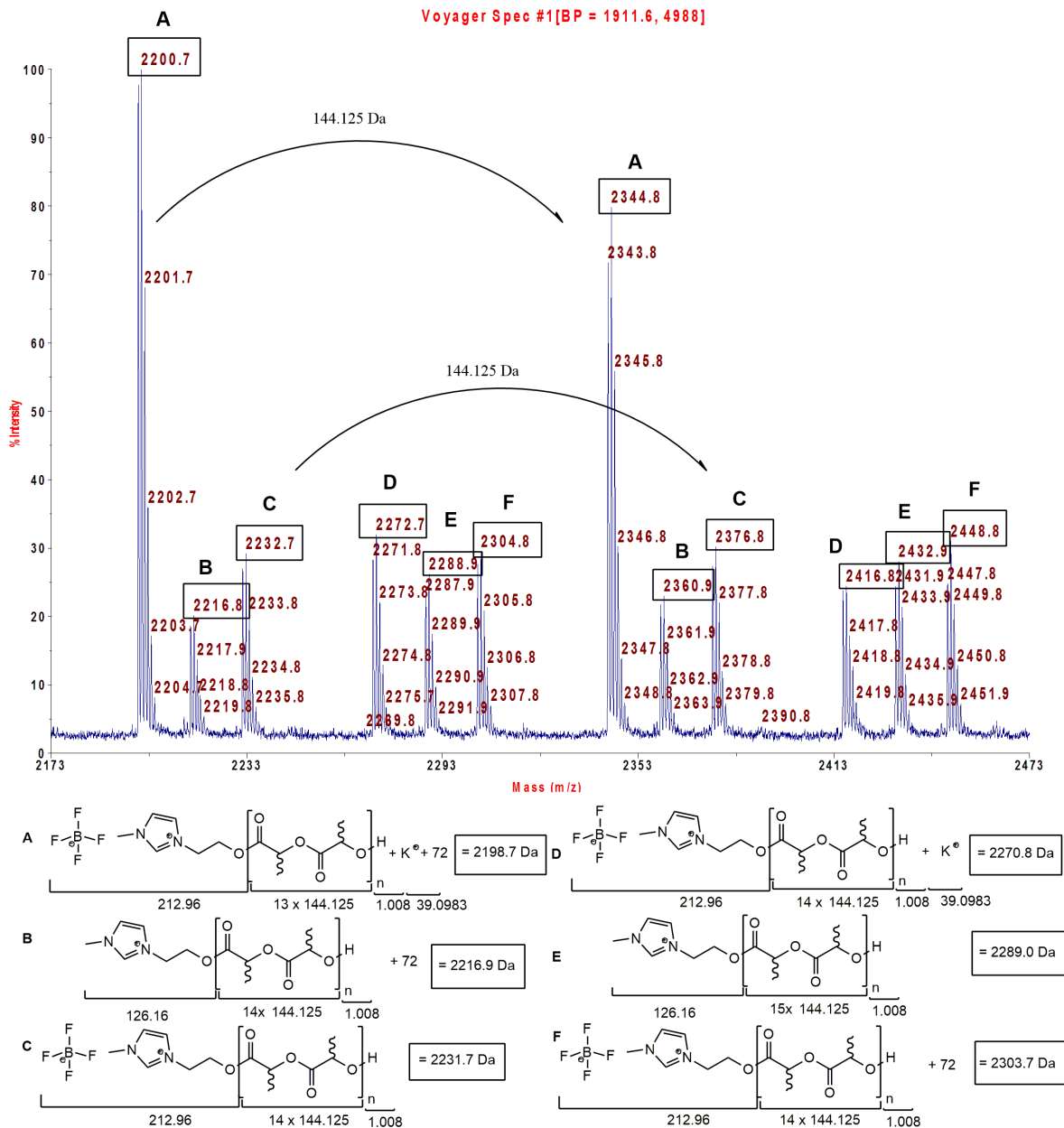


**Figure 8**. Zoomed positive ion MALDI-TOF mass spectrum for PLLA-IS (DCTB magic matrix + KTFA). Conditions: **L-LA** (200 equiv.), $[\text{L-LA}]_0 = 1$ M, **IS-OH** (3 equiv.), $\text{Zn}(\text{C}_6\text{F}_5)_2$toluene (1 equiv.), 80 °C, toluene.

PLLA-IS (**Table 1, entry 13**) was applied in the solvent casted preparation of a novel PLLA-IS/rGO nanocomposite film containing 1 wt% of reduced graphene oxide (rGO), named **PLLA-IS/rGO-1%**. The good dispersion of the rGO in the final material is possibly explained by the low range $\pi^+$-$\pi$ interactions between the PLLA-IS imidazolium

ring and the rGO. In contrast, when commercial PLLA with a similar molecular weight (to PLLA-IS) was used, a phase separation was observed within a few minutes after pouring the mixture into the mold (**Figure 9**), indicating that hydrogen bonding forces between PLLA and rGO are not enough to disperse rGO in the solution.
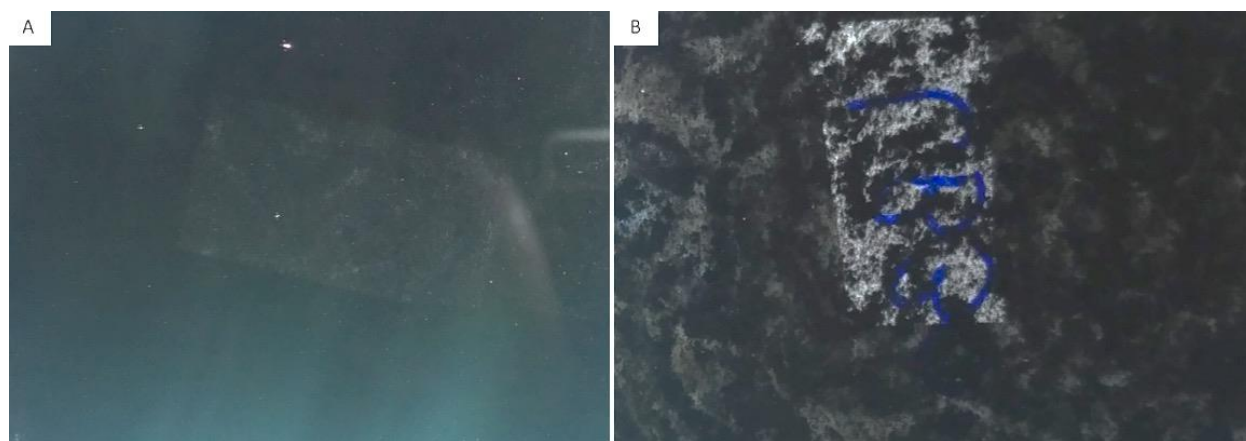


**Figure 9**. Photographs of the rGO dispersion in the solvent casting of (A) **PLLA-IS/rGO-1%** and (B) **PLLA-rGO-1%**, before solvent evaporation.

SEM micrographs indicated a good interaction between PLLA-IS polymer and rGO, showing the formation of a controlled morphological structure of PLLA spheres encapsulated by the graphene network (**Figure 10**). The average size of these spheres was approximately 50 µm, being considered microspheres. This morphological structure, the presence of IS, and the good graphene dispersion makes **PLLA-IS/rGO-1%** a potential material of interest for various applications.

Chapter III - Organometallic-Catalyzed Synthesis of High Molecular Weight Poly-(L-Lactic Acid) with a
Covalently Attached Imidazolium Salt: Performance-Enhanced Reduced Graphene Oxide-PLLA
Biomaterials

95



**Figure 10**. SEM micrographs of (A) **PLLA-IS** (**Table 1**, **entry 13**) (scale bar = 100 µm);
(B) **PLLA-IS** (scale bar = 2 µm); (C) **PLLA-IS/rGO-1%** (scale bar = 100 µm); (D) **PLLA-IS/rGO-1%** (scale bar = 50 µm); (E) **PLLA-IS/rGO-1%** (scale bar = 10 µm); and (F)
**PLLA-IS/rGO-1%** (scale bar = 2 µm).

The thermal properties of **PLLA-IS/rGO-1%** were compared with those of PLLA-IS (**Table 2**). The incorporation of rGO resulted in a significant gain of 15 ºC for the $T_{50\%}$, which indicates that the graphene acted as a shield increasing the thermal resistance of encapsulated PLLA-IS.

**Table 2**. Thermal properties of PLLA-IS films.

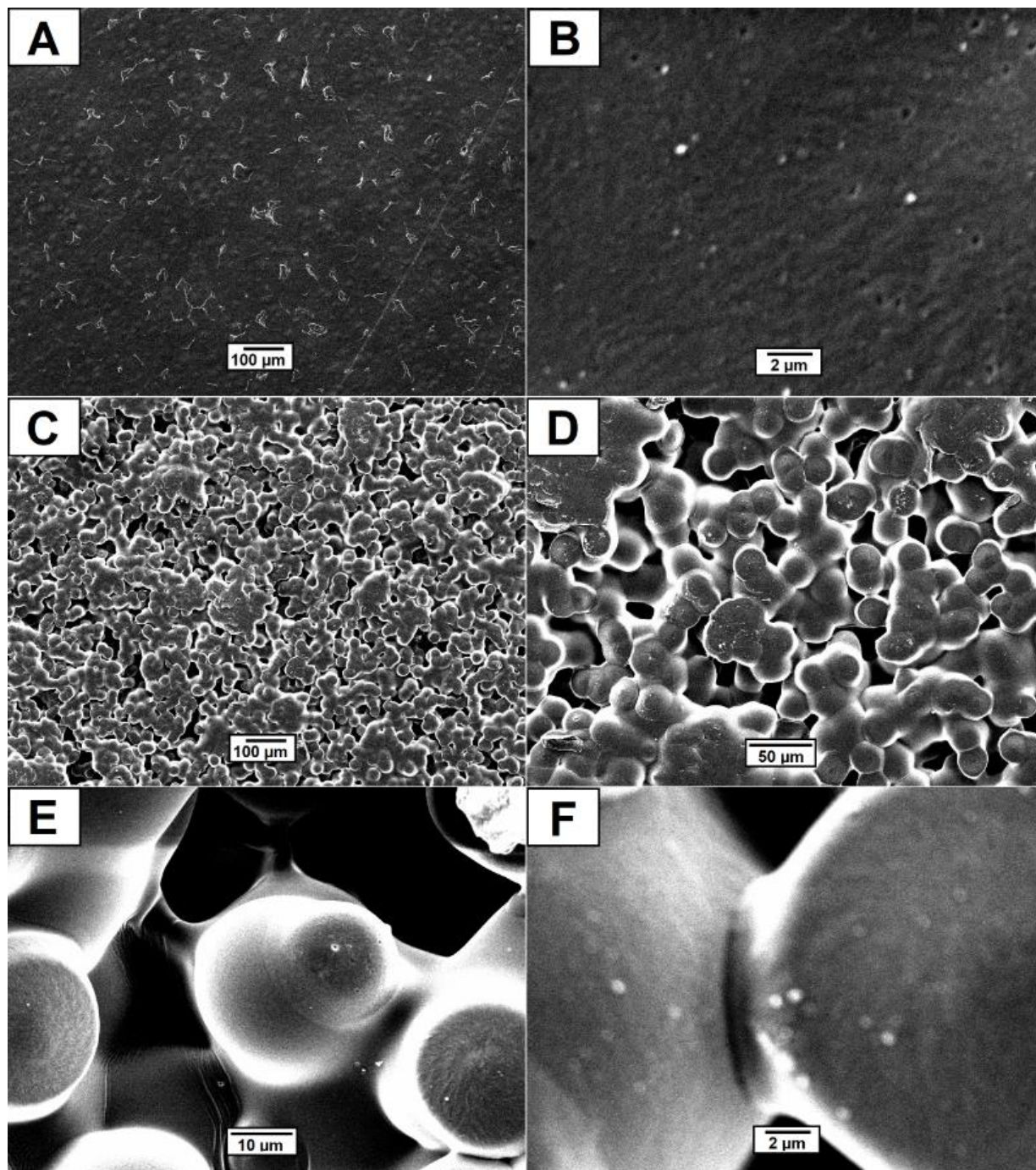| Entry | Sample | $T_{5\%}$ [°C][a] | $T_{10\%}$ [°C][b] | $T_{50\%}$ [°C][c] | Residue [%][d] |
|-------|--------|------------------|-------------------|-------------------|----------------|
| 1 | PLLA-IS[e] | 151.2 | 291.3 | 367.4 | 0.00 |
| 2 | **PLLA-IS/rGO-1%** | 119.9 | 299.2 | 382.8 | 0.85 |

[a] Temperature at 5 wt% weight loss as determined by TGA. [b] Temperature at 10 wt% weight loss as determined by TGA. [c] Temperature at 50 wt% weight loss as determined by TGA. [d] Residual weight at 550 °C as determined by TGA. [e] Table 1, entry 13.

The dynamical mechanical properties of **PLLA-IS** and **PLLA-IS/rGO-1%** were also investigated (**Table 3**). **PLLA-IS/rGO-1%** showed an increase of 105% in the storage modulus when compared to **PLLA-IS** at 30 °C. Besides that, **PLLA-IS/rGO-1%** exhibited a significant increase of 148% in the loss modulus in comparison to **PLLA-IS** at 30 ºC.

The performance-enhanced mechanical properties of **PLLA-IS/rGO-1%** around physiological temperature are of particular interest since such a biomaterial is commonly used as prosthesis in the human body. At higher temperature (55 ºC), both films behave similarly for the storage and loss moduli. Compared to **PLLA-IS**, the stiffness of **PLLA-IS/rGO-1%** was 38% higher at 30 ºC and 48% lower at 55 ºC, and the Tg decreased by 5 °C.

These results suggest that graphene promoted both a greater PLLA chain-mobility and increased hardness, although the final material was less crumbly. Altogether, the presence of an IS group covalently bonded to PLLA lead to a stronger, more rigid and less brittle material with 1 wt% of graphene.

Chapter III - Organometallic-Catalyzed Synthesis of High Molecular Weight Poly-(L-Lactic Acid) with a
Covalently Attached Imidazolium Salt: Performance-Enhanced Reduced Graphene Oxide-PLLA
Biomaterials

97

**Table 3**. Dynamical mechanical properties of PLLA-IS films.

| Entry | Sample | G'30 [Mpa][a] | G'55 [Mpa][b] | G''30 [Mpa][c] | G''55 [Mpa][d] | S30 [N/M][e] | S55 [N/m][f] | Tg [°C][g] |
|-------|--------|------|------|------|------|------|------|------|
| 1 | PLLA-IS[h] | 386.9 | 241.4 | 25.6 | 34.1 | 42,097 | 26,259 | 64.8 |
| 2 | **PLLA-IS/rGO-1%** | 795.7 | 243.4 | 63.5 | 38.7 | 58,028 | 17,753 | 59.8 |

[a] Storage modulus at 30 °C. [b] Storage modulus at 55 °C. [c] Loss modulus at 30 °C. [d] Loss modulus at 55 °C. [e] Stiffness at 30 °C. [f] Stiffness at 55 °C. [g] Glass transition temperature as determined by DMA. [h] Table 1, entry 13.

**PLLA-IS** had a water contact angle of 71.0 ± 0.3° (**Figure 11**). A significant increase occurred with the incorporation of 1 wt% rGO as **PLLA-IS/rGO-1%** reached a water contact angle of 98.4 ± 0.2º.  This behavior can be explained by the presence of the more hydrophobic graphene network around the polymer surface leading to a final material with a more hydrophobic character.
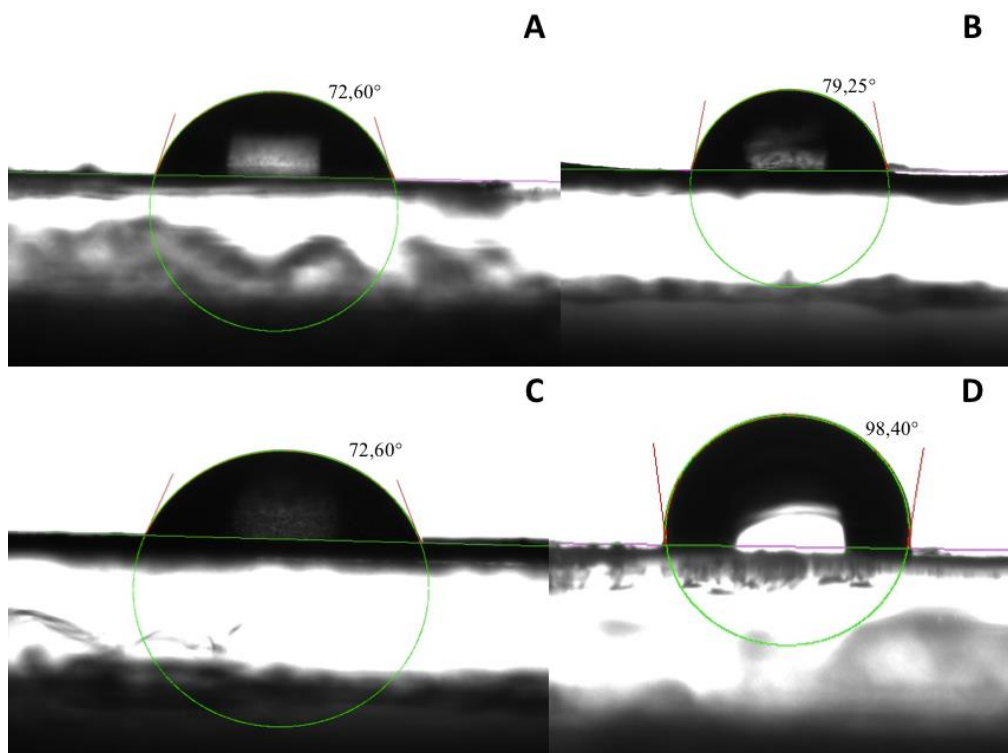


**Figure 11**. Images of deposition of water droplets on the polymer films (A) PLLA commercial; (B) PLLA commercial + rGO-1%; (C) **PLLA-IS**; and (D) **PLLA-IS/rGO-1%**.

In this study, it was possible to verify that the antibiofilm activity of the imidazolium salt was maintained when covalently bounded to the PLLA, which resulted in an inhibition percentage of 56% with *Candida tropicalis*. Nevertheless, the *C. albicans* biofilm formation was not prevented by **PLLA-IS**. Interestingly, with the incorporation of graphene oxide into the biomaterial, **PLLA-IS/rGO-1%** provided antibiofilm activity against both *C. tropicalis* (43%) and *C. albicans* (34%), which might be related to its higher hydrophobicity.

## 4.3 Conclusion

In conclusion, the controlled synthesis of PLLA-IS with an organometallic complex - $Zn(C_6F_5)_2$toluene - as catalyst and IS-OH as initiator was performed under ROP for the first time. A higher molecular mass PLLA-IS product was prepared by this organometallic approach and a reasonable of polydispersity and chain-length control could be achieved. The presence of an imidazolium end-group improved the dispersion of rGO, which resulted in the preparation of a novel PLLA-IS/rGO biomaterial with better mechanical and thermal properties. In addition, this material was able to inhibit the formation of biofilms of *C. tropicalis* and *C. albicans*, having the potential to be applied in medical devices and in the bioengineering field.

## 4.4    References

[1]    T. McDonnell, S. Korsmeyer, *Nature* **1991**, *354*, 56–58.

[2]    J. Chen, B. Liu, X. Gao, D. Xu, *RSC Adv.* **2018**, *8*, 28048–28085.

[3]    J. M. Raimond, M. Brune, Q. Computation, F. de Martini, C. Monroe, *Science* **2004**, *306*, 666–670.

[4]    H. Kim, A. A. Abdala, C. W. MacOsko, *Macromolecules* **2010**, *43*, 6515–6530.

[5]    J. R. Potts, D. R. Dreyer, C. W. Bielawski, R. S. Ruoff, *Polymer* **2011**, *52*, 5–25.

[6]     A. K. Geim, K. S. Novoselov *Nat. Mater.* **2007**, *6*, 183 – 191.

[7]    B. Sun, G. Zhou, H. Zhang, *Prog. Solid State Chem.* **2016**, *44*, 1–19.

[8]    H. Zou, S. Wu, J. Shen, *Chem. Rev.* **2008**, *108*(*9)*, 3893–3957.

[9]    A. A. Balandin, S. Ghosh, W. Bao, I. Calizo, D. Teweldebrhan, F. Miao, C. N. Lau, *Nano Lett.* **2008**, *8*, 902–907.

[10]    X. Du, I. Skachko, A. Barker, E. Y. Andrei, *Nat. Nanotechnol.* **2008**, *3*, 491–495.

[11]    Z. Lei, B. Chen, Y. M. Koo, D. R. Macfarlane, *Chem. Rev.* **2017**, *117*, 6633–6635.

[12]    R. L. Vekariya, *J. Mol. Liq.* **2017**, *227*, 44–60.

[13]    J. Lu, F. Yan, J. Texter, *Prog. Polym. Sci.* **2009**, *34*, 431–448.

[14]    S. Livi, J. Duchet-Rumeau, J. F. Gérard, *Macromol. Symp.* **2014**, *342*, 46–55.

[15]    B. G. Soares, *J. Mol. Liq.* **2018**, *262*, 8–18.

[16]    J. Claus, F. O. Sommer, U. Kragl, *Solid State Ion.* **2018**, *314*, 119–128.

[17]    C. M. L. Schrekker, Y. C. A. Sokolovicz, M. G. Raucci, B. S. Selukar, J. S. Klitzke, W. Lopes, C. A. M. Leal, I. O. P. de Souza, G. B. Galland, J. H. Z. dos Santos,  R. S. Mauler, M. Kol, S. Dagorne, L. Ambrosio, M. L. Teixeira, J. Morais, R. Landers, A. M. Fuentefria, H. S. Schrekker *ACS Appl. Mater. Interfaces* **2016**, *8,* 21163–21176.

[18]    F. Meyer, J.M. Raquez, O. Coulembier, J. de Winter, P. Gerbaux, P. Dubois, *Chem. Commun.* **2010**, *46,* 5527–5529.

Chapter III - Organometallic-Catalyzed Synthesis of High Molecular Weight Poly-(L-Lactic Acid) with a
Covalently Attached Imidazolium Salt: Performance-Enhanced Reduced Graphene Oxide-PLLA
Biomaterials

101

[19]   T. Biedron, M. Brzezinski, T. Biela, P. Kubisa, *J. Polym. Sci. Pol. Chem.* **2012**, *50*,
4538–4547.

[20]   T. Biedron, Ł. Pietrzak, P. Kubisa, *J. Polym. Sci. Pol. Chem.* **2011**, *49*, 5239–
5244.

[21]   G. Schnee, C. Fliedel, T. Avilés, S. Dagorne, *Eur. J. Inorg Chem.* **2013**, 3699–
3709.

# 5   GENERAL CONCLUSION

In this study, the $CO_2$ hydroboration was successfully performed with aluminum-hydride anionic catalysts. In addition, a mechanism different from the one reported for M-H catalysts has been proposed. This mechanism follows the activation of the hydroborane by the formate group formed after $CO_2$ migratory insertion into the Al-H bond. Selectivity towards the formic acid and methanol precursors, formoxyborane and methoxyborane, respectively, was achieved by changing the anion (hydride *vs* formate) of the catalyst.

With this knowledge, we hypothesized that simple acetate salts could be able to catalyze the same reaction. Indeed, this occurred in the hydroborane-mediated $CO_2$ reduction. In addition, methoxyborane selectivity was obtained through the reaction using potassium, sodium and tetrabutylammonium acetate catalysts.

Finally, the PLLA containing an IS-end chain group was synthesized via ROP using an organometallic complex for the first time. Thus, a high molecular mass (5x higher) than that reported in the literature was obtained. Using this PLLA-IS, a novel nanocomposite material (PLLA-IS/rGO) was synthesized under solvent casting, which showed improvements in thermal, mechanical and antibiofilm properties.

# 6 EXPERIMENTAL SECTION AND SUPPORTING INFORMATION

## 6.1 SI Chapter I - Aluminum Tripod (O-O-O) Hydride Complexes Catalyze the Borane-Mediated Reduction of Carbon Dioxide into Methoxyborane and Formoxyborane

### 6.1.1 General procedures

All reactions and manipulations were performed under a dry nitrogen atmosphere using a MBraun Unilab glovebox. Molecular sieves (4 Å, Merck) were activated under high vacuum at a temperature of 150 °C for 3 days. Dichloromethane, pentane and toluene were purchased from Sigma-Aldrich, dried in a MBraun SPS purification system, and stored over activated molecular sieves (4 Å) for at least 20 h. Tetrahydrofuran was purchased from Sigma-Aldrich, distilled with Na/benzophenone, and stored over activated molecular sieves (4 Å) for at least 48 h. Benzene-$d_6$ and dichloromethane-$d_2$ were purchased from Sigma-Aldrich and dried over molecular sieves (4 Å) for at least 20 h. HBpin and all other chemicals not described above were purchased from Sigma-Aldrich and used as received. $^1$H, $^{11}$B and $^{13}$C NMR spectra were recorded at room temperature in Bruker 300, 400 and 500 MHz NMR equipments.

### 6.1.2 Aluminium tripod complexes syntheses

The four Al catalysts were prepared according to procedures established by Hild *et al.* (**Scheme S1**).[1]
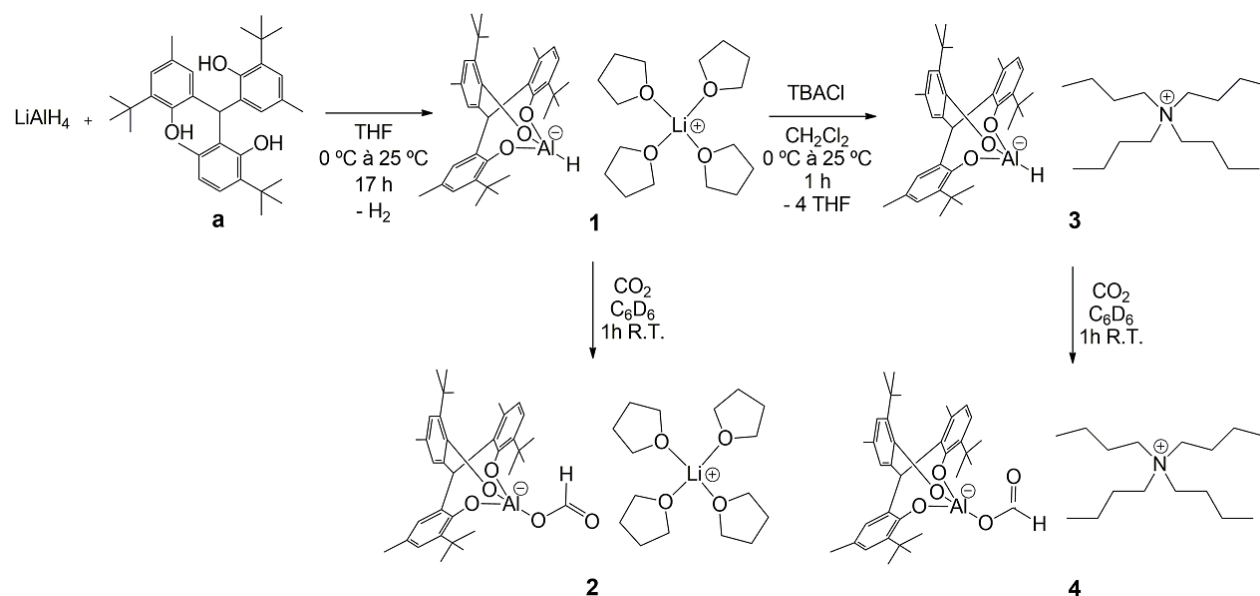


**Scheme S1**. Synthesis of the aluminium tripod(O-O-O) complexes.

$\eta^3$-O,O,O-{(C$_{11}$H$_{14}$O)$_3$CH}AlH Li(THF)$_4$ (1): A pre-cooled 1 M THF suspension of lithium aluminium hydride (1.00 mL, 1.00 mmol) was added drop-wise to a pre-cooled solution of ligand **a** (0.50 g, 1.00 mmol) in THF (5 mL). The reaction mixture was stirred in a closed screw-capped flask at 25 °C for 17 h. From time to time the flask was opened to release the hydrogen pressure, and a colorless solution was obtained. Evaporation of the solvent afforded a white solid, which was purified by precipitation in a 5:1 THF:pentane mixture to obtain the desired product, compound **1**, as a white solid (0.45 g, 0.55 mmol, 55% yield). **Anal. calcd** for C$_{47}$H$_{68}$AlLiO$_8$ (822.56): C, 72.96; H, 9.31; found: C, 72.44; H, 9.83. **$^1$H NMR (400 MHz, C$_6$D$_6$):** δ 7.07 (d, $^3J_{HH}$ = 2.0 Hz, Ar, 3H); 7.00 (d, $^3J_{HH}$ = 1.6 Hz, Ar, 3H); 5.37 (s, CH, 1H); 3.35 (brs, THF, 16H); 2.13 (s, CH$_3$, 9H); 1.59 (s, $^t$Bu, 27H); 1.31 (brs, THF, 16H). **$^{13}$C NMR (75 MHz, CD$_2$Cl$_2$):** δ 156.0 (C$_{ipso}$); 139.0 (C$_{ipso}$); 133.3 (C$_{ipso}$); 130.8 (C$_{ipso}$); 125.8 (C$_{ipso}$); 125.2 (C$_{ipso}$); 68.3 (THF); 59.5 (CH); 34.7 ($^t$Bu); 30.4 (CH$_3$); 25.4 (THF); 20.4 ($^t$Bu). **$^{13}$C NMR (126 MHz, C$_6$D$_6$):** δ 156.5 (C$_{ipso}$); 140.0 (C$_{ipso}$); 133.8 (C$_{ipso}$); 131.3 (C$_{ipso}$); 126.6 (C$_{ipso}$); 126.1 (C$_{ipso}$); 68.1 (THF); 59.9 (CH); 35.3 ($^t$Bu); 30.7 (CH$_3$); 25.5 (THF); 21.0 ($^t$Bu).

$\eta^3$-O,O,O-{(C$_{11}$H$_{14}$O)$_3$CH}AlOCOH Li(THF)$_4$ (2): A solution of **1** (30.0 mg, 36.0 μmol) in C$_6$D$_6$ (0.7 mL) was placed into a J-Young NMR tube and cooled in liquid N$_2$. Subsequently, the tube was pressurized with CO$_2$ (1.5 bar, 15 mL, 920 μmol). After 1 h at 25 °C, complex **2** was obtained and isolated as a white solid (27.0 mg, 34.0 μmol, 93% yield). **Anal. calcd** for C$_{50}$H$_{72}$AlLiO$_7$ (794.49): C, 71.01; H, 8.62; found: C, 68.22; H, 8.23. **$^1$H NMR (300 MHz, C$_6$D$_6$):** δ 8.10 (s, OCOH, 1H); 7.10 (d, $^3J_{HH}$ = 2.1 Hz, Ar, 3H); 7.07 (d, $^3J_{HH}$ = 2.0 Hz, Ar, 3H); 5.72 (s, CH, 1H); 3.45 – 3.37 (m, 12 H); 2.16 (s, CH$_3$, 9H); 1.51 (s, $^t$Bu, 27H); 1.37 – 1.31 (m, 12 H). **$^{13}$C NMR (126 MHz, C$_6$D$_6$):** δ 169.84 (C$_{OCOH}$); 156.0 (C$_{ipso}$); 138.7 (C$_{ipso}$); 133.9 (C$_{ipso}$); 132.7 (C$_{ipso}$); 126.7 (C$_{ipso}$); 126.4 (C$_{ipso}$); 68.1 (THF); 60.1 (CH); 35.1 ($^t$Bu); 30.7 (CH$_3$); 25.6 (THF); 21.0 ($^t$Bu).

$\eta^3$-O,O,O-{(C$_{11}$H$_{14}$O)$_3$CH}AlH TBA (3): A pre-cooled suspension of tetrabutylammonium chloride (0.17 g, 0.63 mmol) in dichloromethane (2 mL) was added dropwise to a pre-cooled solution of **1** (0.52 g, 0.63 mmol) in dichloromethane (5 mL). Subsequently, the reaction mixture became turbid. After stirring 1 h at 25 °C, the LiCl formed during the reaction was filtered. The solvent was evaporated to give **3** as a white

solid (0.45 g, 0.58 mmol, 93% yield). **Anal. calcd** for $C_{50}H_{80}AlNO_3$ (769.60): C, 77.98; H, 10.47; N, 1.82; found: C, 77.63; H, 10.01; N, 1.72. **$^1$H NMR (400 MHz, $CD_2Cl_2$):** δ 6.88 (d, $^3J_{HH}$ = 2.0 Hz, Ar, 3H); 6.84 (d, $^3J_{HH}$ = 1.6 Hz, Ar, 3H); 5.07 (s, CH, 1H); 3.09 (t, $^3J_{HH}$ = 7.6 Hz, $CH_2$, 8H); 2.22 (s, $CH_3$, 9H); 1.61 (m, $CH_2$, 8H); 1.46 (m, $CH_2$, 8H); 1.42 (s, $^tBu$, 27H); 1.05 (t, $^3J_{HH}$ = 6.8 Hz, $CH_3$, 12H). **$^{13}$C NMR (126 MHz, $CD_2Cl_2$):** δ 158.0 ($C_{ipso}$); 138.8 ($C_{ipso}$); 134.3 ($C_{ipso}$); 131.4 ($C_{ipso}$); 125.4 ($C_{ipso}$); 124.2 ($C_{ipso}$); 61.0 (CH); 59.5 ($CH_2$); 35.1 ($^tBu$); 30.3 ($CH_3$); 24.3 ($CH_2$); 20.9 ($CH_3$); 20.1 ($CH_2$); 13.8 ($^tBu$).

**$\eta^3$-O,O,O-{$(C_{11}H_{14}O)_3$CH}AlOCOH TBA (4)**: A J-Young NMR tube containing a solution of **3** (30.0 mg, 39.0 μmol) in $C_6D_6$ (0.7 mL) was cooled in liquid $N_2$. Subsequently, $CO_2$ (15 mL, 1.5 bar, 920 μmol) was injected. After 1 h at 25 °C, **4** was isolated as a white solid (30.0 mg, 37.0 μmol, 95% yield). **Anal. calcd** for $C_{50}H_{80}AlNO_3$ (828.61): C, 75.24; H, 9.90; N, 1.72; found: C, 68.32; H, 9.56; N, 1.69. **$^1$H NMR (400 MHz, $C_6D_6$):** δ 9.41 (s, OCOH, 1H); 7.24 (d, $^3J_{HH}$ = 1.8 Hz, Ar, 3H); 7.15 (d, $^3J_{HH}$ = 2.4 Hz, Ar, 3H); 5.82 (s, CH, 1H); 2.44 (d, $^3J_{HH}$ = 7.8 Hz, $CH_2$, 8H); 2.25 (s, $CH_3$, 9H); 1.68 (s, $^tBu$, 27H); 1.01 – 1.02 (m, $CH_2$, 16H). **$^{13}$C NMR (126 MHz, $CD_2Cl_2$):** δ 164.0 ($C_{OCOH}$); 157.0 ($C_{ipso}$); 139.0 ($C_{ipso}$); 133.7 ($C_{ipso}$); 131.8 ($C_{ipso}$); 125.9 ($C_{ipso}$); 125.5 ($C_{ipso}$); 60.2 (CH); 59.4 ($CH_2$); 35.1 ($^tBu$); 30.2 ($CH_3$); 24.3 ($CH_2$); 20.8 ($CH_3$); 20.1 ($CH_2$); 13.8 ($^tBu$).

### 6.1.3  General procedure for the aluminum-catalyzed reduction of $CO_2$ with boranes

Initially, a J-Young NMR tube was charged with a solution of the internal hexamethylbenzene standard in $C_6D_6$ (0.5 mL). The aluminum catalyst (5.00 mg, 6.07 μmol, 1.00 equiv) and the borane species (HBpin) were added sequentially. In the case of catalyst contents less than 2 mg, catalyst solutions were used and the solvent was removed under high vacuum for 1 h at room temperature, before addition of the borane species. Next, the tube was cooled with liquid $N_2$ and $CO_2$ (15 mL, 1.5 bar, 920 μmol) was injected (**Figure S1**), and the reaction was warmed to the temperature of interest (**Figure S2**). The conversions were calculated based on the boron NMR spectra, using

the integrals of specific signals characteristic of the internal standard, reagents and products.



**Figure S1**. $CO_2$ injection system

**Figure S2**. Catalytic $CO_2$ reduction with boranes in J-Young NMR tubes.

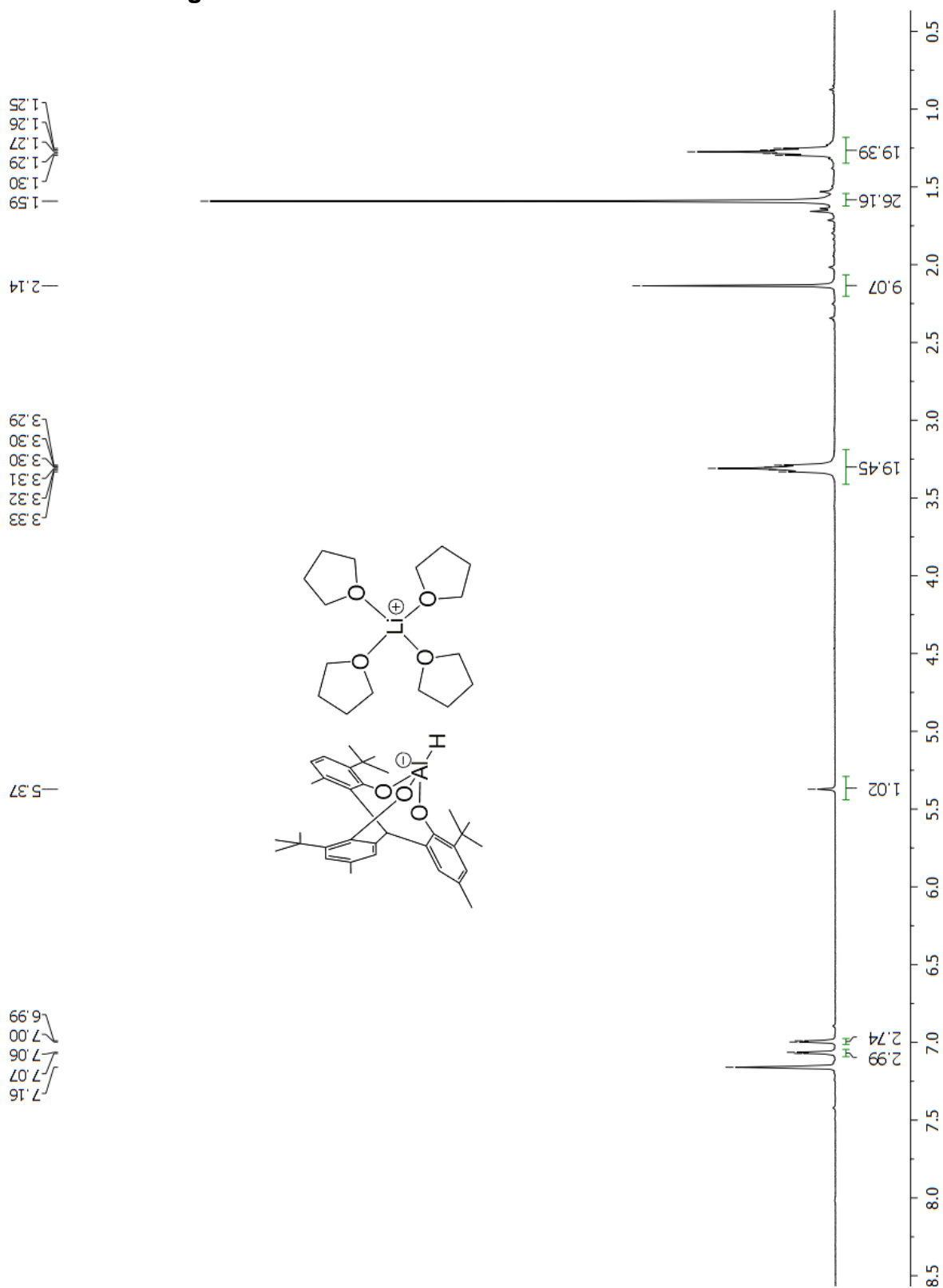## 6.1.4  Nuclear Magnetic Resonance



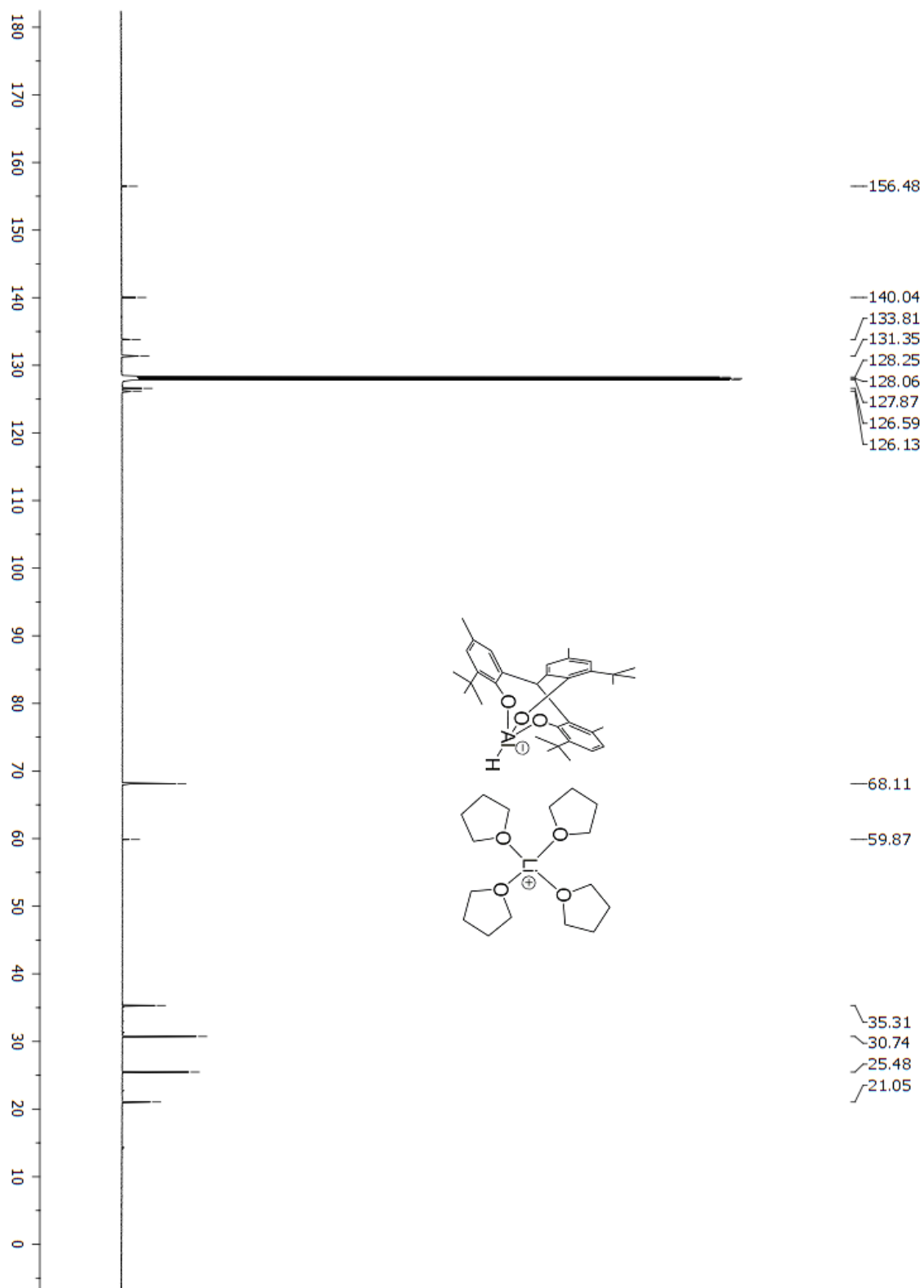**Figure S3**. $^1$H NMR spectrum (400 MHz, C$_6$D$_6$) of the aluminum complex **1**.

**Figure S4**. $^{13}$C NMR spectrum (126 MHz, $C_6D_6$) of the aluminum complex **1**.
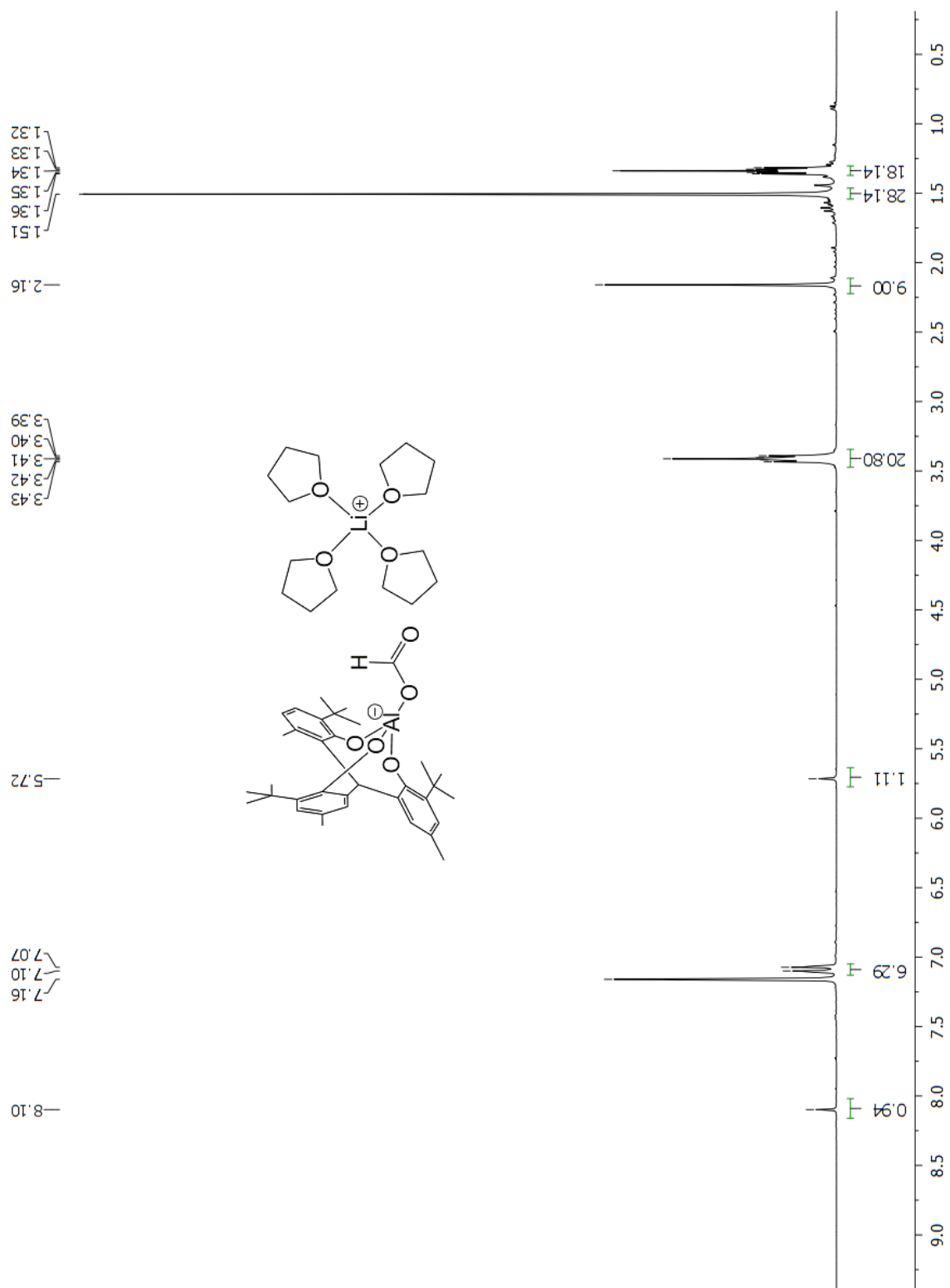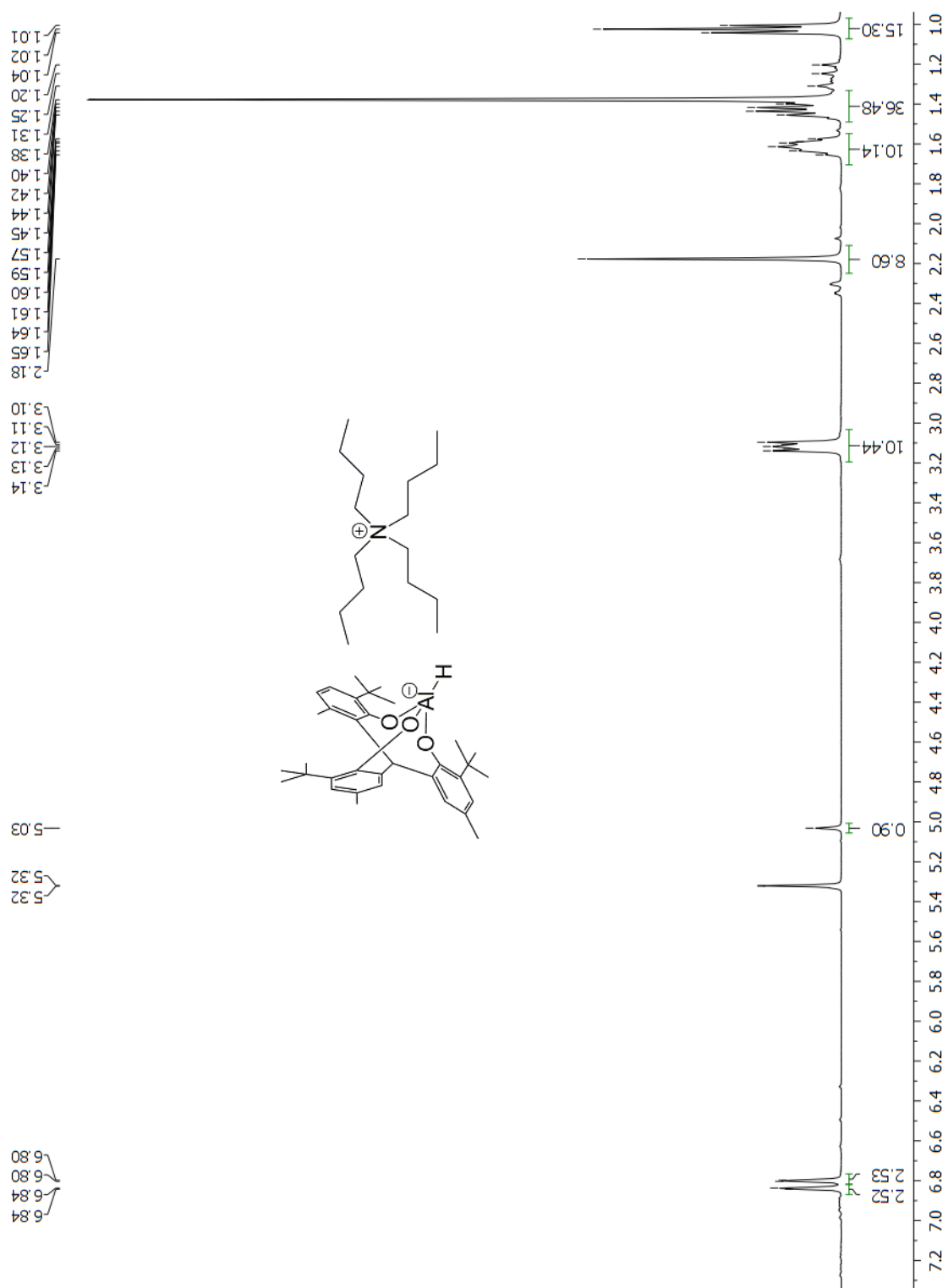
**Figure S5**. ^{1}H NMR spectrum (300 MHz, C$_6$D$_6$) of the aluminum complex **2**.
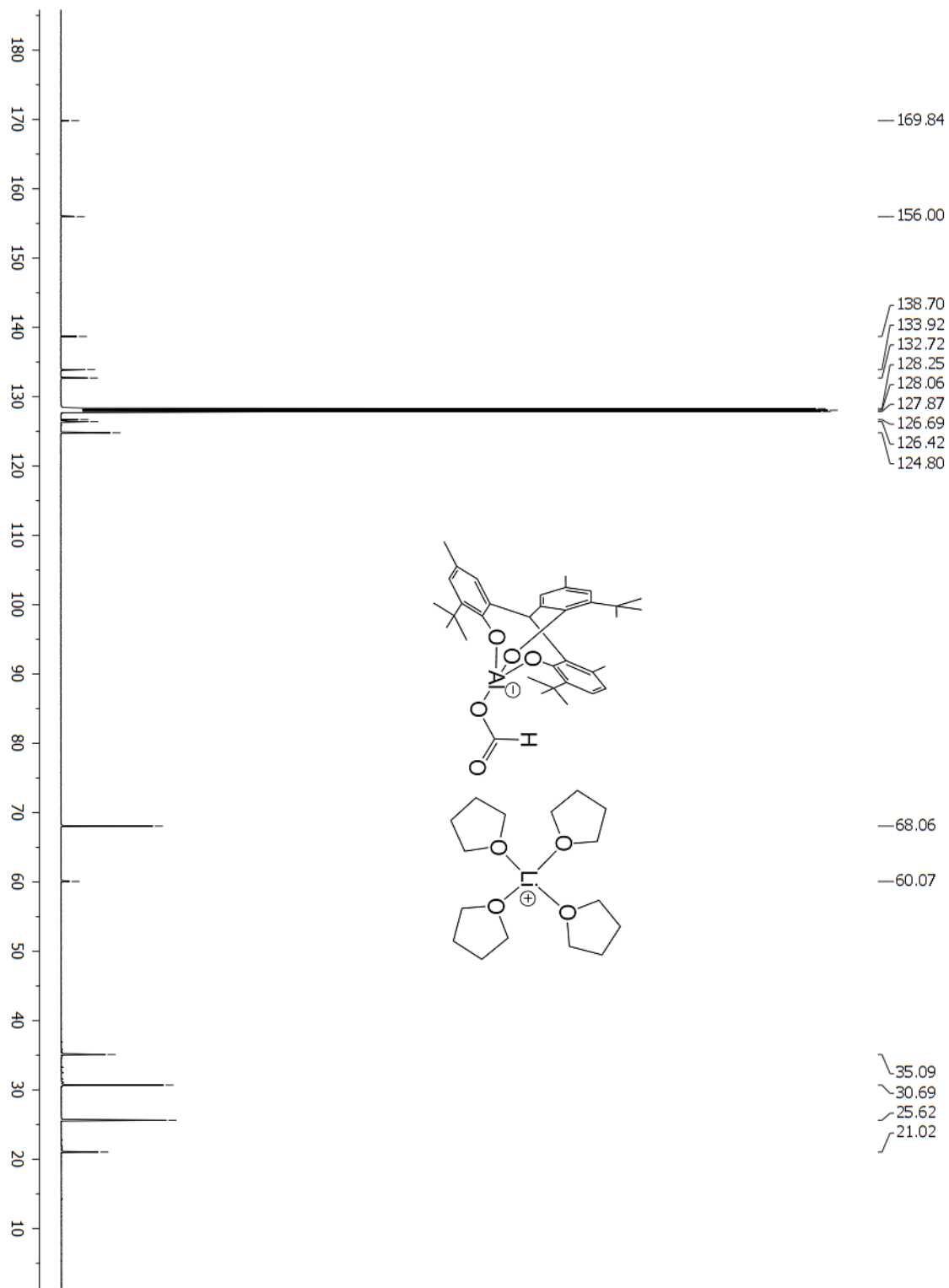
**Figure S6**. $^{13}$C NMR spectrum (126 MHz, $C_6D_6$) of the aluminum complex **2**.

**Figure S7**. $^1$H NMR spectrum (400 MHz, CD$_2$Cl$_2$) of the aluminum complex **3**.
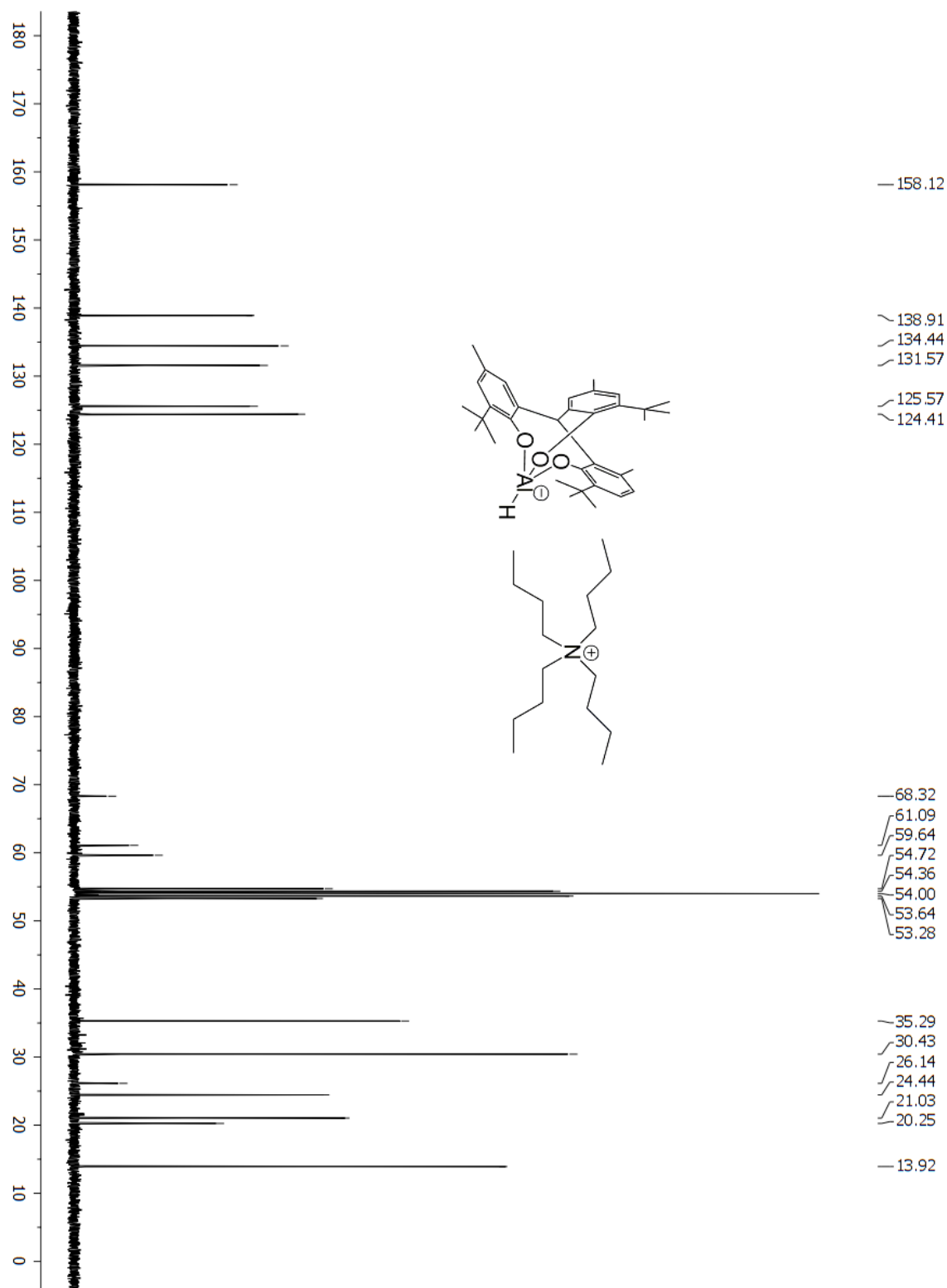
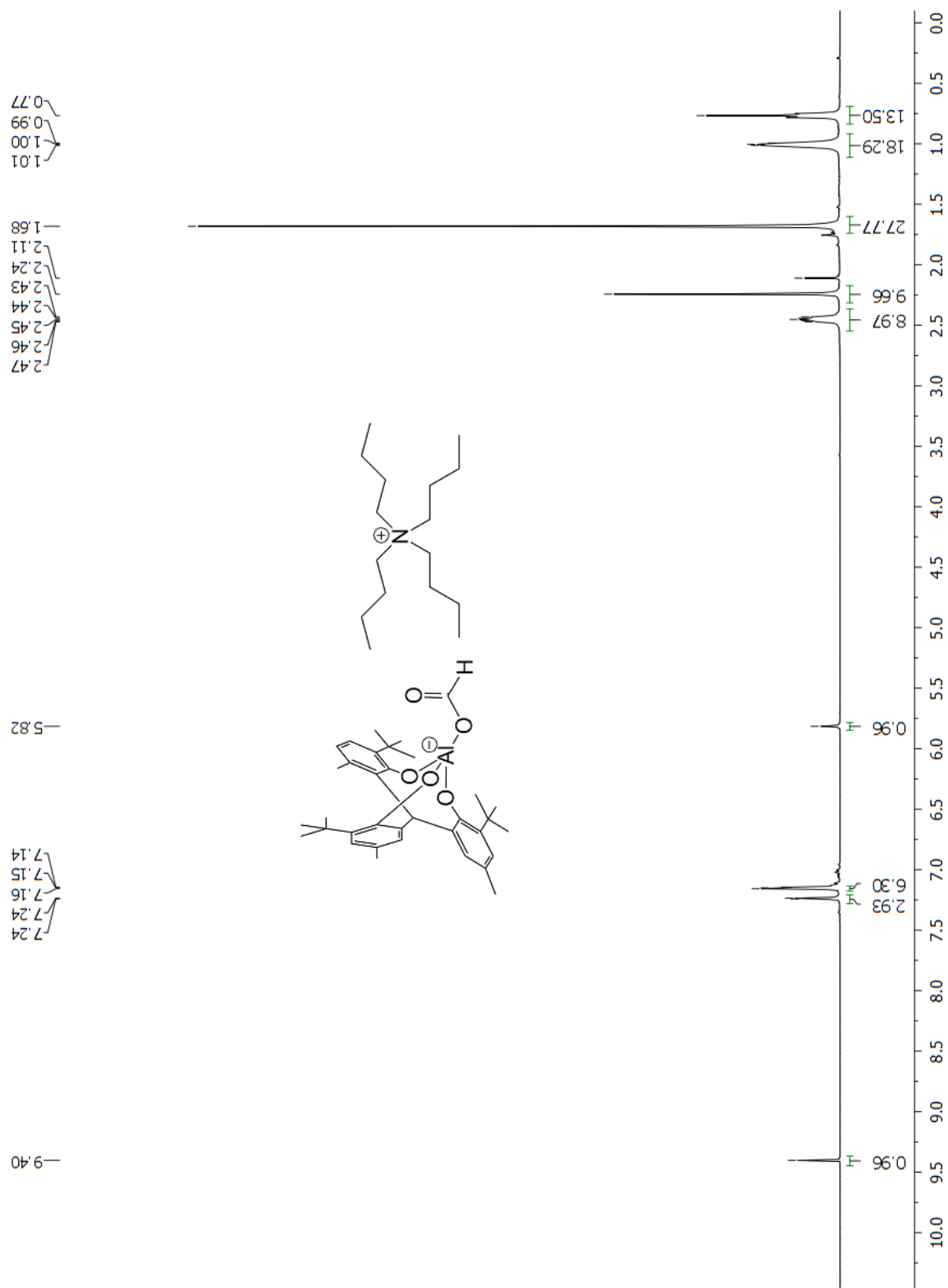**Figure S8.** $^{13}$C NMR spectrum (126 MHz, CD$_2$Cl$_2$) of the aluminum complex **3**.

**Figure S9**. $^1$H NMR spectrum (400 MHz, C$_6$D$_6$) of the aluminum complex **4**.
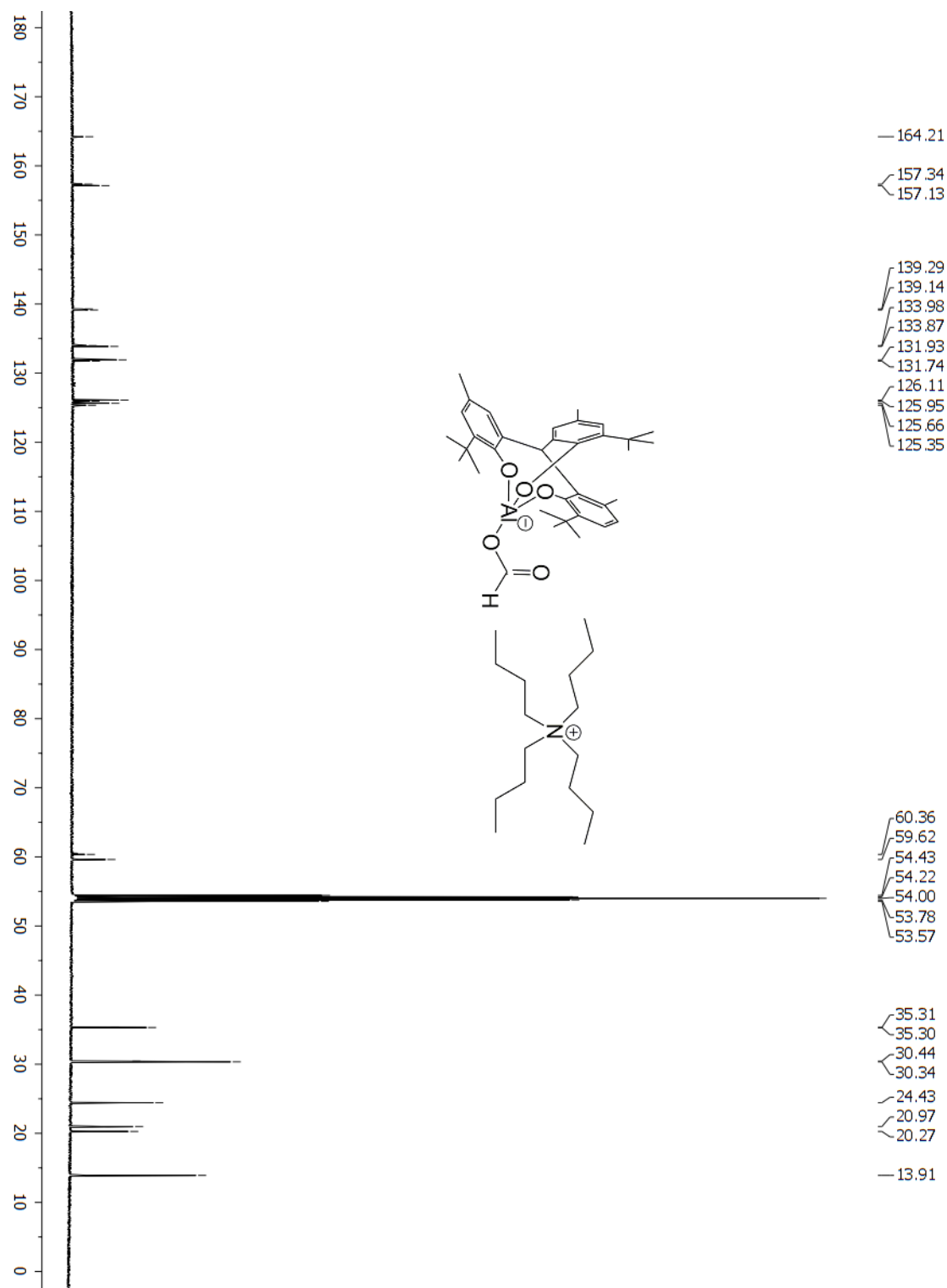
**Figure S10.** $^{13}$C NMR spectrum (126 MHz, CD$_2$Cl$_2$) of the aluminum complex **4**.

### 6.1.5  References

[1] F. Hild, S. Dagorne, unpublished results.

## 6.2  SI Chapter II - Access to Methanol: Conversion of Carbon Dioxide Through Hydroboration Catalysis using the Simple Acetate Anion as Catalyst

### 6.2.1  General considerations

Pinacolborane (HBpin), borane dimethyl sulphide, $C_6D_6$ and $C_6D_5Br$ were purchased from Sigma-Aldrich and stored over molecular sieves (4 Å) for at least 20 h. Tetrabutylammonium acetate (TBAAc) was synthesized in a cationic exchange reaction between potassium acetate and tetrabutylammonium chloride (1:1), using dry methanol as solvent. Sodium acetate and potassium acetate were purchased from Sigma-Aldrich and dried at 100 ºC under high vacuum for 24 h. Methanol was distilled over KOH and stored over activated molecular sieves (4 Å) for at least 48 h. The $^1H$, $^{11}B$ and $^{13}C$ NMR spectra were recorded before and after the $CO_2$ injection, using Bruker AC 300 MHz, 400 MHz, 500 MHz and 600 MHz NMR spectrometers. The conversions were calculated based on the boron NMR spectra, using the integrals of specific signals characteristic of the internal standard, reagents and products.

### 6.2.2  Basic procedure for the acetate-catalyzed hydroboration of $CO_2$

The reduction of $CO_2$ in the presence of boranes was divided in two steps. First, a J-Young NMR tube was filled with the reagents inside a nitrogen-filled MBraun Unilab glovebox. A $C_6D_6$ solution (0.5 mL) of the acetate catalyst was transferred into the tube, followed by the desired amount of borane. Second, the tube was cooled with liquid $N_2$ outside the glovebox, using Schlenk-line techniques. The tube was pressurized with 1.5 bar of $CO_2$, transferring 15 mL of $CO_2$. After stabilizing the temperature within a few minutes at room temperature, the tube was placed into an oil bath, previously adjusted to the desired reaction temperature, to start the reaction.

### 6.2.3  TBAAc-catalyzed hydroboration of $CO_2$
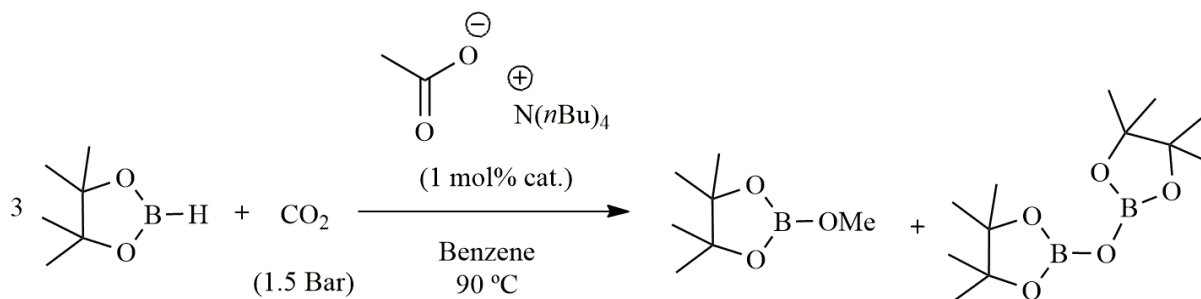


TBAAc (5.0 mg, 16.6 µmol, 1.0 equiv.), HBpin (212 mg, 1.66 mmol, 100 equiv.), and hexamethylbenzene (4 mg, 24.65 mmol, 1.5 equiv.) as an internal standard in $C_6D_6$ (0.5 mL) were transferred to a J-Young NMR tube. After $CO_2$ pressurization, the tube was heated at 90 °C for 20 h. The $^1$H and $^{11}$B NMR spectra showed the consumption of 96% of HBpin to form $CH_3OBpin$. The turnover number (TON) was calculated by the integration of the $^1$H NMR signals of the products HOCOBpin (8.23 ppm) and methoxyborane (3.44 ppm), using the hexamethylbenzene signal (2.06 ppm) as reference. After 20 h, the reaction achieved more than 98% of selectivity towards the methoxyborane. The methoxyborane and the co-product $O(Bpin)_2$ were observed in the $^{11}$B NMR spectrum at 22.49 and 21.52 ppm, respectively.
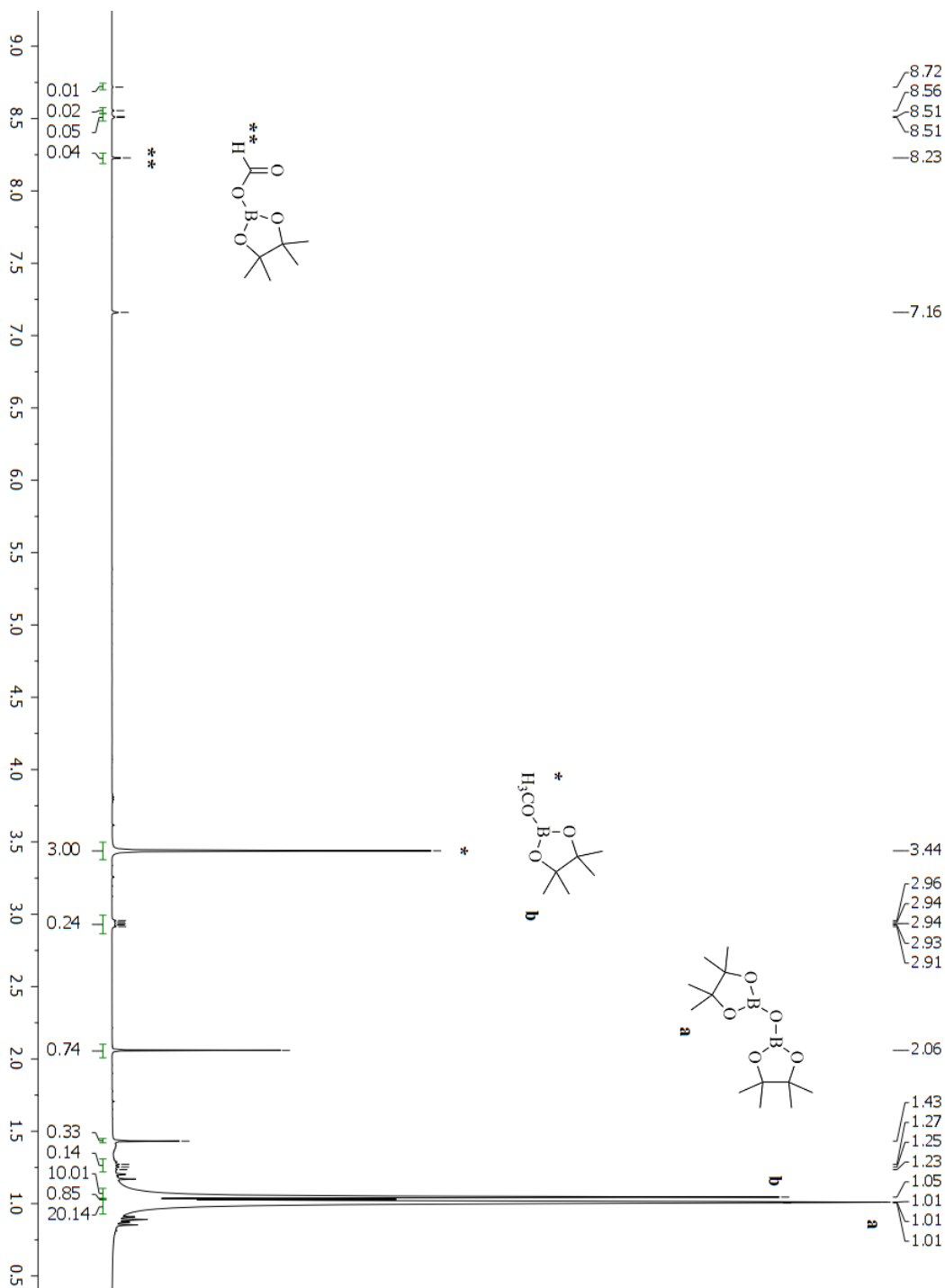
### 6.2.4  Nuclear Magnetic Resonance



**Figure S1**. $^1$H NMR spectrum (400 MHz, $C_6D_6$) after the reduction of $CO_2$ in the presence of HBpin and TBAAc (1 mol%). Conditions: $C_6D_6$; T = 90 °C; time = 20 h; internal standard = hexamethylbenzene. Conversion = 96%.

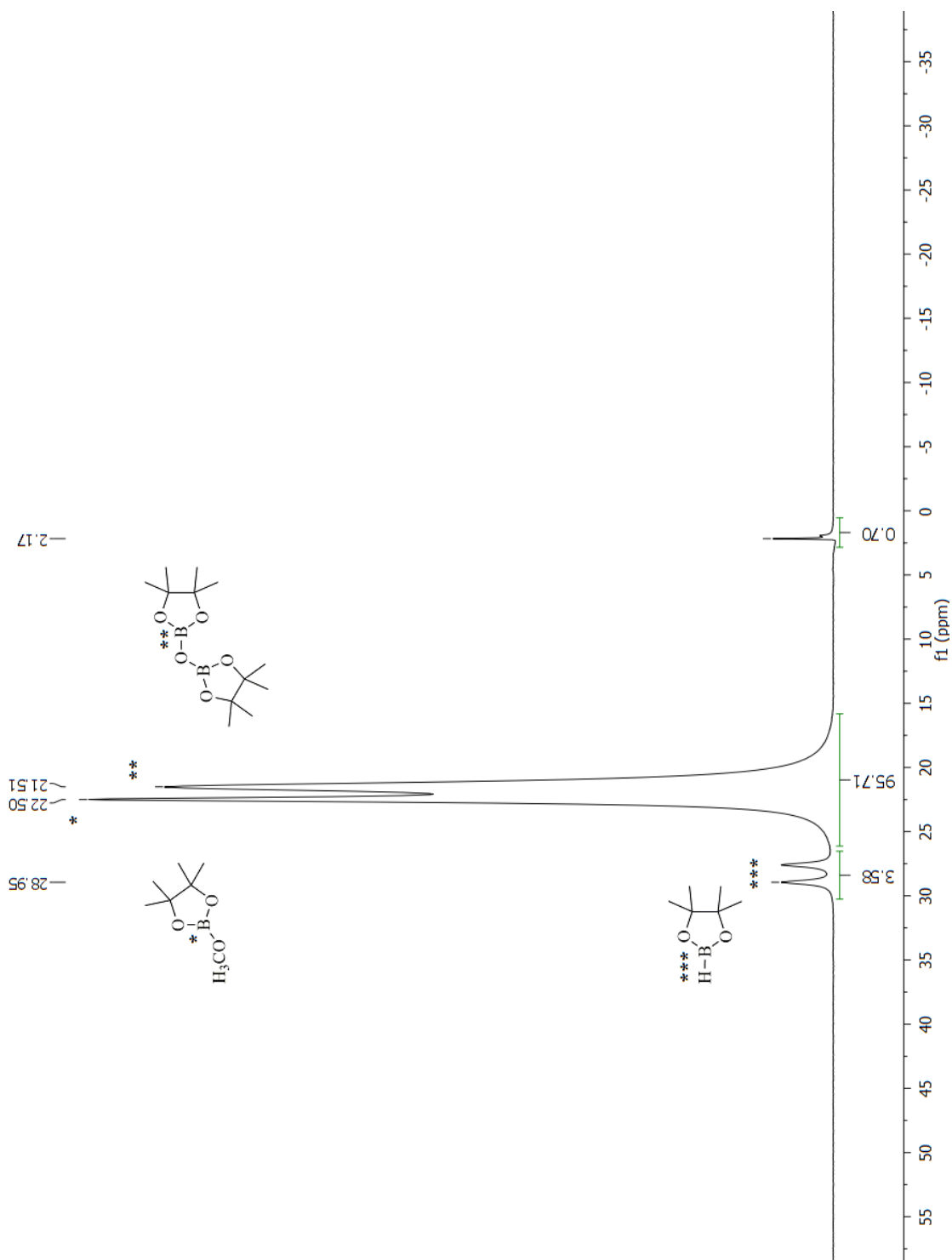**Figure S2**. ^{11}B NMR spectrum (128 MHz, $C_6D_6$) after the reduction of $CO_2$ in the presence of HBpin and TBAAc (1 mol%). Conditions: $C_6D_6$; T = 90 °C; time = 20 h; internal standard = hexamethylbenzene. Conversion = 96%.
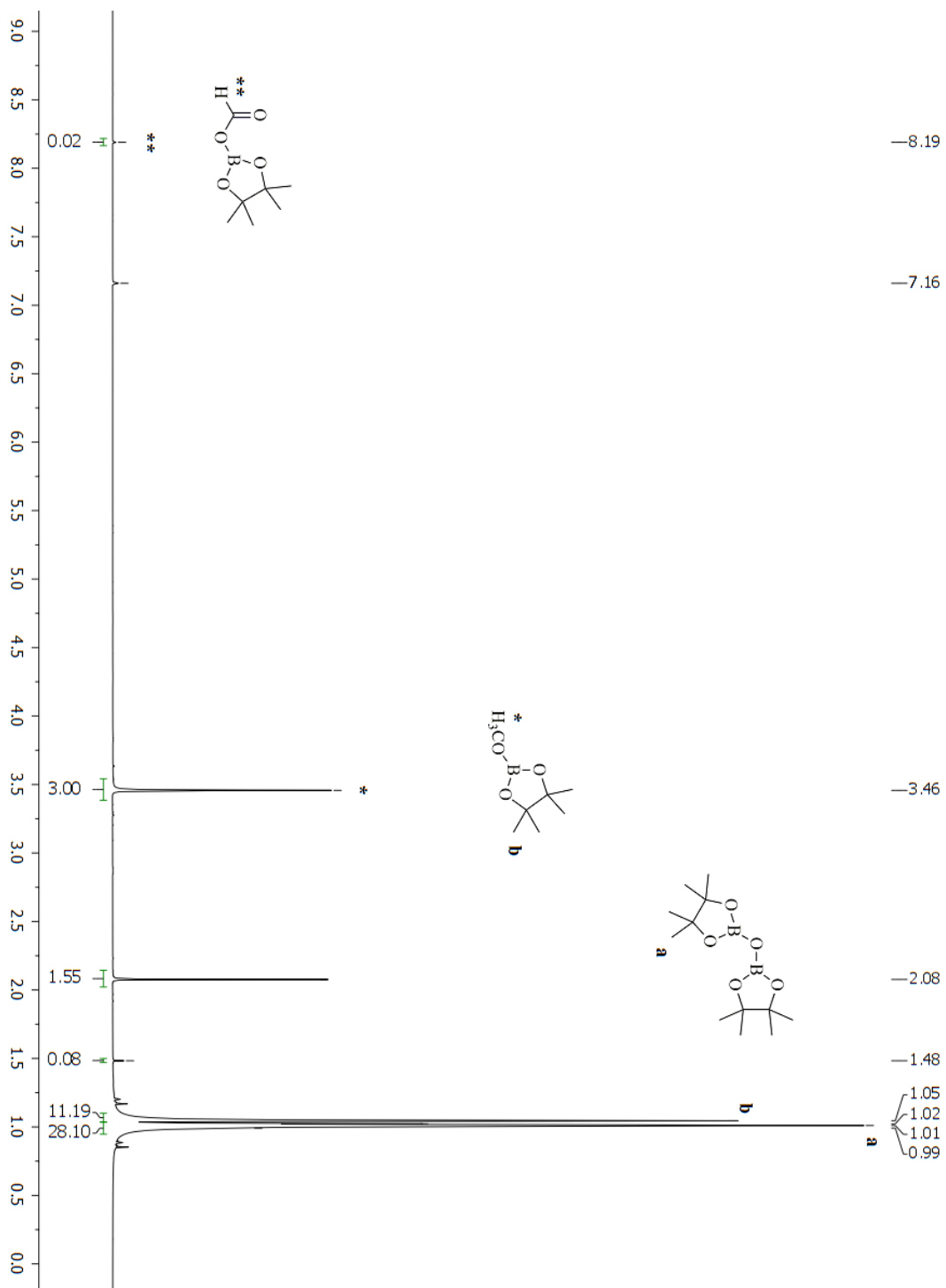
**Figure S3**. $^1$H NMR spectrum (400 MHz, $C_6D_6$) after the reduction of $CO_2$ in the presence of HBpin and TBAAc (0.1 mol%). Conditions: $C_6D_6$; T = 90 °C; time = 46 h; internal standard = hexamethylbenzene. Conversion = 94%.
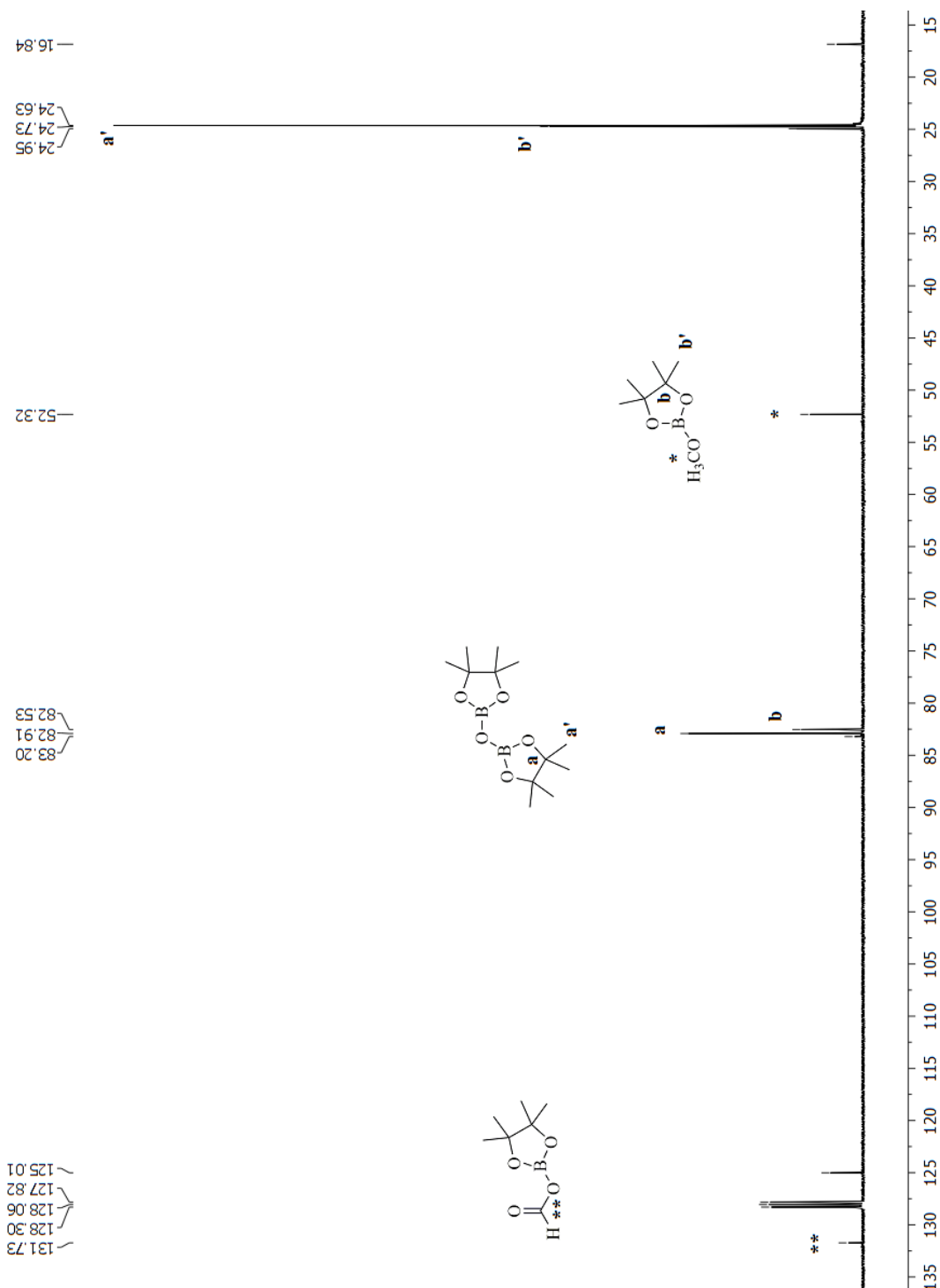
**Figure S4**. $^{13}C$ NMR spectrum (101 MHz, $C_6D_6$) after the reduction of $CO_2$ in the presence of HBpin and TBAAc (0.1 mol%). Conditions: $C_6D_6$; T = 90 ºC; time = 46 h; internal standard =  hexamethylbenzene. Conversion = 94%. Unreacted HBpin: ($CH_2$, 83.20 ppm; $CH_3$, 24.95 ppm).
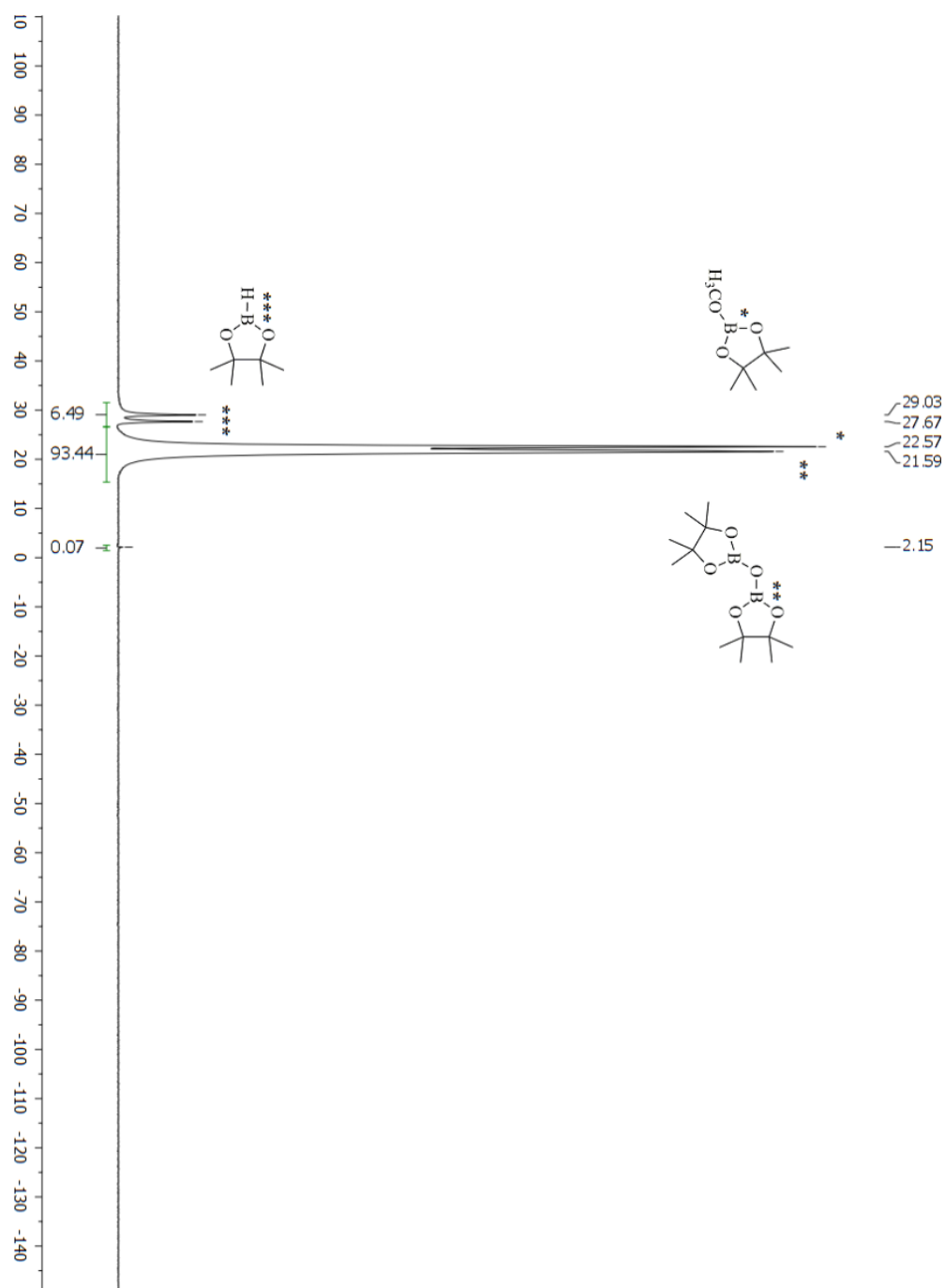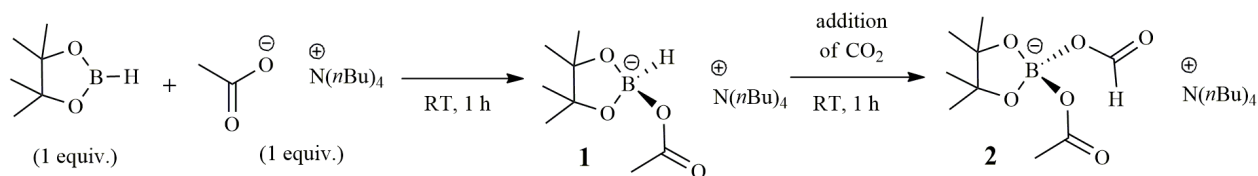
**Figure S5**. $^{11}$B NMR spectrum (128 MHz, $C_6D_6$) after the reduction of $CO_2$ in the presence of HBpin and TBAAc (0.1 mol%). Conditions: $C_6D_6$; T = 90 °C; time = 46 h; internal standard = hexamethylbenzene. Conversion = 94%. Unreacted HBpin (29.03 ppm; 27.67 ppm), $H_3COBpin$ (22.57 ppm), (Bpin)$_2$O (21.59 ppm).

## 6.2.5   Control reactions under stoichiometric conditions



Under a nitrogen atmosphere, a $C_6D_6$ solution (0.5 mL) containing TBAAc (15 mg, 49.75 µmol) and BHpin (6.37 mg, 49.75 µmol) was transferred to a J-Young NMR tube. The $^1H$, $^{11}B$ and $^{13}C$ spectra were recorded after 1 h at room temperature, showing the formation of product **1**. Attempts to isolate this compound were unsuccessful as it decomposed in the solid state. After the formation of **1**, 15 mL of $CO_2$ was injected at 1.5 bar into the previously liquid $N_2$ cooled tube. The $^1H$, $^{13}C$, HSQC and HMBC spectra showed after 1 h at room temperature the formation of product **2**, which also showed being unstable when isolated. Compound **1**: $^1H$ NMR (400 MHz, $C_6D_6$, δ): 3.46 – 3.25 (m, $CH_2$, 2H), 2.18 (s, $CH_3$, 3H), 1.64 – 1.50 (m, $CH_2$, 2H), 1.49 – 1.36 (m, $CH_2$, 2H), 1.32 (s, $CH_3$, 3H), 1.00 (t, $CH_3$, 3H). $^{11}B$ NMR (128 MHz, $C_6D_6$, δ): 10.35 (s, B). $^{13}C$ NMR (101 MHz, $C_6D_6$, δ): 172.51 ($OCOCH_3$), 79.18 ($C_{tert}$), 58.41 ($CH_2$), 26.31 ($CH_3$), 25.08 ($CH_3COO$), 24.42 ($CH_2$), 20.2 ($CH_2$), 14.08 ($CH_3$). Compound **2**: $^1H$ NMR (300 MHz, $C_6D_6$) δ 9.18 (s, HCOO, 1H), 3.27 – 2.88 (m, $CH_2$, 2H), 2.06 (s, $CH_3$, 3H), 1.52 – 1.40 (m, $CH_2$, 2H), 1.40 – 1.34 (m, $CH_2$, 2H), 1.32 (s, $CH_3$, 3H), 0.95 (t, $CH_3$, 3H). $^{11}B$ NMR (128 MHz, $C_6D_6$, δ): 8.35 (s, B). $^{13}C$ NMR (101 MHz, $C_6D_6$, δ): 171.40 ($OCOCH_3$), 165.97 (OCOH), 79.64 ($C_{tert}$), 58.53 ($CH_2$), 25.97 ($CH_3$), 24.61 ($CH_3COO$), 24.21 ($CH_2$), 20.1 ($CH_2$), 13.95 ($CH_3$).
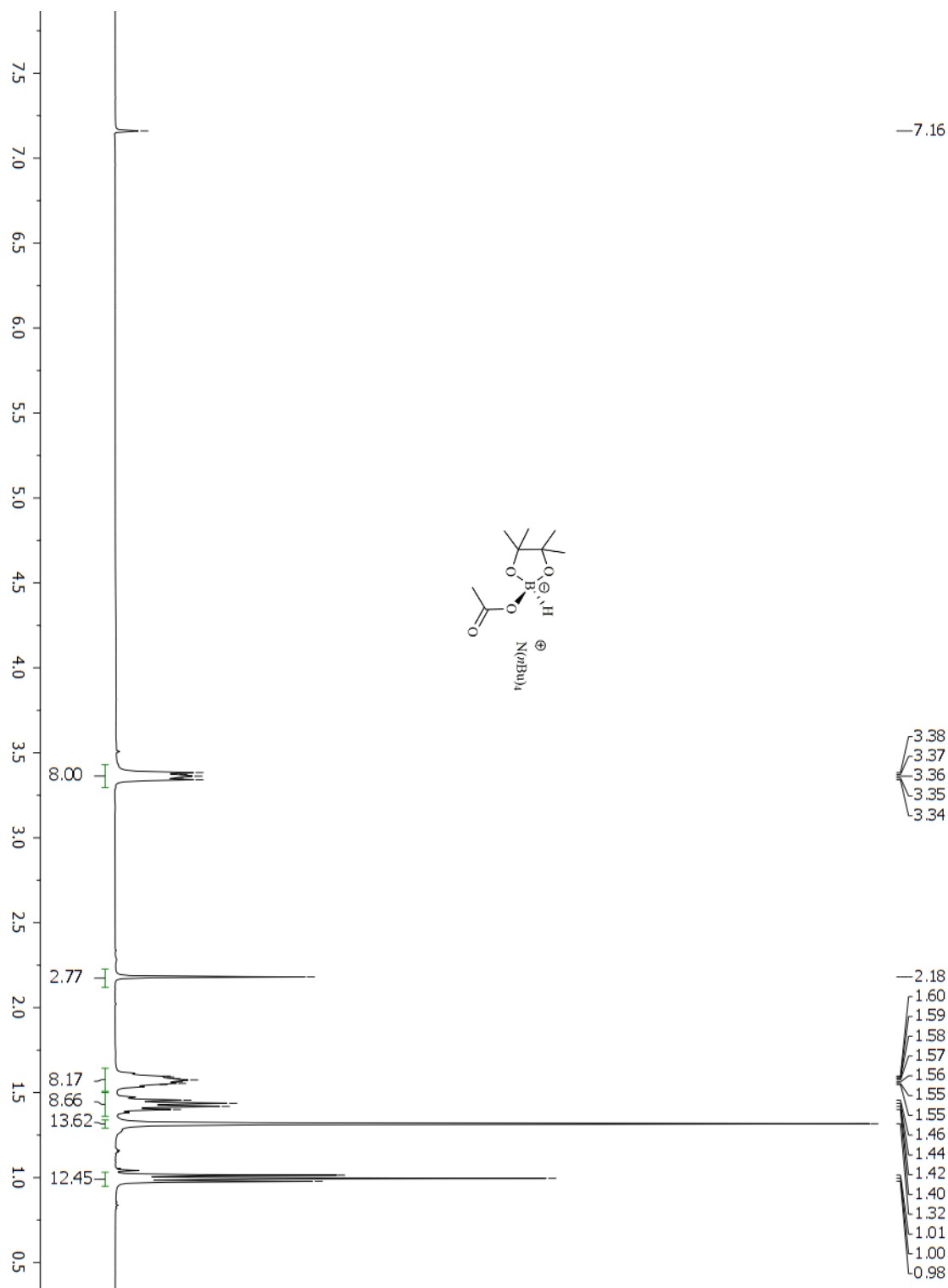
**Figure S6**. ¹H NMR spectrum (400 MHz, C₆D₆) of the stoichiometric reaction between TBAAc and HBpin, after 1h at room temperature.
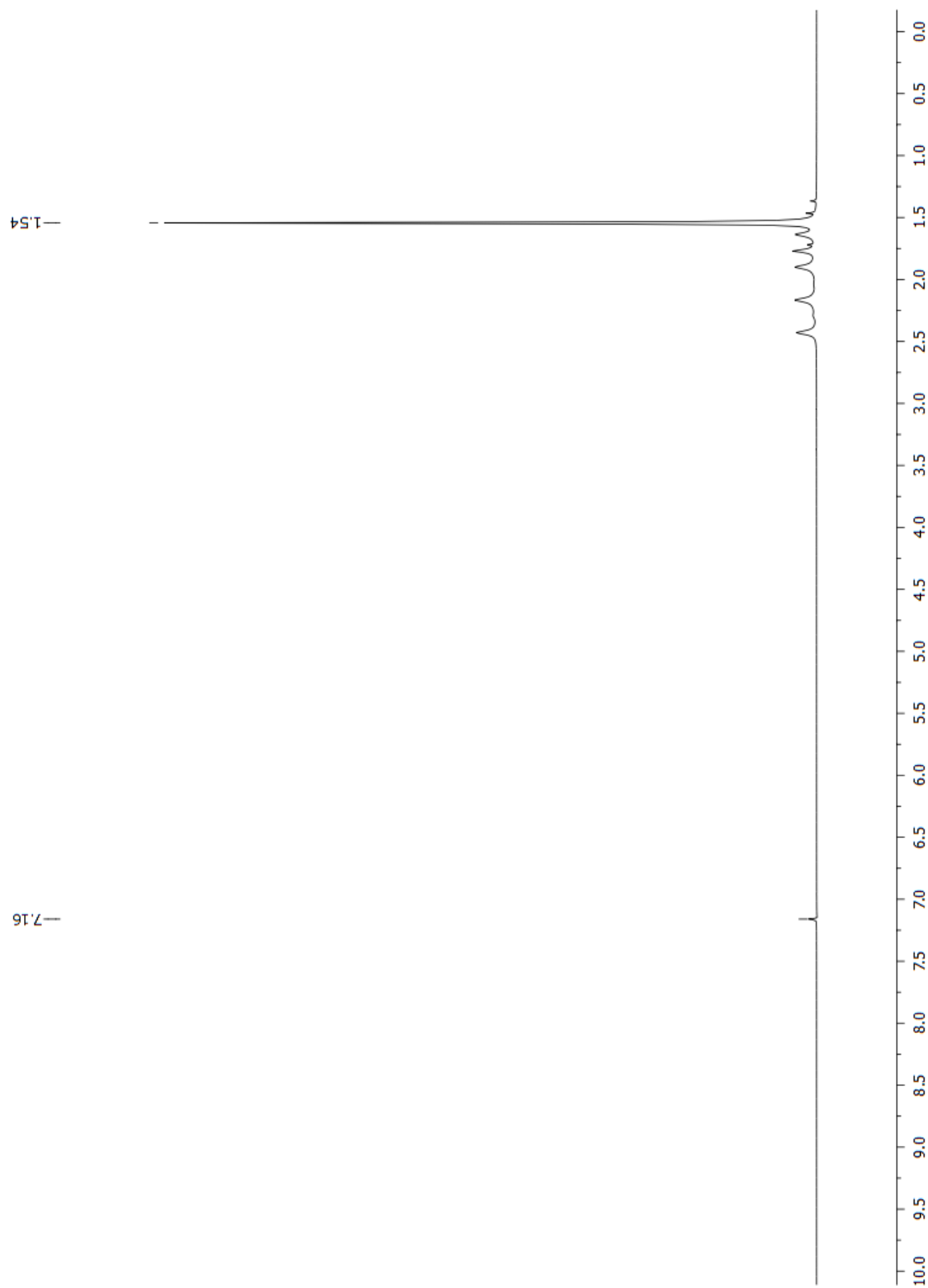
**Figure S7**. $^1$H NMR spectrum (400 MHz, $C_6D_6$) of $BH_3.S(Me)_2$.
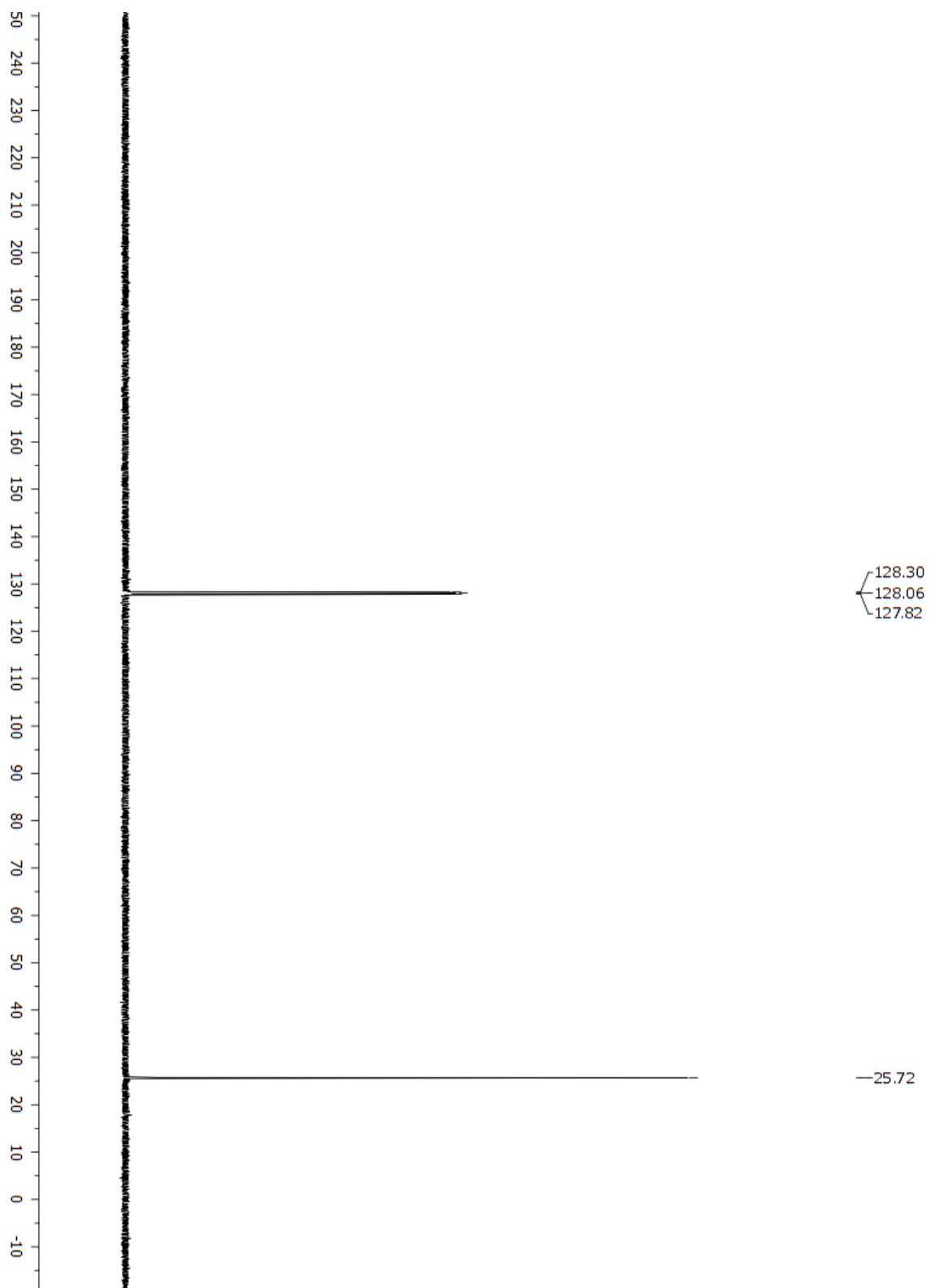
**Figure S8**. $^{13}$C NMR spectrum (101 MHz, C$_6$D$_6$) of BH$_3$.S(Me)$_2$.
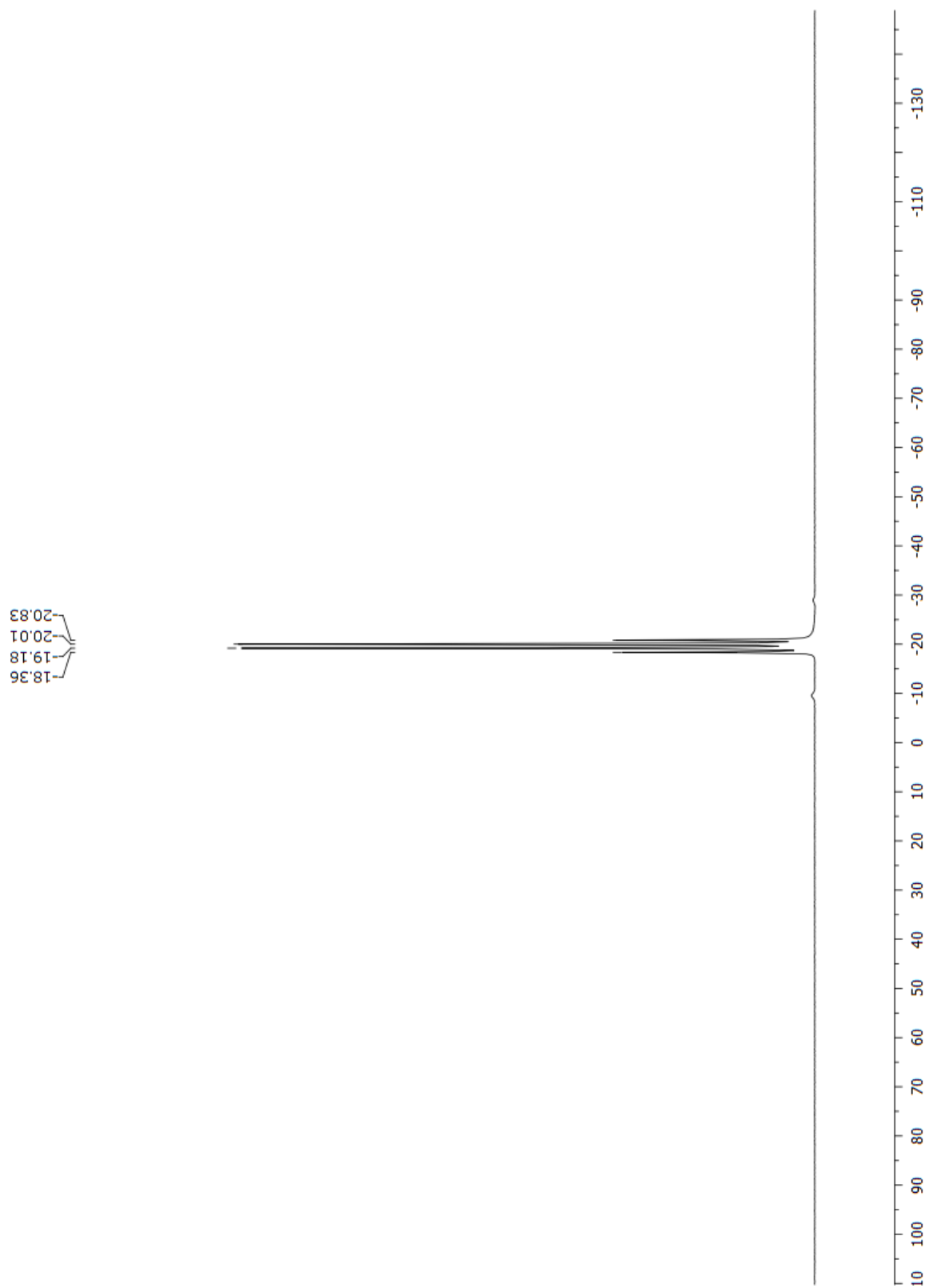
**Figure S9**. $^{11}$B NMR spectrum (128 MHz, $C_6D_6$) of $BH_3.S(Me)_2$.
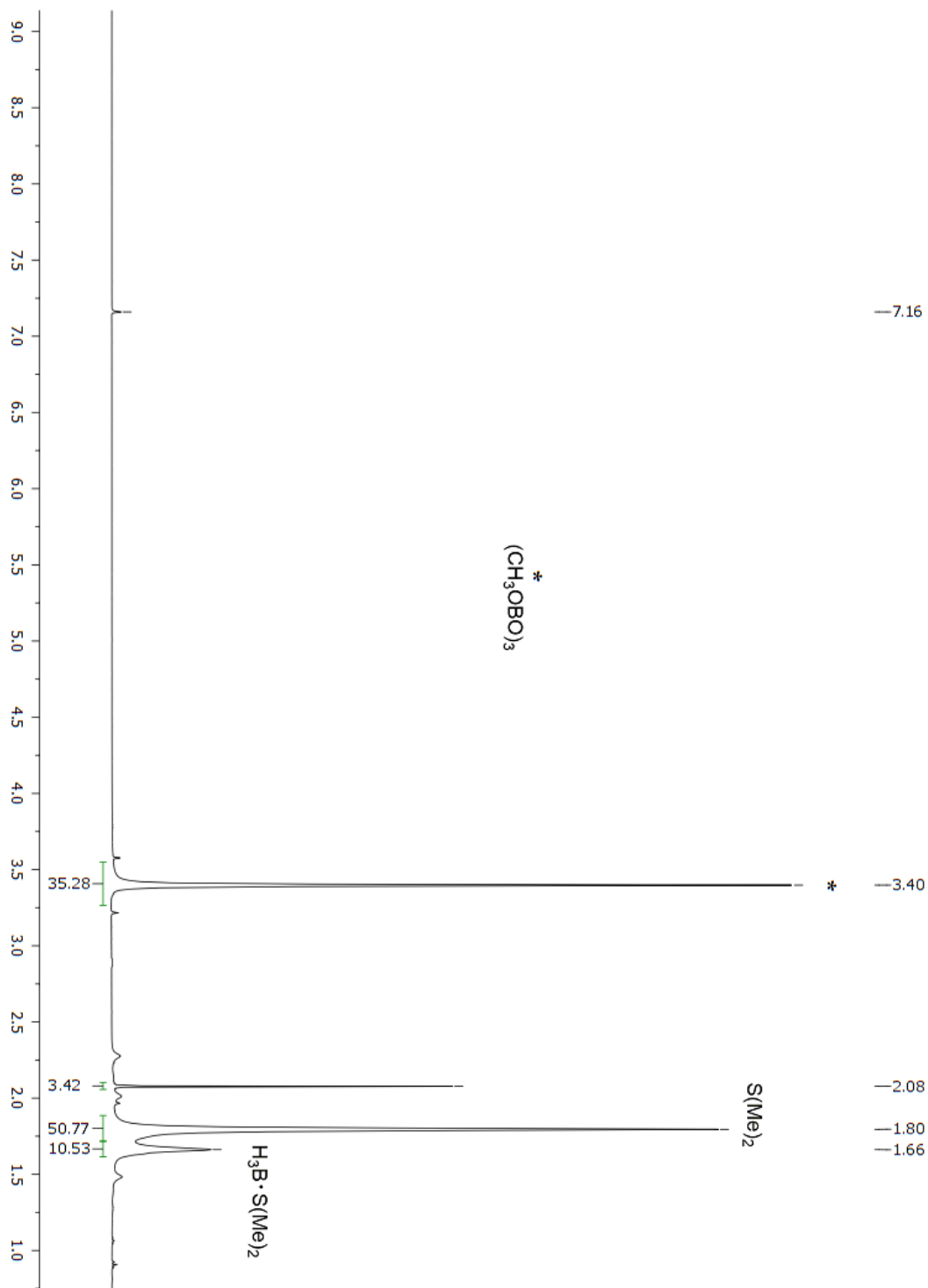
**Figure S10**. $^1H$ NMR spectrum (400 MHz, $C_6D_6$) after the reduction of $CO_2$ in the presence of $H_3B$-$S(Me)_2$ and TBAAc (0.1 mol%). Conditions: $C_6D_6$; T = 60 °C; time = 20 h; internal standard = hexamethylbenzene. Conversion = 83%.

**Figure S11**. $^{1}$H NMR spectrum (400 MHz, $C_6D_6$) after the reduction of $CO_2$ in the presence of $H_3B$-$S(Me)_2$ and TBAAc (0.1 mol%). Conditions: $C_6D_6$; T = 40 $^{o}$C; time = 19.5 h; internal standard = hexamethylbenzene. Conversion = 41%.

131.74
128.30
128.06
127.82
124.95

(CH₃OBO)₃
*

—51.43

H₃B·S(Me)₂

S(Me)₂

—25.80

17.81
16.85
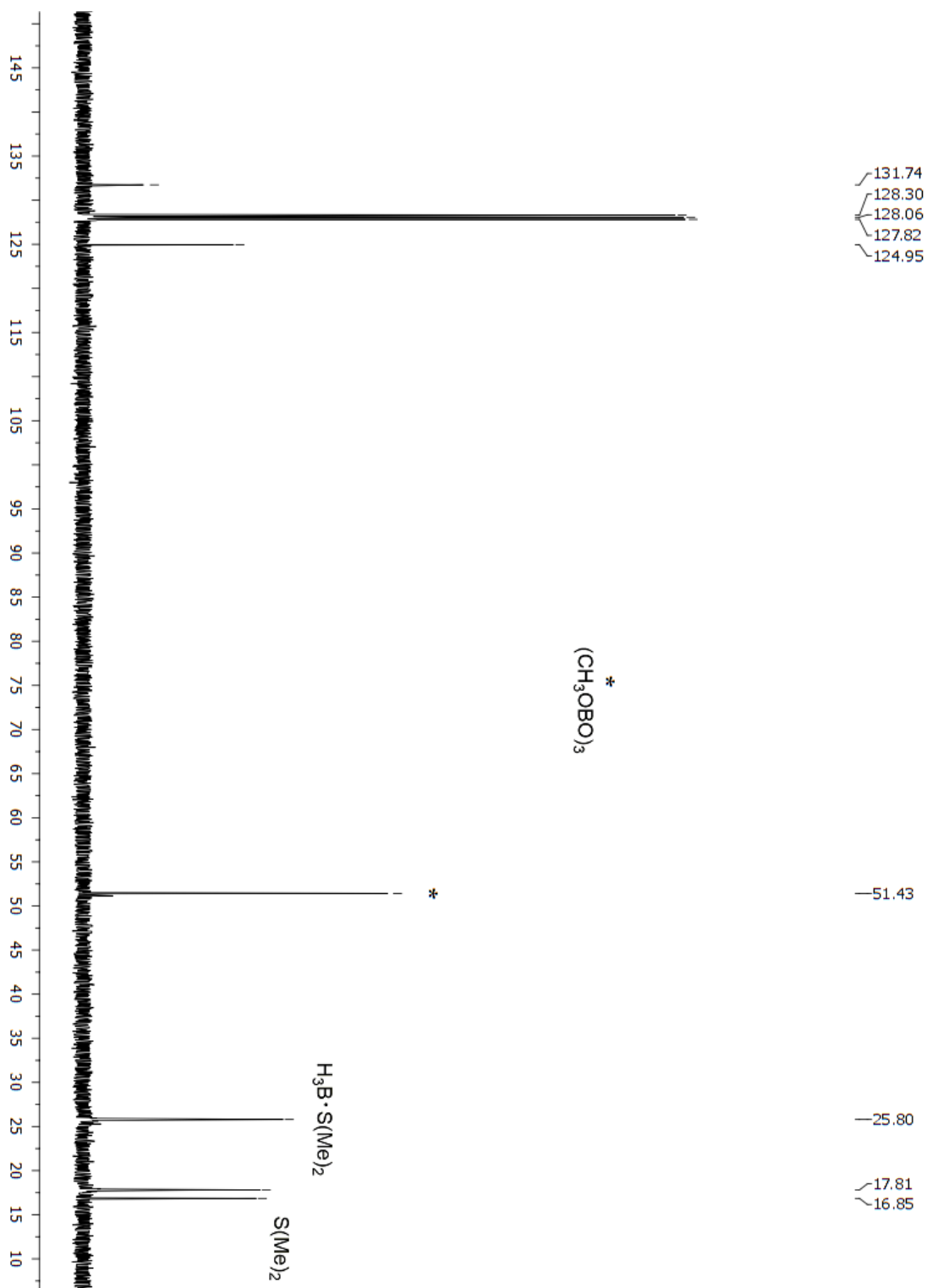
**Figure S12**. $^{13}C$ NMR spectrum (101 MHz, $C_6D_6$) after the reduction of $CO_2$ in the presence of $H_3B$-S(Me)$_2$ and TBAAc (0.1 mol%). Conditions: $C_6D_6$; T = 40 ºC; time: 19.5 h; internal standard = hexamethylbenzene. Conversion = 41%.
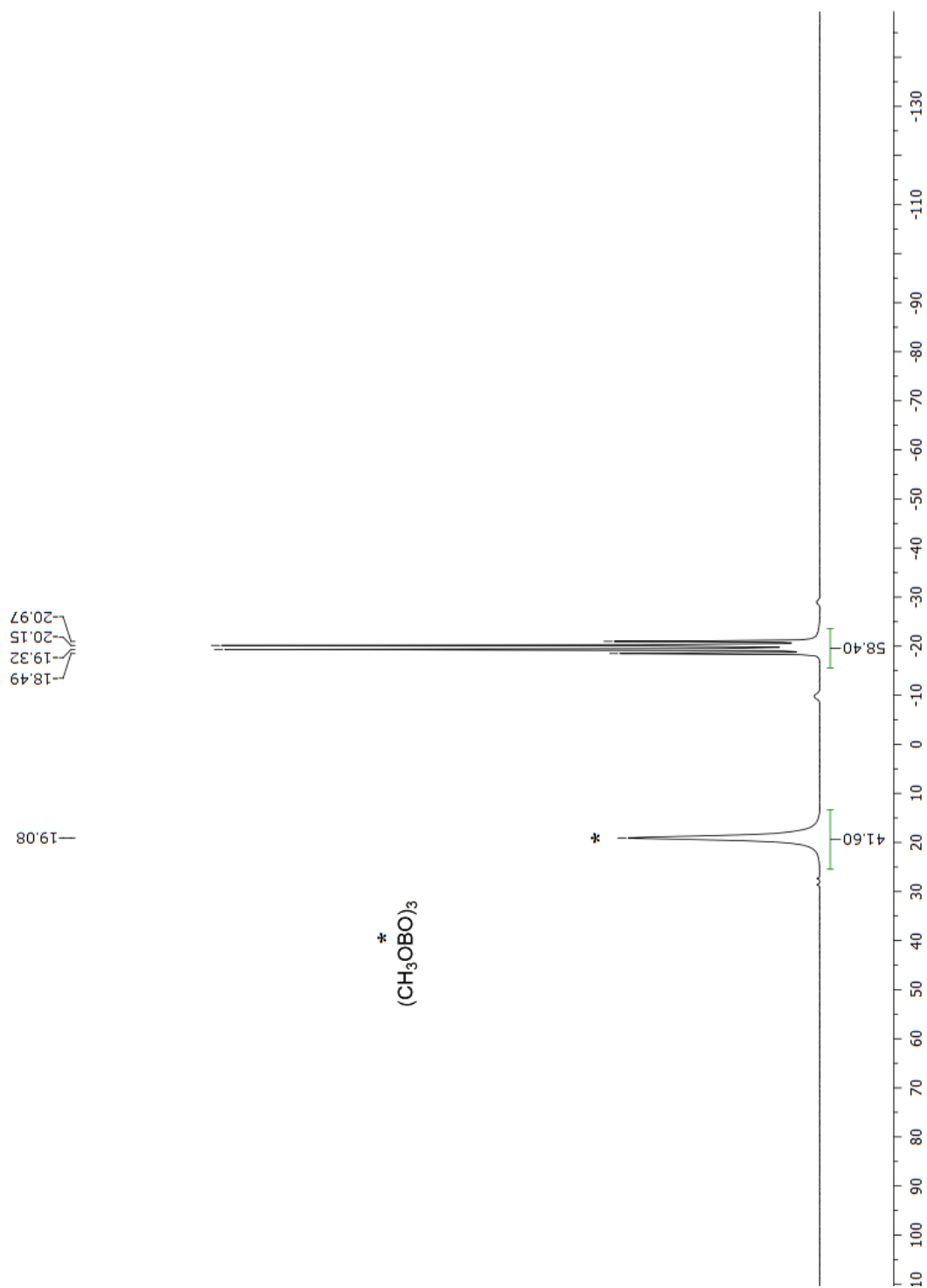
**Figure S13**. ^{11}B NMR spectrum (128 MHz, $C_6D_6$) after the reduction of $CO_2$ in the presence of $H_3B$-$S(Me)_2$ and TBAAc (0.1 mol%). Conditions: $C_6D_6$; T = 40 ⁰C; time = 19.5 h; internal standard = hexamethylbenzene. Conversion = 41%.

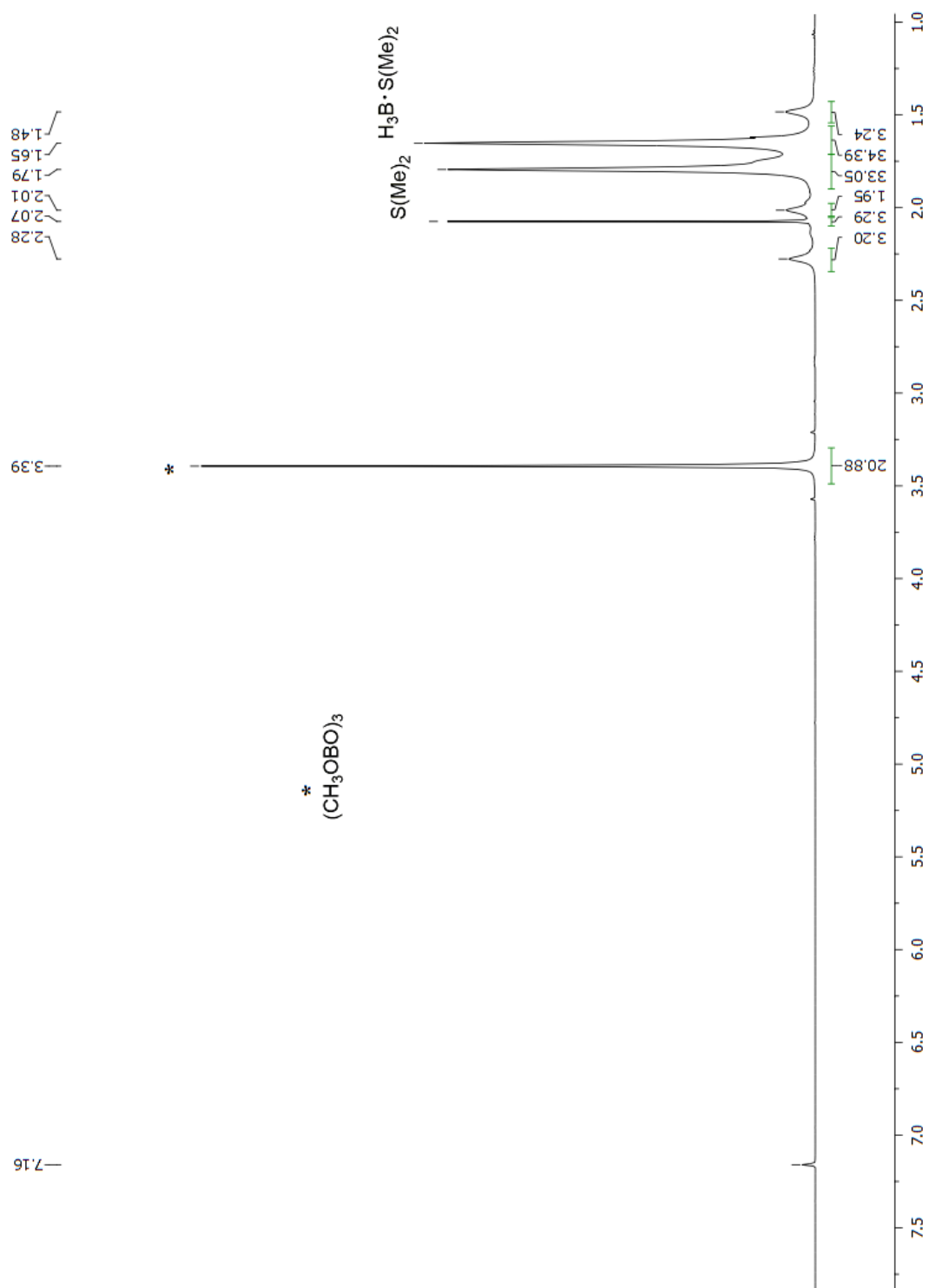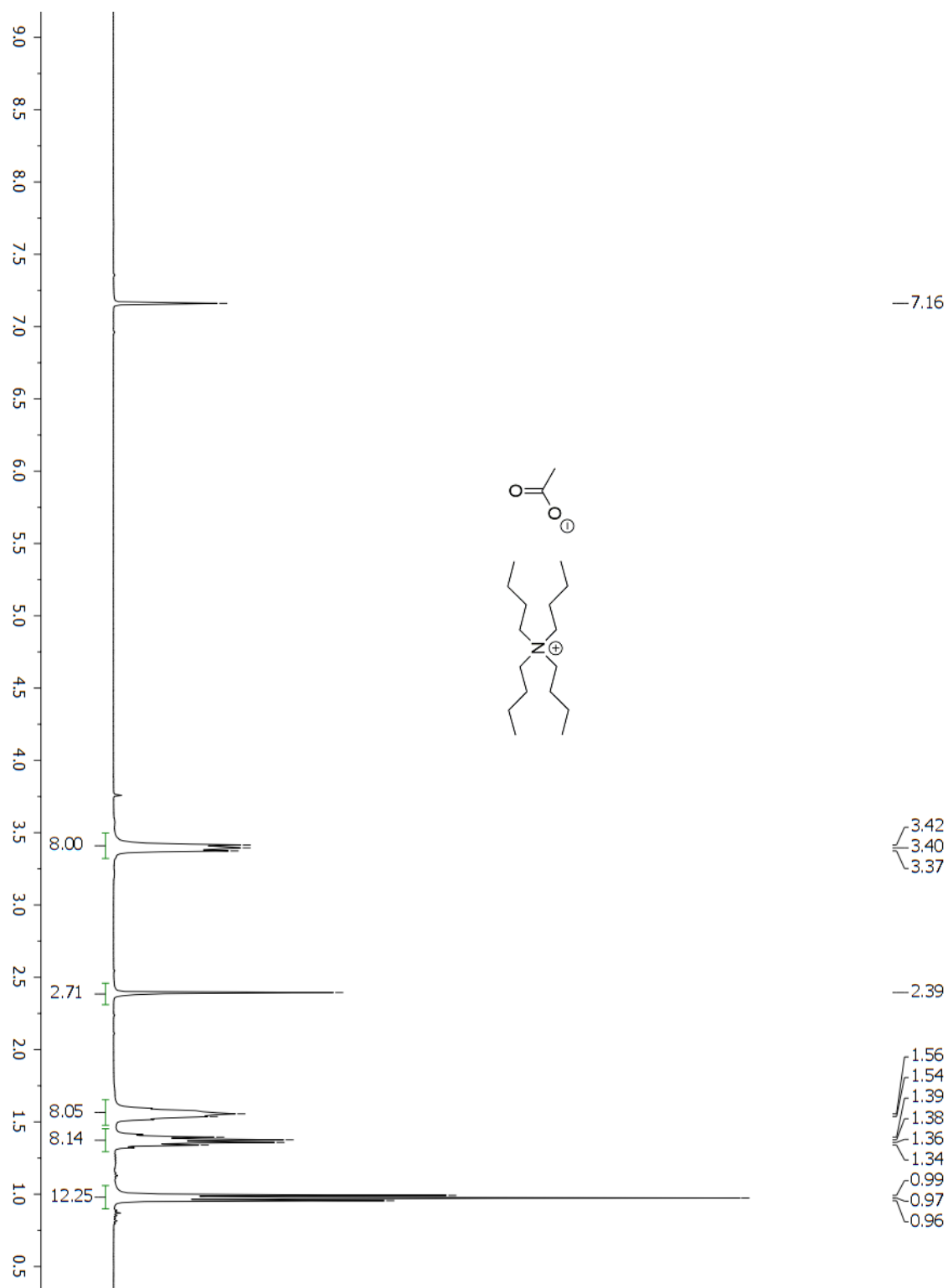**Figure S14**. $^1$H NMR spectrum (400 MHz, C$_6$D$_6$) of TBAAc.
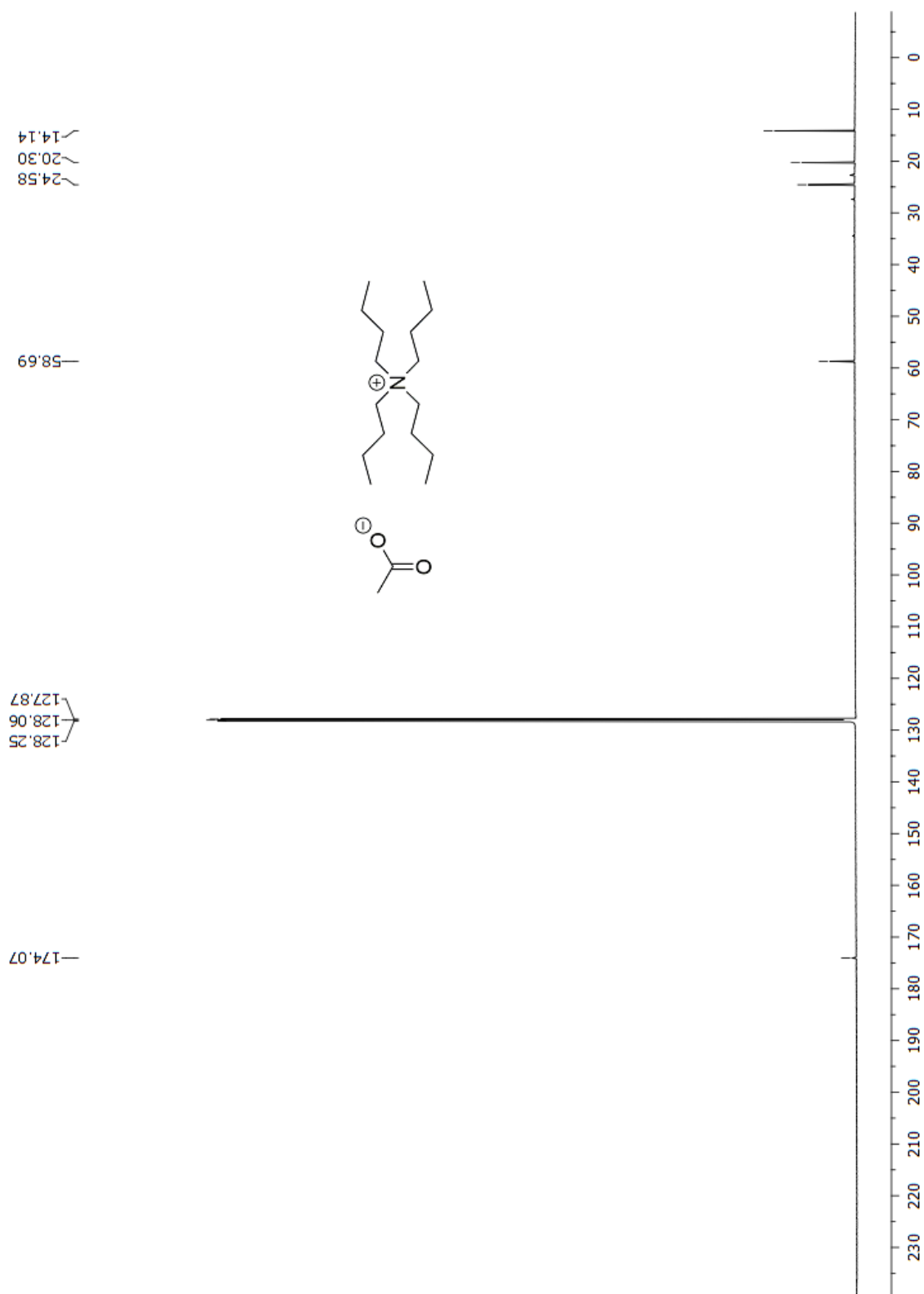
**Figure S15**. $^{13}C$ NMR spectrum (101 MHz, $C_6D_6$) of TBAAc.
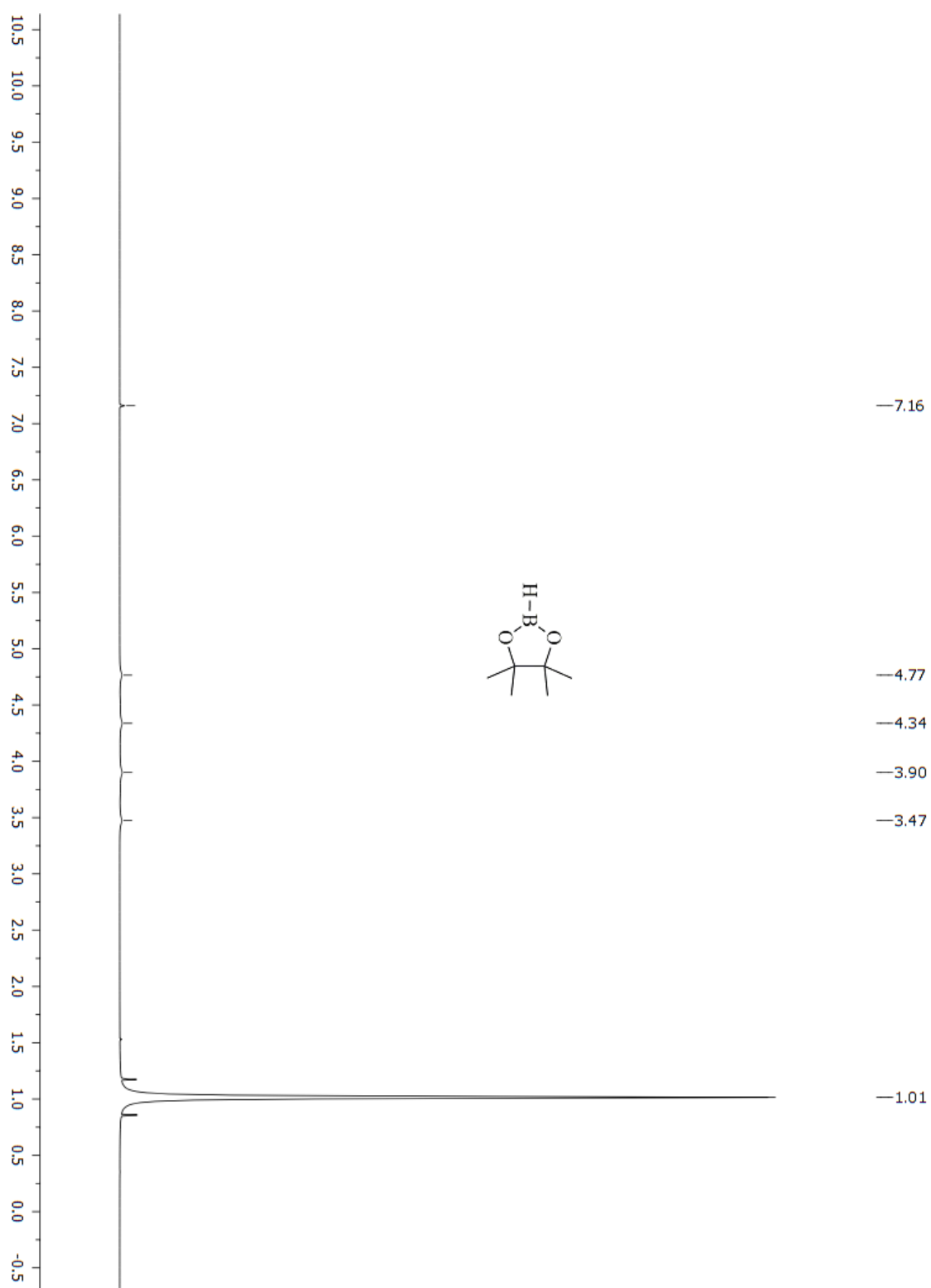
**Figure S16**. $^1$H NMR spectrum (400 MHz, C$_6$D$_6$) of HBpin.
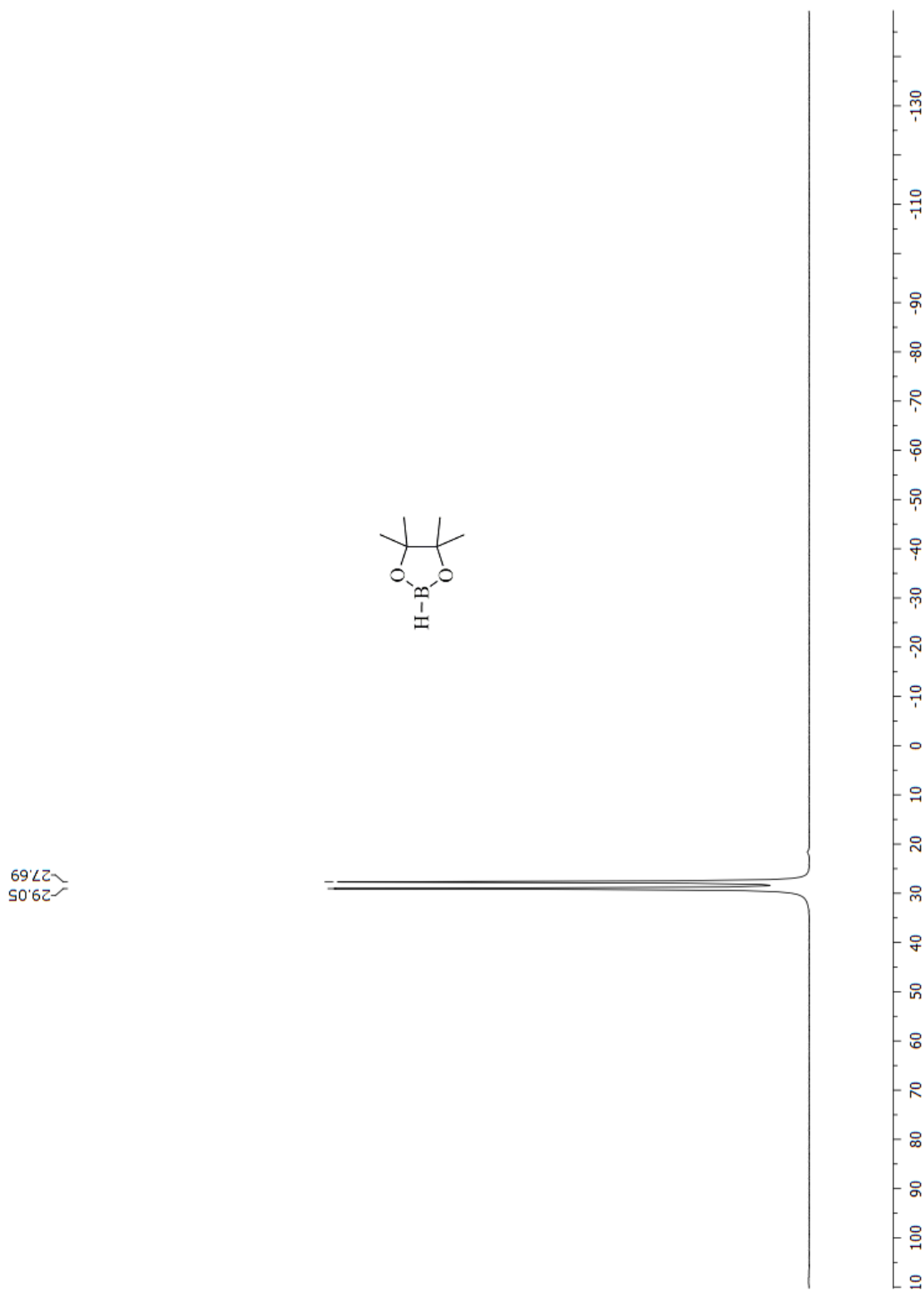
**Figure S17**. $^{11}$B NMR spectrum (128 MHz, C$_6$D$_6$) of HBpin.
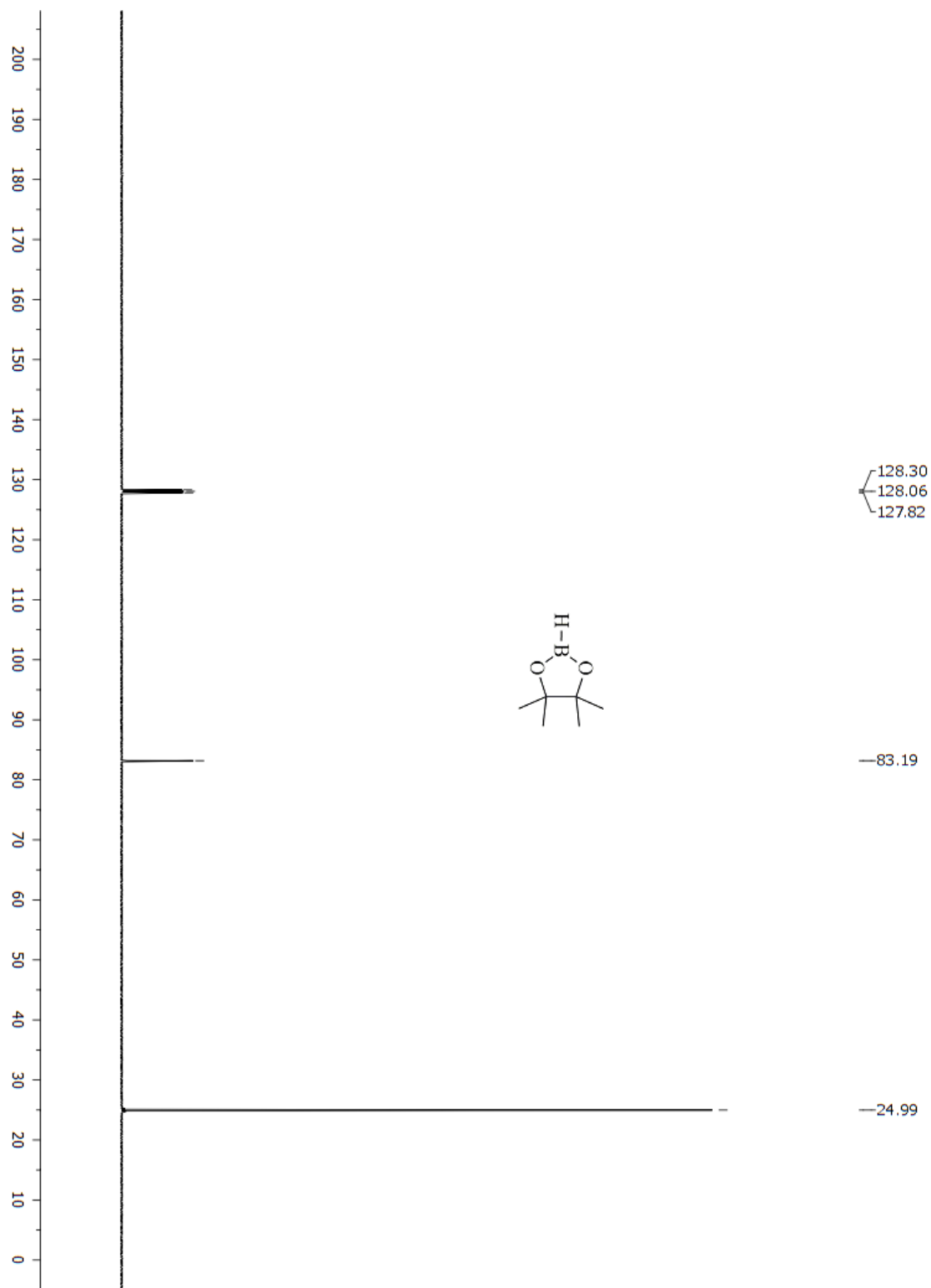
**Figure S18**. $^{13}$C NMR spectrum (101 MHz, C$_6$D$_6$) of HBpin.

**Figure S19**. $^1$H NMR spectrum (400 MHz, C$_6$D$_6$) of commercial H$_3$COBpin.

**Figure S20**. $^{11}$B NMR spectrum (128 MHz, $C_6D_6$) of commercial $H_3COBpin$.

### 6.3    SI Chapter III - Organometallic-Catalyzed Synthesis of High Molecular Weight Poly-(L-Lactic Acid) with a Covalently Attached Imidazolium Salt: Performance-Enhanced Reduced Graphene Oxide-PLLA Biomaterials

#### 6.3.1    Experimental Procedures

#### 6.3.1.1    General considerations

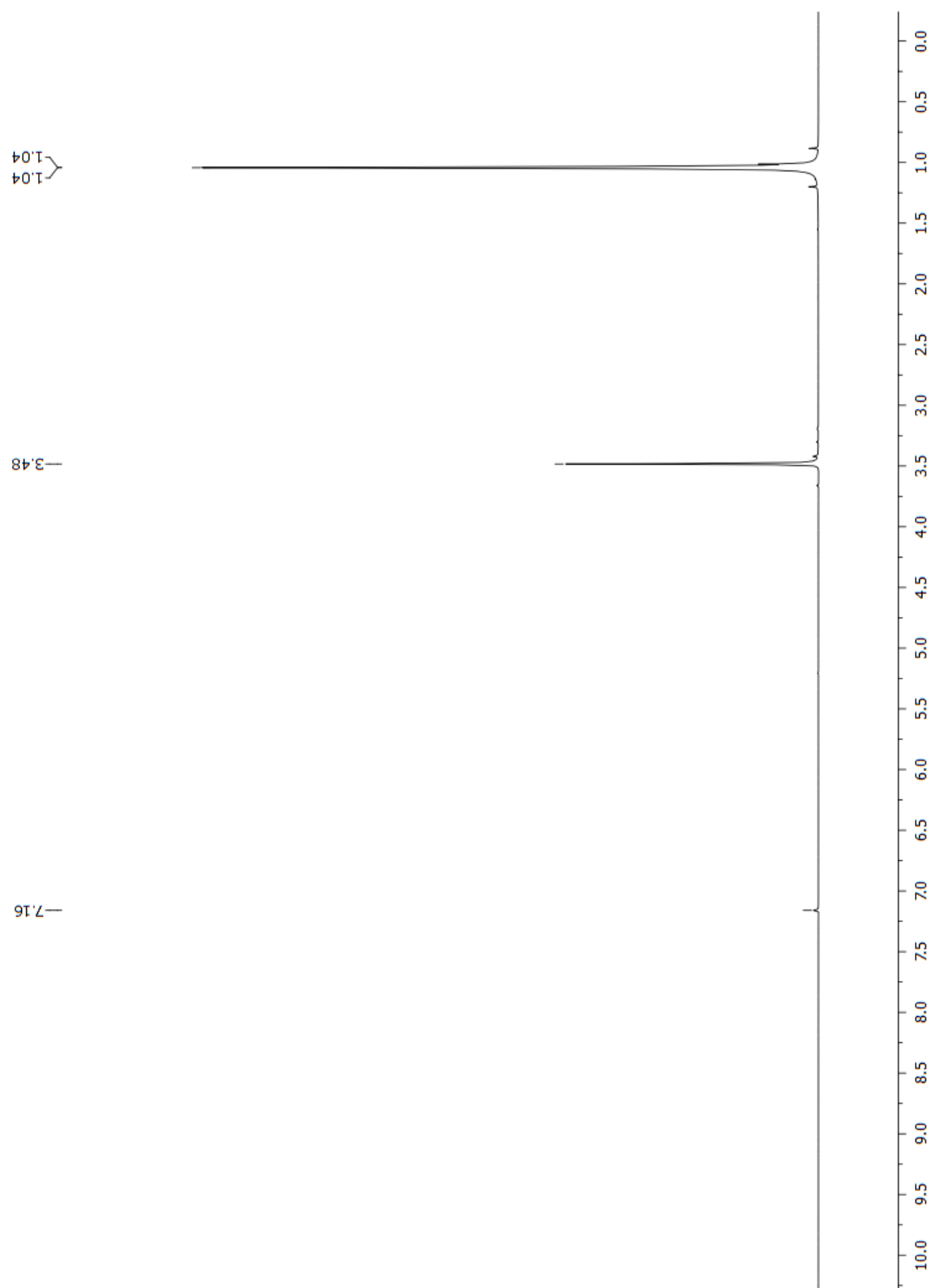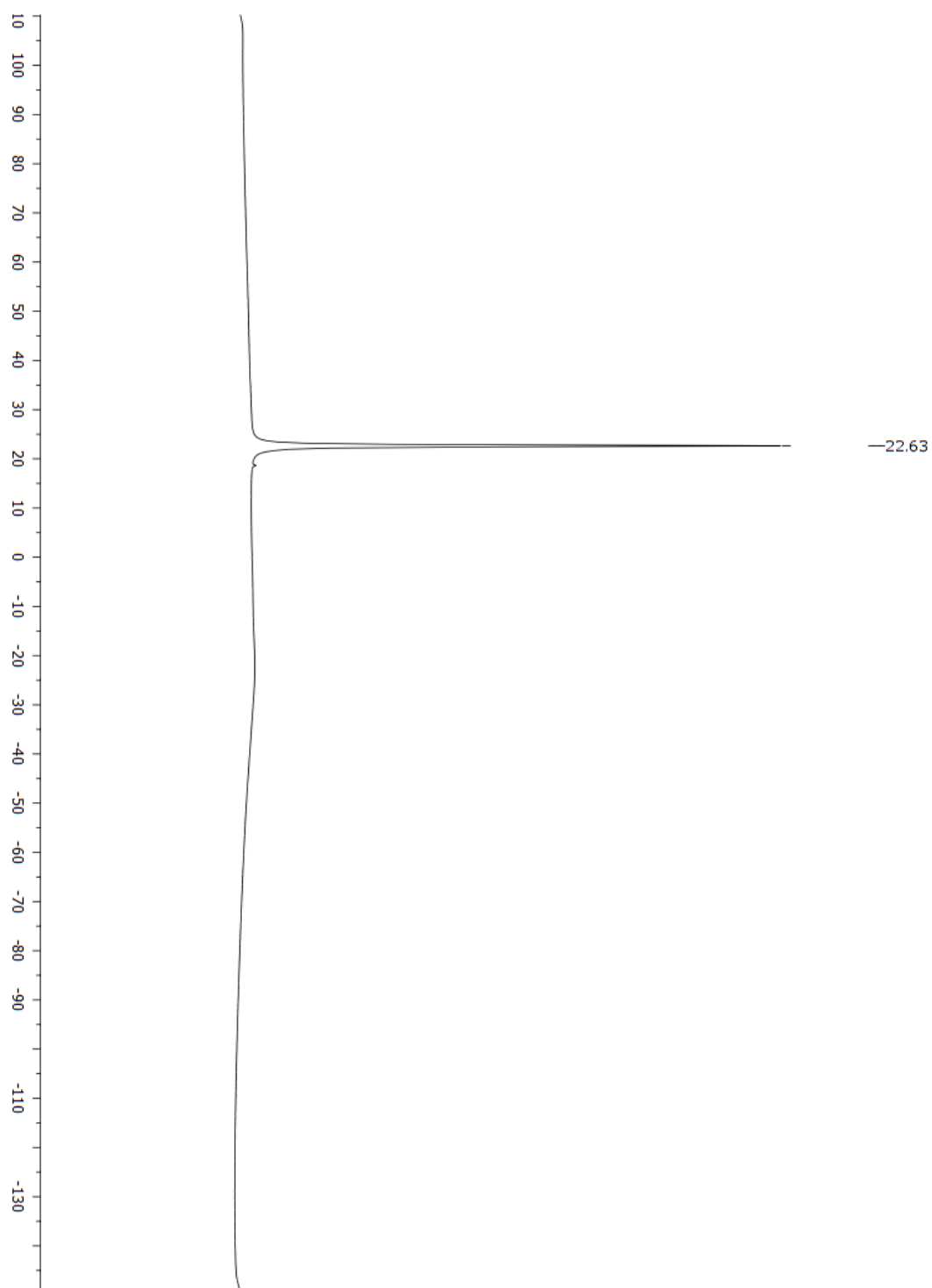All reactions and manipulations were performed under a $N_2$ atmosphere in a MBraun Unilab glovebox. Molecular sieves (4 Å) were activated under high vacuum at a temperature of 150 °C for at least 3 days. Dichloromethane (DCM), pentane and toluene were purchased from Sigma-Aldrich, and were first dried using a MBraun SPS purification system and then stored over activated molecular sieves (4 Å) for at least 20 h. Tetrahydrofuran (THF) was purchased from Sigma-Aldrich, distilled over Na/benzophenone and stored over activated molecular sieves (4 Å) for at least 48 h. Chloroform-$d_1$ and benzene-$d_6$ ($C_6D_6$) were purchased from Sigma-Aldrich and stored over activated molecular sieves (4 Å) for at least 20 h. PLLA (PURAPOL L100IXS) was provided by Corbion Purac. L-lactide (**L-LA**) was purchased from Sigma-Aldrich and purified by recrystallization from toluene, and then sublimed under inert atmosphere of $N_2$. The chemical compounds diethylzinc (ZnEt$_2$), tris(pentafluorophenyl)borane and bromopentafluorobenzene were purchased from Sigma-Aldrich, immediately stored inside the glovebox, and used as received. The imidazolium salt 1-(2-hydroxyethyl)-3-methylimidazolium tetrafluoroborate (**IS-OH**) was purchased from ABCR, dried under high vacuum for 48 h at 60 ° C and then dried over activated molecular sieves (4 Å) for 5 days. The organometallic $Zn(C_6F_5)_2$toluene complex was synthesized according to the procedure previously described in the literature.[1] Sulfuric acid (97%, Química Moderna), nitric acid (65%, Química Moderna) and hydrochloric acid (37%, Merck) were used as received. All other chemicals not described above were purchased from Sigma-Aldrich and used as received. The $^1H$ and $^{13}C$ NMR spectra were recorded at room temperature on Bruker AC instruments (300, 400 and 500 MHz). Chemical shifts (δ) are given in parts per million (ppm) and referenced to SiMe$_4$ or residual solvent signals. GPC analyses of the polymer samples were all performed on a system equipped with a Shimadzu RID10A refractometer detector using HPLC-grade THF as an eluent (with

molecular weights and polydispersity indices (PDIs) calculated using polystyrene standards). In the case of molecular weight number ($M_n$), these were corrected with the appropriate correcting factor (0.58 for PLA) for the $M_n$ values. Mass spectrometric analyzes were performed on a MALDI-TOF PerSeptive Biosystems Voyager-DE STR mass spectrometer and the samples were analyzed with the DCTB "magic matrix" and KTFA.

### 6.3.1.2  General procedure for synthesis of PLLA-IS

In a glovebox, the desired quantities of **IS-OH** and **L-LA** were weighed into a vial and diluted in toluene. The solution was kept under magnetic stirring until the total solubilization of the monomer. A toluene solution of the desired amount of $Zn(C_6F_5)_2$toluene catalyst was then transferred into the vial and the reaction mixture heated to the desired temperature. After the time of interest, the solvent was removed under high vacuum and $^1H$ NMR estimated the PLLA-IS conversion. The polymer product was dissolved in DCM and re-precipitated with addition of methanol, dried under high vacuum for 6 h at 80 °C and fully characterized by $^1H$, $^9F$, $^{11}B$ and $^{13}C$ NMR; GPC and MALDI-TOF spectrometry.

### 6.3.1.3  General procedure for the synthesis of reduced graphene oxide (rGO)

The oxidation of graphite grafine was performed by the Staudenmaier method.[2] In this process, an acidic mixture of 160 mL of $H_2SO_4$ (97%) and 90 mL of $HNO_3$ (65%) was prepared in a reactor with a mechanical glass rod. The reactor was placed in an ice bath for 1 h to cool the system. After this period, 10 g of graphite grafine was added to the acid mixture under constant stirring. Subsequently, 110 g of $KCl_3$ were added, and the reaction was continued for 24 h. To quench the reaction, 580 mL of an aqueous solution of HCl (10% by volume) were added to remove excess salts by centrifugation (5000 rpm, 15 min), discarding the supernatant. To obtain the graphene oxide (GO), the precipitate was suspended in distilled water and placed into an ultrasound bath (40 kHz) for 4 h, and then the suspension was transferred to an osmotic membrane, which was dipped in a beaker with water. The water of the beaker was changed and the pH checked every 1-hour until pH 6 was reached. The GO suspension was dried in an oven at 150 °C. The resulting GO film was placed in a quartz ampoule and placed into a

heating furnace. The thermal reduction of GO was carried out at the temperature of 1000 °C for 10 s to obtain **rGO**.

### 6.3.1.4 General procedure for the synthesis of PLLA-IS/rGO

PLLA-IS (0.5 g) was weighed in a screw-capped vial, and 15 mL of $CHCl_3$ were added. This mixture was stirred for 10 min, and 5 mg of **rGO** (1 wt%) were added to the PLLA-IS solution. The final mixture was homogenized for 15 min under ultrasound at 40 KHz and 60 °C for 1 h under stirring at room temperature. Finally, the mixture was poured into a mold and solvent casted to obtain a film of **PLLA-IS/rGO-1%**.

### 6.3.1.5 Thermogravimetric analysis (TGA)

TGA was performed using a Q50 equipment of TA Instruments. The films were heated from 30 °C to 600 °C, with a heating rate of 20 °C/min. Analyzes were conducted under $N_2$ atmosphere with a gas flow rate of 60 mL/min. An average sample weight of 10 mg was analyzed in a platinum pan, and an empty pan was used as reference.

### 6.3.1.6 Dynamic mechanical analysis (DMA)

DMA was performed in a Q800 equipment of TA Instruments. Rectangular samples with a length of 11.6327 mm and width of 6.9750 mm were tested in multifrequency strain mode, applying a tension of 125%. The moduli were tested in the range of 30-90 °C with a heating rate of 3 °C/min and at constant and static force of 0.01 N. The storage modulus (E '), the loss factor δ (E''/E') and the loss modulus (E'') were recorded.

### 6.3.1.7 Water contact angle analysis

The water contact angles were determined on a Drop Shape Analyzer DSA100 (KRUSS). An automated syringe deposited deionized water (3 µL) on the samples. The contact angle was determined from the tangent line appropriately positioned on the contour of the drop in relation to the flat surface. The contact angles were measured using the software (Advance - Drop Shape) of the equipment.

### 6.3.1.8 Scanning electron microscopy (SEM) analysis

The morphological analysis of the films was performed using a JEOL JSM 6060 scanning electron microscope operating at 5 kV. The samples were placed on stubbs

with PELCO carbon conductive tape, and covered with a layer of carbon to raise the electrical conductivity.

### 6.3.1.9 Minor antibiofilm concentration assay

The capacity of the PLLA-IS films to inhibit the growth of biofilms was determined by the minor antibiofilm assay, following the protocols CLSI M27-A3 (http://shop.clsi.org/microbiology-documents/M27.html) and MM38-A2 (http://shop.clsi.org/microbiology-documents/M38.html) with modifications. Pure and young yeast colonies of the biofilm forming *Candida tropicalis* ATCC 13803 and *Candida albicans* ATCC 44858 species were grown in Petri dishes on Sabouraud agar with chloramphenicol at 36 °C for 24 h. This was followed by the preparation of a $10^6$ colony forming unit (CFU)/mL yeast inoculum (100% transmittance for 0.9% saline and 90% transmittance for the $10^6$ CFU/mL yeast inoculum) in sterile saline (0.9%). Aliquots of 20 µL were transferred into 96-well microplates and complemented with 180 µL of Roswell Park Memorial Institute (RPMI) culture medium. The PLLA-IS films (cut in circles of 5 mm in diameter) were sterilized by UV for 30 min, added, and incubated at 36 °C for 24 h. All samples were tested in quadruplicate. After removal of the PLLA-IS films from the wells, these were washed with 1 mL of sterile saline (0.9%) to remove nonadherent cells. Subsequently, the PLLA-IS films were placed into another 96-well microplate, followed by the addition of 160 µL of 3-(4,5-dimethylthiazol-2-yl)-2,5-diphenyltetrazolium bromide to stain the viable cells adhered to the materials. After 3 h, the 3-(4,5-dimethylthiazol-2-yl)-2,5-diphenyltetrazolium bromide solution was removed, and the PLLA-IS films were treated with 160 µL of isopropanol for 15 min. The absorption intensities at the wavelengths of 570 and 690 nm were determined with a Biochrom EZ Read 400 microplate reader, using 100 µL samples of the each isopropanol solution. PLLA without IS was used as the positive control test (20 µL of yeast inoculum and 180 µL of RPMI). As a negative control, 200 µL of RPMI medium was applied.[3] The following formula was used to determine the impediment percentage of biofilm formation on the PLLA-IS samples: 100 - [(average assay absorbance) ÷ (average absorbance of the positive control)] x 100.
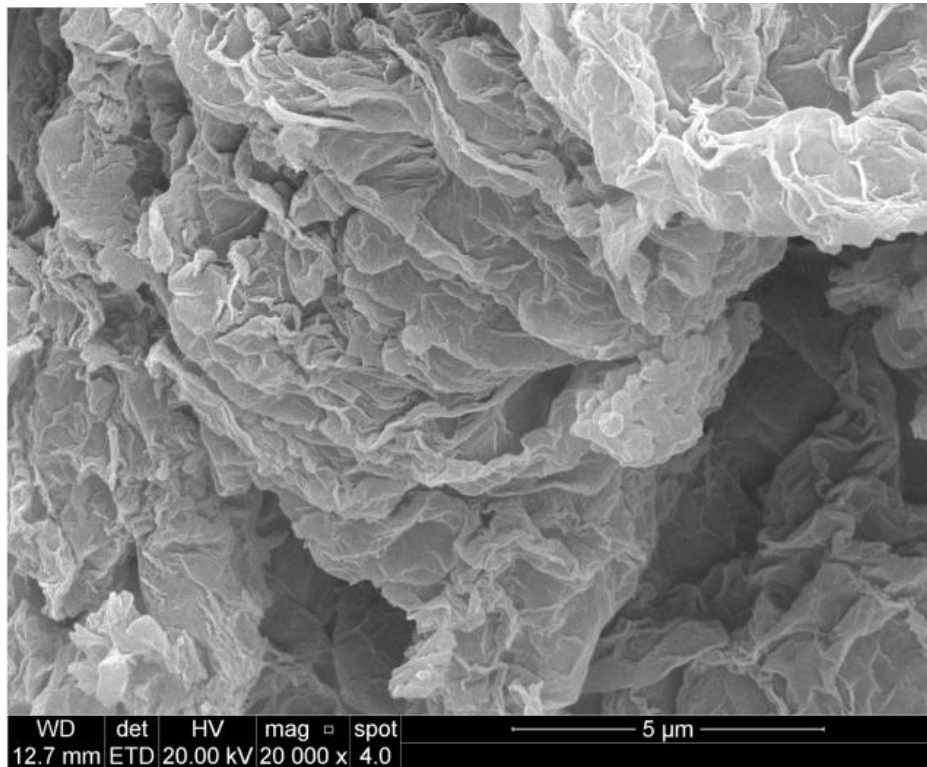
**Figure S1**. SEM image of rGO that was used in the synthesis of PLLA-IS/rGO.

**Figure S2**. Photograph of a **PLLA-IS** film.



**Figure S3**. Photograph of a **PLLA-IS/rGO-1%** film.
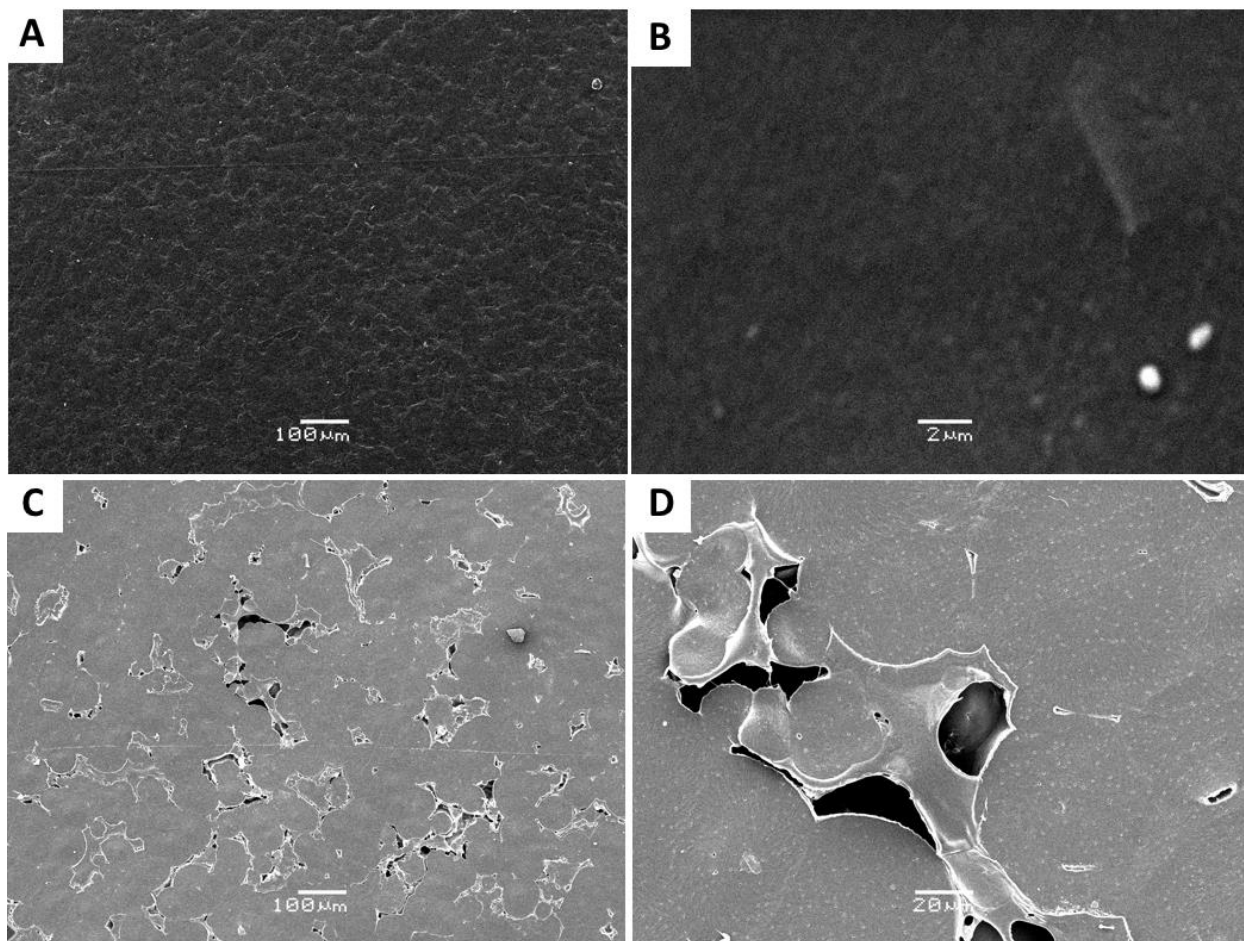
**Figure S4**. Micrographs of: (A) commercial PLLA film (scale bar = 100 µm); (B) commercial PLLA film (scale bar = 2 µm); (C) commercial PLLA + rGO-1% (scale bar = 100 µm); (D) commercial PLLA + rGO-1% (scale bar = 20 µm).

### 6.3.2 Nuclear Magnetic Resonance
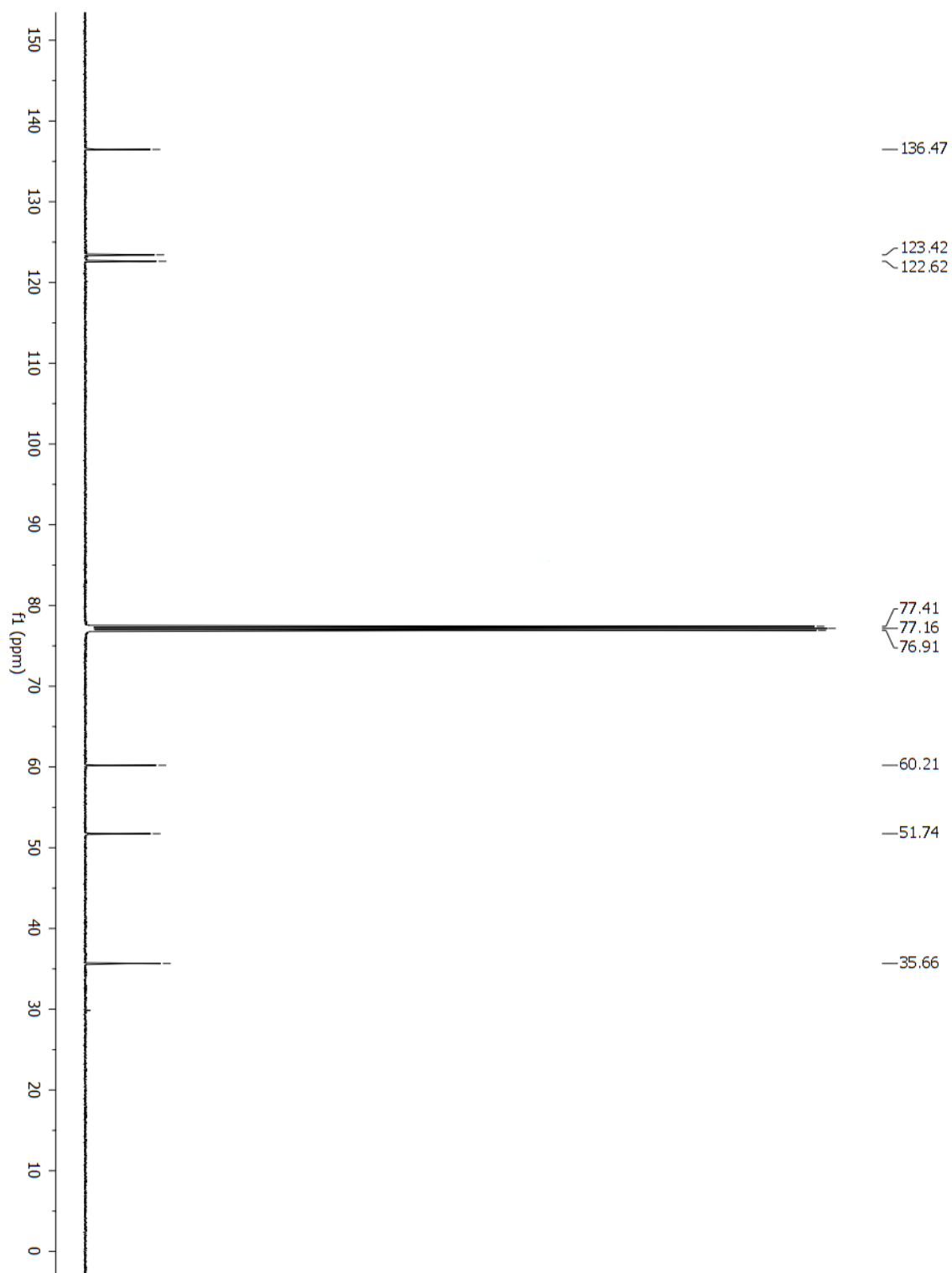


**Figure S5**. $^{13}$C NMR spectrum (101 MHz, CDCl$_3$) of the IS.
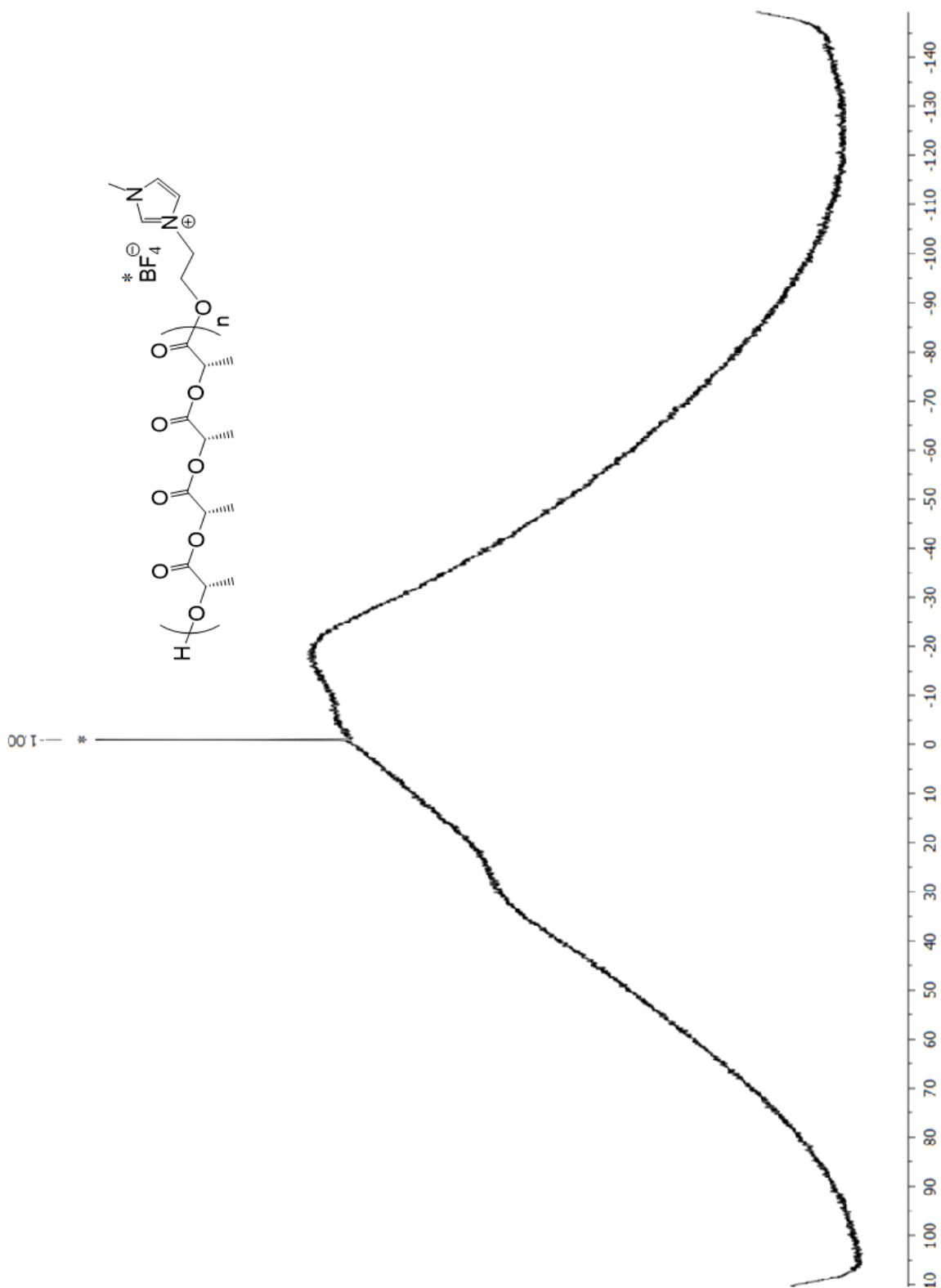
**Figure S6**. $^{11}$B NMR spectrum (128 MHz, CDCl$_3$) of PLLA-IS. Conditions: **L-LA** (1000 equiv.), [L-LA]$_0$ = 1 M, **IS-OH** (20 equiv.), Zn(C$_6$F$_5$)$_2$toluene (1 equiv.), 80 ºC, toluene.
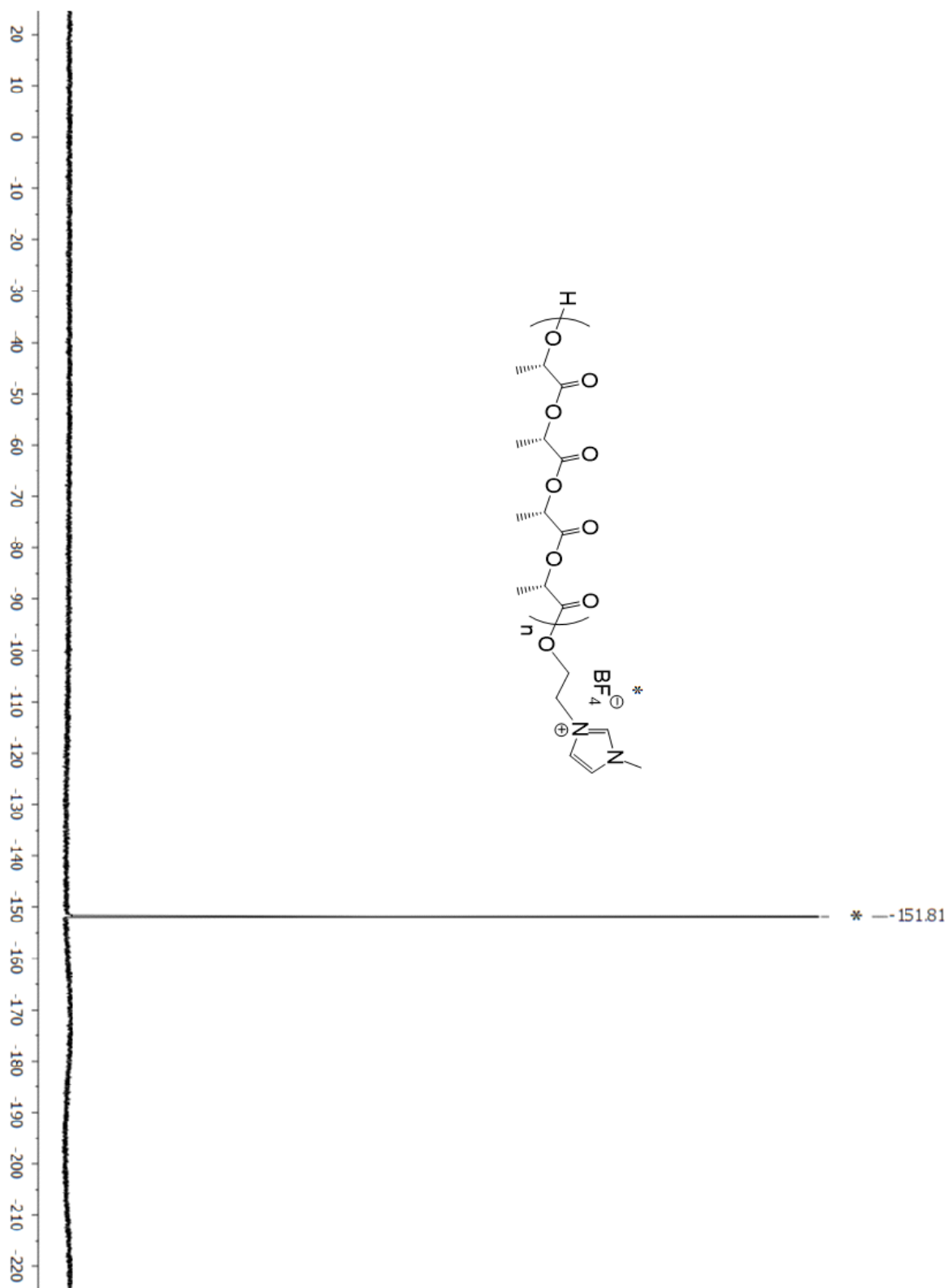
**Figure S7**. $^{19}$F NMR spectrum (282 MHz, CDCl$_3$) of PLLA-IS. Conditions: **L-LA** (1000 equiv.), [L-LA]$_0$ = 1 M, **IS-OH** (20 equiv.), Zn(C$_6$F$_5$)$_2$toluene (1 equiv.), 80 ºC, toluene.

### 6.3.3  References

[1]  A. W. Walker, T. J. Woodman, D. L. Hughes, M. Bochmann, *Organomet.* **2001**, *20*, 3772.

[2]  M. J. McAllister, J. L. Li, D. H. Adamson, H. C. Schniepp, A. A. Abdala, J. Liu, M. Herrera-Alonso, D. L. Milius, R. Car, R. K. Prud'homme, I. A. Aksay, *Chem. Mater.* **2007**, *19*, 4396–4404.

[3]  E. A. Trafny, *Int. J. Occup. Med. Environ. Health* **2013**, *26*(*1*), 4–15.

# 7   RÉSUMÉ DES RÉSULTATS IMPORTANTS

## 7.1 Complexes tripodaux (O-O-O) aluminium hydrure pour la réduction catalytique de $CO_2$ par un borane en méthoxy et formoxyborane.

Nous avons étudié la réduction de $CO_2$ avec HBpin en utilisant pour la première fois deux catalyseurs de type hydrure d'aluminium (complexes **1** et **3**) ainsi que deux catalyseurs de type formiate d'aluminium (**2** et **4**), comme illustré à la **Figure 1**.
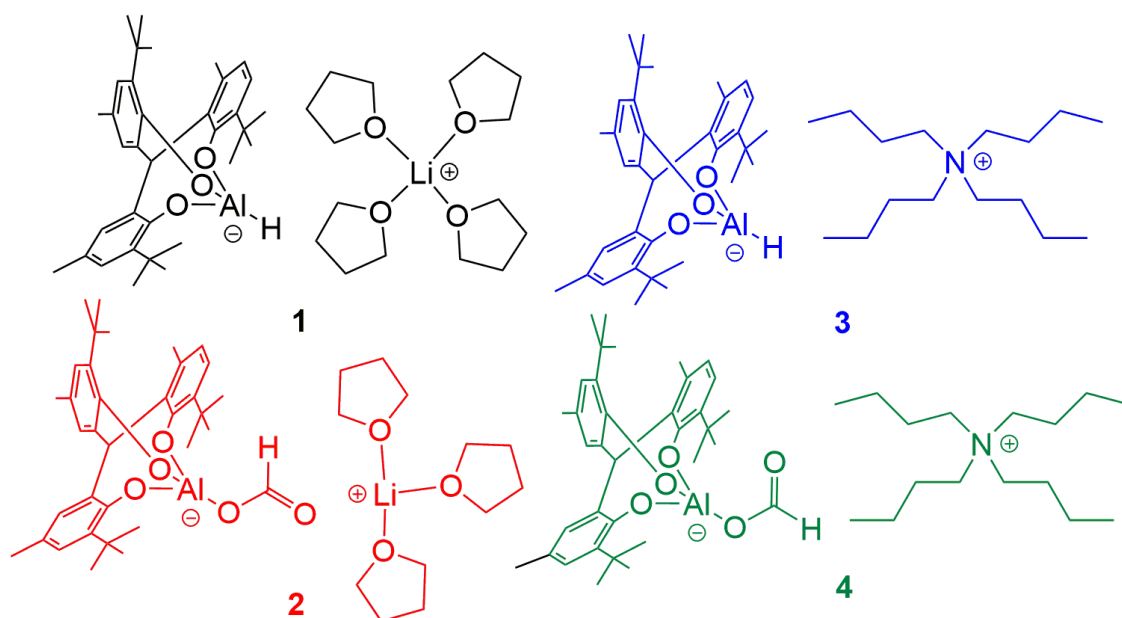


**Figure 1** Complexes d'aluminium utilisés pour la réduction de $CO_2$ en présence de HBpin.

Tous étaient des catalyseurs actifs dans la réduction du $CO_2$ induite par le borane. Selon la quantité de catalyseur utilisée, des précurseurs importants pour le secteur de la chimie et de l'énergie ont été formés, le formoxyborane et le méthoxyborane (**Tableau 1**), qui peuvent être facilement transformés en acide formique et méthanol, respectivement.

**Tableau 1.** Complexes tripodes d'aluminium utilisés comme catalyseurs pour la réduction du $CO_2$ par les boranes.
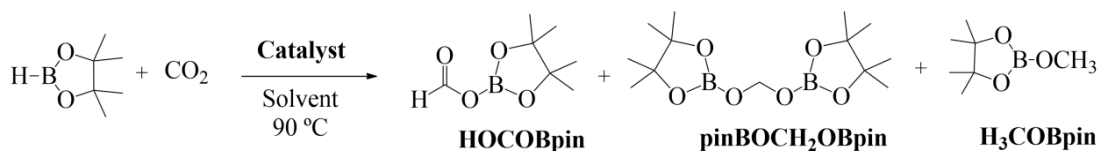


| Entrée | Catalyseur | Catalyseur mol% | Solvant | Temp. (ºC)[a] | durée (h) | Conv. (%)[b] | TON[c] | TOF (h⁻¹)[d] | HOCOBpin (%)[e] | pinBOCH₂OBpin (%)[e] | H₃COBpin (%)[e] |
|---|---|---|---|---|---|---|---|---|---|---|---|
| 1 | **1** | 10 | $C_6D_6$ | 90 | 44 | 96" | 9.6 | 0.22 | - | 2 | 98 |
| 2 | **2** | 10 | $C_6D_6$ | 90 | 74 | 99" | 9.9 | 0.13 | - | 2 | 98 |
| 3 | **3** | 10 | $C_6D_6$ | 90 | 6 | 95" | 9.5 | 1.6 | 97 | 3 | - |
| 4 | **3** | 1 | $C_6D_6$ | 90 | 1 | 11" | 11 | 11 | 99 | 1 | - |
| 5 | **3** | 1 | $C_6D_6$ | 90 | 2 | 14" | 14 | 7 | 98 | 2 | - |
| 6 | **3** | 1 | $C_6D_6$ | 90 | 3 | 15" | 15 | 5 | 77 | 4 | 18 |
| 7 | **3** | 1 | $C_6D_6$ | 90 | 4 | 18" | 18 | 5 | 52 | 5 | 43 |
| 8 | **3** | 1 | $C_6D_6$ | 90 | 5 | 21" | 21 | 4 | 32 | 4 | 63 |
| 9 | **3** | 1 | $C_6D_6$ | 90 | 19 | 61" | 61 | 3 | 5 | 1 | 94 |
| 10 | **3** | 1 | $C_6D_6$ | 90 | 25 | 71" | 71 | 3 | 4 | 1 | 95 |
| 11 | **3** | 1 | $C_6D_6$ | 90 | 49 | 95" | 95 | 2 | 4 | 0 | 96 |
| 12 | **3** | 0.1 | $C_6D_6$ | 90 | 45 | 95" | 950 | 21 | 1 | - | 99 |
| 13 | **3** | 0.1 | - | 90 | 22 | 97' | 970 | 44 | 1 | - | 99 |
| 14 | **3** | 0.05 | - | 90 | 40 | 96' | 1920 | 48 | - | - | 100 |
| 15 | **4** | 10 | $C_6D_6$ | 90 | 6 | 87' | 8.7 | 1.5 | 99 | 1 | - |

[a] Temp. = température. [b] Conv. = conversion - calculée par (') ¹H RMN par intégration des signaux caractéristiques de l'étalon interne et des produits ou (") par ¹¹B RMN par intégration des signaux du produit. [c] TON = numéro de chiffre d'affaires. [d] TOF = fréquence de renouvellement = TON / temps de réaction. [e] Sélectivité - Déterminée par ¹H RMN via l'intégration entre les signaux des trois produits.

 

La haute sélectivité pour la formation de méthoxyborane est représentée dans les spectres de RMN ¹H (**Figure 2**) et la formation d'un signal à 3,51 ppm est observée (en utilisant 1% en moles de catalyseur) et le signal augmente avec le temps de réaction. Ce signal est décrit dans la littérature comme le pic caractéristique de $H_3CO$-Bpin dans $C_6D_6$. Dans les spectres RMN ¹¹B (**Figure 3**) de $C_6D_6$, du formoxyborane (22,3 ppm) est observé dans les premières heures comme étant le produit principal après l'injection de $CO_2$. Cependant, à mesure que la réaction progresse, on observe une conversion complète en méthoxyborane (22,8 ppm) et en pinB-O-Bpin (21,9 ppm) (avec 1% en moles de catalyseur). Dans les spectres de RMN ¹³C, on observe la

formation d'un pic caractéristique de méthoxyborane à 52,22 ppm. Tous ces signaux sont des signaux caractéristiques en accord avec ceux précédemment rapportés dans la littérature ce qui confirment le succès de la réduction du $CO_2$.
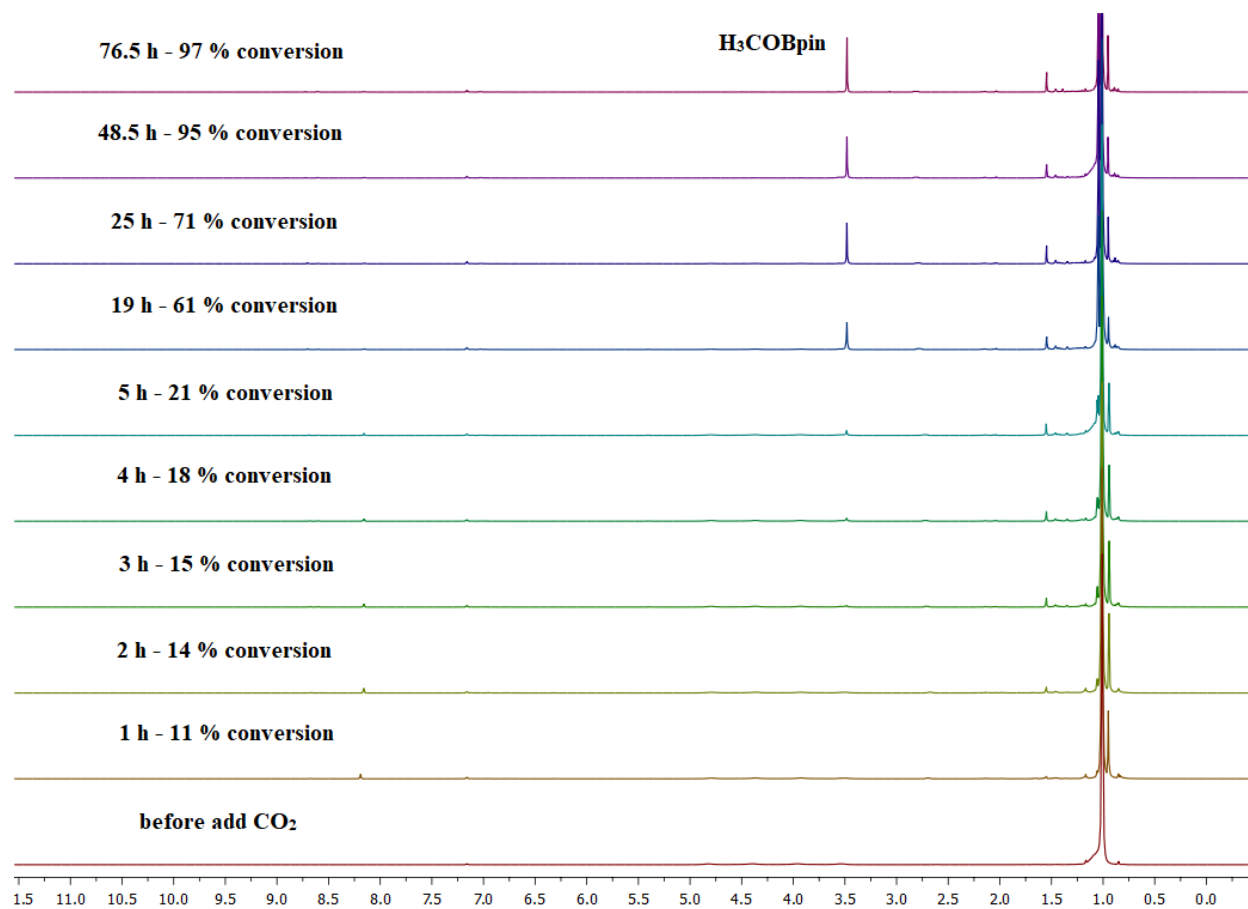


**Figure 2** Spectre RMN $^{1}$H de la réduction de $CO_2$ en présence de HBpin et du complexe **3** (1% en mole). Conditions : $C_6D_6$ ; Température : 90 ºC.
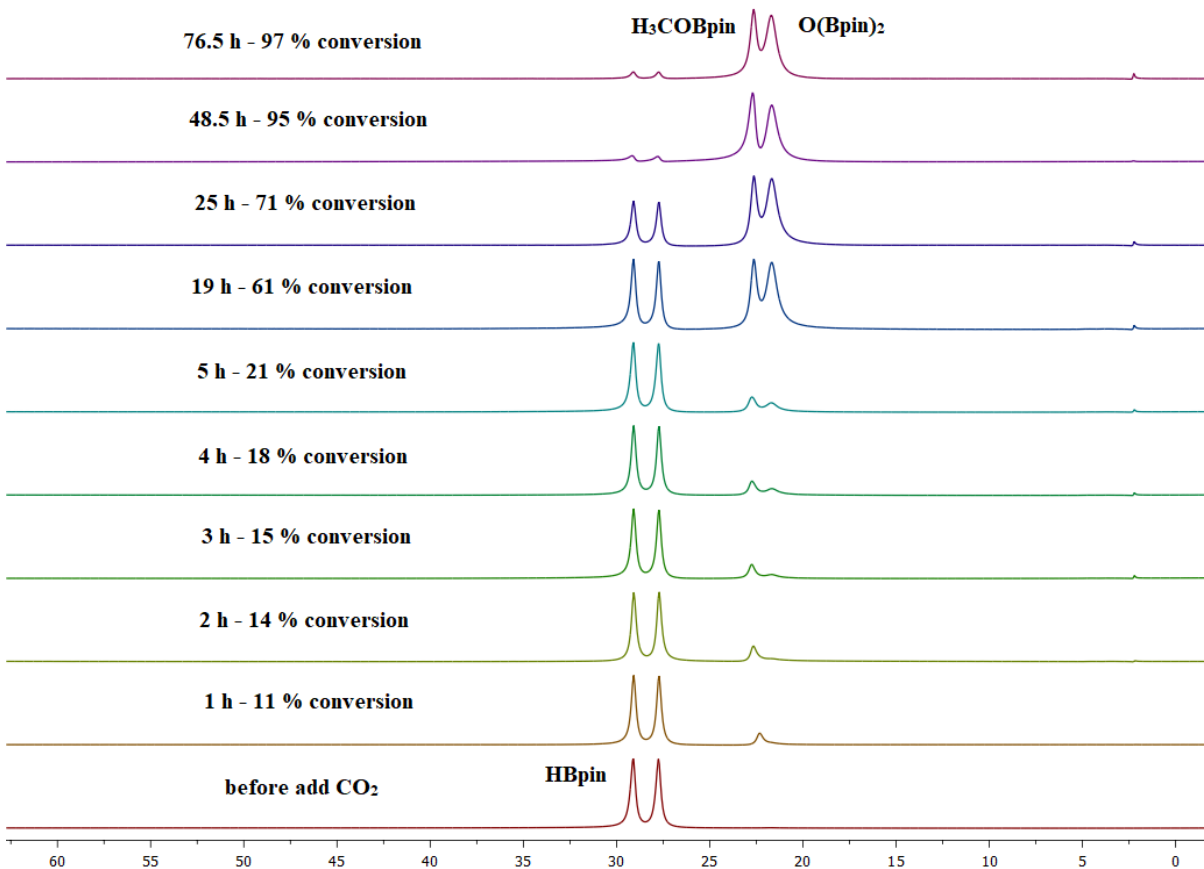
**Figure 3** Spectres RMN $^{11}$B de la réduction de $CO_2$ en présence de HBpin et du complexe **3** (1% en moles). Conditions : $C_6D_6$ ; Température : 90 ºC.

La réduction du $CO_2$ en présence de HBpin et de nouveaux catalyseurs à base d'aluminium synthétisés et caractérisés dans le cadre de ce projet peut conduire à la formation de 3 produits de réduction différents. Ceci a été suivi in situ et est illustré à la **Figure 4**. Initialement, le premier produit de réduction HOCOBpin est formé sélectivement. Une fois que le rapport du deuxième produit de réduction pinBOCH$_2$OBpin augmente, il est rapidement consommé, ce qui explique pourquoi sa concentration est faible tout au long du processus. Ensuite, le formoxyborane et le méthoxyborane sont formés en quantités similaires. Au fil du temps de réaction, la sélectivité s'est déplacée vers la formation de méthoxyborane.
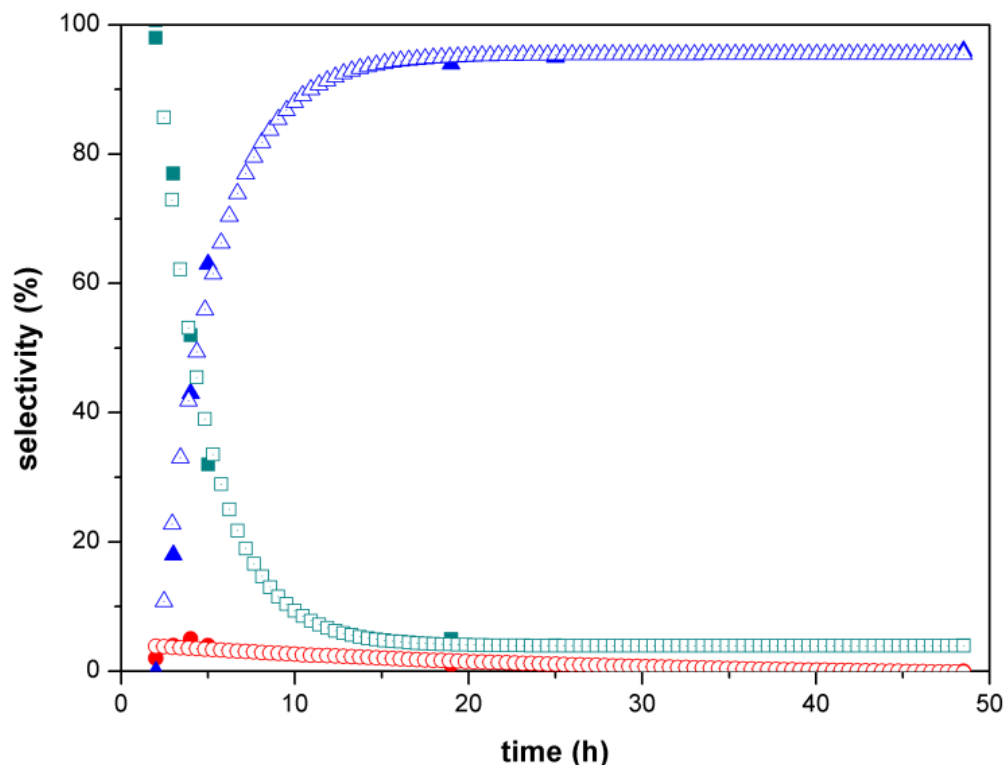
**Figure 4** Suivi cinétique de la réduction de $CO_2$ en présence de HBpin et du complexe **3** (1 mol%). Conditions : $C_6D_6$ ; 90 ºC. Formation des produits dans le temps : HOCOBpin (cyan foncé    ), pinBOCH$_2$Bpin (rouge    ) et H$_3$COBpin (bleu    ).

Nous supposons que le mécanisme mis en jeu diffère des mécanismes précédemment décrits pour les espèces à hydrure métallique. Nous suggérons un mécanisme qui commence par la coordination du $CO_2$ avec l'hydrure d'aluminium formant un composé de formiate d'aluminium (L) Al-OCOH après insertion migratoire de l'hydrure (**Schéma 1**). Dans la suite, le groupe acétate Al-OCOH sert de base à l'activation de HBpin. Par la suite, la réaction avec le $CO_2$ provoque la libération du premier produit de réduction, le formoxyborane, ou continue à réagir jusqu'à la formation du méthoxyborane.
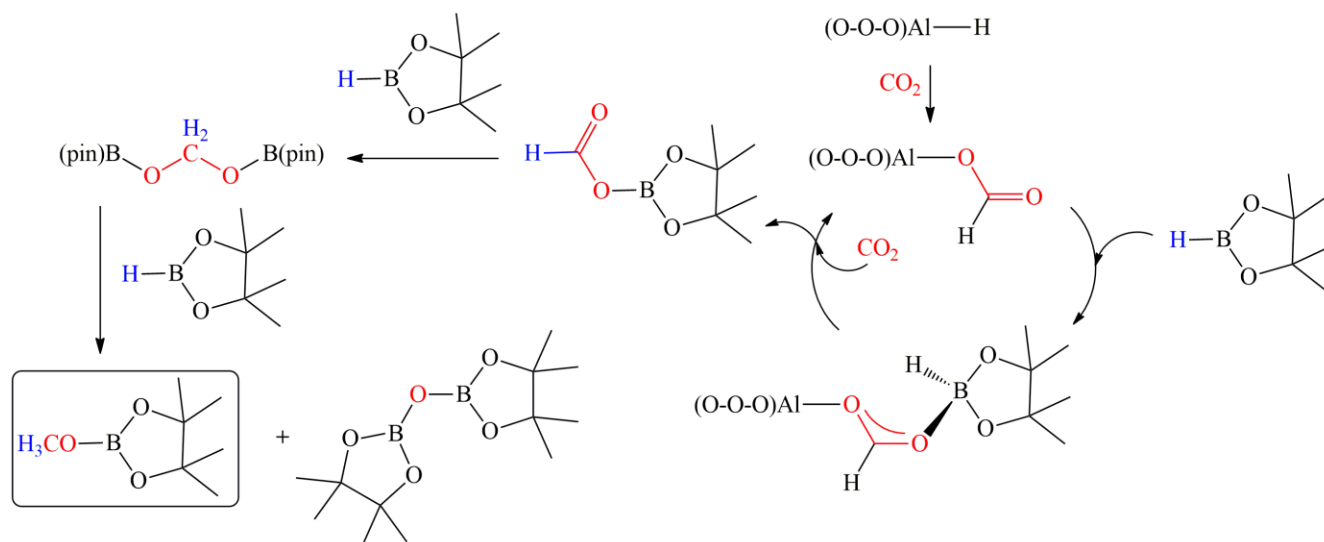
**Schéma 1** Mécanisme proposé pour la réduction de $CO_2$ avec des hydroboranes et des complexes tripodes (O-O-O) d'hydrure d'aluminium comme catalyseurs.

## 7.2   Accès au méthanol : conversion du $CO_2$ par catalyse d'hydroboration en utilisant l'anion acétate simple comme catalyseur.

Les sels d'acétate sont disponibles à grande échelle, peu coûteux, stables et non toxiques, ce qui en fait des catalyseurs de choix pour des processus durables. Nous rapportons l'utilisation de sels d'acétate très simples, peu coûteux et stables - acétate de sodium, de potassium et de tétrabutylammonium - pour la réduction du $CO_2$ avec les hydroboranes HBpin et BMS pour la première fois (**tableau 1**). De manière intéressante, ce système catalytique permet de réaliser cette réaction dans des conditions sans solvant. En conséquence, cette stratégie pourrait contribuer au développement d'une industrie basée sur les bioraffineries.

**Tableau 1** Réduction du $CO_2$ catalysée par un sel d'acétate par hydroboration en méthoxyborane et boroxine.
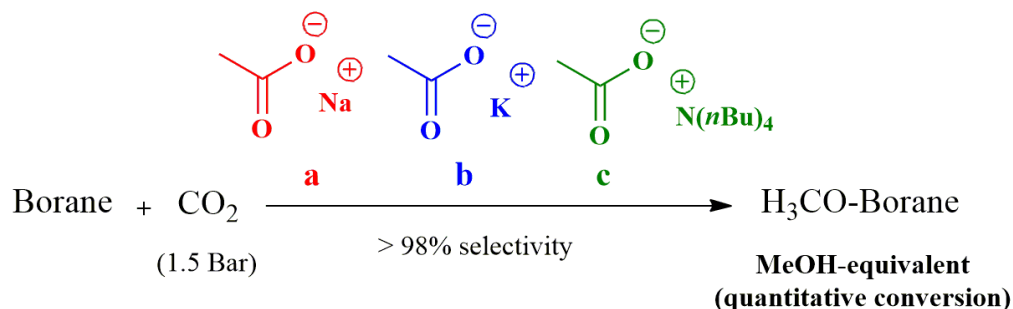


| Entrée | Borane | Catalyseur | Catalyseur (mol%) | Solvant | Temperature (ºC) | Durée (h) | Conv.[a] (%) | TON[b] | TOF (h-1)[c] |
|--------|--------|------------|-------------------|---------|------------------|-----------|--------------|--------|--------------|
| 1 | HBpin | a | 0.6 | $C_6D_5Br$ | 120 | 65 | 96 | 580 | 9 |
| 2 | HBpin | b | 0.1 | $C_6D_5Br$ | 120 | 65 | 94 | 940 | 14 |
| 3 | HBpin | c | 0.1 | $C_6D_6$ | 90 | 46 | 94 | 940 | 20 |
| 4 | HBpin | c | 1 | $C_6D_6$ | 90 | 20 | 96 | 96 | 5 |
| 5 | HBpin | c | 0.1 | - | 90 | 19 | 97 | 970 | 51 |
| 6 | $H_3B$-$S(Me)_2$ | c | 0.1 | $C_6D_6$ | 40 | 40 | 63 | 1890 | 47 |
| 7 | $H_3B$-$S(Me)_2$ | c | 0.1 | $C_6D_6$ | 60 | 20 | 83 | 2490 | 124 |
| 8 | $H_3B$-$S(Me)_2$ | c | 0.1 | - | 40 | 20 | - | - | - |

[a] Conv. = conversion. [b] TON = numéro de chiffre d'affaires; calculé par intégration des signaux spécifiques à la RMN ^{1}H des produits HOCOBpin (8,21 ppm), pinBOCH2OBpine (5,49 ppm) et méthoxyborane (3,51 ppm),[12] en utilisant l'hexaméthylbenzène comme étalon interne ; et par comparaison des spectres RMN [11]B du réactif et des produits. [c] TOF = fréquence de retournement = TON / temps de réaction.

La réduction par hydroboration a été suivie à la fois par RMN ^{1}H et [11]B. Les spectres de l'hydroboration de $CO_2$ catalysée par TBAAc (0,1 mol%) (1,5 bar) avec HBpin dans $C_6D_6$ à 90 °C sont représentés sur le **Figure 1** (^{1}H) et **Figure 2** ([11]B). En regardant la **Figure 1**, nous pouvons observer une augmentation de l'intensité du méthoxyborane à 3,46 ppm. La **Figure 2** montre une diminution constante de l'intensité du doublet HBpin à 29,03 et 27,67 ppm, ce qui correspond à sa consommation. Deux nouveaux signaux sont apparus à 22,57 et 21,59 ppm, correspondant respectivement à $H_3COBpin$ et à pinBOBpin. Ces signaux ont augmenté avec le temps, en accord avec la formation sélective du précurseur de méthanol cité dans la littérature.
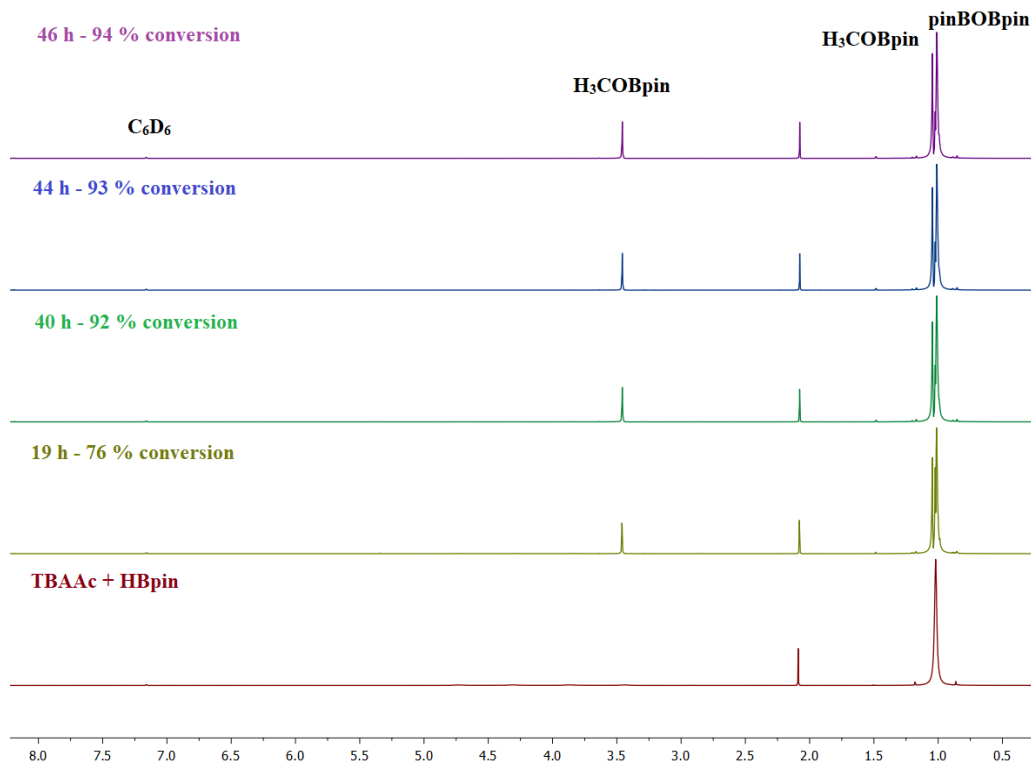
**Figure 1** Spectre RMN $^{1}$H de la réduction de $CO_2$ en présence de HBpin et de TBAAc (0,1 mol%). Conditions : $C_6D_6$ ; T: 90 ° C ; Étalon interne : hexaméthylbenzène.

Le rôle du catalyseur à base d'acétate dans la réduction de $CO_2$ par HBpin a été étudié dans des conditions stœchiométriques, en effectuant une série d'études RMN (**Figure 3**).

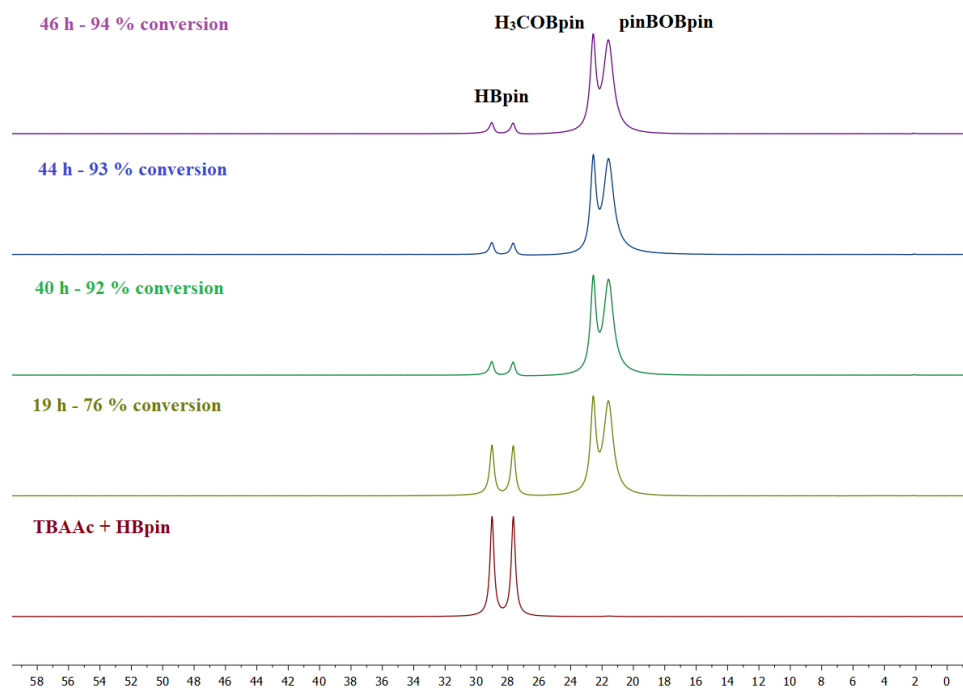**Figure 2** Spectres RMN $^{11}$B de l'hydroboration de $CO_2$ catalysée par TBAAc (0,1 mol%) (1,5 bar) avec HBpin dans $C_6D_6$ à 90 ° C ; Étalon interne : hexaméthylbenzène.
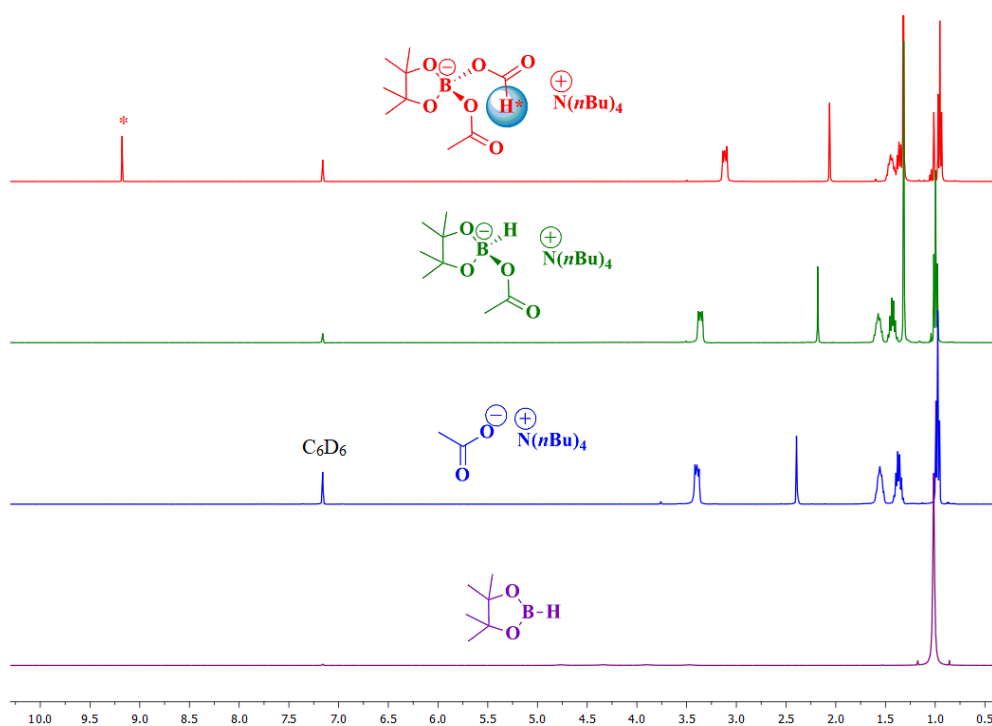


**Figure 3** Spectres RMN $^1$H enregistrés dans $C_6D_6$ de HBpin ; TBAAc ; un mélange 1: 1 de TBAAc et de HBpin après 1 heure à température ambiante ; et après addition ultérieure de $CO_2$ et 1 heure à température ambiante.

Nous proposons le cycle catalytique présenté dans le schéma 1. Initialement, le catalyseur acétate active le borane, formant ainsi l'espèce hydroborate plus nucléophile **1**. Cela permet à la réaction du $CO_2$ dans la liaison B-H de former **2**. La réaction entre **2** et HBpin; et l'ajout d'un autre équivalent de $CO_2$ génère HOCOBpin et régénère **2**. HOCOBpin réagit avec une autre HBpin pour former pinBOCH$_2$OBpin, qui, en présence d'un autre équivalent de HBpin, génère finalement CH$_3$OBpin et pinBOBpin.
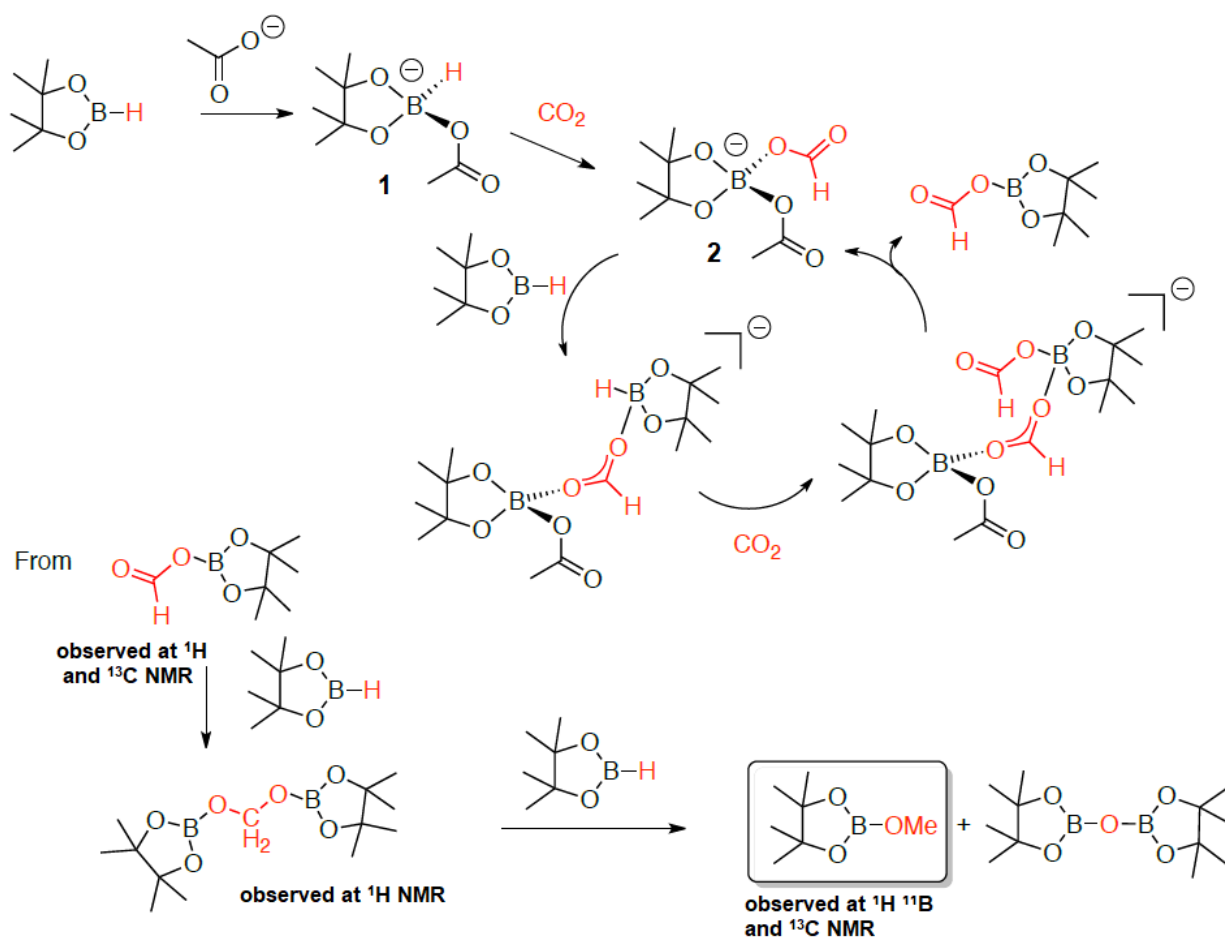


**Schéma 1** Mécanisme proposé pour la réduction de $CO_2$ par HBpin catalysée par l'acétate.

### 7.3 Synthèse Par Catalyse Organométallique De Poly- (Acide L-Lactique) de Haut Poids Moléculaire avec un Sel D'imidazolium Attaché De manière Covalente: Biomatériaux D'oxyde de Graphène Réduit à Performance Améliorée.

Ici, nous avons étudié pour la première fois la ROP de L-lactide renouvelable (L-LA) avec un complexe organométallique de Zn en utilisant un sel d'imidazolium (IS) contenant un groupe alcool comme initiateur pour fonctionnaliser la chaîne de PLLA avec un groupe de terminaison IS (PLLA-IS). Le complexe de $Zn(C_6F_5)_2$-toluène a catalysé la ROP en donnant du PLLA-IS de masse moléculaire plus élevée, ce qui a amélioré l'interaction interfaciale avec l'oxyde de graphène réduit (rGO). De nouveaux bionanocomposites PLLA-IS / rGO coulés dans un solvant (**Figure 1**) dotés de propriétés mécaniques et thermiques améliorées, ainsi que d'une activité antibiofilm fongique ont été obtenus, suggérant ainsi leur application potentielle en tant que biomatériaux.
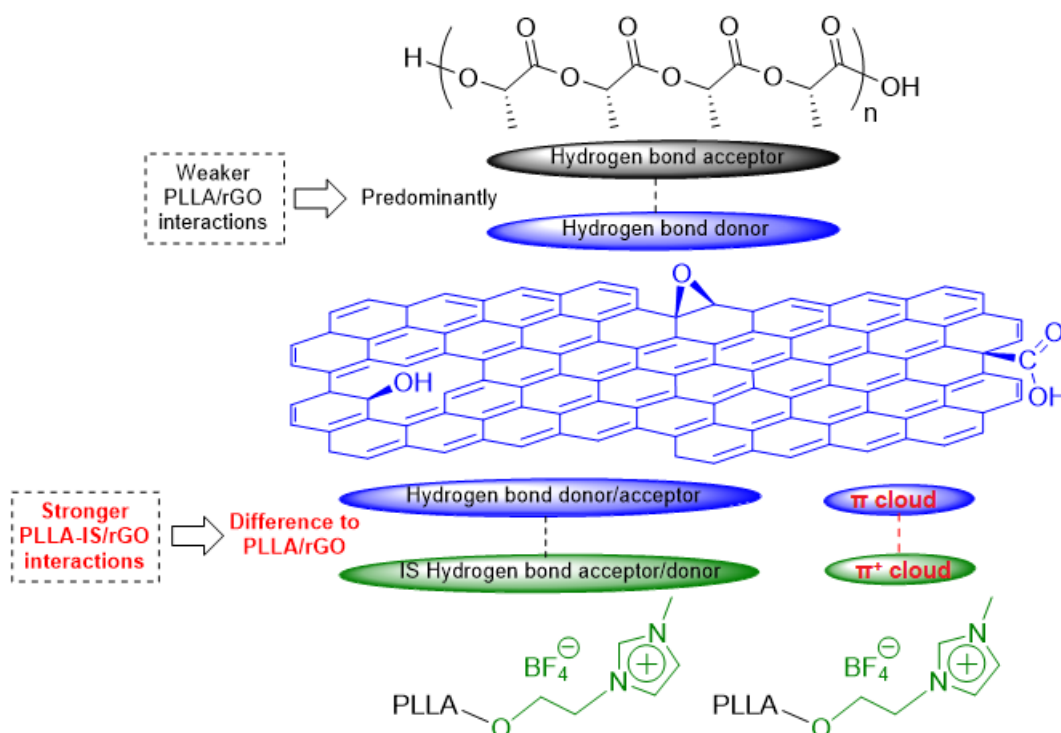


**Figure 1** Interaction proposée entre PLLA-IS et l'oxyde de graphène réduit.

La présente étude visait à combiner la capacité de dispersion du graphène et les propriétés antibiofilm du PLLA fonctionnalisé IS pour former un nouveau biomatériau renforcé. Il a été démontré que les PLLA fonctionnalisés aux extrémités IS (PLLA-IS) étaient accessibles via la ROP du lactide par des voies organocatalytiques, mais seulement les PLLA-IS de faible poids moléculaire - maximum 10 000 g/mol. Ici, nous avons montré que l'utilisation de $Zn(C_6F_5)_2$ comme catalyseur (**Tableau 1**) permettait pour la première fois l'accès au PLLA-IS de haut poids moléculaire, Mn jusqu'à 48 000 Da (**Tableau 1, entrée 13**), ce qui présente un intérêt particulier pour un point de vue industriel.

**Table 1. L-LA** ROP catalysée par $Zn(C_6F_5)_2$ toluène /IS-OH.[a]
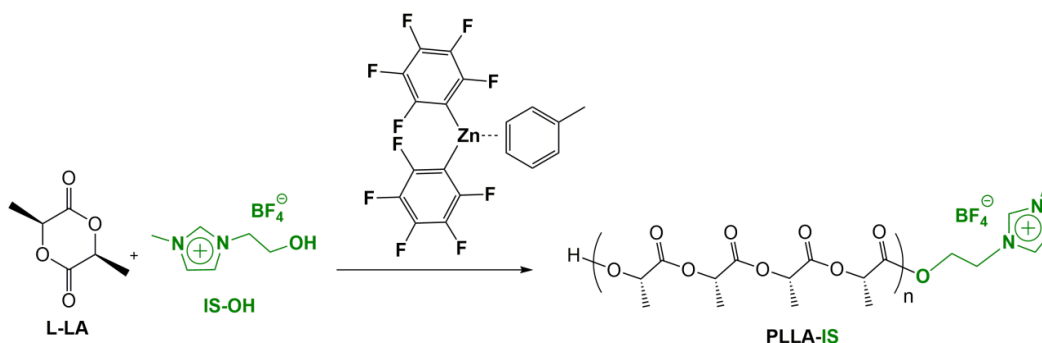


| Entréé | Zn/IS-OH/L-LA | [L-LA]/[IS-OH | t (min)[b] | Conv (%)[c] | $M_{n\ theor}$[d] | $M_n$[e] | PDI[f] |
|--------|---------------|---------------|------------|-------------|-------------------|----------|--------|
| 1 | 1/3/150 | 50 | 45 | 90 | 6,678 | 13,294 | 1.24 |
| 2 | 1/3/150 | 50 | 80 | 95 | 7,049 | 15,200 | 1.12 |
| 3 | 1/3/200 | 66 | 60 | 95 | 9,331 | 12,077 | 1.20 |
| 4 | 1/3/200 | 66 | 32 | 77 | 7,563 | 8,608 | 1.20 |
| 5 | 1/3/300 | 100 | 30 | 33 | 4,827 | 6,596 | 1.49 |
| 6 | 1/3/300 | 100 | 45 | 66 | 9,654 | 13,208 | 1.37 |
| 7 | 1/3/300 | 100 | 50 | 91 | 13,310 | 10,450 | 1.51 |
| 8 | 1/3/300 | 100 | 80 | 97 | 14,188 | 19,372 | 1.44 |
| 9 | 1/3/300 | 100 | 100 | 97 | 14,188 | 21,140 | 1.51 |
| 10 | 1/5/300 | 40 | 32 | 74 | 6,558 | 5,773 | 1.17 |
| 11 | 1/3/600 | 200 | 45 | 30 | 8,712 | 19,802 | 1.21 |
| 12 | 1/3/600 | 200 | 100 | 72 | 20,909 | 55,748 | 1.33 |
| 13 | 1/5/1000 | 200 | 6 h | 97 | 28,169 | 48,181 | 1.50 |
| 14 | 1/10/1000 | 100 | 6 h | 98 | 14,334 | 16,701 | 1.52 |
| 15 | 1/20/1000 | 50 | 6 h | 98 | 7,272 | 9,044 | 1.35 |

[a] Conditions : Toluène, [L-LA] 0 = 1 M, 80 ºC. [b] Temps de réaction en minutes. [c] Conversion L-LA. [d] Mn théorique [[(ML-LA) 0 x MwL-LA / (IS-OH)] + MwIL-OH] x. [e] Mesuré par CPG dans du THF (30 ºC) en utilisant un standard de polystyrène et un facteur de correction de 0,58. [f] Polydispersité obtenue par CPG dans du THF (30 °C).

Nous proposons le mécanisme du monomère activé (**Schéma 1**) pour la fonctionnalisation du PLLA avec IS (PLLA-IS). Le mécanisme commence par l'activation du carbonyle du groupe ester par la coordination de l'espèce d'acide de Lewis, $Zn(C_6F_5)_2$, et par l'attaque nucléophile ultérieure de l'IS sur le groupe carbonyle. Ensuite, le processus de polymérisation commence par le clivage de la liaison O-acyle. Dans l'étape suivante, l'étape de propagation est lancée à mesure que davantage de molécules de monomères participent à la réaction. De manière intéressante, le groupe IS alcoxy du nucléophile reste dans la chaîne de polymère formant ensuite le PLLA-IS.
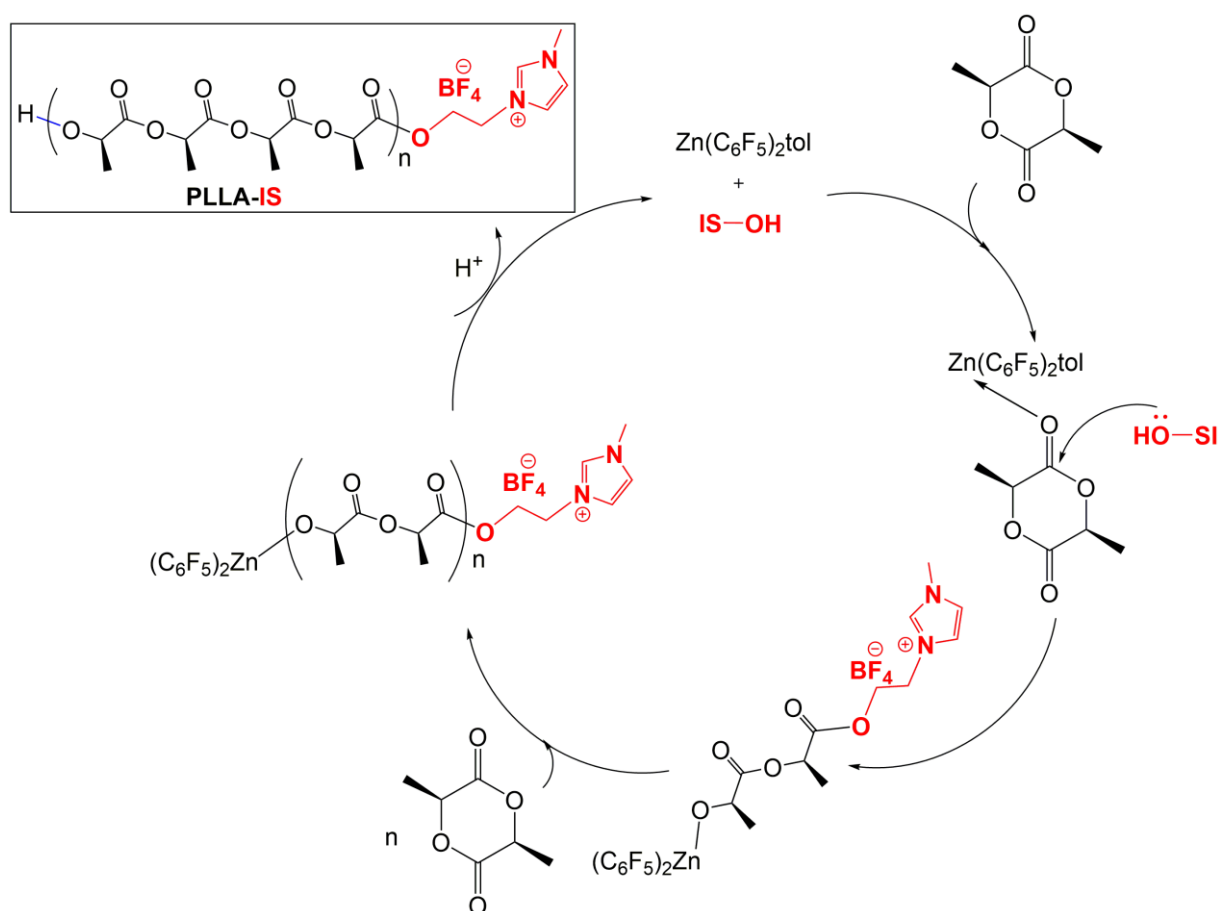


**Schéma 1** Mécanisme du monomère activé pour la formation de PLLA-IS avec le catalyseur organométallique $Zn(C_6F_5)_2$tol.

La bonne dispersion du graphène dans le matériau final est probablement expliquée par la faible gamme d'interactions π$^+$-π entre le noyau imidazolium PLLA-IS et le rGO. En revanche, lors de l'utilisation de PLLA commercial ayant un poids moléculaire similaire (à PLLA-IS), une séparation de phase a été observée quelques minutes après le coulage du mélange dans le moule (**Figure 2**), indiquant que les forces de liaison hydrogène entre PLLA et rGO ne suffisent pas pour disperser rGO dans la solution.
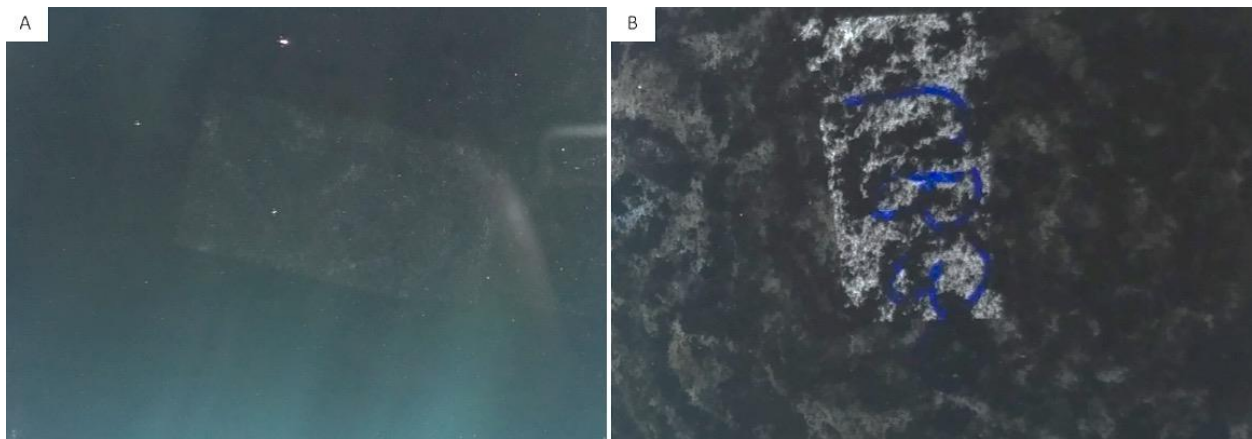
Dispersion en solution:



**Figure 2** Photographies de la dispersion de rGO dans la coulée du solvant de (A) PLLA-IS/rGO-1% et (B) PLLA-rGO-1%, avant évaporation du solvant.

Les micrographies au MEB indiquent une bonne interaction entre le polymère PLLA-IS et le rGO, montrant la formation d'une structure morphologique contrôlée de sphères de PLLA encapsulées par le réseau de graphène (**Figure 3**). La taille moyenne de ces sphères était d'environ 50 µm et était considérée comme une microsphère.
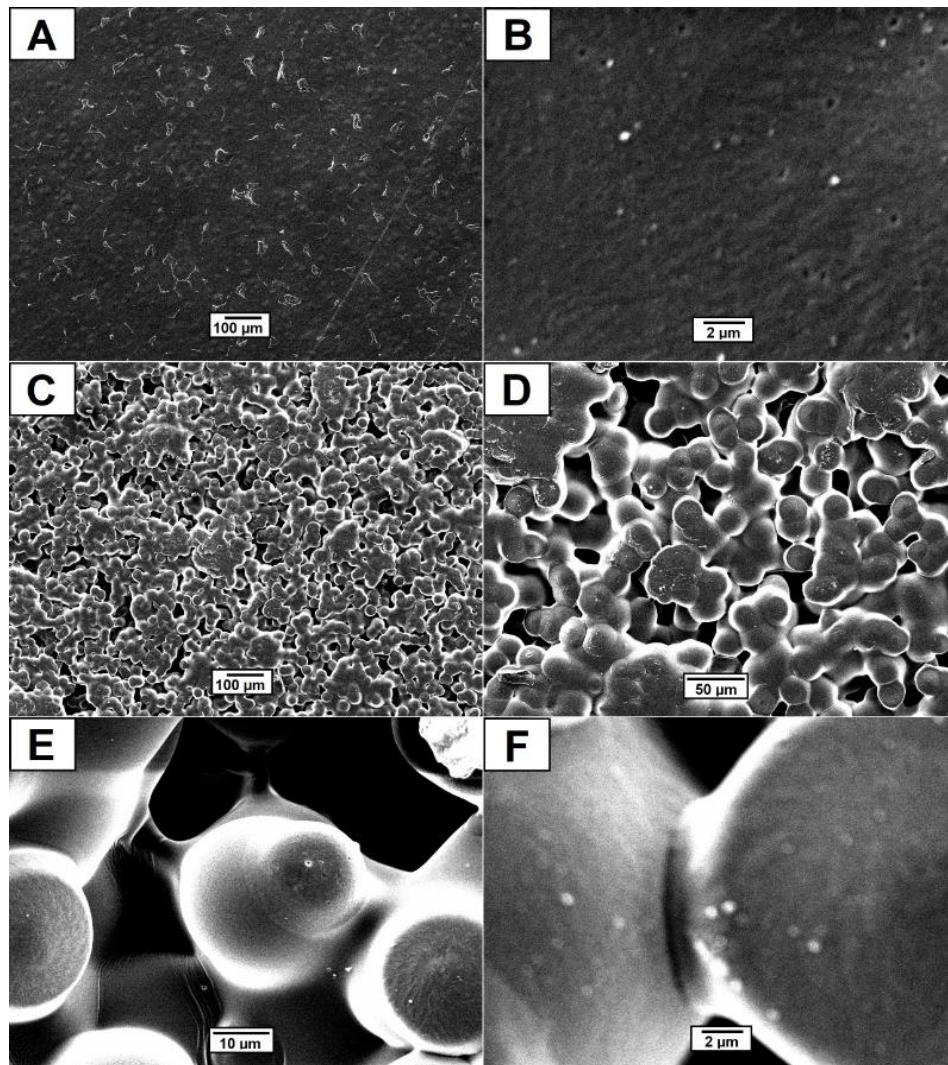


Figure 3. Micrographies MEB de (A) PLLA-IS (tableau 1, entrée 13) (barre d'échelle = 100 µm) ; (B) PLLA-IS (échelle = 2 µm) ; (C) PLLA-IS / rGO-1% (barre d'échelle = 100 um) ; (D) PLLA-IS / rGO-1% (barre d'échelle = 50 um) ; (E) PLLA-IS / rGO-1% (barre d'échelle = 10 um) ; et (F) PLLA-IS / rGO-1% (échelle = 2 µm).

Les propriétés thermiques de PLLA-IS / rGO-1% ont été comparées à celles de PLLA-IS (**Tableau 2**). L'incorporation de rGO a entraîné un gain significatif de 15 ° C pour le $T_{50\%}$, ce qui indique que le graphène a agi comme un bouclier augmentant la résistance thermique du PLLA-IS encapsulé. Les propriétés mécaniques dynamiques de PLLA-IS et PLLA-IS/rGO-1% ont également été étudiées (**Tableau 3**). Le PLLA-IS/rGO-1% a montré une augmentation de 105% du module de conservation par rapport au PLLA-IS à 30 °C. En outre, PLLA-IS/rGO-1% a présenté une augmentation significative du module de perte de 148% par rapport au PLLA-IS à 30 ºC.

**Tableau 2** Propriétés thermiques des films PLLA-IS.

| Entrée | Echantillon | $T_{5\%}$ [°C][a] | $T_{10\%}$ [°C][b] | $T_{50\%}$ [°C][c] | Résidu [%][d] |
|--------|-------------|-----------|------------|------------|-----------|
| 1 | PLLA-IS[e] | 151.2 | 291.3 | 367.4 | 0.00 |
| 2 | **PLLA-IS/rGO-1%** | 119.9 | 299.2 | 382.8 | 0.85 |

[a] Température avec une perte de poids de 5% en poids, déterminée par TGA. [b] Température avec une perte de poids de 10% en poids, déterminée par TGA. [c] Température à une perte de poids de 50% en poids, telle que déterminée par TGA. [d] Poids résiduel à 550 °C déterminé par TGA. [e] Tableau 1, entrée 13.

**Tableau 3** Propriétés mécaniques dynamiques des films de PLLA-IS.

| Entrée | Echantillon | G'30 [Mpa][a] | G'55 [Mpa][b] | G''30 [Mpa][c] | G''55 [Mpa][d] | S30 [N/M][e] | S55 [N/m][f] | Tg [°C][g] |
|--------|-------------|------|------|------|------|------|------|------|
| 1 | PLLA-IS[h] | 386.9 | 241.4 | 25.6 | 34.1 | 42,097 | 26,259 | 64.8 |
| 2 | **PLLA-IS/rGO-1%** | 795.7 | 243.4 | 63.5 | 38.7 | 58,028 | 17,753 | 59.8 |

[a] Module de stockage à 30 °C. [b] Module de stockage à 55 °C. [c] Module de perte à 30 °C. [d] Module de perte à 55 °C. [e] Rigidité à 30 °C. [f] Rigidité à 55 °C. [g] Température de transition vitreuse déterminée par DMA. [h] Tableau 1, entrée 13.

Le PLLA-IS avait un angle de contact avec l'eau de 71,0 ± 0,3 ° (**Figure 4**). Une augmentation significative est survenue avec l'incorporation de 1% en poids de rGO alors que PLLA-IS / rGO-1% atteignait un angle de contact avec l'eau de 98,4 ± 0,2º, formant un matériau plus hydrophobe.
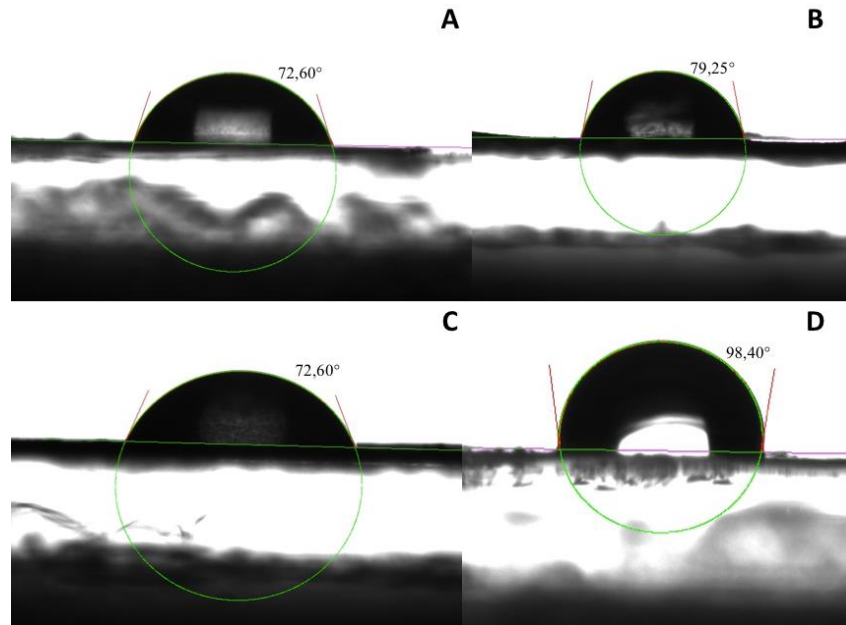
**Figure 4**. Images de dépôt de gouttelettes d'eau dans les films de polymère (A) PLLA commercial (B) commercial + rGO-1%, (C) PLLA-IS et (D) PLLA-IS / rGO-1%.

# 8 PUBLICATIONS

# NJC

Check for updates

# Organometal-catalyzed synthesis of high molecular weight poly-(L-lactic acid) with a covalently attached imidazolium salt: performance-enhanced reduced graphene oxide−PLLA biomaterials†

Yuri Clemente Andrade Sokolovicz, [ab] Clarissa Martins Leal Schrekker, [a]
Frédéric Hild, [b] Leonardo de Oliveira Bodo, [a] Júlia Lacerda Couto, [a]
Joice Sandra Klitzke, [a] Thuany Maraschin, [c] Nara Regina de Souza Basso, [c]
João Henrique Zimnoch dos Santos, [a] Samuel Dagorne [*b] and
Henri Stephan Schrekker [*a]

Herein, we report on the synthesis of imidazolium salt end-functionalized PLLA (**PLLA-IS**) and its application in the preparation of reduced graphene oxide−PLLA composites. When applying the imidazolium salt 1-(2-hydroxyethyl)-3-methylimidazolium tetrafluoroborate as the initiator, the organometallic $Zn(C_6F_5)_2$toluene complex polymerized L-lactide into high molecular weight **PLLA-IS** ($M_n$ up to 56k). The presence of this imidazolium functionality enhanced the PLLA−reduced graphene oxide interaction, which promoted a homogenous dispersion of this filler when applying a solvent casting procedure. Significant improvements in the mechanical properties were achieved, reaching 148% and 105% for the loss and storage moduli, respectively. Besides, the **PLLA-IS/rGO-1%** composite inhibited the growth of fungal biofilms, including *C. tropicalis* (43%) and *C. albicans* (34%). Altogether, these materials exhibit properties for novel applications, including as biomaterials.